

Decarbonization of Urban areas: Thermal and Electrical grid integration

Original

Decarbonization of Urban areas: Thermal and Electrical grid integration / Neirotti, Francesco. - (2022 Dec 02), pp. 1-208.

Availability:

This version is available at: 11583/2976596 since: 2023-03-06T10:43:32Z

Publisher:

Politecnico di Torino

Published

DOI:

Terms of use:

openAccess

This article is made available under terms and conditions as specified in the corresponding bibliographic description in the repository

Publisher copyright

(Article begins on next page)



Politecnico
di Torino

ScuDo

Scuola di Dottorato - Doctoral School
WHAT YOU ARE, TAKES YOU FAR

Doctoral Dissertation

Doctoral Program in Energy and Nuclear Engineering (34th cycle)

Interactions and relations between electricity generation and the heating and cooling sector

Development and potential evaluation of an adsorption prototype

By

Francesco Neirotti

Supervisor(s):

Prof. Marco Simonetti, Supervisor

Ing. Michel Noussan, Supervisor

Doctoral Examination Committee:

Prof. Davide Astiaso Garcia , Università di Roma La Sapienza

Prof. Marcello Aprile, Politecnico di Milano

Prof. Forrest Meggers, Princeton University

Prof. Kamel Abu Ghali, American University of Beirut

Politecnico di Torino

2022

Declaration

I hereby declare that, the contents and organization of this dissertation constitute my own original work and does not compromise in any way the rights of third parties, including those relating to the security of personal data.

Francesco Neirotti

2022

* This dissertation is presented in partial fulfillment of the requirements for **Ph.D. degree** in the Graduate School of Politecnico di Torino (ScuDo).

Dedicated to my beloved sons, Leonardo and Federico

Acknowledgements

Ci tengo a ringraziare le persone che mi hanno accompagnato in questi anni di studi, che culminano in questo lavoro di ricerca.

Ringrazio i miei genitori. Voi mi avete dato la libertà di seguire i miei interessi, di studiare ed arrivare fino a qui. Grazie.

Ringrazio mia sorella, Caterina, da sempre fonte di ispirazione, di consolazione, di consigli e di forza vitale.

Ringrazio Marco Simonetti e Michel Noussan che nel tempo si sono trasformati e hanno assunto per me diversi ruoli: professori negli anni di studi, tutori durante il dottorato, compagni di grandi giri in bici e di camminate nella natura. Siete, per me, modelli da perseguire e amici da tenere vicino. Grazie di tutto.

Ringrazio i miei compagni di avventura, dal primo anno di Politecnico fino all'ultimo anno di Dottorato: Riccardo, Luca, Vincenzo, Giulia, Alessandro, Daniele, Alessandro. Sono assolutamente convinto che la bellezza e l'intensità di questo percorso sia dovuta soprattutto a tutti voi. Grazie!

Grazie Alessia, collega di studi, amica, fidanzata, moglie e mamma. Grazie per il tuo sostegno nei momenti felici e nei momenti dove il nervoso, la paura e l'ansia erano predominanti. Per la serenità che hai portato nella mia vita e per la tua forza, che tanto mi aiuta ogni giorno. Grazie, soprattutto, per aver deciso di imbarcarti con me nel viaggio più bello e intenso: quello della Vita.

Ringrazio infine questi 10 anni di vita accademica, che tanto mi hanno regalato, che tanto mi hanno fatto vivere e che mi hanno visto entrare come matricola e uscire come papà.

Abstract

The electrification of final uses refers to the process of substituting fossil-based technologies with electricity-driven ones to exploit the renewable energy source (RES) production to decrease the CO_2 and pollutant emissions. Is a complete switch to electricity the right solution? What are the real benefits of this solution today? And what will they be in a future dominated by renewable energy sources? The first major synergy between the electricity and heat sectors is found in district heating systems. Simulations of different solutions for lowering the temperature in heat grids have been carried out to show that the interaction with heat pumps does not always seem to improve these two indices. In fact, the developed simulation, decreasing temperature (towards $60^\circ C$) in already built networks seems to have the potential to reduce energy losses and consumption while maintaining the indoor temperature in an acceptable range. Indeed, if the building is well insulated and/or new construction, $60^\circ C$ can be even too much. For this reason, the booster heat pump can play a major role in keeping the temperature level of the network ring lower (towards $45-50^\circ C$) and boost up the temperature just where it is needed. From the simulated cases, this can be an effective solution, but it presents a drawback. In fact, the solution with HP presents higher primary energy consumption (about 30%) and higher carbon dioxide emissions (in a range of 140 to 227 tCO_2 more) with respect to the $60^\circ C$ cases. But this outcome may be related to the usage of average coefficients (primary energy factor and CO_2 -factor) which can be no longer valid in a time of strong energy transition. The actual consumption data of different real heat pump installations were matched with hourly energy production data for 10 different European countries. The actual HP consumption mix is compared with the annual generation mix of each country to assess the extent to which an hourly analysis differs from an annual average and whether the additional data requirements are justified by the more accurate results that can be obtained. The results do not provide any particular differences from the averages under the working hypothesis (about 5-6% difference),

although some peaks do ring alarm bells for the near future: likely, the average values will no longer be representative of reality in a short time, as the share of renewable energies increases rapidly. Then, according to IEA estimates, cooling will be the most energy-intensive sector by 2050. Countries with hot, humid, and summery climates all year round are equipping themselves with air conditioning and cooling systems at an exponential rate. This leads to high loads on the electricity grid and higher emissions of refrigerant gases, which affect the greenhouse effect and are generally harmful to the environment. Adsorption refrigeration systems can offer some advantages to limiting energy consumption and improving the management of high humidity in summer in equatorial climates. The ReCognition project (H2020-LC -SC3-2018) has developed and integrated renewable technologies to improve the energy efficiency of buildings and local energy consumption. In this dissertation, the development of a prototype for cooling (HySun) based on adsorption is reported. The main objective of HySun is to improve efficiency compared to traditional compression cycles and to work with multiple sources and multiple energy vectors to generate cooling power and drive the regeneration cycle. This system has been designed and implemented. First, a coating technique has been implemented and tested to verify the performance of coating which has been found to be lower than the pure material, but still with a large possibility to improve. Moreover, a simulation code was developed to understand HySun behaviour and the dependencies of the variables. A parametric analysis and a dynamic simulation show the possibilities of the system as well as some disadvantages that must be considered in the real operation of the prototype. Temperature levels, such as the one used in the developed simulation, allow the integration of several renewable energy technologies for the adsorption and regeneration phases, which is important from the point of view of increasing renewable penetration. The developed simulations present important results as the HySun prototype seems to outperform the market compression cycle. In fact, the estimate COP varies between 2.85 and 5.2, which are peak values for commercial units. One of the major drawbacks of this type of system is that, given the non-linear behaviour of the adsorbent material, precise and targeted control must be envisaged to ensure a constant and stable cooled airflow. In summary, this dissertation shows that choices in heating, cooling and mobility could have a major impact on the electricity sector. Cooperation between traditional heating and electrification could provide stable and profitable results. Special attention needs to be paid to cooling, which is expected to be the ruler of electricity consumption in

the near future. Adsorption systems, like HySun, can be fundamental to increase the efficiency of the whole sector.

Contents

List of Figures	xi
List of Tables	xviii
Nomenclature	xx
1 Electrification of Final Uses	1
2 Heating and Electricity: possible collaboration points	9
2.1 From District Heating to Smart Energy System	9
2.2 Modernization of today Thermal Grid and High Energy Related Users	15
2.2.1 Methodology	16
2.2.2 Case Studies	20
2.2.3 Results	23
2.2.4 Booster Heat Pumps	27
2.2.5 Conclusions	29
2.3 Heat pumps electricity Consumption: Effective Energy Mix Con-	
sumption	31
2.3.1 Methodology	39
2.3.2 Results	41
2.3.3 A comparison with electric mobility	46

3	Recognition EU Project and the HySun prototype	52
3.1	The Recognition Project	52
3.1.1	The ReC Objective	53
3.2	HySun: The Hybrid-Solar Cooling Prototype	56
3.2.1	Adsorption fundamentals	57
3.2.2	Adsorbents	59
3.3	The Prototype	62
3.3.1	Project, Schemes and Working Principles	65
3.4	Silica Gel Coating	73
3.4.1	Coating Recipe and Fundamentals	73
3.4.2	Aluminium plates: adsorption and regeneration tests	75
3.4.3	HX Drying Machine	79
4	Dynamic Simulation of the Adsorption Process	83
4.1	Main Adsorption Process Models	83
4.1.1	Langmuir model	83
4.1.2	Dubinin-Polanyi model	84
4.2	Developed Adsorption Model	86
4.2.1	Numerical Equations	94
4.2.2	Auxiliary Equations	99
4.3	Literature Comparison - A Model Validation	100
4.4	Parametric Analysis	105
4.4.1	Performance Coefficients	107
4.4.2	Results of the parametric analysis	111
4.5	Dynamic Simulation for Turin City	133
4.5.1	Input Parameters	134
4.5.2	Results	136

4.5.3	Influence of switch time	140
4.5.4	Influence of air flow rate	143
5	Conclusions	148
	References	153
	Appendix A Heat Pump Profiles and Electricity Energy Mix	165
	Appendix B Adsorption model	175
B.1	Convergence analysis	175
B.2	Parametric Analysis	177
B.2.1	Heat Exchanger Length	177
B.3	HySun and Dryer: Scheme and Drawings	179

List of Figures

1.1	Annual population increase and relative projections, divided by specific countries. Author's elaboration from [1]	2
1.2	Global Electric passenger car stock. Author's elaboration from [8] .	3
1.3	Installed HP stock trend for selected countries. Author's elaboration from [15]	5
1.4	(Left) Global AC unit stock from 1990 to 2020 and projection towards 2050. (Right) Share of global electricity demand growth to 2050. Author's elaboration from [18]	6
1.5	Share of latent load in a traditional compression cycle with respect to the sensible one. Author's elaboration of data from [21]	7
2.1	Evolution of District Heating System [31]	10
2.2	Specific emissions for DH with allocation methods and for GB . . .	13
2.3	Specific emissions for DH with allocation methods and for GB - Detail of minor contribution	14
2.4	Modelica model of the typical User [23]	17
2.5	Modelica model of simulated system [23]	19
2.6	Plant Load profile: comparison for the different use cases.	24
2.7	Indoor temperature: comparison for the different use cases.	24
2.8	setpoint Factor comparison across the different solutions	26
2.9	Schematic representation of the distributed HP [23]	27

2.10	Comparison of annual performance of HP and different supply temperatures [23]	29
2.11	Primary Energy Consumption of the different strategies [23]	29
2.12	Electricity Generation share by source. Author's elaboration from [75]. "Other" represent Biofuels, waste and not fully verified data.	32
2.13	Monthly RES share variation for selected US states. Author's elaboration from [81]	34
2.14	Monthly RES share variation for selected EU countries. Author's elaboration from [82]	35
2.15	Average electricity mixes in 2019 on an annual basis in different European countries [28]	36
2.16	Average Heat Pump electrical load from [83, 27]	38
2.17	Average Heat Pump electrical load from [27, 84]	39
2.18	ITALY - electricity production mix compared with the electricity consumption mix of the different HP systems	42
2.19	Austria - Monthly variation of the energy mix share and the HP consumption share [27]	43
2.20	C3 Load profiles with respect to different countries [27]	45
2.21	ITALY - Monthly variation of the energy mix share and the HP consumption share	46
2.22	Different EV charging profiles [28]	48
2.23	Comparison of direct hourly emission factors in selected European countries.	49
2.24	Variability of annual emission factors of EV charging in each country (with variable year and charging profile).	50
3.1	Recognition Work Packages	56
3.2	Typical Adsorption Isotherm Shape [116]	59
3.3	Silica gel grains	59

3.4	a) Primary unit of zeolites types A, X and Y; b) unit cell of zeolites type A; c) unit cell of zeolites types X and Y	61
3.5	Activated carbon	61
3.6	Activated alumina pellets	61
3.7	Typical equilibrium adsorption isotherms of water vapor for various adsorbent materials at 25°C [118]	62
3.8	Block Diagram of the Solar Hybrid Cooling System	63
3.9	Process air transformation. Classic Compression cycle (red) against the theoretical HySun transformation (blue)	64
3.10	CAD scheme of the Solar Hybrid Cooling System	66
3.11	CAD scheme: Legend	67
3.12	Water and Air flow with active components and sensors location	70
3.13	HySun Adsorption Unit. 3D assembly from SolidWorks Software.	71
3.14	Adsorption Unit. Real Prototype picture	71
3.15	Adsorption Unit. Real Prototype picture	72
3.16	HySun Adsorption Unit, CAD scheme. Extrapolation from the main CAD in figure 3.10	72
3.17	Heat Pump Detail, CAD scheme. Extrapolation from the main CAD in figure 3.10	73
3.18	(a) Aluminium testing plate with coated surface, (b) mixture in progress	75
3.19	Adsorption Boxes	76
3.20	Kern KB 360-3N	76
3.21	Adsorption tests: experimental results for different tested conditions	77
3.22	Heat Exchanger drying machine	80
3.23	Drying Machine	81
3.24	Drying Machine: HX chamber detail	82
4.1	Pictorial representation of the Mass diffusion through pores	88

4.2	Electrical Equivalent of the mass transfer resistance	88
4.3	Electric resistance scheme for thermal resistances between silica gel and water	92
4.4	Adsorption Isotherm for silica gel form model	100
4.5	Outlet Air temperature comparison [135]	101
4.6	Humidity ratio comparison [135]	101
4.7	Outlet Air temperature comparison [136]	105
4.8	Humidity ratio comparison [136]	105
4.9	Adsorption heat exchanger geometrical configuration	107
4.10	(a) Temperature, (b) specific humidity of outlet air and (c) silica-gel water uptake for different heat exchanger lengths	111
4.11	Instant COP_{el} variation during adsorption	113
4.12	(a) Sensible, (b) latent and (c) global cooling power for different heat exchanger lengths	114
4.13	Simulated Heat Pump power load	115
4.14	Overall Thermal COP and Water Heating Power during Regeneration	116
4.15	Average moisture removal as a function of heat exchanger length . .	116
4.16	(a) Temperature, (b) specific humidity of outlet air and (c) silica-gel water uptake for different regeneration water temperatures	117
4.17	Instant and average COP_{el} as a function of hot water temperature . .	118
4.18	(a) Sensible, (b) latent and (c) total cooling power as a function of the regeneration temperature variation	119
4.19	Heat pump electric power load as a function of regeneration temper- ature	120
4.20	Overall Thermal COP and Water Heating Power during Regeneration with different the regeneration temperature	121
4.21	Average moisture removal as a function of regeneration water tem- perature	121

4.22	Temperature, specific humidity of outlet air and silica-gel water uptake for different cold water temperatures	122
4.23	Instant and average COP_{el} for different cold water temperatures . . .	123
4.24	Sensible, latent and total cooling power for different adsorption water temperatures	124
4.25	Heat pump electric power consumption for different adsorption water temperatures	125
4.26	(a) Thermal COP, (b) Water Heating Power and (c) Average moisture removal for different adsorption temperature	126
4.27	(a) Temperature, (b) specific humidity ratio of outlet air and (c) silica-gel water uptake as a function of air velocity	127
4.28	Instant and average COP_{el} as a function of air velocity	128
4.29	(a) Sensible, (b) latent and (c) total cooling power as a function of air velocity	129
4.30	(a) Fan and (b) heat pump electric power for different air stream velocities	130
4.31	(a) Thermal COP, (b) Water Heating Power and (c) Moisture removal effectiveness for different air stream velocity	131
4.32	HySun COP comparison with respect to different market ready HP technologies.	132
4.33	Temperature (a), specific humidity ratio (b) of outlet air and silica-gel water uptake (c)	136
4.34	Outlet air temperature and specific humidity ratio for the complete system	137
4.35	Sensible cooling power	138
4.36	Latent cooling power	138
4.37	Total cooling power	139
4.38	Average outlet air temperature for different switch times	140
4.39	Average air moisture removal	141

4.40	Sensible (a), latent (b) and total (c) cooling power as switch time varies	142
4.41	Average outlet air temperature for different air flow rates	144
4.42	Average air moisture removal for the investigated air flow rates . . .	144
4.43	(a) Sensible, (b) latent and (c) total cooling power for the investigated air flow rate	145
A.1	POLAND - electricity production mix compared with the electricity consumption mix of the different HP systems	166
A.2	GERMANY - electricity production mix compared with the electricity consumption mix of the different HP systems	167
A.3	AUSTRIA - electricity production mix compared with the electricity consumption mix of the different HP systems	168
A.4	IRELAND - electricity production mix compared with the electricity consumption mix of the different HP systems	169
A.5	SWITZERLAND - electricity production mix compared with the electricity consumption mix of the different HP systems	170
A.6	DENMARK - electricity production mix compared with the electricity consumption mix of the different HP systems	171
A.7	FRANCE - electricity production mix compared with the electricity consumption mix of the different HP systems	172
A.8	NETHERLANDS - electricity production mix compared with the electricity consumption mix of the different HP systems	173
A.9	UNITED KINGDOM - electricity production mix compared with the electricity consumption mix of the different HP systems	174
B.1	Maximum air outlet temperature during adsorption and computational time as a function of Δz	176
B.2	Maximum air outlet temperature during adsorption and computational time as a function of Δt	177
B.3	Average COP_{el} variation	177

B.4	(a) Fan and (b) water pump electric power request for different heat exchanger lengths	178
B.5	HySun COP comparison with respect to different market ready HP technologies. Cooling Output Power Limited to 5kW	178
B.6	Adsorption Unit. Real Prototype	179
B.7	Adsorption Unit. Real Prototype	180
B.8	CAD scheme: Auxiliary Cooler connection(left) and Heater (right) .	181
B.9	3D scheme of the drying machine	182
B.10	Dryer Machine	183
B.11	Dryer Machine	184

List of Tables

2.1	Annual energy performance of the different cases	25
2.2	CO ₂ emission factors for the different energy sources	41
2.3	Summary of the different EF and their variation for the HP systems .	44
2.4	Emission factors for electricity generation from different sources [70, 85]	49
2.5	Variation of annual emission factors over charging profile and years for each country	51
3.1	Barriers and Opportunities for further development of RES integra- tion and improvement in the buildings sector	54
3.2	Sum-Up table reporting the project partners and their role	55
3.3	Main HySun Components. Please, refer to figure 3.10	68
3.4	Theoretical coating recipe	74
3.5	Water Uptake comparison between pure Silica Powder and Coated Silica	78
3.6	Main sample and coating data	79
4.1	Experimental conditions from [135]	102
4.2	Experimental conditions, reference [136]	104
4.3	Input Parameters for Silica-Gel Layer and Geometrical Shape of the HX	106
4.4	Water and Airflow tested condition	107

4.5	Heat Pump Technical Data. An Example of available observation from [137].	134
4.6	External Input Conditions	135
4.7	Air and water flow conditions	135

Nomenclature

Greek Symbols

α ratio of heat exchange area on air side to heat exchanger volume [m^{-1}]

β friction factor [-]

η efficiency [-]

ρ density [$kg\ m^{-3}$]

σ ratio of minimum free flow area to frontal area [-]

τ_s tortuosity factor [-]

ε porosity [-]

Subscripts

a air

b adsorption battery

o initial condition

s silica-gel

w water

Other Symbols

ΔP pressure drop [Pa]

\dot{G} mass transfer rate [$kg\ m^{-3}\ s^{-1}$]

\dot{m}	mass flow rate [$kg\ s^{-1}$]
\dot{Q}_{cool}	cooling power [W]
\dot{V}	volumetric flow rate [$m^3\ s^{-1}$]
\dot{W}_{el}	electric power [W]
A	area [m^2]
a	specific area [$m^2\ m^{-3}$]
A_o	minimum free flow area [m^2]
A_{hx}	heat exchange area [m^2]
COP_{el}	electric coefficient of performance [-]
COP_{th}	thermal coefficient of performance [-]
d_h	hydraulic diameter [m]
d_i	pipes inner diameter [m]
D_m	molecular diffusivity [$m\ s^{-1}$]
D_o	surface diffusion constant [$m\ s^{-1}$]
d_o	pipes outer diameter [m]
D_s	surface diffusivity [$m\ s^{-1}$]
D_{eff}	effective diffusivity [$m\ s^{-1}$]
D_{kn}	Knudsen diffusivity [$m\ s^{-1}$]
dv	Infinitesimal volume [m^3]
dz	Infinitesimal length [m]
e	enthalpy [$J\ kg^{-1}\ K^{-1}$]
f	friction factor [-]
h	convective heat transfer coefficient [$W\ m^{-2}\ K^{-1}$]

h_m	convective mass exchange coefficient [$kg\ m^{-2}\ s^{-1}$]
H_{ads}	heat of adsorption [$J\ kg_w^{-1}$]
k	thermal conductivity [$W\ m^{-1}\ K^{-1}$]
K_f	mass transfer coefficient [$m\ s^{-1}$]
K_g	overall mass transfer coefficient [$kg\ m^{-2}\ s^{-1}$]
L_p	pipes length [m]
L_x	adsorption battery width [m]
L_z	adsorption battery height [m]
L_z	adsorption battery length [m]
N_p	number of pipes [-]
Nu	Nusselt number [-]
P	pressure [Pa]
p_f	fin pitch [m]
R	gas constant [$JK^{-1}mol^{-1}$]
r_p	average pore radius [m]
Re	Reynolds number [-]
RH	relative humidity [-]
Sc	Schmidt number [-]
Sh	Sherwood number [-]
T	temperature [$^{\circ}C$]
t	time [s]
t_s	silica-gel layer thickness [m]
U	global heat transfer coefficient [$W\ m^{-2}\ K^{-1}$]

v	velocity [$m \ s^{-1}$]
W	water uptake [$kg_w \ kg_s^{-1}$]
x	specific humidity [$kg_v \ kg_a^{-1}$]
X_l	longitudinal fin pitch [m]
X_t	transversal fin pitch [m]
V	volume [m^3]

Acronyms / Abbreviations

AC	Air Conditioning
ACC	Air Conditioning and Cooling
ADS	Adsorption
AHX	Adsorption Heat Exchanger
CHP	Combined Heat and Power
CO2EF	CO ₂ Emission Factor
DH	District Heating
DHS	District Heating System
EIA	Energy Information Administration
EU	European Union
EV	Electric Vehicle
GB	Gas Boiler
HC	Heating and Cooling
HP	Heat Pump
HX	Heat Exchanger
IEA	International Energy Agency

LCF Life Cycle Factors

LTDH Low Temperature District Heating

NGCC Natural Gas Combined Cycle

PEF Primary Energy Factor

ReC ReCognition

RES Renewable Energy Source

RET Renewable Energy Technology

SCP Specific Cooling Power

SDG Sustainable Development Goal

TAC Thermally-Driven Air Conditioning

TMY Typical Meteorological Year

TSO Transmission System Operator

WHR Waste Heat Recovery

Chapter 1

Electrification of Final Uses

The Earth population is growing year by year and it is forecast to reach 8.5 billion in 2030 and 10.9 billion in 2100 [1]. As reported in the following figure, selected areas of the world are at the lead of this exponential growth. In fact, Asia and sub-Saharan Africa will be at the lead of the projected growth, even if with different growth rates between Africa and Asia. Specifically, more than half of the increase in global population (to 2050) is expected to come from just 9 countries: India, Nigeria, Pakistan, Democratic Republic of Congo, Ethiopia, The United Republic of Tanzania, Indonesia, Egypt and the United States of America (USA).

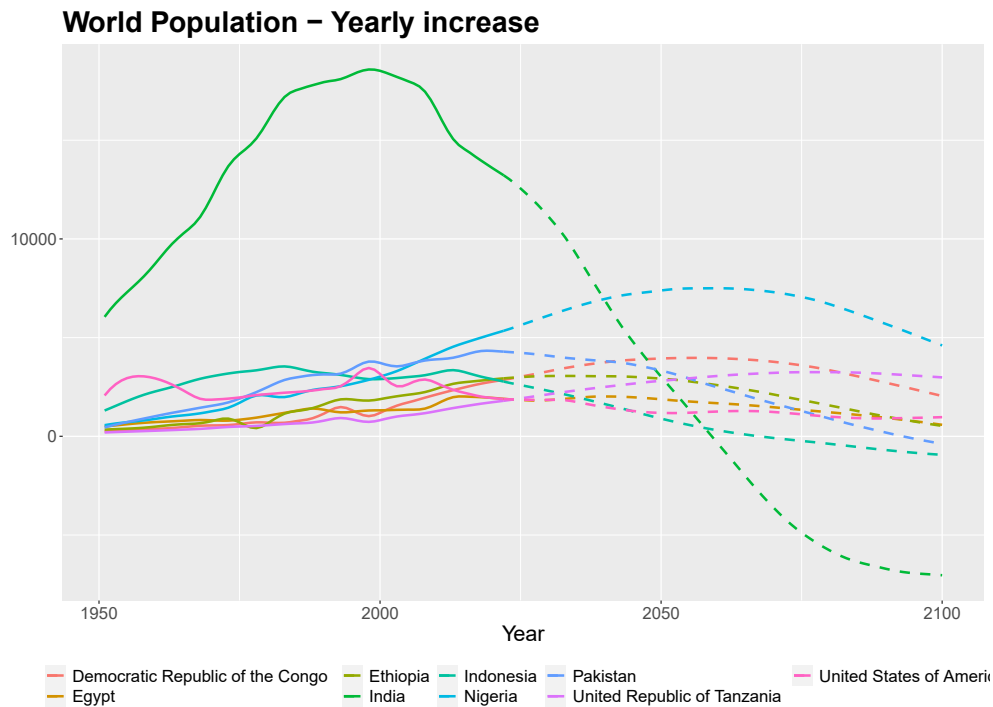


Fig. 1.1 Annual population increase and relative projections, divided by specific countries. Author's elaboration from [1]

It is important to notice that the fastest growing countries are also the least developed (African countries, Indonesia, etc.) or the ones which are experimenting a rapid growth rate, as India. This means that demographic and economic growth will proceed side by side in those areas, leading to great economic and environmental pressure and challenging policy makers and governments to ensure a sustainable development, following the Sustainable Development Goals (SDGs) set by the United Nations [1, 2]. SDGs are pushing a 360° sustainability. In particular, for energy, it is pushing for higher efficiency, clean energy (especially in cities) and more renewable energy for final uses. A well known solution is the electrification. The electrification of final uses refers to the process of substituting fossil-based technologies with electricity-driven ones in order to exploit the renewable energy sources (RES) production to improve efficiency and decrease the CO_2 and pollutant emissions [3]. The climate change related issues are pushing the carbon intensive sectors toward this solution contributing to the steep growth rate of the electricity vector presence in global final energy consumption which moves from 15% in 2000 to 19% in 2017 and it is expected to reach 25-30% by 2040 depending on the

different scenarios depicted by the International Energy Agency (IEA) [4, 5]. The transport and the heating and cooling (HC) sectors are at the lead of this rise, driven by dedicated policies and incentive schemes in large part of the developed world as they still heavily rely on fossil fuels [6, 4].

Electric Vehicles

Electric vehicles (EVs) overcome the 10 million units on the road in 2020, according to the IEA, doubling in just 3 years (2018 to 2020) [7]. Of course, the youth of this technology in the mass-market makes it easy to have important growth-rates and its distribution is unfair around the world as reported in figure 1.3. Nevertheless, EVs are an important driving force for electricity consumption and peak power issue as it is expected to dramatically increase in numbers.

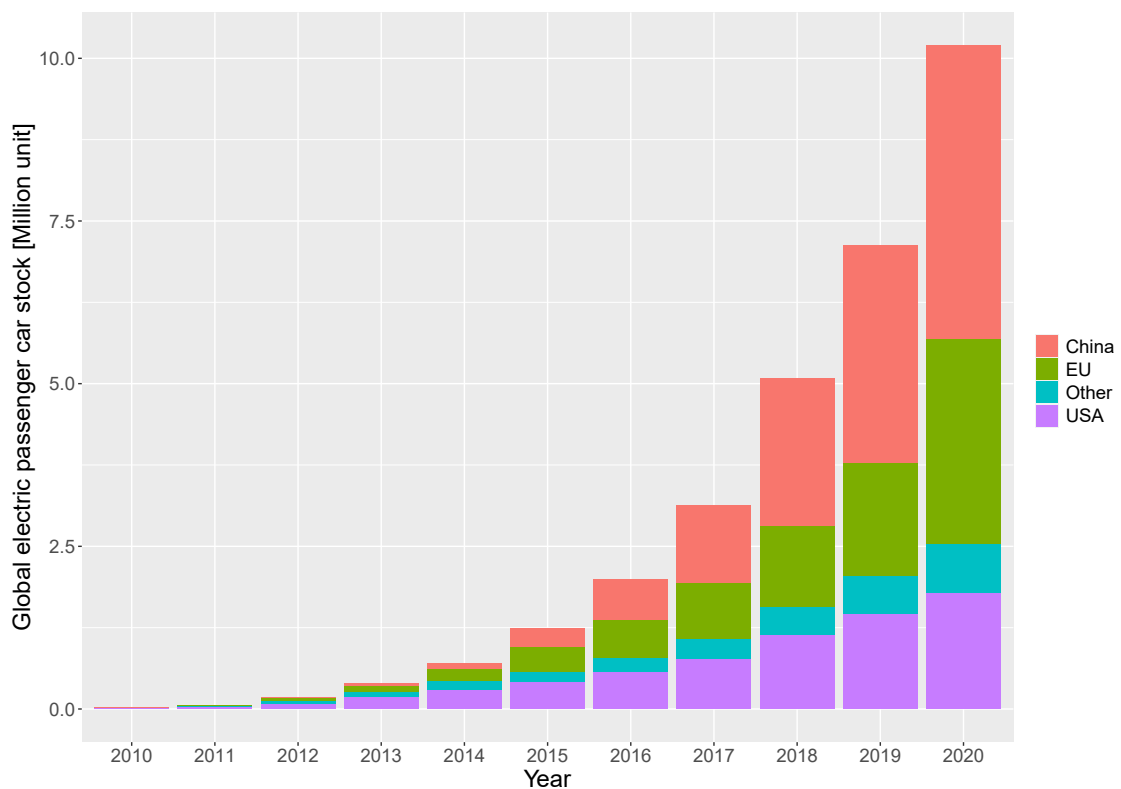


Fig. 1.2 Global Electric passenger car stock. Author's elaboration from [8]

Heating and Cooling

The HC sector is running on the same road as EVs in EU, shifting towards electricity as main energy vector especially for heating. The heating sector represents the largest energy sector in 25 out of 28 EU countries, followed by the electricity one, and still it relies heavily on fossil fuels. Today, only 21 countries worldwide have sustainable heating policies against the 114 that have electricity ones [9, 10] highlighting a lack of consideration and knowledge about the impact of the heating sector. Large amount of energy for heating purposes is spent in cities, which are responsible of around 70% of overall CO_2 emissions. Moreover, it is expected that cities will dramatically increased their citizens numbers, leading to higher energy needs [11], and planning specific policies is needed to contain the energy-related emissions.

Heat Pumps (HPs) are one of the promising solutions for the heating sector thanks to their potentialities in reducing CO_2 emissions, which are very well know and addressed in the literature [12, 13]. Despite HPs undeniable advantages, supporting policies are quite new. In [14] the authors retrace the evolution of heat pumps policies from 70's to 2015 situation, which mark an important year for HP policies [15]. It is highlighted that, even if the technical potentialities of this technology are well demonstrated, socio-economic barriers always keep the boosting policies for HP overshadow in favour of fossil fuels. Even in recent years, natural gas was pushed at the expense of HPs in several countries. Today, many authorities from local governments to national institutions are pushing towards this technology to improve the efficiency of the heating and cooling sector. Even if global absolute numbers about HPs market are extremely hard to find, due to the wide number of applications and technologies under heat pump umbrella definition, is it possible to see that in different areas of the world the volumes are running-up: in Europe the annual sales, related to the building sector only, move from around 800k units in 2010 to over 1.4 million in 2019 [16] and this trend is expected to increase also due to the multiple incentive policies in place in all the EU member countries [17]. In the USA around 45% of the newly constructed buildings have HP as main heating technology while in China HP water heaters sales have tripled in the last 10 years [15]. Even if today only 5% of the residential heat demand is covered by HP [15], this technology is at the center of policies around Europe [17] and the world [3] and their heating coverage, in the building sector, is expected to move towards 20% in 2030 [15].

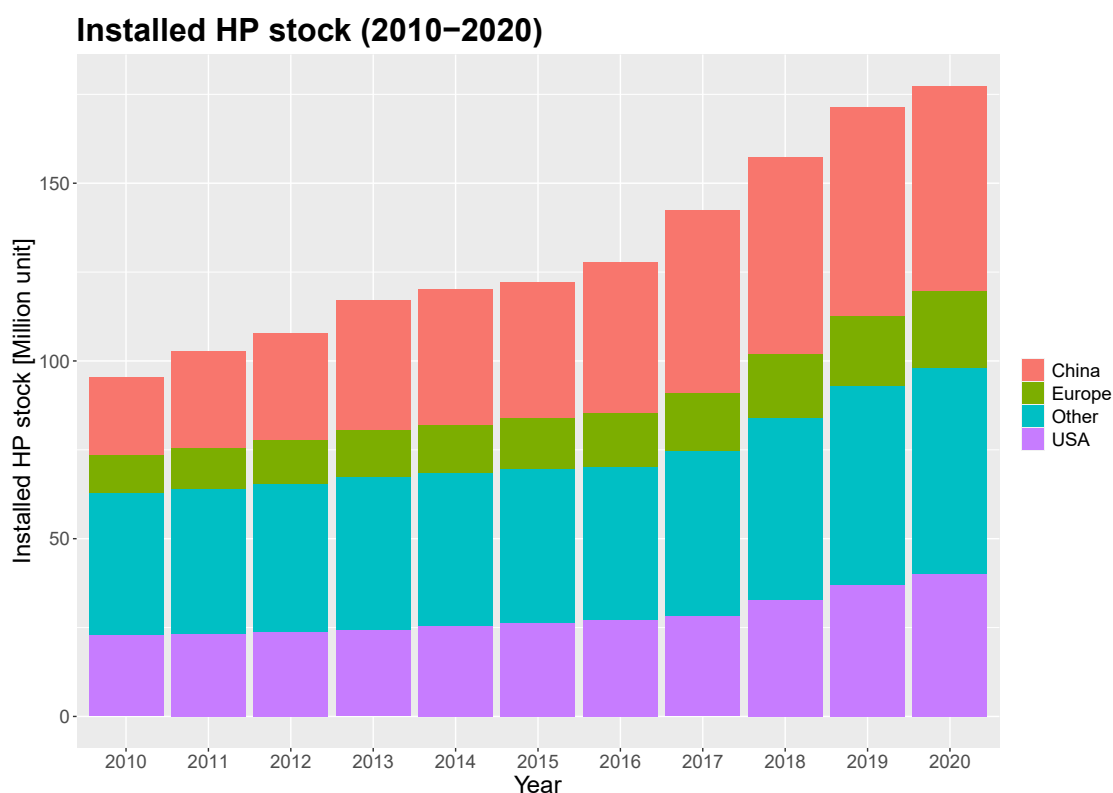


Fig. 1.3 Installed HP stock trend for selected countries. Author's elaboration from [15]

Finally, the cooling sector, which is already today one of the major electrical energy consumers and it is one of the fastest growing end-use in buildings, with a 3-fold increase between 1990 and 2016 and it is expected to be the leading share in final energy consumption in 2050 [18, 19] as reported in figure 1.4. Already today, it is basically fully electricity-driven [3, 18]. Focusing on residential AC units, today EU is among the largest markets, together with the USA and Japan, with a final energy consumption of 152 TWh (equal to 1.2% of the overall building final energy use in 2016) [20, 19]. It is expected that this trend is going to continue in the near and long-term future, guided by the world's economic growth and the demographic one.

As notable from fig. 1.4, it is likely that tropical and sub-tropical countries will lead the cooling rise, with Indonesia, China, India and Africa having the future leading role. In fact, more than any other areas in the world, they are rapidly increasing their income, quality of life and the needs of more services and goods, resulting into the increase of electrical appliances, including AC units. As previously

highlighted, the Eastern part of the globe will be the leading energy consumer, together with Africa, in the upcoming future.

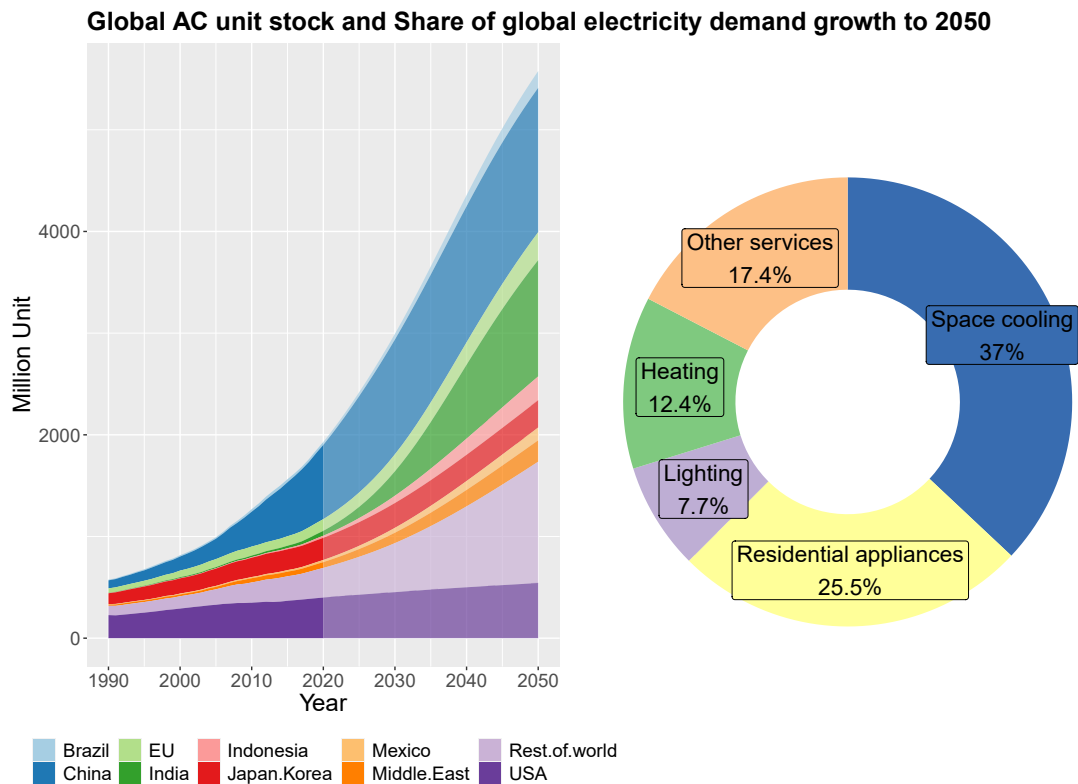


Fig. 1.4 (Left) Global AC unit stock from 1990 to 2020 and projection towards 2050. (Right) Share of global electricity demand growth to 2050. Author's elaboration from [18]

This trend is going to overlap to the already intense use of cooling energy from USA and the rest of the developed countries. China, Indonesia and India are the leading energy-growing countries and they present a hot and humid climate which is a challenging condition for traditional chillers. In fact, high water content in the air means low temperature at the evaporator side to effectively remove, by condensation, the moisture in the supply air as reported in fig. 1.5. The figure represents the share of energy related to the Latent Load in a traditional compression cycle for six of the most developing cities in the world in terms of economy and population.

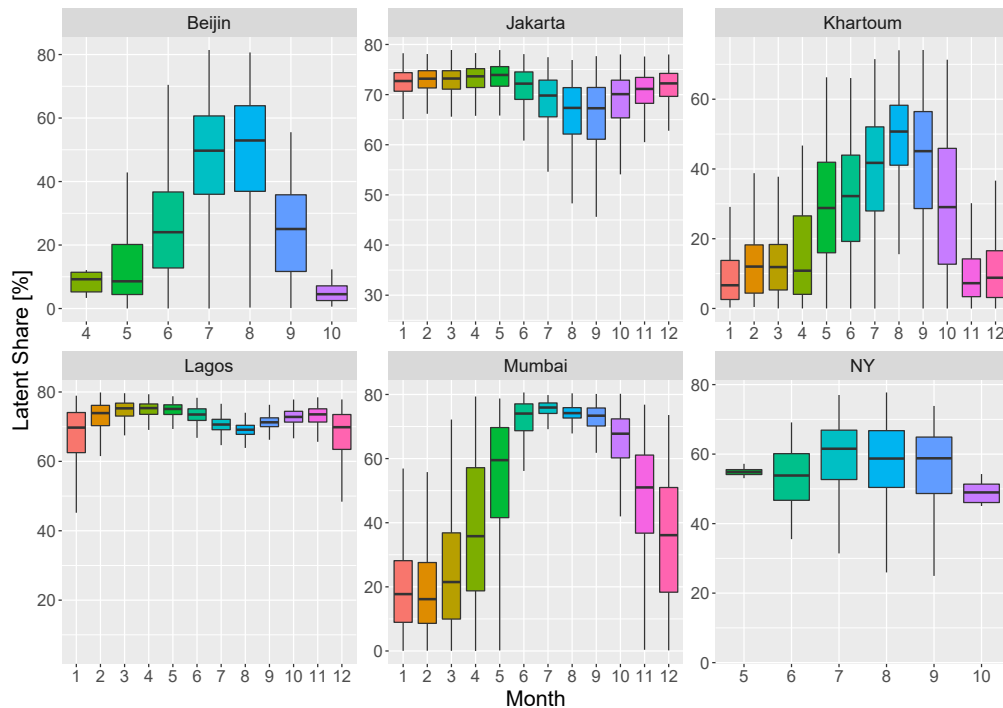


Fig. 1.5 Share of latent load in a traditional compression cycle with respect to the sensible one. Author's elaboration of data from [21]

The above graph has been built starting from hourly temperature and humidity data, for selected countries, taken from [21] for the years from 2010 to 2020 (11 years). The data have been processed in order to retrieve the theoretical energy needs, as enthalpy difference, to bring the outside air from ambient condition to an arbitrary inlet condition of 23°C and 50% relative humidity (which are the typical inlet condition in Italy) taking into account an air flow rate of 1 kg/s . The latent energy is the one needed to remove the water content (1-sat to 2-sat in fig. 3.9 while the other two iso-tile transformations (OUT to 1-sat and 2-sat to INLET) represent the sensible part of the energy consumption. The first outcome of the graph is that in 4 out of 6 cities cooling is required throughout all the year (Jakarta, Khartoum, Lagos and Mumbai). The second one is that the water removal process is often the largest slice of the total energy consumption of a traditional compression cycle. These outcomes underline the nowadays and future importance of cooling energy needs and the urgency of taking concrete action to effectively take under control the cooling-related energy consumption.

The electricity grids around the world are already experiencing stress periods and frequent overloads, especially in summer. The expected increase in power demand and the number of inefficient devices is posing important questions about grid reliability and energy security. Indeed, in the USA where AC units are widely adopted in households and service buildings, 70% of the summer peak demand is due to air conditioning units and this situation is expected to spread around the globe in the following years [19]. There is no doubt about the future role of the cooling services in terms of human impact on Earth and policy action. Still, technology improvements are expected to mitigate and shave the steep rise which is going to happen. New building regulations and refurbishment incentives are pushing toward more sustainable uses of energy, together with tight regulations on minimum efficiency requirements, to decrease the overall energy demand.

In conclusion, it is worth just to mention also the great possibilities and challenges for electrification of the industry sector and centralized heating and cooling systems. Thus, less than 4% of the industrial heat process is delivered by electricity driven technologies [4, 3]. This lack is mainly due to (i) difficulties in matching the needed temperature levels, especially for heavy industries and (ii) cultural mismatch of the already available solutions. In fact, industrial HP systems can already deliver temperatures in the range of -100 °C to 150 °C (with specific temperature difference) which are compatible with many industrial processes such as food and beverage and the textile one. Finally, centralized systems, such as District Heating Systems (DHS), can benefit from the integration with the electrical grid, creating the so called "Smart Energy System" [22, 23]. This integration can have important benefits in terms of energy efficiency, environmental impact [24] and can foster the implementation of HPs systems in booster configuration [25] and to increase the efficiency of industries, especially low temperature ones. This last paragraphs is just to quickly sum-up other possible studies which can relate to this work and which can constitute future investigation, but the specific industry application is out of the scope of this PhD work.

Chapter 2

Heating and Electricity: possible collaboration points

This chapter focuses on the possible interaction and collaboration between the electricity network and the thermal sector in order to better exploit renewable energy sources, waste heat recovery and decrease the overall CO_2 emissions. Part of the results and methodology reported in this chapter has been already published in previous scientific work from the author [23, 26–28].

2.1 From District Heating to Smart Energy System

District heating (DH) systems are a mature technology that offers numerous advantages for the heating and cooling sector in cities. A single heat network can be connected to multiple generating units, including combined heat and power (CHP) plants and waste heat recovery (WHR) from industry, increasing the efficiency of the whole system. In addition, DH has in many cases enabled the integration of renewable energy sources (RES) such as wood biomass and municipal solid waste (whose organic content is often considered renewable) to support the decarbonisation of heating and cooling in large cities.

DH systems were originally deployed during the oil crisis in the 1970s to improve the efficiency of oil use due to the high price of oil. The unused heat from power plants, treated as a waste product, became a useful resource for heating purposes [29].

Today, due to environmental and climate concerns, waste heat recovery measures and CO_2 pricing, they are receiving a second push[30] in order to further improve the efficiency of heating and cooling systems. The configuration of water heaters has changed over the years, from a single steam-based source (1st generation) to multiple RES and fossil sources with technical water as the energy vector (4th generation).

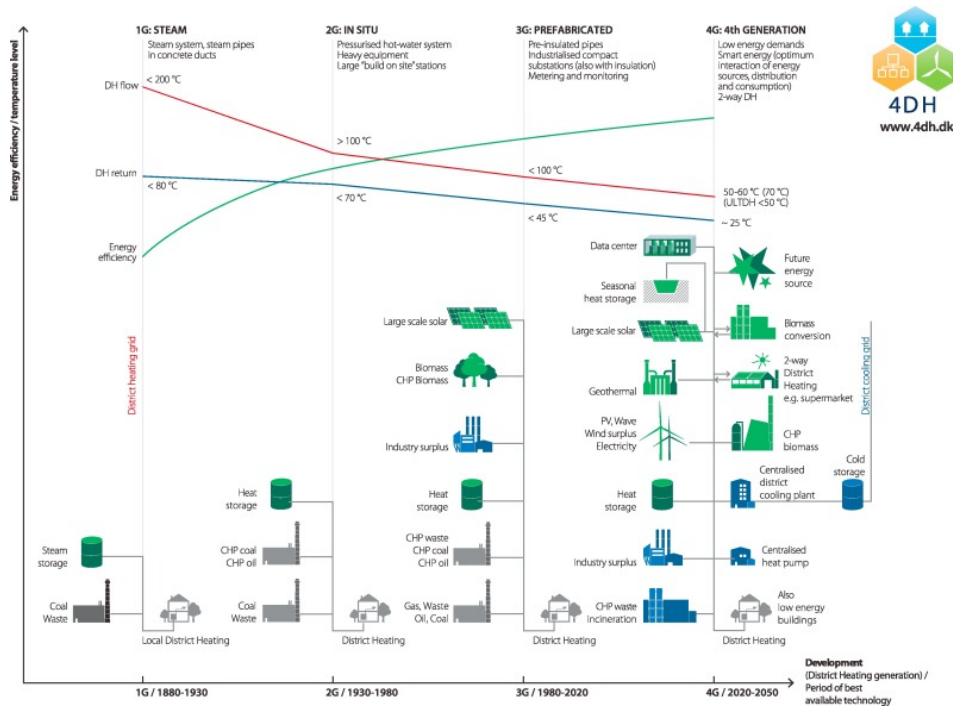


Fig. 2.1 Evolution of District Heating System [31]

The total number of DH systems worldwide is estimated at 80,000 units with about 600,000 km of piping [9]. Russia, China and the EU are the main regions accounting for about 85% of the total heat supplied by DH systems. Globally, hot water district heating systems still rely heavily on fossil fuels with 90% of heat provided, while, in RES based network, biomass is the main fuel. In the EU, the share of fossil fuels is 70%, mainly from CHP plants, which are mainly used in the northern regions of the EU, in contrast to China and Russia [29] where their full potential is still underestimated. Indeed, well-designed CHP plants can lead to fuel savings and higher efficiency compared to separate heating and power plants [32, 33], especially when supported by storage systems [34]. Even though hot water systems have been developed to make better use of fuels and waste heat, waste heat recovery (WHR) is not yet widespread. The northern regions of the EU have a high

WHR share; for example, almost 100% of incinerators are connected to some grids. Nevertheless, waste heat recovery, in different forms, is gaining momentum in China and Russia [29]. In particular, industrial WHR is not widely used for various reasons, such as the wide variety of temperature levels and non-constant production, which limits the affordability and reliability of the system. However, recent studies are investigating the possibility of connecting the growing data centre market with DH systems. The derived heat, which is stable and constant, could be used as a heat source for HPs or for direct use in DHS, as highlighted in [35, 36].

DHS provides 10% of the EU thermal energy demand [37] with the northern countries of EU presenting large utilization of DH even with shares over 40% [38]. In Denmark, more than 60% of the 2.75million Danish heat installations are connected to DH, representing one of the higher shares in the world [39–41]. Chinese DHSs predominantly rely on fossil coal [32]. Heat market directive still gives priority to large coal CHP and boiler plants, especially in winter periods [42], to ensure reliability on the electrical grid. The debate around DH systems in China is a main issue nowadays. Back in 1950, the central government imposed the DH in the northern part of the country, while the southern regions must use other distributed technologies [43]. This is due to social, historical and technical problems. However, it is under discussion the possibility to enlarge the area where DH can be operated [43]. DH in USA is almost non-existent apart from the large steam-based DH system in Manhattan which represent an important installation as it is one of the largest and oldest system ever built. Nevertheless, strong possibilities are in place in the US cities as in [38], where an analysis is conducted using GIS software. The results show that around 12-14% of the national heat demand can be satisfied using DH. In [44], the use of geothermal energy for DH in the USA is investigated and only 21 geothermal DH systems have been detected, for a total of 100 MW_t . The authors identify 3 main barriers for geothermal diffusion such as lack of knowledge and lack of policies procedures. Lack of policies is one of the main barriers also in the UK, where DH systems are not well regulated and widely known, even if different studies, such as [45], show that benefits can be important.

As already pointed out, today the most used heat sources are conventional fossil boilers and CHP plants. Besides them, heat pumps, waste heat and renewable sources are getting more and more space [37]. CHP plants are widely used and several publications describe the CHP+DH combination [46–50]. In [50], a real data analysis is performed on a large district heating system in Turin, highlighting the

great contribution of CHP plants on the overall thermal energy supply, and how the consumer behaviour can improve or worsen the performance of the overall grid. In order to be economically and energetically advantageous, DH systems have to be properly designed, and this is particularly true when dealing with CHP technology since the production of heat and electricity are in competition [51]. The higher usage of electricity from HP can produce electricity price variations and an overall reduction of DH operational costs. Nevertheless, the HP utilization can modify the original CHP working schedule, decreasing its power output.

The environmental benefits of DH systems are well known, and the global specific CO₂ emission factor (kg_{CO_2}/MJ) has almost been constant from 1990, even if more and more users have been connected, meaning that efficiency of the systems is growing. Between the largest users (China, EU, Russia), EU is the one that is pushing more towards cleaner district heating systems, both for new and renovated ones. In fact, the EU specific emissions decreased by 35% with respect to 1990 value [29], mainly due to the large use of CHP units that allows CO₂ reduction if well operated [52, 46]. Nevertheless, it is important to carefully evaluate the combination of DH plus gas fired CHP, because different allocation methods can lead to different environmental and LCA impacts [26]. Indeed, the following study has been carried out focusing on gas fired CHP units. Since DH systems based on CHP units are producing electrical power and heat, attention needs to be paid to the allocation of the emissions between the two energy vectors. Some methodologies, as the Exergy one, give priority to the electricity allocation, and very few emission output is charged to the heat. Other methods simply split the two energy forms with a common weighted average, as the Energy method does [33]. In Figure 2.2 and Figure 2.3 the Climate Change impacts calculated for the heat supply by DH or a Gas Boiler (GB) unit are reported, in terms of $kgCO_{2eq}$ over useful kWh divided in the different construction and operation phases of the system.

The overall impact in terms of GHG emissions for a single gas boiler (GB) equals to $0.27 kgCO_{2eq}/kWh$, while for DH it equals to 0.47 and 0.10 $kgCO_{2eq}/kWh$ for the Energy and Exergy methodologies respectively. It is clear that the main contribution derives from the natural gas combustion, followed by the natural gas import in both cases. Since the system construction is irrelevant, the common practice of considering operational data when evaluating climate change impacts is an acceptable approximation.

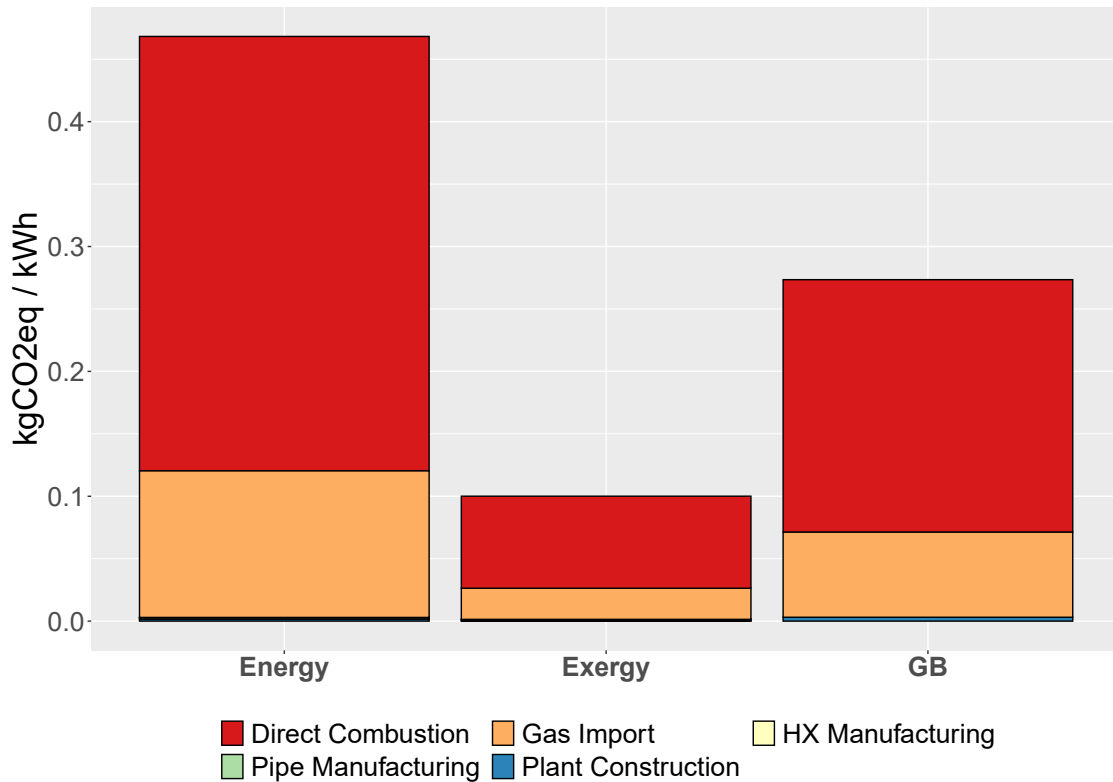


Fig. 2.2 Specific emissions for DH with allocation methods and for GB

As the diagram shows, the allocation method has a dramatic effect on the final results, as the effect of DH heat can be lower or higher than that of the individual natural gas boilers. In the case study [26] discussed, a large gap between the two approaches can be seen. In fact, the exergy calculation strengthens the competitiveness of CHP by giving less importance to heat production and presenting CHP as a key technology to reduce the emission factor of heat supply. In contrast, the energy methodology proposes a less interesting emission factor for CHP heat supply, which is much higher than the solution with individual boilers. Other variables such as the reference temperature considered or the definition of the reference energy system in the alternative generation methodology can also lead to different results. This large variation is related to the perspective with which cogeneration is considered and an appropriate choice of allocation factor is really important for the future development of cogeneration technologies. It is worth noting that the above results apply to hot water systems like the one in Turin, where CHP contributes to 95% of the total heat supplied [53]. Nevertheless, other realities could have different production shares

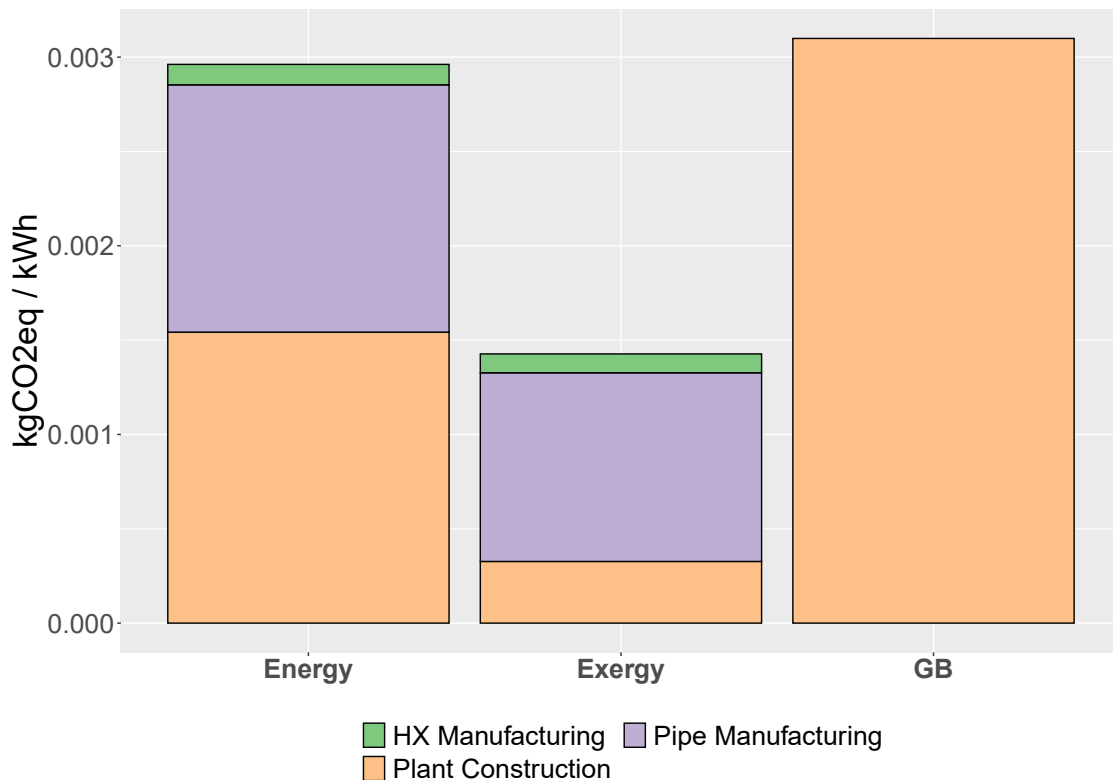


Fig. 2.3 Specific emissions for DH with allocation methods and for GB - Detail of minor contribution

and important GB contributions for peak and low demand periods, affecting the overall performance and efficiency.

However, the environmental and economical benefits of DH still need to be fully exploited and the new generation [31] seems to step towards a better connection between source, network and users. In fact, world policies are becoming more stringent as they pose ambitious targets for all the energy chain from generation to consumption [54]. Numbers of projects and activities are running in EU about Heating and Cooling (H&C) sector[55] and DH is seen as a fundamental technology to boost the decarbonization of H&C sector [9, 10]. The big challenge faced by fourth-generation DH [31] is the need of lowering the operational temperature of DH systems to foster the integration of additional technologies including solar energy, heat pumps and low-temperature waste heat [22]. Moreover, the buildings sector is facing huge changes, as the minimum energy performance level is stepping up, leading to a higher presence of low temperature distribution systems, RES technologies for heating and cooling and smart electrical appliances at user side. All

these modifications are pushing DH systems to evolve in what is called the “4th Generation of District Heating System” (4GDHS) [31]. Lund et. al give the definition of 4GDHS as “*a coherent technological and institutional concept, which by means of a smart thermal grid assists the appropriate development of sustainable energy system*”, through the supply of low-temperature water, to decrease grid losses, integrate RES and WHR, be part of the smart energy system and have a suitable planning framework. In the next generation of DHS, the three subsystems have to evolve to fulfil the 4th generation requirements. (i) Buildings: will face deep renovation to decrease their energy consumption and auto-produce part of it. The word “prosumer” [56] will be soon associated to DHS and, more in general, to heating and cooling energy infrastructures. Moreover, increasing numbers of sensors are needed in different zones to gather data for optimal control. In particular, controllability and optimal scheduling require precise load forecast [57], as it represents an important variable which can be of notable importance to efficiently operate the system [50, 58]. (ii) Grid: insulated twin pipes made of cheap material will lead to decreasing the energy losses and higher economic feasibility. Old grid could be used as source for low-temperature ring [59], allowing for a step by step conversion for old generations. (iii) Low distribution temperature opens the door to a wider selection of heat generators such as solar thermal systems [56, 60–62] and Waste Heat Recovery with/without HPs as booster technology [35, 36, 59]. The effective integration of different resources is the key to move towards a more sustainable and clean energy dispatching along the grid. Moreover, the design and the construction of new networks should be supported by tailored tool [52]. Moreover, the complexity of the future network will require important data analysis to get the inefficiencies and control the design quality. Deep data analysis can highlight unbalance in the seasonal thermal storage and the great importance of auxiliary energy consumption in LTDH system [63].

2.2 Modernization of today Thermal Grid and High Energy Related Users

One of the problems with the new generation of district heating systems are the “old users”, as they pose a lower limit for the supply temperature. In fact, on the very same thermal ring different temperature level are often requested. High efficiency

users are fed with high temperature water because usually users are connected to the primary ring even if they do not need it.

To overcome this problem, different strategies are in place. For example, it is becoming popular to connect a secondary ring to serve high energy efficiency areas [29], as simulated in [59]. This solution is quick and does not require important modifications on the users side but could require important modifications on the network topology and architecture. On the opposite, changing the users' heating systems is a valuable solution, to decrease the needed temperature. Nevertheless, major renovation can be an issue for tenants as important time, effort and resources have to be spent [56].

Another interesting solution is to use a main ring for low temperatures and distributed boosters HP to raise the temperature level exactly where it is needed. The idea behind this strategy is that even though most users will live in high performance buildings in the future, some areas would still not be able to improve their energy efficiency because they do not allow the use of low temperature sources. In this configuration, a DH low-temperature flow is used as a source on the evaporator side of the HP to increase the temperature on the user side. This technical approach makes it possible to keep the grid temperature at a lower level, thus expanding the possible energy source portfolio, especially RES and WHR. Furthermore, raising the temperature level locally improves the overall performance of the drinking water network, as a lower temperature also means lower distributed energy losses.

A simulation model for a hot water system was defined to evaluate the impact of lowering the water temperature in the distribution network under different conditions. The model consists of the end user and the distribution network of a central water heating system, comparing three different use cases: (i) the current condition of the third generation water heating system, (ii) a low-temperature network with continuous operation during the night, and (iii) a low-temperature network with energy-efficient buildings.

2.2.1 Methodology

The simulation model was developed in Modelica using the Dymola programming environment [64] alongside the Building Library, developed by Lawrence Berkeley National Laboratory, for dynamic simulation of the energetic behavior of single

The heating system is represented as a closed loop between the radiator block and the DH heat exchanger DH_HX . The radiator parameters consist of the data provided by the manufacturers (European standard EN 442-2), including nominal mass flow, nominal flow temperature and temperature difference, and heat output. The decision to use a single radiator instead of several is mainly related to the fact that it is a single large volume with homogeneous characteristics. A larger number of radiators would not have changed the simulation result significantly (but would have increased the complexity of the simulation and the time needed).

Furthermore, the Radiator has two heat port connections with the building representing the convective \dot{Q}_c and the radiative \dot{Q}_r heat flow rate. It was assumed that the air and radiative temperature of the building are equal, and the heat transfer rate is modelled as follows:

$$\dot{Q}_c = \frac{\text{sign}(T_i - T_a)(1 - f_r)UA}{N |T_i - T_a|^n} \quad (2.1)$$

$$\dot{Q}_r = \frac{\text{sign}(T_i - T_r)(f_r)UA}{N |T_i - T_r|^n} \quad (2.2)$$

where N denotes the number of elements used to discretize the radiator and i represents the single radiator element. T_i is the water temperature of the i -element, T_a is the temperature of the room air, T_r is the radiative temperature, f_r is the fraction of radiant to total heat transfer (set to 0.35 [66]), UA is the UA-value of the radiator, calculated from nominal conditions, and n is an exponent for the heat transfer (set to 1.24 [66]).

The model of a discretized coil made of two flow paths which are in opposite direction has been used for the district heating heat exchanger. The heat transfer driving force is, of course, the temperature difference between the fluid and the solid. The water flow is controlled thanks to a variable speed pump model [65]. Based on the nominal mass flow rate, a pressure curve is calculated in order to retrieve the electrical power consumption and efficiency.

$$W_{flo} = |\dot{V}\Delta P| \quad (2.3)$$

where \dot{V} is the volume flow rate and ΔP is the pressure rise. The efficiencies are computed as:

$$\eta = W_{flo}/P_{ele} = \eta_{hyd}\eta_{mot} \quad (2.4)$$

$$\eta_{hyd} = W_{flo}/W_{hyd} \quad (2.5)$$

$$\eta_{mot} = W_{hyd}/P_{ele} \quad (2.6)$$

Where η_{hyd} and η_{mot} are respectively the hydraulic and motor efficiency.

Finally, the district heating system is modelled by an ideal plant block *IdealPlant* and pipe block for the piping network representation. The DH load is composed by 9 users, interconnected in parallel, by the piping system, with the central plant.

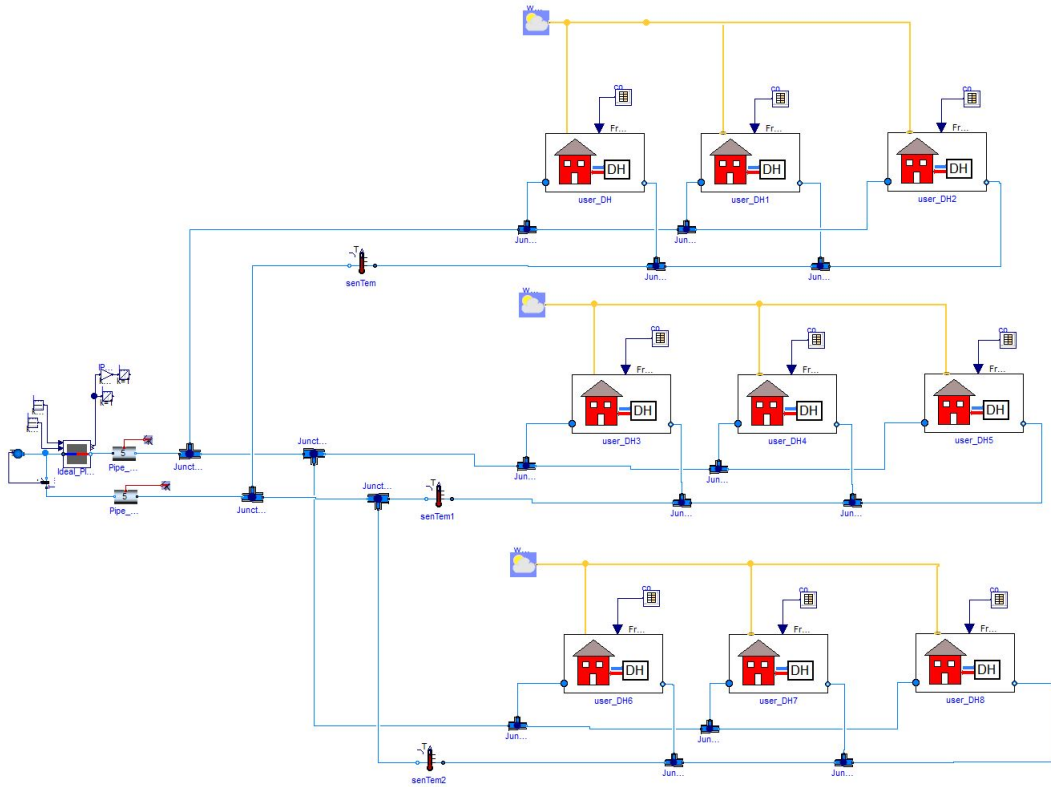


Fig. 2.5 Modelica model of simulated system [23]

Each load is connected to the network in parallel by means of junctions *Junct* that take as parameter the nominal mass flow rate per each branch and the relative pressure drop correlated as follows:

$$\dot{m} = K\sqrt{\Delta P} \quad (2.7)$$

Where \dot{m} is the mass flow rate, ΔP is the pressure drop and K is a constant that is calculated at $\dot{m}_{nominal}$ and $\Delta P_{nominal}$ and it is assumed to be constant at different mass flow rates.

Right after the plant there are two pipes, *Pipe_Main_Flow* and *Pipe_Main_Return*, respectively for flow and return. The Pipe component takes as parameter the length [m], the insulation thickness [m] with its thermal conductivity [W/mK], nominal mass flow rate [kg/s] and the velocity of the fluid [m/s]. Moreover it is possible to specify the diameter [m] or let the block compute it as:

$$d = \sqrt{\frac{4\dot{m}}{\rho\pi v}} \quad (2.8)$$

Unlike junctions, it takes into account thermal losses since all the geometric data are available and it is possible to set the outside condition.

Weather data component *WeaDat* reads Typical Meteorological Year (TMY3) data where “A Typical Meteorological Year is a collation of selected weather data for a specific location, listing hourly values of meteorological elements for a one-year period.” TMY represents annual average values and it is used, for buildings simulation, to address expected energy consumption and costs. However, TMY is not suited to design components in worst-case conditions. In our simulations TMY data has been obtained from the EnergyPlus web site [67].

2.2.2 Case Studies

Using the described simulator, 3 main simulations have been run in order to assess the DH performance and the effect of network temperature and configuration. For author’s knowledge reason, the city of Turin (Italy) has been chosen as location.

Case 0

Case 0 is the reference case because it represents the status quo of the large DH water network. The network is operated with a nominal supply temperature of 90 °C and the users are old residential buildings that are poorly insulated, have a high energy demand and whose heating system is designed for the worst case. The users’

heating systems are switched on during the day and switched off at night. In Italy, buildings are usually not heated at night because Italian regulations limit the number of heating hours per day. This operation leads to a significant morning peak in the heat load profile, which requires oversizing the capacity of the DH heat generators or installing a suitable heat storage system. The simulator was tuned using planning parameters from the city of Turin. The users are sized to represent residential blocks with volumes $3 \cdot 1800 \text{ m}^3$, $3 \cdot 2400 \text{ m}^3$ and $3 \cdot 3000 \text{ m}^3$, corresponding to a total heated volume of $21,600 \text{ m}^3$ allocated to nine users. The radiators were sized taking into account the usual design conditions for Turin: they have an average installed nominal heat output of $30\text{-}40 \text{ W/m}^3$. The nominal output of the radiators, usually defined considering reference values for a supply temperature of $75 \text{ }^\circ\text{C}$ and a return temperature of $65 \text{ }^\circ\text{C}$, was therefore calculated for each building as follows

$$\dot{Q}_{rad} = 40 * V \quad (2.9)$$

$$\dot{m} = \dot{Q}_{rad} / (c_{pw} * \Delta T_{rad}) \quad (2.10)$$

where \dot{m} is the mass flow rate, \dot{Q}_{rad} is the nominal power, c_{pw} is the specific heat of water and ΔT_{rad} is the temperature difference between inlet and outlet of the radiator.

Looking at the user parameters, free gains were set to zero as a conservative hypothesis, in order to investigate just the impact of the heating system parameters variation. The thermal conductance, representing the walls, is set equal to:

$$U_{theCon} = \dot{Q}_{rad} * f_{corr} / \Delta T_{worst} \quad (2.11)$$

where \dot{Q}_{rad} is the nominal power of the radiator and ΔT_{worst} is the design delta temperature between inside and outside equal to 28°C in Turin representing an outside temperature of -8°C . f_{corr} is an empirical correction factor that is needed to correlate the nominal power of the heating systems with the real performance when they are required to heat up the buildings in the morning in the worst conditions. In this study, this factor has been adjusted to a value of 0.5, which was empirically evaluated in accordance with an acceptable transitory duration during the morning peak. The heat capacity of the building was chosen in order to have a temperature

during the night of around 16 °C. This empirical approach was chosen to be consistent and general enough with respect to the real operation of the heating systems, disregarding the unknown multitude of aspects that would affect the definition of the average building heat capacity, including the geometry, the materials of the walls and the furniture. The building temperature is controlled by a PI controller varying the radiator mass flow rate.

Case 1

Lowering the grid temperature is one of the most effective measures to reduce losses, increase efficiency and open up the grid to low-temperature sources such as solar thermal systems and waste heat recovery. However, in existing systems, simply lowering the operating temperatures would not guarantee setpoint conditions for the users, as the nominal design parameters for this have not been studied. In this case, a different operating schedule must be considered to avoid having to modify the building or the heating system. The aim of this case was to investigate possible problems in lowering the temperature of the network and to understand which components of the building and the heating system could be affected. In particular, continuous operation during the day and night was analysed as a feasible way to lower the grid supply temperature by trying to avoid the morning and evening demand peaks of the radiators, as they lead to large losses [34, 58]. In fact, there are several strategies in the literature and in the industry to limit these events, such as heat storage systems to flatten the load profile. The supply water temperature is then reduced from 90 °C to 50 °C and the building heating system is operated 24 hours per day (which is already a valuable option for specific Italian territories). To allow a fair comparison between the two cases, the same heating system with the same design parameters as in case 0 is used. The temperature values of the buildings' heating systems were thus calculated by the simulation model by operating the radiators under non-design conditions based on the nominal values of their design parameters. The building temperature set point was set equal to 20 °C. Moreover the controller was changed: instead of a PI, a simple on/off controller is used, working within 20 °C \pm 0.5 °C.

Case 2

Instead of working on the generation side, insulation of buildings can provide an effective driver for lowering the network temperature without the need for modifying the heating system operations. In this case, the aim was to understand if a partial insulation of the building allows meeting the setpoint conditions while keeping the same heating behaviour of Case 0. Indeed, due to the lower heat losses of the building, the radiators can be operated at a lower temperature, leading to a lower heat demand and consequently to the possibility of operating the radiators at a lower temperature. The values of the design parameters for this case are the same as Case 1, except for the thermal conductance of the users that was reduced by 40% while maintaining the same heat capacity. The reduction rate of the thermal conductance was set by considering a reasonable target obtained through energy efficiency measures (including the substitution of the windows and the insulation of the walls) performed on existing residential buildings in the context of Turin, based on the experience of the authors from real refurbishment interventions in the city. Due to the focus of this research work, a more detailed simulation of the building was not performed, leading to some approximations. For the same reason, the heat capacity was not varied accordingly, due to missing information of the specific characteristics of the buildings and the consequent need of an arbitrary new value.

2.2.3 Results

The heat demand and temperature profiles of the three cases for a given day (January 1st) are compared in the following figures 2.6 and 2.7. The major difference is noticeable during the morning peak, while some minor variances appear throughout the day. Both Cases 1 and 2 allow to reduce significantly the morning peak, approximately from 1 MW to 350–400 kW. This goal can therefore be reached with both approaches, although without building insulation the building needs to be heated also during the night. In particular, the controller lowers the room temperature in the afternoon in the alternative scenarios, leading to a sharp decrease in heating demand. The deep drop is due to the fact that all the simulated users have been set with the same behavior. This is not compliant with the real world where multiple users have generally different behaviors. It is reasonable to think that, in such a situation, load and temperature profiles would be more stable, with small fluctuations around the

rated power. This is a limit for the current simulator, but in future developments this model can be corrected by considering real data for different buildings.

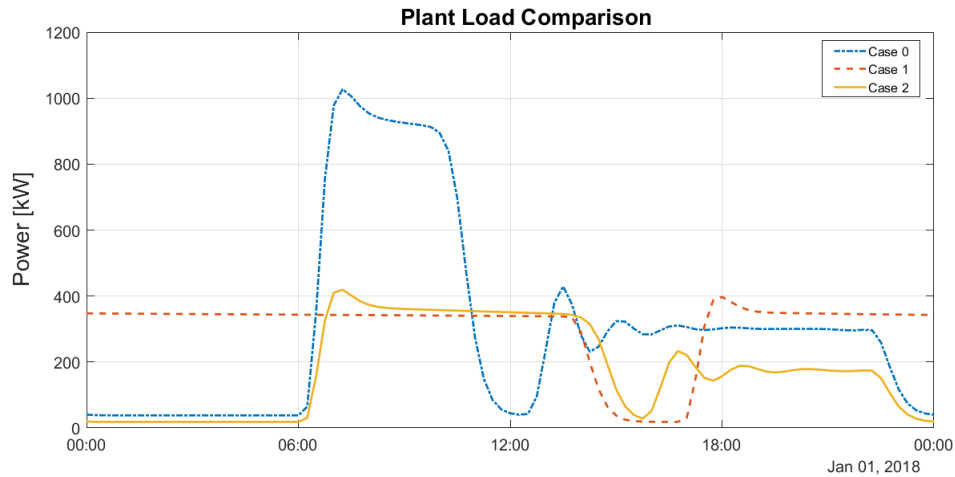


Fig. 2.6 Plant Load profile: comparison for the different use cases.

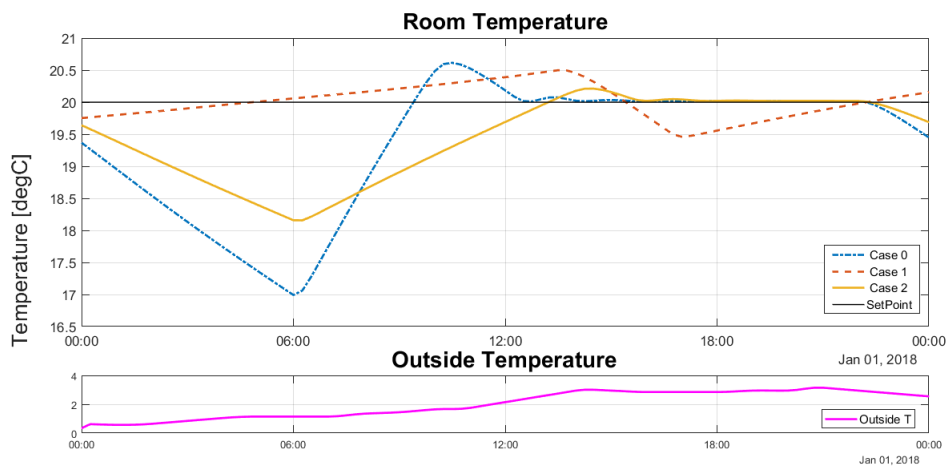


Fig. 2.7 Indoor temperature: comparison for the different use cases.

To ease the discussion, the previous figures were limited to a single day simulation in order to better understand the profile differences while the following table (2.1) summarizes the performance of the system for the entire year.

Table 2.1 Annual energy performance of the different cases

Case	User Demand (MWh)	DH supply (MWh)	Network losses (-)
Case 0	910	1,075	18.0 %
Case 1	941	1,019	8.3 %
Case 2	548	628	14.5 %

With respect to the reference case, Case 1 (continuous operation) leads to a slightly higher energy demand by the user, which is however compensated by lower network losses (due to the lower operation temperatures), thus resulting in a lower heat generation from the entire DH system and to lower running costs for the network. This can be seen as a driver for better cost allocation and, therefore, for lower tariffs. On the other hand, in Case 2, the user shows a substantial decrease of energy consumption due to the insulation, and the network losses are comparable to Case 1, but obviously with a higher relative share. In this case, the energy savings are obviously more related on the users side while, for the network and the plant operator, it can be seen as a problem as the losses increase their share and importance on the overall energy balance.

In order to better understand the impact of lowering the network temperatures, a sensitivity analysis was performed by considering three additional temperature levels: 45 °C, 55 °C and 60 °C. Moreover, to run a proper comparison, a “SetPoint Factor” quantity to calculate the amount of hours in which the indoor temperature is in the range from 20 °C to 21 °C was defined as:

$$SF = \frac{h_{OSP}}{h_{heatingDay}} \quad (2.12)$$

Where h_{OSP} is the amount of hours that the indoor temperature is over the set point and $h_{heatingDay}$ is the amount of hours where the heating system is on; in our case between 7AM and 10PM. It is important to say that even in the Case 1 scenario it has been taken into account just the day hours since the night operation has to be seen like an extra benefit. The results are summarized in Figure 2.8, where Cases 1 and 2 have been simulated for different supply temperatures and compared against Case 0.

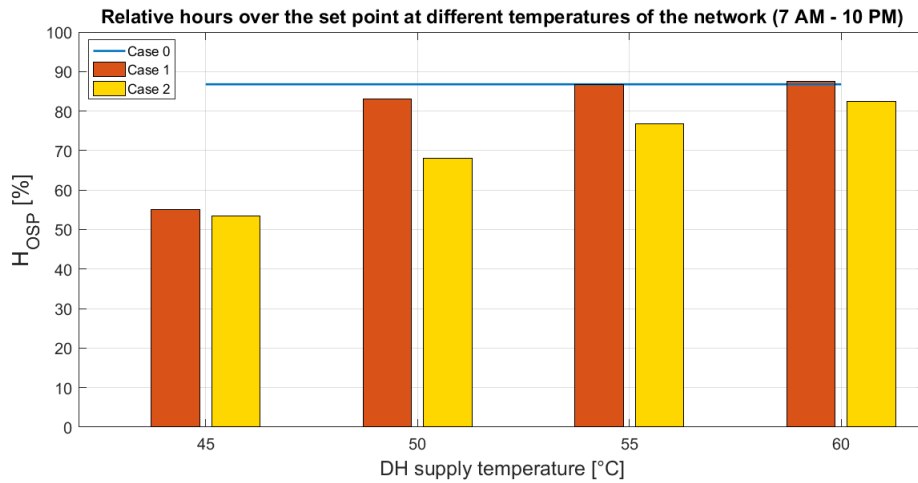


Fig. 2.8 setpoint Factor comparison across the different solutions

The sensitivity analysis reveals some interesting aspects: Compared to the other scenarios, not even case 0 can guarantee a setpoint factor of 100%, mainly due to the temperature fluctuations in the morning towards the set point of 20 °C. In fact, it is possible to observe that the setpoint factor in case 1 at 55°C is the same as in case 0. Taking this aspect into account, case 1 guarantees an acceptable performance at a supply temperature of only 50°C, while a further decrease means a significant drop in the setpoint factor. In fact, at 45°C the indicators are slightly above 50%, which means that half the time the indoor temperature is not in the standard range. The numerical analysis therefore suggests that such a low temperature requires further measures to achieve an adequate setpoint level, such as installing radiators with a larger exchange area or insulating the building. On the other hand, case 2 seems to have a lower performance across all analysed temperatures and for this reason cannot be considered as a real alternative to case 0, even at medium temperatures such as 55°C. In this case, possible solutions can be found in continuous operation similar to case 1 or in increasing the radiator surface.

Alternatively, in order to compensate for the network temperature decrease, distributed "booster" Heat Pumps can be exploited, as proposed in the following section and already discussed in section 2.1.

2.2.4 Booster Heat Pumps

The goal is to substitute the heat exchanger between the network and the user with a heat pump in order to boost up the temperature to 60°C, for space heating, just where it is needed. The main idea here is that even if in a next future the major part of the users will live in high energy performance buildings, still some cities areas (as protected historical buildings) will not be able to improve their energy performances in order to use low-temperature heat sources. HPs use district heating water at the evaporator side to heat up the user's heating system water (see figure 2.9). Thanks to this configuration, it is possible to keep the network temperature at lower values with respect to the today standard of about 100°C, increasing the potential RES and WHR shares, and increase the temperature locally only for the users for which the temperature decrease is not a viable option.

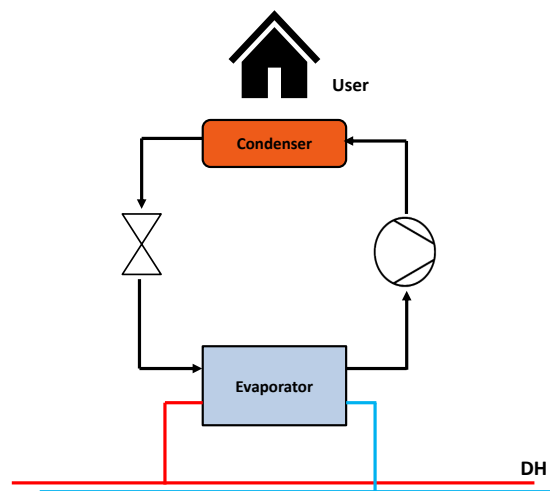


Fig. 2.9 Schematic representation of the distributed HP [23]

The HP model is included in the building library already cited at the beginning of this paragraph. It represents a vapour compression HP that takes as main parameters the nominal mass flow rate, the nominal heat flow rate, the nominal temperature difference and the pressure drop at both evaporator and condenser sides. The condenser leaving water temperature represents a control input for the block and its COP is calculated as given by the following equations:

$$COP = \eta_{canot,0} COP_{carnot} \eta_{PL} \quad (2.13)$$

$$COP_{carnot} = \frac{T_{condenser}}{T_{condenser} - T_{evaporator}} \quad (2.14)$$

$$\eta_{pl} = a_1 + a_2 y_{PL} + a_3 y_{PL}^2 + \dots \quad (2.15)$$

where $\eta_{canot,0}$ is the Carnot Effectiveness, COP_{carnot} is the Carnot efficiency, η_{PL} is a polynomial expression to take into account partial load operation and y_{PL} is the partial load ratio. The Carnot Effectiveness coefficient can be set manually or it can be calculated as:

$$\eta_{canot,0} = \frac{COP_0}{COP_{carnot,0}} \quad (2.16)$$

where COP_0 is the efficiency value in nominal conditions and $COP_{carnot,0}$ is the Carnot efficiency in nominal conditions. Since no accurate data were available, $\eta_{canot,0}$ was set equal to 0.4 and η_{PL} equal to 1 [68, 69]. Consequently, the COP was calculated as:

$$COP = \eta_{canot,0} COP_{carnot} \quad (2.17)$$

Since the use of distributed HPs involves a significant electricity consumption, a proper comparison with the previous cases should be performed by considering the primary energy consumption (PEC). In this comparison, the crucial aspect becomes the RES share in the power grid, which can vary from country to country but also shows a significant variability over time [33, 27]. This issue will be addressed in the following section (section 2.3. In this work reference Primary Energy Factors for Italy was considered: 1.05 for natural gas and 2.42 for electricity [70, 71]. The DH heat was considered as produced by a natural gas boiler with a 90% efficiency (conservative approach).

Figure 2.10 clearly illustrates as the HPs integration enables the network to operate at lower temperature and to achieve an acceptable setpoint for the users. However, the HPs operation requires a significant power consumption, which cannot be ignored in a systemic analysis. With the assumptions made in this work, the

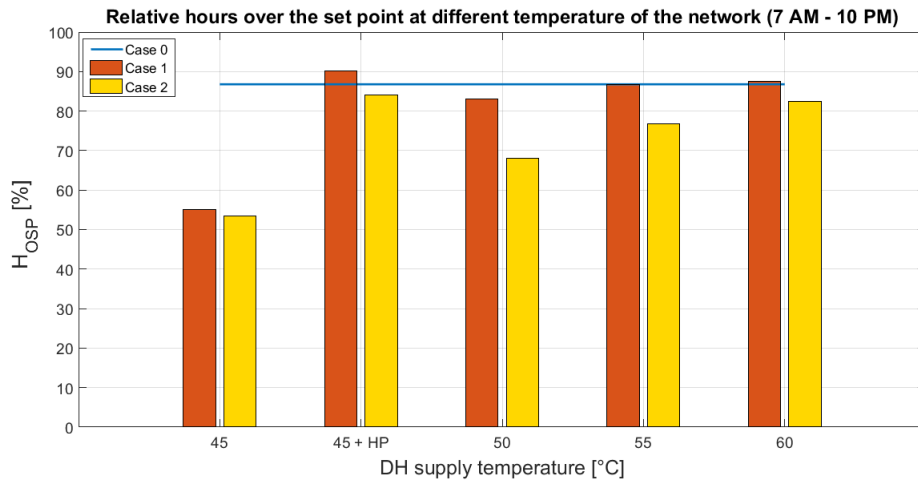


Fig. 2.10 Comparison of annual performance of HP and different supply temperatures [23]

HPs have a larger impact than other solutions in terms of total primary energy consumption.

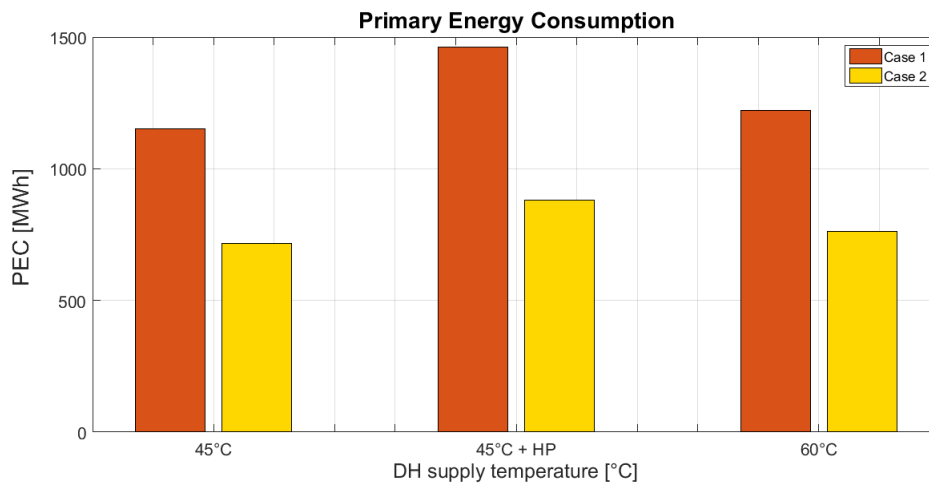


Fig. 2.11 Primary Energy Consumption of the different strategies [23]

2.2.5 Conclusions

The results of this study highlight the potential of optimizing the current heat generation logics in high-temperature DH systems. A continuous operation of the existing heating system could support a decrease of the network supply temperature, as the buildings would require a much lower heat rate. The slight increase of energy

demand of the users would be highly compensated by a reduction of the network losses, thanks to a lower average network temperature. Proper regulation rules are required to support this transition by sharing the potential benefits among the final users and the DH system operators.

The refurbishment of buildings can lead to significant energy savings, but it not necessarily guarantee a shift toward a low-temperature DH operation. A critical parameter would be the amount of energy savings that are obtained, as without changing the existing radiators their heat supply is strictly related to their operation temperature.

The analysis of the HPs behaviour leads to a more complex model, as multiple parameters have an impact on their operation and different indicators can be chosen to evaluate their contribution. In particular, the shift towards low-temperature DH networks coupled to booster HPs is a promising solution where the integration of RES is of primary interest. On the other hand, if the DH generation plant remains fossil-based (considering a simple natural gas boiler), with the Italian data used for PEF, HPs are not leading to a decrease of the total primary energy consumption of the system. HPs environmental benefit is therefore strictly dependent on the source of this electricity, with reference to its renewable share and CO_2 emission factor.

In fact, also in terms of CO_2 emissions the distributed HPs do not give a real benefit. In fact, comparing the CO_2 emissions of $45^\circ C$ case and the $45^\circ C + HP$ case, for Case 1 and Case 2, the obtained outcome are slightly higher emission values with the HPs case: around $150 tCO_2$ against $140 tCO_2$ for case 2 and $250 tCO_2$ against $227 tCO_2$ for Case 1. For sake of clarity, the emission factor and the primary energy factor used are the 2017 values reported from ISPRA [71, 72].

Nevertheless, PEF and CO_2 factor are not constant during the day, the month and the year. This means that, probably, the use of average values for these assessments are not recommended, especially in transition periods as the one we are living in. RES are increasing their shares every year, and the multiple coal phase out policies in EU countries are decreasing the overall PEF and CO_2F . In the following section, a detailed analysis on CO_2F has been done, in order to understand the possible effect of more refined analyses with respect to the direct use of annual average values.

2.3 Heat pumps electricity Consumption: Effective Energy Mix Consumption

As stated at the beginning of this document, the main purpose of the electrification wave is to reduce the use of fossil fuels for final energy consumption, exploiting the renewable energy production to decarbonize a specific target sector and to increase the efficiency of final uses. In fact, this is true for the HC and EVs sectors, where fossil fuels currently represent the main energy source and, as a consequence, they are among the largest CO_2 and pollutants emitters [3, 73].

The power generation mix is of fundamental importance to effectively decarbonize the targeted sector and do not simply shift the emissions from final uses to the power plants. Significant progresses have been made all around the world about power generation from RES and in fact, as reported in Figure 2.12, the renewable installed capacity is stepping-up basically all over the globe with different increasing steepness ratios. Europe is doing impressive progresses from its first legislative action pack, published back in 2009 [74] when the famous 20% by 2020 target has been imposed. North America and Asia Pacific regions are also moving towards a cleaner energy systems, with smaller steepness coefficients, but with stable progresses since 2010.

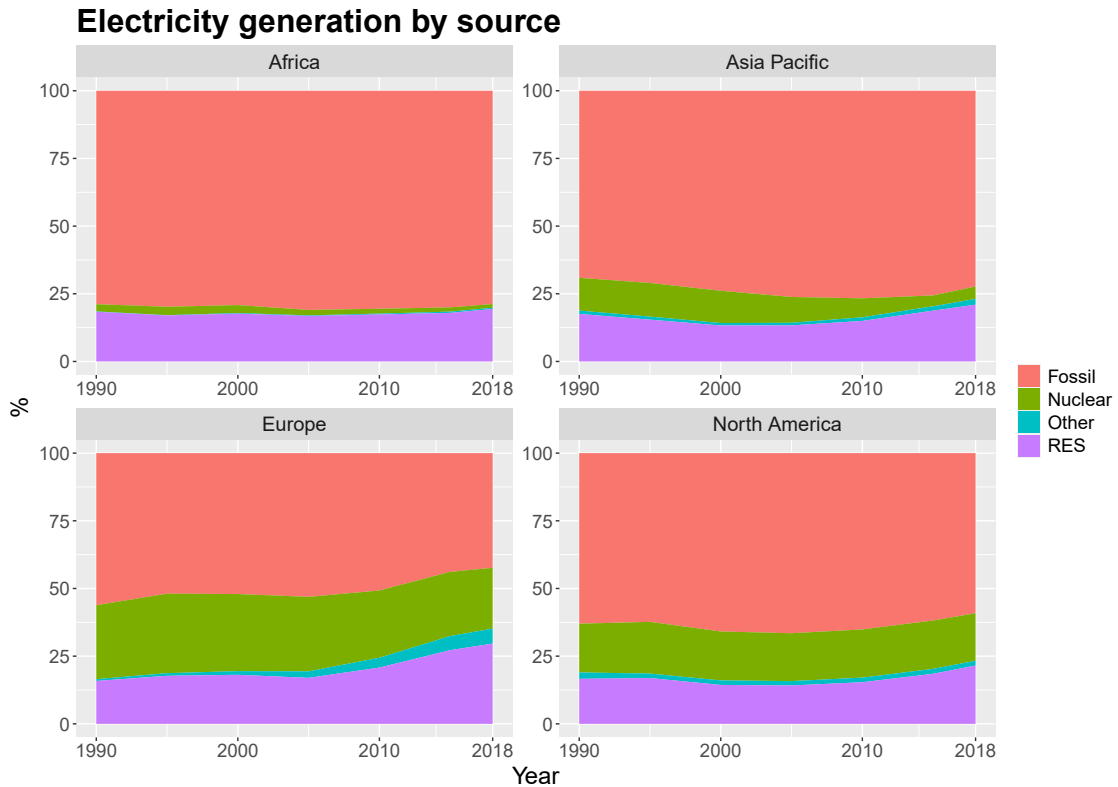


Fig. 2.12 Electricity Generation share by source. Author's elaboration from [75]. "Other" represent Biofuels, waste and not fully verified data.

The target of net zero emissions by 2050 has been announced by large part of the major CO_2 emitters and related policies and regulations are popping-up to change the current generation share, moving the RES production to the highest step of the podium. As stated from IEA, 44 countries and the EU have pledged to meet a net zero emission target [76] by 2050 or even before (resulting in a total coverage of around the 70% of global CO_2 emissions). Nevertheless, just 10 of them have set legal obligations, while the others are in the proposition phase or have just stated their will in official documents. This means that there is still a wide gap between theory and action, and still more actions need to be done.

Despite the general overview of the annual share of electricity generation, it is also important to analyse the generation mix with a more precise temporal resolution. Indeed, both electricity consumption and generation show seasonal, monthly, weekly and daily fluctuations, and since production units have to adjust their energy production to consumer demand, this leads to a large variation in the actual electricity

generation mix at small time intervals [77]. Consequently, key indicators such as the primary energy factor (PEF) of electricity generation and the CO_2 emission factor (CO2EF) show significant ranges of variation depending on the energy sources available in each country and their generation and dispatch profiles [78, 79]. For example, figures 2.13 and 2.14 show the monthly RES share variation for selected regions using the violin plot (please, refer to the next paragraph for the used data details). The "violin shape" represents the density estimate of the variable: the more data points in a given area, the larger the violin for that area. It is similar to a boxplot, but allows for a better understanding of the distribution of the variable under study. Please, be ware that the y-axis are different per each sub-plots in figure 2.13.

The charts highlight that the RES share variation can be narrow, as in the cases of Florida or New York state. In these cases, considering an annual average value can generally lead to a good estimation of the environmental impact of a technology or PEF and CO2EF. But in other cases, such as California or the four cases reported for the EU (Austria, Denmark, Italy and Germany), wide variations are in place across the months and also in each month. The remarkable importance of hydro power in Austria [80], for example, is clearly visible in May and June, when the melting of the snow feeds a large amount of water into lakes and rivers, increasing the hydro output potential and the overall RES share value. In Germany and Italy, in which wind and solar are on the podium of power generation sources, the variability is significant all over the year.

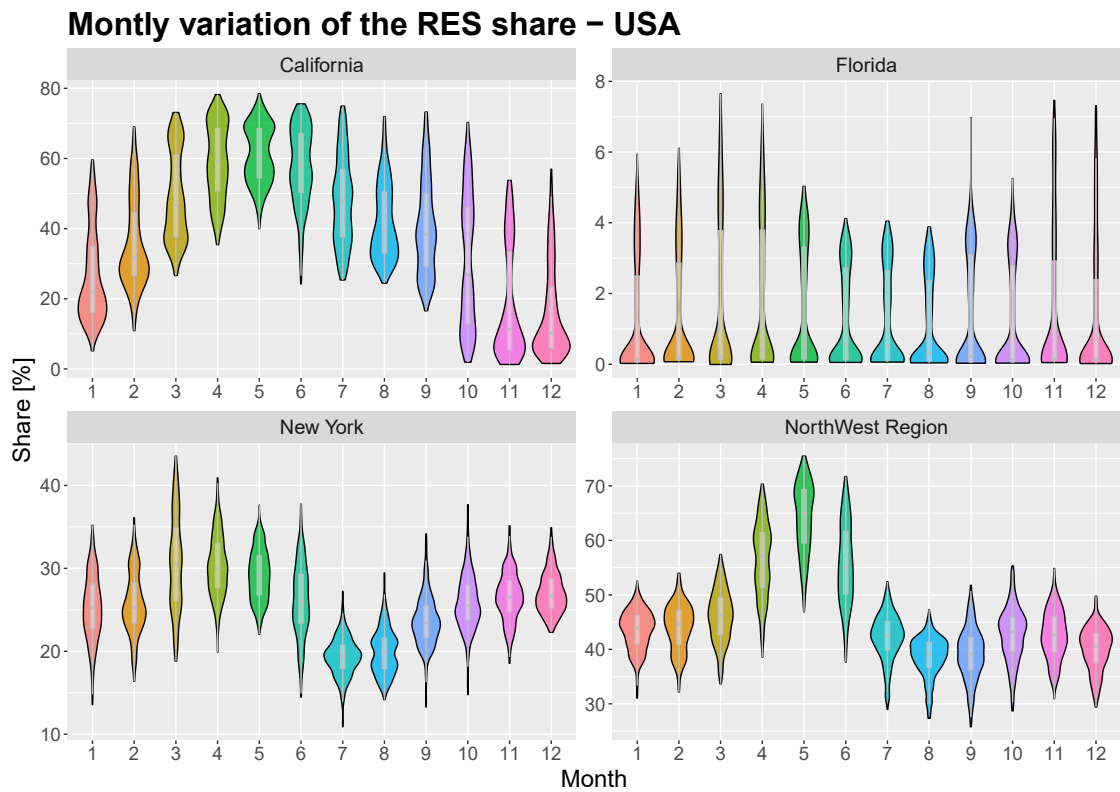


Fig. 2.13 Monthly RES share variation for selected US states. Author's elaboration from [81]

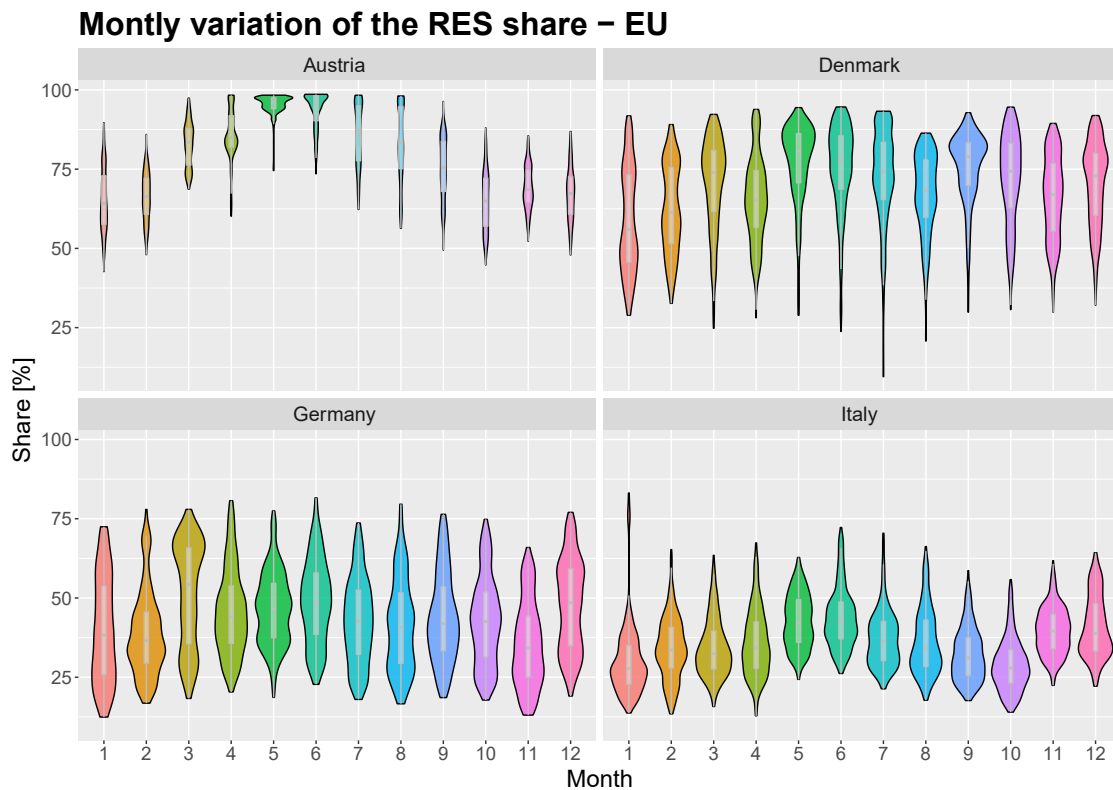


Fig. 2.14 Monthly RES share variation for selected EU countries. Author's elaboration from [82]

The generation mix data for EU countries has been retrieved by the ENTSO-E Transparency Platform [82]. The platform makes the production data available at least with hourly detail for different European countries. The actual generation by energy source has been collected for the year 2019 and the data has been aggregated into a limited number of energy sources (coal, gas, hydro, nuclear, oil, solar, wind and other). The main objective of this simplification has been the definition of meaningful electricity mixes, to be qualitatively compared among each other and to be comparable with the USA data. The generation mix data for the USA has been retrieved by the *Energy Information Administration* (EIA) website [81]. The EIA gives access to different data about USA energy exchange, production and consumption. In particular, they provide hourly total net generation by energy source and the 2020 data has been collected for the purpose of this work and reported in the chart above.

Having these wide variations means that the very same electricity load, from HPs, AC units or any electrical device, can consume different electricity quality, resulting in a good or bad exploitation of the green electricity or the overall grid efficiency. Generally, such analyses are conducted with annual average values, and an hourly evaluation can show if such an approximation can be acceptable.

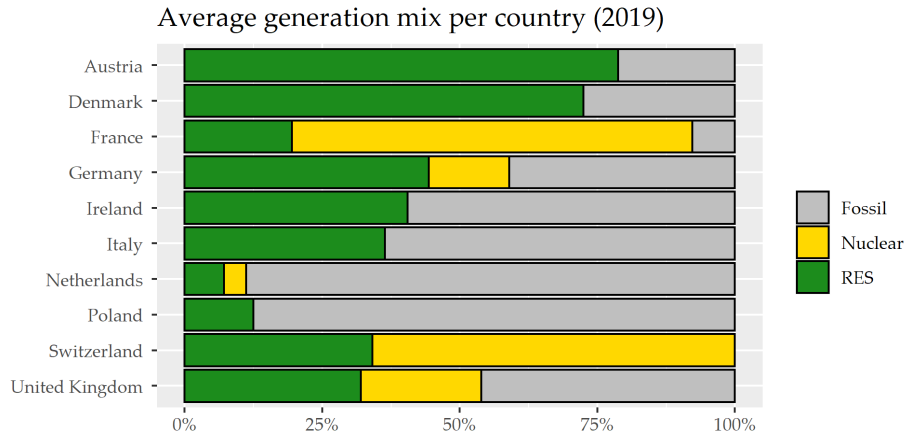


Fig. 2.15 Average electricity mixes in 2019 on an annual basis in different European countries [28]

Taking into account hourly data for both energy generation and demand allows to calculate the actual hourly electricity mix throughout the year, together with the primary energy consumption and the CO_2 emissions associated with the electricity that is consumed by an investigated device. This is a more precise and reliable account of the effective impact of the electricity use. The HPs considered for the analysis are obtained by two distinct data sets, which ensure a wider significance by providing different profiles and operation logic. In figure 2.16, 2.17 the hourly average electrical profiles for 10 different HP installations are displayed for the different months. The first four profiles (C7 to C10) have been provided by GSI [83], an Italian company. The data are based on the operation of three water-to-water geothermal (close loop) vapor compression heat pumps, of which two of them are for residential use (C7, C8), while the other two (C9, C10) are dedicated to an accommodation facility. The HPs are equipped with scroll compressors and electrical valves coupled with inverters, to regulate the power output. In particular, all the monitored plants are located in Italy at different latitudes (in Central and Northern Italy) and present different electrical rated powers. The data has been provided for the years 2018/2019 with one minute step, but the analysis has been carried out

by aggregating the values on hourly basis on the entire heating season (October - April). The data availability was quite accurate, with the main issue being related to a limited number of missing data. However, due to the narrow resolution, it has been decided to fill the occasional lacking values taking the previous data observation, since no particular variation can usually happen in one minute interval. The choice of hourly values is consistent with the available information for power generation mix in most countries, although in some cases values are available each 15 minutes.

The remaining profiles (C1 to C6) have been retrieved from the *London Datastore* [84] which is an open data-sharing portal in London. In this case, the data are recorded with a 15-minute timestamp between the last days of December 2011 to the first days of March 2014. In order to compare the profiles and the consumption with the previous data collection over an entire heating season, the data from October 2012 to April 2013 have been considered. Even if the time windows of the two datasets are not overlapping, multiple real operational profiles are still providing a valuable source for evaluating the effect of the variability in comparison with the usual profiles that are derived from software simulation tools. Unfortunately, no further information (such as technical data and/or heat pump typologies) about the heat pumps systems are available. It can be seen that even this three profiles present the typical residential profile, with the morning and evening peaks of consumption, although with a different relative importance.

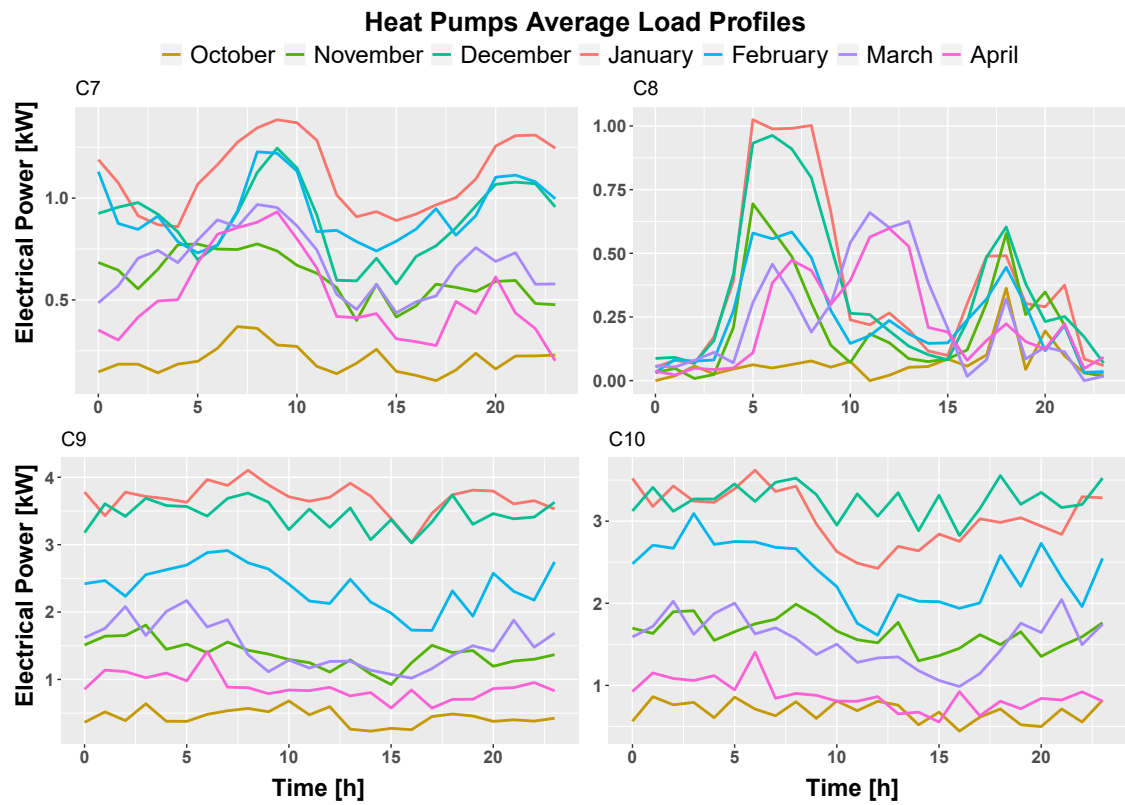


Fig. 2.16 Average Heat Pump electrical load from [83, 27]

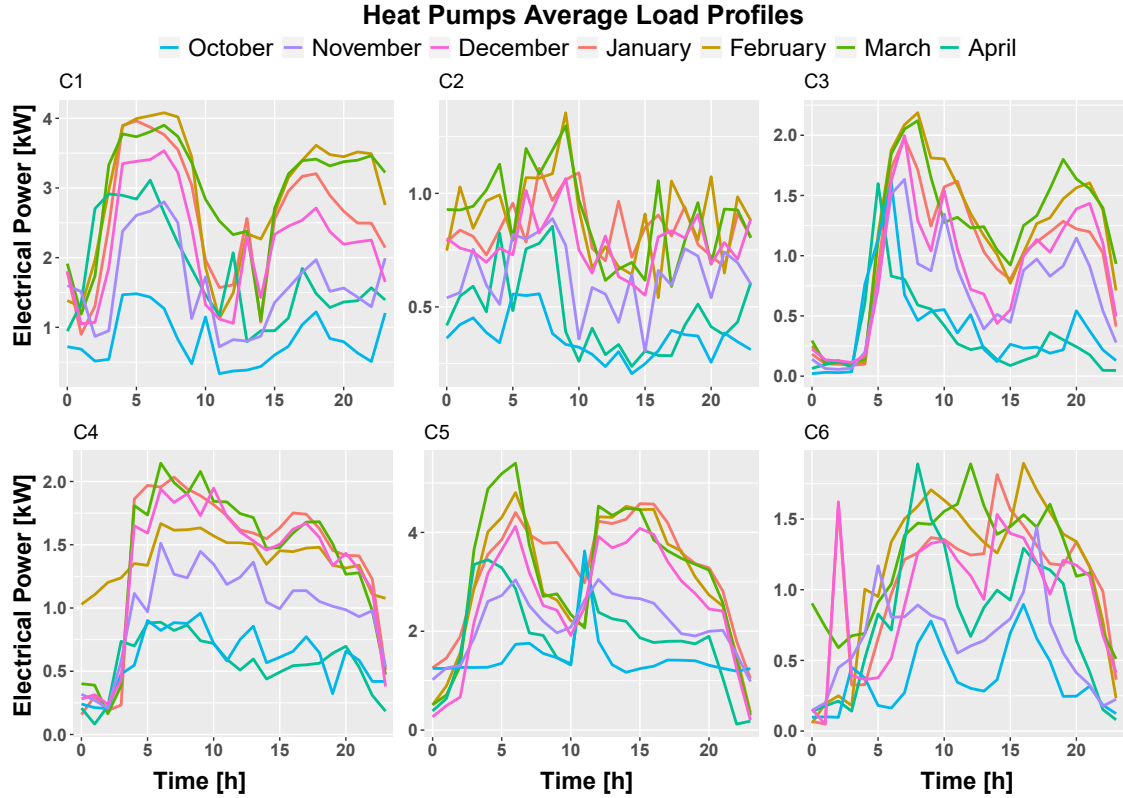


Fig. 2.17 Average Heat Pump electrical load from [27, 84]

2.3.1 Methodology

Using the operational data of power generation, in parallel with detailed information on the HP power demand, is it possible to determine the effective energy consumption by HPs and Chillers. In particular, this method allows to calculate the hourly electricity mix throughout the year, together with the PEC and the CO₂ emissions associated with the electricity that is consumed by the appliance.

The most common indicator to quantify and compare different electricity mixes is the CO₂ emissions factor of the electricity generation. Usually this factor is calculated as an annual average, as:

$$EF_{annual,mean} = \frac{\sum_i EF_i \cdot E_i}{\sum_i E_i} \quad (2.18)$$

Where the average annual electricity emission factor ($EF_{annual,mean}$) is calculated as the sum of the product between the specific emission factors (EF_i) and the annual power generation (E_i) for each energy source, divided by the total power generation in the system. Instead, this research work goes beyond the simple annual average, by defining a weighted average based on the effective electricity consumption profile of each single user. Therefore, the emission factor is calculated by defining an hourly emission factor for each j-th hour:

$$EF_{hourly,j} = \frac{\sum_i EF_{i,j} \cdot E_{i,j}}{\sum_i E_{i,j}} \quad (2.19)$$

to be used for a weighted average based on the electricity consumption of the heat pump in each j-th hour of the heating season ($E_{HP,j}$):

$$EF_{annual,weighted} = \frac{\sum_j EF_{hourly,j} \cdot E_{HP,j}}{\sum_j E_{HP,j}} \quad (2.20)$$

This last value is a more precise representation of the electricity mix related with the HP operation. This indicator is then compared with the annual average for multiple HP profiles and different countries to assess the range of variation of the results. In order to calculate the emission factors for the different profiles and countries, the Intergovernmental Panel on Climate Change (IPCC) [85] CO_2 factors have been considered. The carbon intensity of the different sources take into account the emissions related to the whole life cycle of the production plants, from construction to operation and decommissioning. Using life cycle factors (LCF) allowed us to have a better comparison between the fossil and non-fossil energy sources since, also RES, that are usually considered carbon neutral, have an impact. The IPCC values are detailed at [86] and they are extracted from the *IPCC - 5th Assessment Report* [87] and, in particular, from the following two sections [88, 89]. The emission factors are expressed as CO_2 -equivalent, i.e. taking into account also other gaseous compounds that have an impact on global warming. Of course, for the very same energy vector, it is possible to have different technologies with different efficiency meaning that a single value for CO_2 emissions can be accurate for some technologies and not for other. Nevertheless, the used values are a sort of weighed average emission factor, taking into account the different production technologies.

Table 2.2 CO₂ emission factors for the different energy sources

Energy Source	Emission Factor [gCO ₂ eq/kWh]
Biomass	230
Coal	910
Gas	490
Geothermal	38
Hydro	24
Nuclear	12
Oil	650
Other	490
Solar	45
Waste	620
Wind	11

2.3.2 Results

The aim of this study was to evaluate the effect of different electricity mixes in the actual generation mix of the electricity consumption of HPs. In particular, the real HP consumption is compared with the annual production mix of each country, to evaluate to which extent an hourly analysis differs from an annual average. In this section, it has been reported a couple of results in order to keep the document slim. Nevertheless, in Appendix A all the graphs are reported, with some additional comments.

The bar plot in figure 2.18 represents the shares of the national energy mix of Italy for each of the main energy sources, compared with the corresponding energy mixes weighted for each HP consumption profile. Moreover, it reports the annual average emission factor for each electricity mix (in white at the bottom of each bar) in order to quickly catch the differences between the produced energy and the emissions related to HP consumption. It is possible to quickly see that the different load profiles produce different shares of energy consumption, due to the different load curves in each hour of the day and over specific months. In particular, Austria, which relies heavily on hydro power (see also figure 2.14 and 2.19), shows a deep seasonal variability highlighted also from the different EF values in Table 2.3. For all the different C_n the emission factor is higher than the annual average, and it varies between +9.6% and +1.5%. This is mainly caused by the fact that the hydro power has a high variability during the year: in winter the resource is

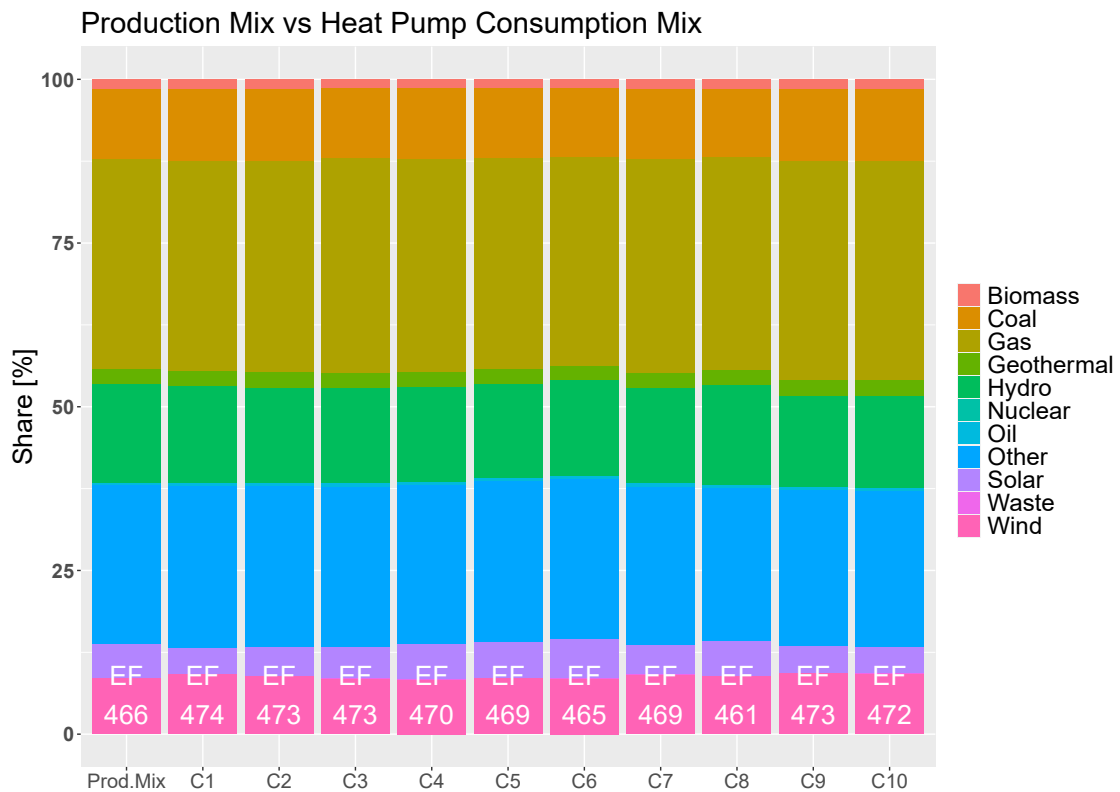


Fig. 2.18 ITALY - electricity production mix compared with the electricity consumption mix of the different HP systems

scarcer, while in spring is abundant as shown in figure 2.14, where April presents 70% of hydro power share in comparison with lower values for the rest of the winter period. Nevertheless, considering the weighted average values for the HP systems, since energy consumption for heating in April is generally very limited, its weight remains marginal in comparison with the annual generation mix. The mismatch between hydro production and HP energy consumption is compensated mainly with natural gas, increasing the EF of the different HPs profiles, moving the local emission towards the production plant.

Conversely, Italy is characterized by a more diversified generation mix with a higher contribution from carbon-intensive sources, produces both positive and negative variations of the EF, between +1.7% and -1.1% depending on the specific HP system. The strongest negative variation corresponds to the HP profile C8 (see fig 2.16), which is characterized by an electricity profile that better exploit the central hours of the day, especially in spring, where the generation from solar energy is higher. Moreover, Italy has a more diversified generation mix than Austria,

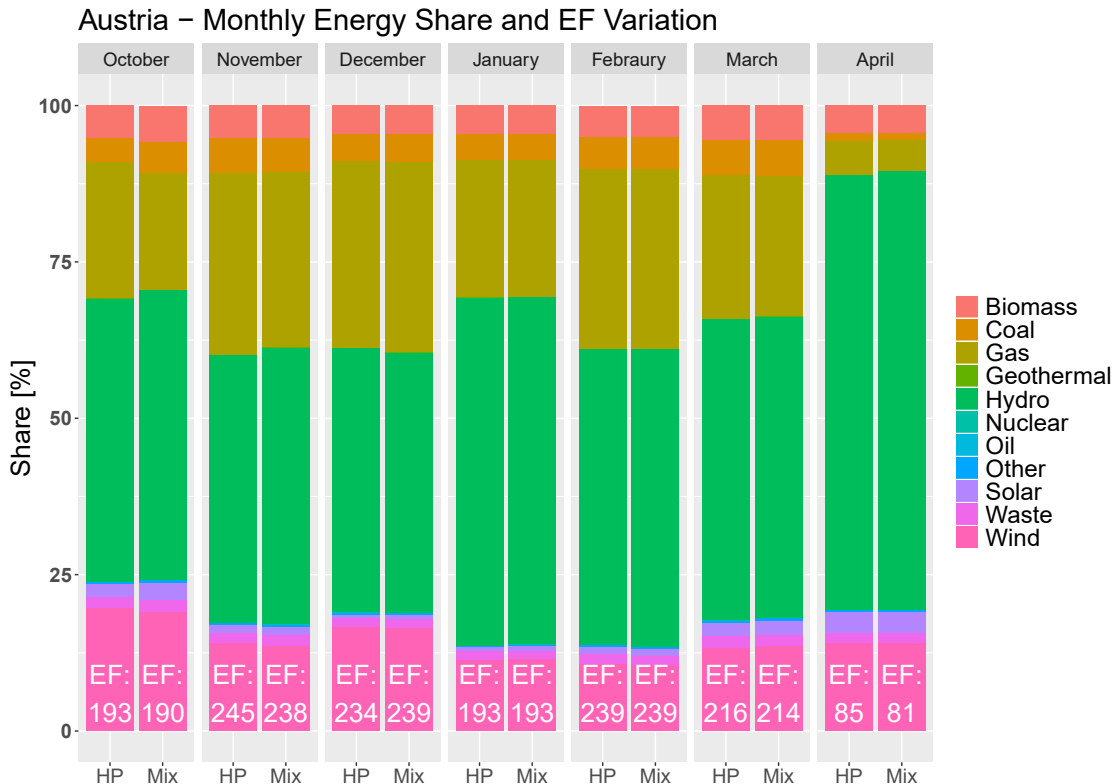


Fig. 2.19 Austria - Monthly variation of the energy mix share and the HP consumption share [27]

presenting different energy integration possibilities: C3, C4, C5 and C6 present higher wind shares in comparison with the annual production mix, decreasing the overall HP fossil consumption with respect to the other profiles.

This result confirms the added value of performing hourly analyses when data are available and reliable. The difference remains generally limited, with average mean absolute differences on a country basis lower than 5-6%. Such low value do not justify the major work needed in detailed analysis. Nevertheless, future energy portfolio development can change this pictures. The strongest effects appear in Austria and Denmark (as also remarked in Figure 2.20), both characterized by significant energy generation from RES, suggesting that the expected increase in RES shares in future years may increase the gap between hourly and annual evaluations. For specific HP profiles the difference can be as high as 9.6% or as low as -3.0%, but in the majority of the cases the emissions of HPs are underestimated when using annual emission factors.

Table 2.3 Summary of the different EF and their variation for the HP systems

Country	EF - Energy Mix	Mean Difference Absolute Value	Max EF Difference	Min EF Difference
	[gCO ₂ eq/kWh]	[%]	[%]	[%]
Austria	198	5,86%	+ 9,6%	+ 1,5%
Denmark	348	4,51%	+ 7,5%	+ 1,7%
France	67	2,54%	+ 7,5%	- 3,0%
Germany	420	1,52%	+ 2,4%	- 2,9%
Ireland	369	1,17%	+ 1,4%	- 2,2%
Italy	466	1,09%	+ 1,7%	- 1,1%
Netherlands	360	1,28%	+ 3,3%	- 1,1%
Poland	765	0,39%	+ 0,8%	- 0,4%
Switzerland	17	0,00%	0,0%	0,0%
United Kingdom	326	0,58%	+ 0,6%	- 2,5%

An important aspect to be highlighted is the current limited weight of variable RES in the electricity generation mixes, especially in winter, which is the analysed period. As highlighted by Figure 2.21, different behaviours could be expected if the same analysis should have been conducted looking at summer time, where solar source has a strong share in some country mixes. The challenging decarbonization goals that are being set by different European countries will require significantly higher shares of integration, which will be also combined with various flexibility options (including storage, demand side response, sector coupling and networks interconnections). In this framework any evaluation on the increased electricity penetration in final users will need to be based on hourly simulations, to provide an accurate and timely evaluation of the emission savings that are obtained. Again, this aspect highlights the importance of integrated planning of energy demand and supply, as electrification alone is not a solution to decarbonize the energy system, if it is not matched with a parallel deployment of power generation from low-carbon sources. The installation of new HPs should be fostered together with heat storage and advanced monitoring and control systems, to allow a higher degree of flexibility in their operation.

The role of policies will be crucial in supporting an effective and efficient energy transition. A coordination at different levels and across different sectors is required to ensure the adherence between the expected results from simulations and the actual behavior of energy systems in their real operation. In this context, flexibility will become more and more important, to increase the power grid resilience against the

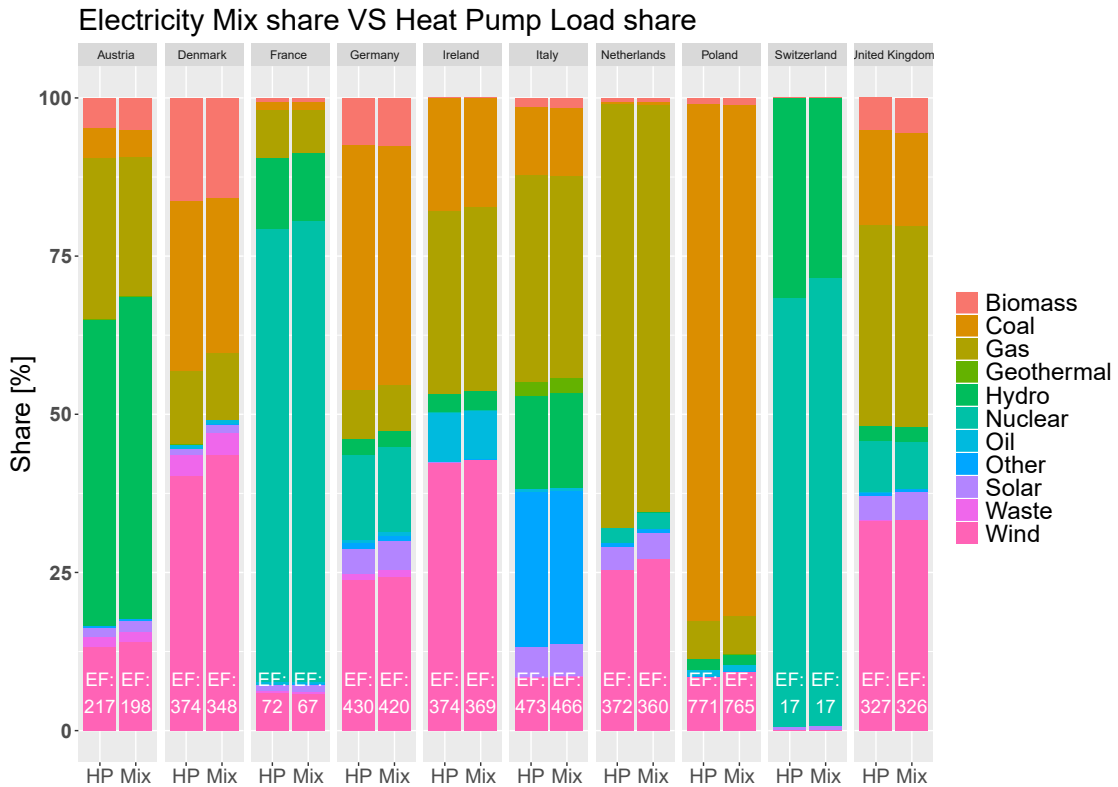


Fig. 2.20 C3 Load profiles with respect to different countries [27]

variability caused both on the supply side and on the demand side. Finally, it is worth remembering that all these aspects need to be based on an economic value awarded to the carbon emission savings that may be obtained. While the environmental benefit may be clear, the lack of an effective pricing of carbon emissions on a wide basis may prove to be a strong burden to the development of decarbonization solutions.

The results of this analysis may be further improved by considering a larger number of operational profiles of HPs in different countries and for different final users. Furthermore, the analysis could be further extended to summer time operation, since many reversible HPs are also supplying cooling, and RES like solar and hydro are abundant. These analyses are currently limited by the scarcity of reliable historical data of HPs operation with acceptable time resolution. Moreover, the availability of longer historical trends for generation mixes may increase the reliability of the results that have been presented. Moreover, the current analysis is performed on the underlying hypothesis that the HPs are already existing, and therefore they do not modify the current electricity mix of the grid. Conversely, if these results may be used

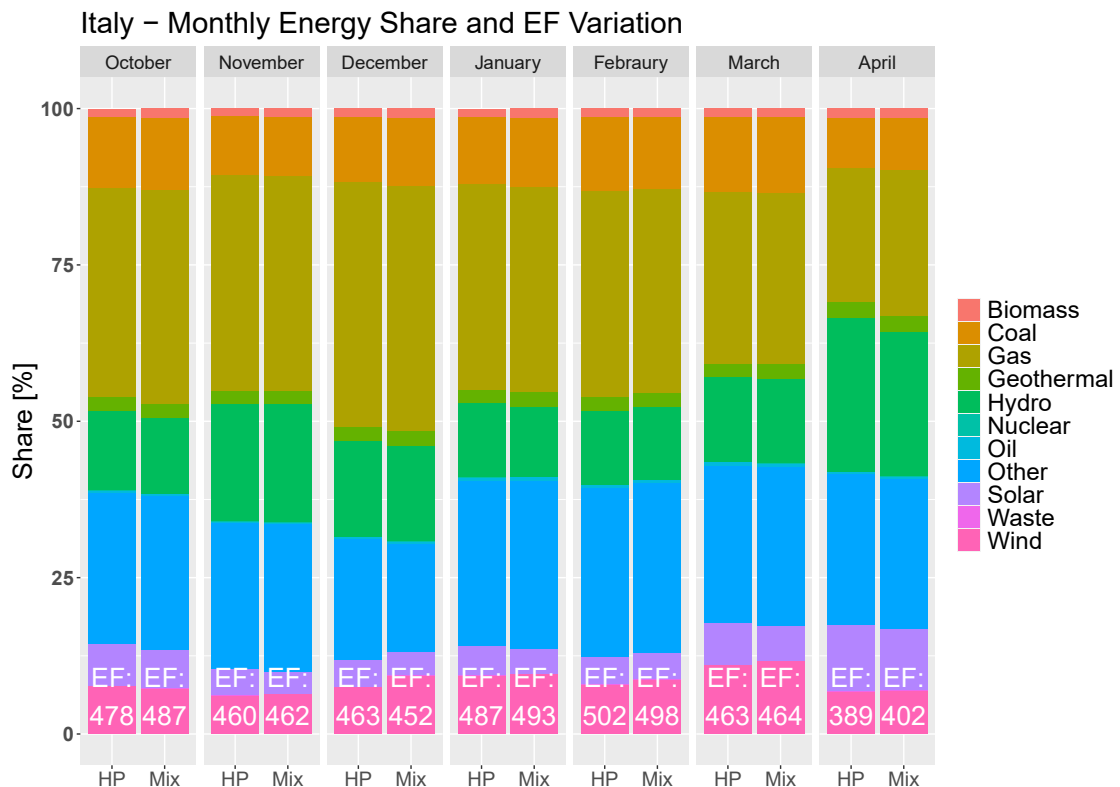


Fig. 2.21 ITALY - Monthly variation of the energy mix share and the HP consumption share

to evaluate the planning of a large number of new appliances consuming electricity, their deployment would increase and possibly modify the shape of the power system demand profile. Additional analyses will be required to assess the potential rebound effects that they may cause on the generation mix, such as increasing the need of dispatching fossil-based generation to compensate the lack of electricity from RES.

2.3.3 A comparison with electric mobility

As already said in chapter 1, EVs are among the key driving sectors for electrification since they can lead to significant benefits related to the decrease of climate emissions, as well as some local pollutants, especially in cities [90]. In this section, using the very same methodology explained in section 2.3.1, a comprehensive assessment of the impact on greenhouse gases (GHG) emissions on multiple countries is performed. Climate impacts have been evaluated by considering detailed temporal analyses for both electricity generation and EVs charging profiles. The EVs electrical

consumption, based on 3 main charging archetypes, has been compared with the national energy production mixes (the same used in section 2.3) on an hourly basis, to evaluate the differences between the average annual energy mix and the actual EV consumption patterns.

The purpose of this comparison is to investigate the possible impacts of having more variables, with respect to the HPs case, in terms of electrical load patterns. In fact, the EVs are charged in different locations and at different times over the the day, while HPs have usually a more stable behaviour with morning and evening peaks.

EV Charging profiles

The charging profiles taken into consideration have been chosen with the aim of comparing archetypal profiles related to EV charging in three different locations: at home, at work and in public charging stations. The charging points considered in this study have a power capacity ranging from 3.7 kW to 22 kW (i.e. no fast-charging has been considered). The profiles are the result of an analysis based on several data from real charging profiles in Germany, based on a model which takes into consideration different car segments, households characteristics and charging behaviours, to create a set of representative profiles for home, work and public charging [91]. The profiles have been normalized on the total demand of a weekday for each type of charging, to analyze comparable results considering the same amount of energy supplied to a vehicle. Figure 2.22 represents the three different profiles compared for a weekday and a weekend, with a representation of the contribution of each hour of the day on the total charging over a weekday.

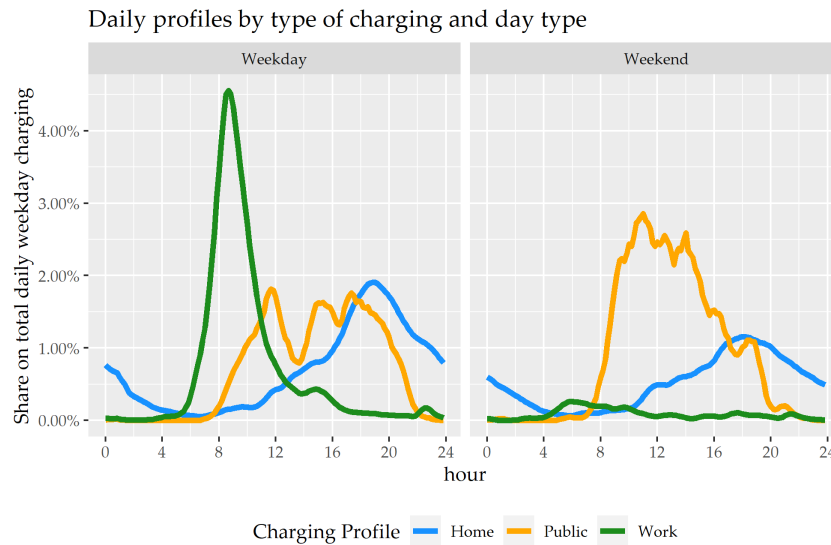


Fig. 2.22 Different EV charging profiles [28]

The considered profiles are representative for Germany and this can be a potential limitation for this work. Nevertheless, this approximation is also related to the unavailability of a large set of data over different countries but the author believe that the assumptions on which these charging behaviours have been built can still be an acceptable representation for the European countries that are being considered in this study.

In order to extend a bit the analysis performed for HPs, a comparison between LCA emission factors and direct emission factors is performed. The values are reported in the following table.

Results

First, hourly emission factors have been calculated and reported in figure 2.23 for direct emissions.

With the exception of Switzerland, which is largely relying on hydro and nuclear energy, the other countries present a large range of emission factors that is the result of seasonal and daily variations in their electricity mixes. These results underline the importance of having detailed assessment considering actual EV charging profiles rather than considering simple average annual emission factors.

Table 2.4 Emission factors for electricity generation from different sources [70, 85]

g_{CO2eq}/kWh_{el}	Direct emissions	LCA emissions
Biomass	0	230
Coal	870	910
Gas	368	490
Geothermal	0	38
Hydro	0	24
Nuclear	0	12
Oil	545	650
Other	368	490
Solar	0	45
Waste	555	620
Wind	0	11

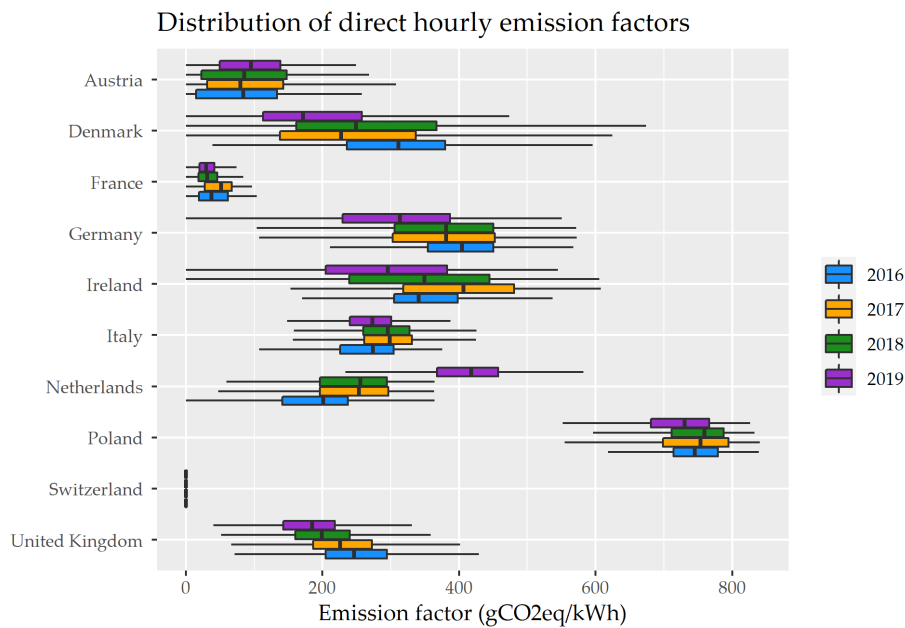


Fig. 2.23 Comparison of direct hourly emission factors in selected European countries.

Annual emission factors for the electricity supplied to EVs have been calculated for each country considering the three different EV charging profiles (fig 2.22, and evaluating them in four different years (2016 to 2019). The combined results, highlighting the variability of direct and LCA emission factors for each country, are showed in Figure 2.24. A summary of the main information related to the range of variation for each country is also reported in Table 2.5.

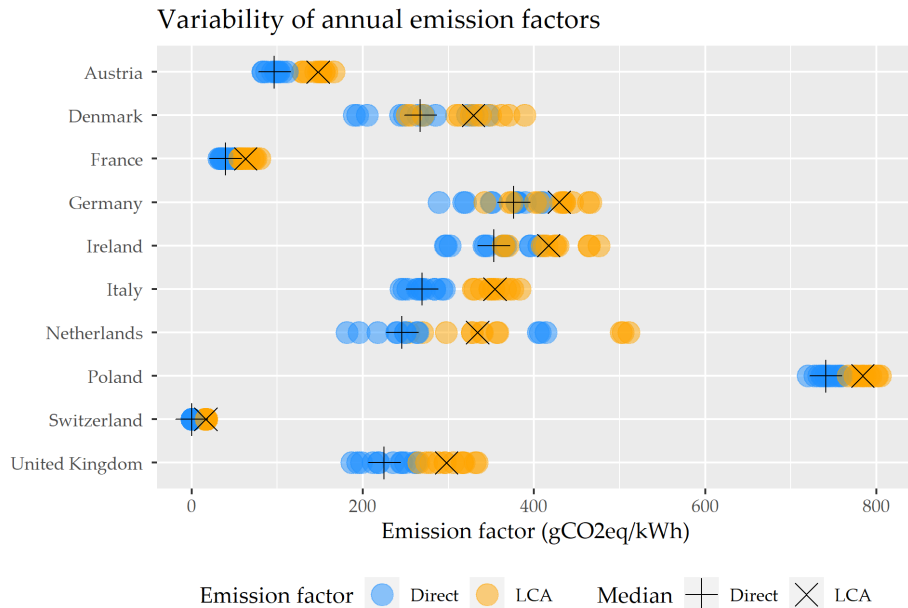


Fig. 2.24 Variability of annual emission factors of EV charging in each country (with variable year and charging profile).

While in some countries the variations remain under 10%, as in Switzerland and Poland, in other cases the maximum variation from the mean can reach values higher than 30%, due to the combined effect of different charging profiles on the demand side as well as different electricity generation mixes on the supply side. Considering all the combinations, the increase of emissions, between annual average and hourly analysis, when considering the LCA perspective is on average around 56 g/kWh with variations in the range $15\text{-}97 \text{ g/kWh}$. This insight highlights that in addition to the variability between countries, which is related to the different production mixes, there is an additional variability related to both the profiles and the years of operation. In particular, for some countries this latter effect appears to be more strong than for the charging profiles.

These results show that when assessing the effect of different charging profiles in a given country and a given year, the variability remains limited, with an average range of variation around 6%. Thus, the difference of different charging strategies appears lower than expected. On the other hand, for any given country and charging profile, the variation of the year of analysis resulted in an average range of variation of 18%, highlighting the significant variability in the electricity mix of these European countries over the years. This fact underlines the importance of considering multiple

2.3 Heat pumps electricity Consumption: Effective Energy Mix Consumption **51**

Table 2.5 Variation of annual emission factors over charging profile and years for each country

gCO_{2eq}/kWh_{el}	Direct emission factor				LCA emission factor			
	Mean	Min	Max	Range vs Mean	Mean	Min	Max	Range vs Mean
Austria	96.9	83.1	111.4	-14% / 15%	147.5	129.1	166.2	-13% / 13%
Denmark	264.0	189.7	346.4	-28% / 31%	332.4	251.8	389.0	-22% / 21%
France	41.0	31.6	54.0	-23% / 32%	65.2	55.8	79.8	-14% / 22%
Germany	363.1	288.7	410.6	-20% / 13%	417.1	342.1	466.3	-18% / 12%
Ireland	351.6	296.5	405.5	-16% / 15%	418.0	363.6	475.8	-13% / 14%
Italy	269.7	244.7	295.1	-9% / 9%	354.5	329.0	383.7	-7% / 8%
Netherlands	277.1	181.6	413.6	-34% / 49%	365.3	253.7	510.5	-31% / 40%
Poland	742.2	720.2	759.2	-3% / 2%	786.6	766.8	804.7	-3% / 2%
Switzerland	0.0	0.0	0.0	-	16.7	15.5	17.4	-7% / 4%
United Kingdom	227.2	186.8	263.1	-18% / 16%	301.7	265.4	333.2	-12% / 10%

years when estimating the emissions related to the use of EVs in any given country, accounting for the potential uncertainty related to varying electricity mixes over the years.

Chapter 3

Recognition EU Project and the HySun prototype

Part of my PhD activities has been developed within the ReCognition EU project, which aims is to develop RES technologies to improve self-consumption and energy efficiency in buildings. My task in this project was to develop a prototype of a hybrid solar cooling system that could use electricity and thermal energy to produce cooled air. The following sections introduce the project and present the prototype. Part of the following work has already been published as a project report. The full list of published documents can be found on the ReCognition main page [92].

3.1 The Recognition Project

The European Union (EU) is among the leading countries for environmental policies and sustainable transition, having one of the strongest decarbonization policies, the “Clean Energy Package for all Europeans” [93] which will lead to the rapid installation of Renewable Energy Sources (RES), increasing the production of clean (but mostly non-programmable) electricity in the grid. The new legislative package set ambitious targets for 2030 to face the climate change and related environmental issues: 32% of RES share in final consumption and -40% CO₂ emissions are among the targets described in the package. The general aim is to reach the carbon neutrality by 2050. These targets have been revised after the COVID19 pandemic. In fact, the new green transition plan is called "*fit for 55*" [94], which again aims for carbon

neutrality in 2050, but proposes a new and challenging target for 2030: reducing CO_2 emissions by 55%. Following the outbreak of the Russia-Ukraine conflict, further discussions are currently taking place. EU activities include proposing projects, promoting events, writing new policies and regulations to guide and accelerate the transition towards a more sustainable society. One of the most famous EU programs is the Horizon 2020 (H2020) research framework, which started back into 2014 with the aim of improving the EU competitiveness and stimulate the research [95]. Recognition (ReC) is a 3-year H2020 project (H2020-LC-SC3-2018) which started back into 2019, related to the implementation of renewable sources and their management in buildings. The acronym Recognition stands for **RE**n**ewable CO**Generation and storage tech**N**ologies **I**ntegr**A**Tion for energy aut**ON**omous buildings [92].

3.1.1 The ReC Objective

As already shown in the introduction (section 1), the building sector is one of the largest energy consumers worldwide and will continue to play an important role in the future. It currently accounts for 40% of the final energy consumed in the EU and a large part of this is derived from fossil fuels, especially in terms of heating and cooling energy. Yet the EU has set ambitious environmental targets for 2030, 2050 and even beyond with the fit for 55 plan [94]. This transition will affect all sectors and all human activities, such as transport, industry, power generation technologies and of course more broadly energy production and consumption. In terms of energy production, this means improving the efficiency of production, reducing consumption and increasing the share of RES. For this last point, there are 2 main approaches to reach the EU targets: a centralised and a decentralised approach. The first aims at introducing renewable capacities in the form of large "power plants" (large PV fields, wind farms, etc.), the second is the opposite: installing a number of small renewable generators close to the consumption points (rooftop photovoltaic/solar thermal, micro-hydro plants, etc.). Both approaches have their advantages and disadvantages, and a smart and effective mix between the two will likely result in meeting effectively the future energy demand.

While the centralised approach is more related to strategic investments and visions at national or regional level, the decentralised system is more complicated as more actors are involved: local authorities, grid operators, prosumers, etc. It is also closely linked to the buildings sector, as some of the available renewable

energy technologies are designed to be installed in buildings. A large part of the EU building stock [96] is more than 50 years old and has very little or no installed renewable energy generation systems. They are also not designed for the installation of renewable energy systems and advanced control and management tools. For this reason, important research is being carried out to effectively integrate this architecture into existing buildings. The ReC project is part of this effort and aims to create a solid mix of software and hardware components to facilitate and promote the integration of multiple renewable energy sources into buildings and improve RES energy use for heating/cooling technologies such as heat pumps. In fact, heat pumps (like all other electrical appliances) can be considered "green" if the electricity they require comes from renewable sources.

Table 3.1 Barriers and Opportunities for further development of RES integration and improvement in the buildings sector

Barriers		Opportunities	
Single-technology integration	RES volatility seldom allows for a total coverage of energy demand. Storage demand-response strategies and integration are needed.	Micro-energy hubs	integrated energy systems are getting momentum in terms of technology and software development.
Different maturity level	RES technologies have a wide maturity level in terms of size, durability, efficiency. Further development is still needed per each technology.	ICT technology	IoT and AI are growing in terms of capability and diffusion. They are playing an important role in energy management systems.
Non performance parameters neglection	Size, aesthetics, disposal, safety and maintainability are often excluded from research activities. Indeed, they can play a major role in technology diffusion.	Policy drivers	EU is pushing hard to become the leader in sustainability. This trend is moving resources, efforts and research towards specific objectives among which the renovation of the building sector
Standardization and interoperability	A wide range of different technologies having an even wider range of standards and protocols create close environments which limit technology diffusion.	Committed industry	Industries are answering positively to researchers and governments actively participating to development and policies formulation.
Cumbersome planning phase	Multiple RES design and installation requires a significant amount of time and effort.		
High initial investment	Typically, a significant capital is needed to install and design multi-RES systems.		
Grid instability	In a steep electrical RES increase scenario, the grid may start to be less stable.		
Lack of standardization measures	Self-consumption must be incentivized. Regions, nations and continents have very different policies and strategies. Uneven distribution of resources and could lead to market instability and disparity.		

The Consortium

The ReC consortium is made of 15 partners divided in 3 universities, 2 research institutes, 7 enterprises, 2 industrial partners and 1 non-profit organization. Their role in the project and their references are reported in Table 3.2.

The main objective for the project is to develop synergies among renewable energy production, conversion, storage and consumption through the development of cross-cutting technologies. ReC aims to address the building energy-autonomy

Table 3.2 Sum-Up table reporting the project partners and their role

Partner	Country	Acronym	Role	WP
Politecnico di Torino [97]	Italy	POLITO	Coordinator Technology Provider Major Pilot	1, 2, 3, 4, 5, 6, 7
Ethniko Kentro Erevnas Kai Technologikis Anaptyxis [98]	Greece	CERTH	Technology Provider Pre-Pilot	1, 3, 4, 5, 6, 7
EnergyWork [99]	Italy	EW	Technology Provider	1, 3, 4, 5, 6, 7
Intracom sa Defense Electronic System [100]	Greece	IDE	System Integrator Test-bed Provider	1, 3, 4, 5, 6, 7
ZH SRL [101]	Italy	ZH	ESCO	1, 2, 3, 4, 5, 6, 7
Ecole Polytechnique Federale de Lausanne [102]	Switzerland	EPFL	Technology Provider	1, 2, 3, 4, 5, 6, 7
Centre Suisse D'electronique et De Microtechnique sa [103]	Switzerland	CSEM	Technology Provider	1, 2, 3, 4, 5, 6, 7
Windcity [104]	Italy	WINDCITY	Technology Provider	1, 2, 3, 4, 5, 6, 7
Micro Turbine Technology BV [105]	Netherlands	MTT	Technology Provider	1, 2, 3, 4, 5, 6, 7
Ellnika Petrelaia AE [106]	Greece	HELPE	Industrial Pilot	1, 2, 3, 4, 5, 6, 7
Servelect	Romania	SVT	ESCO	1, 2, 3, 4, 5, 6, 7
University of Bristol [107]	United Kingdom	UoB	Social Sciences and Humanites	1, 5, 6, 7
Electric Corby Community Interest Company [108]	United Kingdom	ECCIC	Major Pilot	1, 3, 4, 5, 6, 7
EtreI Svetovanje in Druge Stortive Doo [109]	Slovenia	ETREL	Technology Provider	1, 3, 4, 5, 6, 7
Universitatea Technica Cluj-Napoca [110]	Romania	TUCN	Major Pilot	1, 3, 5, 6, 7

through a holistic approach which leverages energy production from multiple renewable energy technologies (RETs) and their coordination to meet the buildings' needs. In order to reach this, (i) new technologies will be developed, to overcome state-of-the-art limitations and to create new energy-coupling possibilities. Then, (ii) a cross multi functional platform optimally harnesses the energy generated taking into account real-time consumption information, storage and grid states and users needs.

The project has been divided in 7 work packages (see fig.3.1) that cover the main gaps and barriers mentioned above in Table 3.1. For more details on the objectives, work packages, key milestones and achievements, please visit the official project website [92], where all results and documents related to the project are available.

My task in the project is to take care of the energy consumption of cooling and in particular to design and realise a hybrid solar cooling machine that can use electricity and heat from other RES. The description, design and realisation of the prototype are described in the following section.

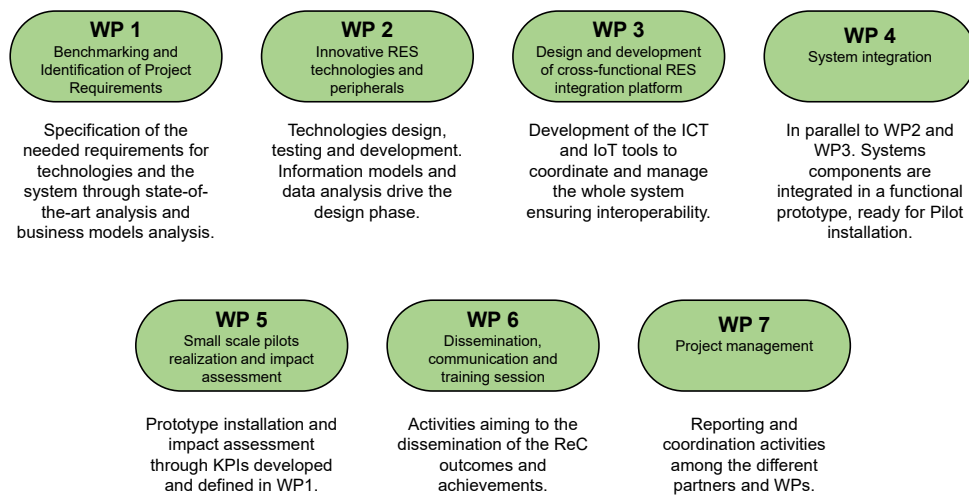


Fig. 3.1 Recognition Work Packages

3.2 HySun: The Hybrid-Solar Cooling Prototype

Air conditioning and cooling (ACC) is forecast to dramatically increase in the next years, quickly surpassing the current 20% of the overall electricity consumption worldwide [19, 20]. As already pointed out in this document, Europe is massively shifting towards RES, with the ambitious target of 32% share by 2030. To reach this goal, the heating and cooling (HC) sector needs to heavily shift towards renewable sources. The cooling demand has been mainly fulfilled till now with electrically driven technology, which leads to huge peak power consumption during hot summer periods, putting pressure on the electrical grid. In fact, most of the worldwide installations are based on compression chillers of different sizes, efficiency, and technology solutions. In a RES-based vision, peak loads must be handled in order to reduce the stress on the national grid and to exploit the distributed sources. Solar-driven technology, such as PV, presents energy production in resonance with the cooling demand and can supply energy to compression chillers when needed. However, as already mentioned, a large part of cooling appliances presents low efficiency, and the request PV power installation will require extended surfaces and high economic investment to be able to supply the requested energy and power input. Latent loads play an important role in producing these consumption peaks. In fact, sub dewpoint condensing is the state-of-the-art technique to remove moisture

from the supply air, and temperatures below the dew point on the evaporator side are needed to effectively remove water. Moreover, most of the human population lives in warm and humid climates, increasing the importance of latent heat load. Looking at this scenario, desiccant solid and liquid materials can have a major role in handling the latent load and lowering the pressure on the electrical grid. In fact, better performances of such systems have been highlighted [111–115], both in terms of energy efficiency and peak consumption, also due to the generally higher temperature levels. Thermally driven technologies have the potential to shift part of the cooling load towards low-grade thermal energy, which can be produced from RES such as solar thermal module or waste heat. Solar dehumidification processes are among the most promising technology. At the end of 2015, an estimated 1350 solar thermal cooling units had been installed and around 80% of them are in Europe [19], meaning that there are large room for improvement all over the world in terms of numbers, technology development and investments.

In the following two paragraphs a brief introduction to adsorption phenomenon and main adsorption materials are described in order to provide the reader with an overview of the adsorption context.

3.2.1 Adsorption fundamentals

Adsorption is a spontaneous physical phenomenon in which the surface of a solid material binds molecules of a gaseous or liquid stream with which it is in contact. There are two types of adsorption: physical, which involves weak intermolecular forces such as Van der Waals forces and electrostatic forces, and chemical, which involves chemical bonds. The first is the one related to this work and the HySun prototype. In general, the interaction can be divided into attractive and repulsive forces between two molecules.

The attractive potential due to dispersion forces, can be expressed as:

$$\phi_D = -\frac{A_1}{r_{12}^6} - \frac{A_2}{r_{12}^8} - \frac{A_3}{r_{12}^{10}} \quad (3.1)$$

where r_{12} is the distance between the molecules and A_1, A_2, A_3 are constants. The terms of this expression represent, respectively, interactions between instantaneous in-

duced dipoles, induced dipole-induced quadrupole and induced quadrupole-induced quadrupole.

When the two molecules are very close to each other, repulsive force takes place, and it can be formulated as:

$$\phi_R = -\frac{B}{r_{12}^{12}} \quad (3.2)$$

where B is a constant.

The attractive and repulsive contributions are considered together thanks to the Lennard-Jones potential. This allowed a single formulation to describe the total potential between two molecules as a function of their distance [116]:

$$\phi = V(r) = 4\varepsilon \left[\left(\frac{\sigma}{r} \right)^{12} - \left(\frac{\sigma}{r} \right)^6 \right] \quad (3.3)$$

where ε is the potential well depth, which corresponds to the equilibrium between attractive and repulsive forces while σ represents the distance between the two molecules at which the potential is equal to zero.

Fundamental to the design of an adsorption machine is, of course, the thermodynamics of the process. It can be effectively described by adsorption isotherms. Isotherms represent, at a fixed temperature, the loading, i.e. the amount of adsorbate on the solid (adsorbent) per unit mass of the solid itself, as a function of the relative pressure of the gaseous phase in equilibrium with the adsorbent at the specified adsorption temperature.

Six main families of adsorption curves can be identified (according to the IUPAC formulation) and they depend on the adsorbent material and the adsorbate fluid.

Adsorption isotherms that exhibit an upward concavity indicate hydrophobic behaviour, as a large relative pressure increase is required to slightly increase the load. A downward concavity, on the other hand, indicates hydrophilic behaviour, as a huge increase in charge is required for small relative increases in pressure. The type I isotherm settles to an asymptotic value as the relative pressure increases, and this behaviour is typical of microporous adsorbents. The types II and III, on the other hand, are characteristic of macroporous materials and differ from each other depending on the strength of the interaction between adsorbate and adsorbent [116].

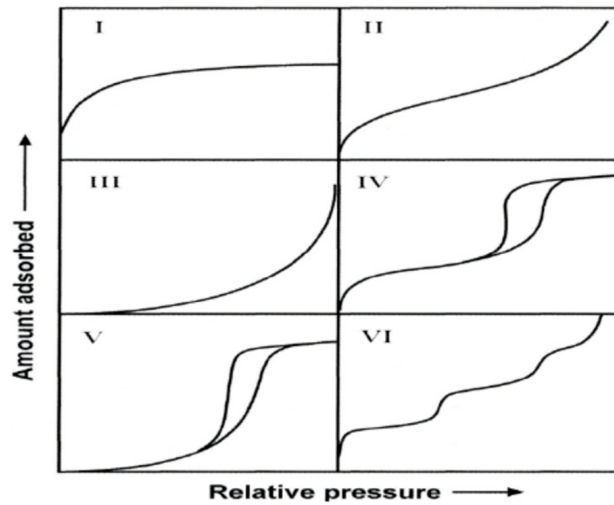


Fig. 3.2 Typical Adsorption Isotherm Shape [116]

The types IV and V describe single- and multilayer adsorption and are characteristic of mesoporous adsorbents and show hysteresis due to capillary condensation. Finally, the type VI describes multilayer adsorption for non-porous materials.

3.2.2 Adsorbents

Silica gel is an incompletely dehydrated form of polymeric colloidal silicic acid, represented as $SiO_2 * nH_2O$. It is produced starting from sodium silicate, and it comes as a granular and semi-transparent material, as can be seen in figure 3.3



Fig. 3.3 Silica gel grains

It is a highly porous material filled with a large number of pores with a diameter of 2 to 20 nm and a pore volume between 0.35 - 1.15 cm^3/g . These geometrical parameters allow the silica gel to have a very large specific surface area (300 to 800 m^2/g). The main advantages of this material are (i) its large water adsorption capacity and (ii) its low regeneration temperature. In fact, it can adsorb up to 40% of its dry mass and can be regenerated from 50 °C to 90 °C. This wide range increases the possible heat sources that can be used. In addition, the manufacturing process of silica gel is simple and the raw material is widely available worldwide, making its price very affordable.

These are also the main reasons why the silica gel has been selected for the HySun prototype.

Zeolites are porous crystalline aluminosilicates mainly composed by SiO_4 and AlO_4 tetrahedra connected to each other through shared O_2 atoms. This means that Zeolites are not characterized by a distribution of pore size having such an ordered structure. The Si/Al ratio never goes under 1.0, without any upper limit and this characteristic makes the different types of zeolites: Aluminum rich sieves, which is hydrophilic, to silicalite, which is hydrophobic. The threshold is generally identified around 8-10 between hydrophobic/hydrophilic zeolites [116]. Unlike the Silica Gel, Zeolites desorption temperature is in the range of 70-250 °C, making the regeneration process a bit harder to drive.

The Zeolites can be divided into two large groups [117]:

1. Type A: where the ratio Si/Al is between 2-2.5, the free diameter is around 0.41 nm.
2. Type X and Y: have Si/Al ratio between 2-3, free diameters of 0.74 nm.

Activated carbon are carbonaceous materials which are processed in order to allow the formation of the porous matrix. Typically, the main three phases are: pelletization, carbonization and activation and this very last one is the most important one. It is made through steam or carbon dioxide at high temperatures between 700 °C and 1100 °C and, as already said, it is needed to open the pores. The resulting structure is composed by microcrystallites of graphite [116]. The ease of regeneration and the specific area are the main advantages of Activated Carbon. Nevertheless, they are nonpolar materials not suitable for water sorption [117].

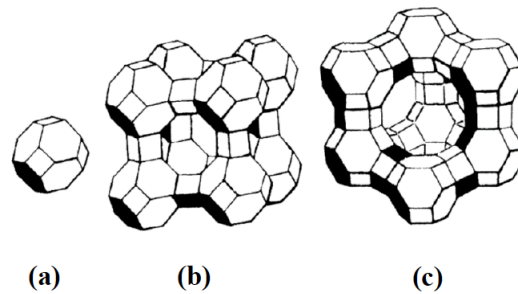


Fig. 3.4 a) Primary unit of zeolites types A, X and Y; b) unit cell of zeolites type A; c) unit cell of zeolites types X and Y .

Activated alumina is derived from bauxite through dehydration and recrystallization at high temperatures. The water affinity at ambient condition is similar to Silica Gel, while at high temperature it presents a stronger interaction. This makes this material suitable for applications like water recovery from steam/thermal processes [116].



Fig. 3.5 Activated carbon



Fig. 3.6 Activated alumina pellets

These are the just a part of the existing sorption materials available, and the following figure shows their specific isotherm curve, in order to recap the materials and compare them in a single picture.

The water uptake is indicated in terms of micro moles of water per unit surface of the adsorbent and the curves respectively refer to [118] (A) Zeolite type X, (B) silicaluminophosphate sieve, (C) activated alumina, (D) silica gel (at 28°C), (E) ionosilica (at 40°C), (F) activated carbon.

The equilibrium adsorption isotherm with respect to zeolite shows a similar trend to the Type I IUPAC adsorption isotherms. Indeed, at low relative pressures it is characterised by hydrophilic behaviour, with a sharp increase in water uptake; thereafter the curve flattens with increasing relative pressure. Activated alumina, on the other hand, shows a trend close to that of the II type of IUPAC adsorption

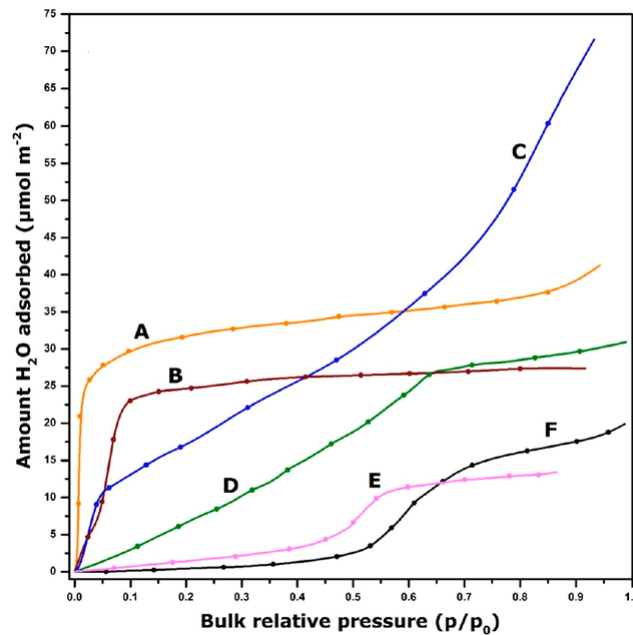


Fig. 3.7 Typical equilibrium adsorption isotherms of water vapor for various adsorbent materials at 25°C [118]

isotherms. The curve of silica gel shows an intermediate behaviour between the IUPAC type I, IV and V adsorption isotherms: water uptake increases almost linearly with relative pressure until a critical point where the sorption curve flattens. Finally, the activated carbon adsorption isotherm resembles the IUPAC isotherm of type V. It exhibits an upward concavity up to intermediate values of relative pressure, corresponding to hydrophobic behaviour. Thereafter, water uptake rises rapidly at a low relative pressure increase, but the curve flattens out thereafter.

3.3 The Prototype

HySun is a hybrid solar cooling system (see Figure 3.8 for a simplified diagram) that combines the benefits of desiccant materials to reduce the latent load and uses clean thermal energy to regenerate the desiccant material. The electricity demand for the technology is lower for the same cooling capacity as conventional air conditioning due to the fact that the temperature level for condenser/evaporator are closer. This means that the temperature lift which has to be produced from the compressor is smaller, resulting in higher efficiencies and lower electricity

consumption from the compressor. Therefore, PV modules can be used to supply the electrical part and solar thermal panels or other heat sources can be used to regenerate the material. This technology increases the possibility of self-consumption of locally generated renewable energy and increases the possible synergies between RES technologies. A side effect is that by having the material take over the latent load, a smaller amount of refrigerant gas is needed, which increases safety and reduces the amount of refrigerants, which are often potent greenhouse gases. Of course, there are already important policies targeting the use of greenhouse gases for air conditioning. Adsorption technologies like HySun can further improve the sustainability of refrigeration machines and work in synergy with running policies.

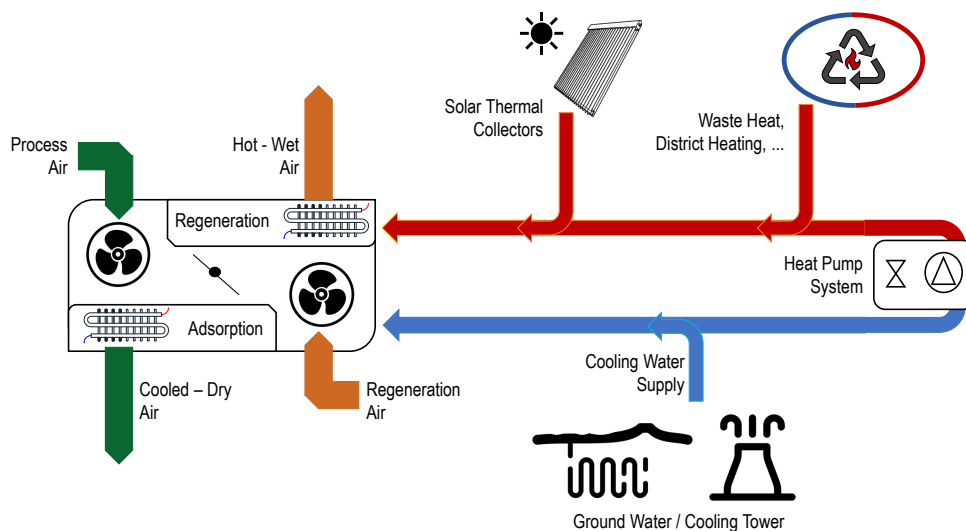


Fig. 3.8 Block Diagram of the Solar Hybrid Cooling System

HySun technology is based on solid sorption materials that physically absorb moisture from the air and release it after a heating process at different temperature levels, depending on different variables (type of material, regeneration time, etc.). In general, the lower is the driving temperature, the greater the choice of available technologies.

HySun's main objective is to improve efficiency compared to conventional compression cycles, using multiple sources and multiple energy vectors to generate the cooling power and drive the regeneration cycle. Conventional chillers use electricity to drive the compression cycle and their flexibility is related with changing the temperature set point and modulate the compressor depending on RES production or

due to grid stability issues are the main degrees of freedom that need to be coupled with user behaviour. HySun offers users new degrees of freedom with the possibility to switch between thermal and electrical energy and, in addition, to switch between different sources as the temperature level used allowed a wider range of feeding technologies. The basic idea for operation is as follows: if a surplus of electricity is available in the building or from the grid, the system HP can be switched on to provide cooling or/and thermal energy. In the same way, it can be switched off when there is a surplus of production from solar thermal panels or another heat source. For example, if a PV system produces more electricity than is consumed, HP can generate the thermal energy needed (the details of the components of the prototype and how it works can be found in the next section). Due to the low temperature level, a wide range of technologies are applicable to this concept, which increases the possibility of demand response techniques that can be used not only for grid stability and/or optimisation of RES, but also to shift the cooling load between the thermal and the electrical grid. Indeed, thermal storage (hot and cold) must be integrated to make the best use of RES production and meet the needs of users. The disadvantage of this solution is clearly the greater complexity of the installation. Indeed, it is necessary to provide for several installations and cross-connections between different hot/cold generators.

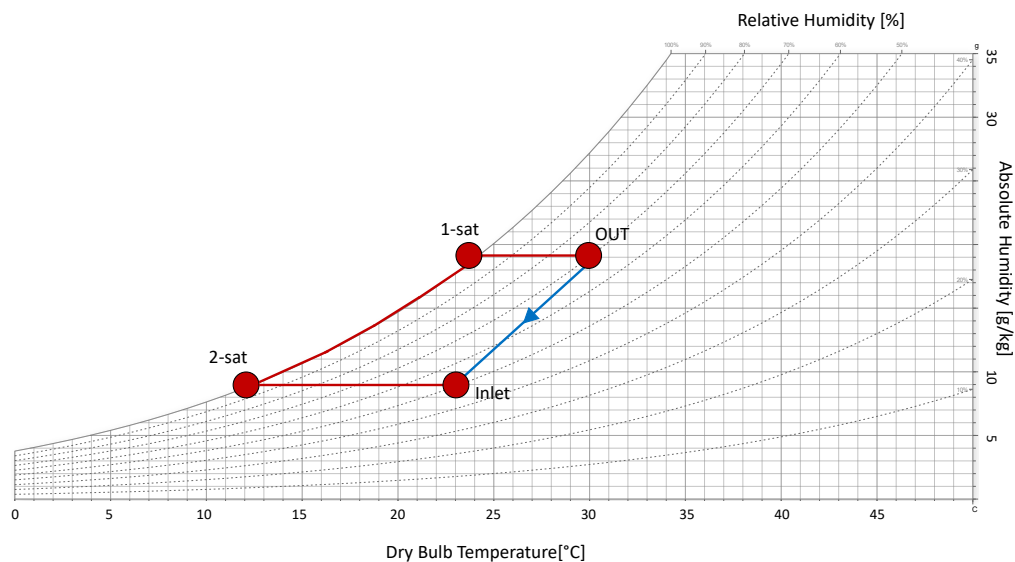


Fig. 3.9 Process air transformation. Classic Compression cycle (red) against the theoretical HySun transformation (blue)

3.3.1 Project, Schemes and Working Principles

The HySun design is reported in this paragraph, together with the list of the main components that are used. The device can be divided in 3 main separate units: (i) The heat pump (CAD in Figure 3.17), (ii) the auxiliary heater and the auxiliary cooler (CAD in Figure B.8) and the (iii) adsorption unit (CAD in Figure 3.16). The overall CAD scheme is reported in Figure 3.10 with a dedicated legend in figure 3.11. Around the 3 main units, there are a list of sensors and auxiliary units which are briefly recapped in table 3.3 and in Figure 3.12.

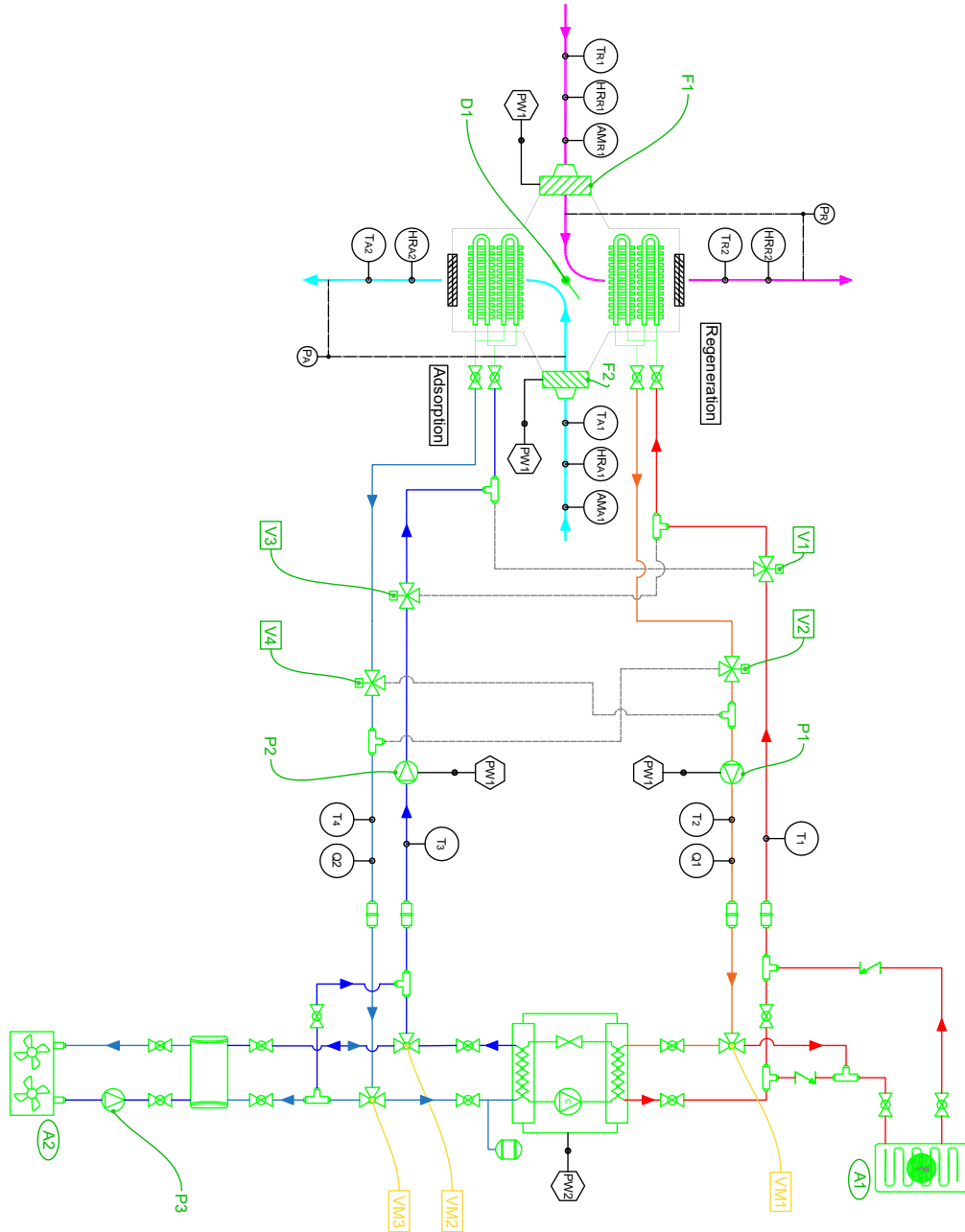


Fig. 3.10 CAD scheme of the Solar Hybrid Cooling System

LEGENDA

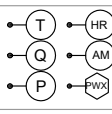
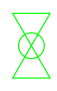
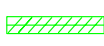
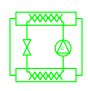

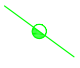


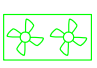

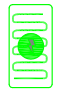



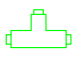








 <p>Temperature, Flow Rate, Delta Pressure, Relative Humidity, Anemometer, Power Meter</p>	 <p>Section Valve</p>
 <p>Manual Damper</p>	 <p>Heat Pump System</p>
 <p>Coated Heat Exchanger</p>	 <p>4 Way Valve - Air</p>
 <p>Quick Connector</p>	 <p>3 Way Valve - Water Automatic</p>
 <p>Dry Cooler</p>	 <p>3 Way Valve - Water Manual</p>
 <p>Electric Boiler with Expansion Vessel</p>	 <p>Centrifugal Fan</p>
 <p>Expansion Vessel</p>	 <p>Pump</p>
 <p>T - Junction</p>	 <p>Non - Return Valve</p>
 <p>Hot Water Feed/Return</p>	 <p>Manual Component TAG</p>
 <p>Cold Water Feed/Return</p>	 <p>Automatic Valve TAG</p>
 <p>Air flows</p>	 <p>Active Component TAG</p>
	 <p>Auxiliary TAG</p>

Fig. 3.11 CAD scheme: Legend

The adsorption unit is the heart of the system, where the air is cooled down and dehumidified. As reported in the CAD scheme (figure 3.10) the adsorption unit uses the cold/hot water produced by the heat pump, to treat the air flow or to regenerate the saturated adsorption battery. The adsorption module, consisting of two ribbed

Table 3.3 Main HySun Components. Please, refer to figure 3.10

Label	Component Name	Function	Note
F1	Air Fan	Supply air towards the adsorption batteries	150 Pa, 1000 m ³ /h max
F2	Air Fan	Supply air towards the adsorption batteries	150 Pa, 1000 m ³ /h max
P1	Hot Water Pump	Supply hot water for regeneration	Variable speed pump
P2	Cold Water Pump	Supply cold water for adsorption	Variable speed pump
P3	Auxiliary cooling pump	Supply cold water in case of external cooling service	Fixed speed pump
V1, V2	3-way water valve	Distribute the hot water flow	Automatic valve
V3, V4	3-way water valve	Distribute the cold water flow	Automatic Valve
VM1	3-way water valve	Direct the hot water towards the used generator	Manual Valve
VM2, VM3	3-way water valve	Direct the cold water towards the used generator	Manual Valve
D5	4 way air damper	Direct the air flow towards regeneration/adsorption	

coils coated with silica gel (thickness of coating 0.5 mm), operates in a batch process. Two centrifugal fans (F1 and F2, 150 Pa, 1000 m³h⁻¹, 100 W_{max}) and the air damper (D1) control the two air streams: the regeneration stream (violet) and the process stream (light blue). The first flow removes the previously collected water vapour, the second satisfies the user's cooling needs and delivers cold (20-25°C) and dehumidified air (humidity < 9 g kg⁻¹). Hot water (50-90°C) circulates between the hot water source (in the general concept can be either solar thermal, heat pump condenser, latent heat storage, waste heat) and the adsorption heat exchanger in regeneration mode, with the (P1) water pump supplying the energy required for water vapour desorption. In the meantime, cold water (15-25°C) circulates (P2) between the cold source (in the general concept can be the evaporator of a heat pump, ground water, evaporation tower) and the adsorption heat exchanger in dehumidification mode, removing the adsorption heat and cooling the air. When the control strategy implemented with a conventional PLC determines the changeover of the batch, a control signal is sent to the actuator of all 3-way valves and air damper (V1, V2, V3, V4, D1) which change their position to redirect the water and the air flow. A series of sensors for air temperature, water temperature, relative humidity, water flow and air velocity monitor the process and the performance of the system under different

climatic conditions (air temperature 25-35°C with RH 40-80%, replicated in the laboratory environment with the available equipment). The sensors are reported in the CAD schemes, each represented by an alpha-numeric code inscribed in a circle (please, see legend in figure 3.11). A brief recap of the sensors and their position is reported hereafter in figure 3.12. HySun has 4 functioning modes: OFF, ON - Cooling service, ON - Standby and ON - Switching:

- *OFF mode*: HySun is switched off or there is a fault in the system which has to be fixed. In this case, all fans and pumps as well as the air and water valves are switched off.
- *ON - Cooling Service*: HySun is ON, generating the requested cooling power. This mode can be activated either by user interaction or by an internal temperature setpoint feedback. The process stream (shown in green in figure 3.8) moves through the adsorption battery where it is dehumidified and cooled, while the regeneration air stream flows through the regeneration battery where it collects the water adsorbed in the material. The pumps supply the regeneration or adsorption battery with heat and cold water and the air dampers are open. As soon as the adsorption battery is saturated, the ON - changeover mode is activated.
- *ON - StandBy*: HySun is active but does not offer a cooling service. The batteries can be regenerated if necessary and if free heat is available. In this case, the regeneration air flow is generated, hot water is supplied to the battery. Regeneration can be done for one battery at a time. As soon as a battery is fully regenerated, the ON - switching mode is activated.
- *ON - Switching*: HySun is active and switches the regeneration and/or adsorption battery. This is an "intermediate phase" that can take place in standby or cooling mode. The heat/cold water flow is stopped (pumps OFF) and the valves change position to redirect the air and water flow to the opposite battery. It is important to note that the new adsorption battery (the one that has just been regenerated) needs a pre-cooling phase to effectively dehumidify the air flow when the changeover occurs in cooling mode (required time 3-5 minutes). For this reason, the cold water flow is provided before the process air flow starts.

HOT WATER LINE		
	Flow	Return
Temperature Sensor	T1	T2
Mass Flow Meter	-	Q1
Power Meter [P1]	-	PW1
3 Way Valve	V1	V2, VM1
Pump [P1]	-	P1
COLD WATER LINE		
Temperature Sensor	T3	T4
Mass Flow Meter	-	Q2
Power Meter [P2]	PW1	-
3 Way Valve	V3, VM2	V4, VM3
Pump [P2]	P2	-
PROCESS AIR		
	Flow	Return
Temperature Sensor	TA1	TA2
AnemoMeter	AMA1	-
Relative Humidity	HRA1	HRA2
Pressure Sensor Differential	PA	-
Power Meter [F2]	PW1	-
REGENERATION AIR		
Temperature Sensor	TR1	TR2
AnemoMeter	AMR1	-
Relative Humidity	HRR1	HRR2
Pressure Sensor Differential	PR	-
Power Meter [F1]	PW1	-

Fig. 3.12 Water and Air flow with active components and sensors location

The heat pump has been provided by ENEREN [119] and it is a custom machine. It is based on the *ENE006WL* model modified in order to work with the prototype temperature levels (e.g. the compressor is selected in order to meet the 65°C temperature water output). The max hot water output is set to 65°C while the cold one is set to 15°C, respectively with a temperature difference of 7 and 5 °C. The expected COP (calculated as reported in UNI14511) is equal to 3.05 and it is equipped with an high efficiency scroll compressor. For further details please refer to the dedicated technical sheet reported here [120].

HySun is located in the Politecnico di Torino laboratory and tests are about to start. The prototype has been designed in AutoCAD and SolidWorks (Figure 3.13) and then realized. The following figures report the real manufactured prototype. Other Pictures are available in the appendix B.3.

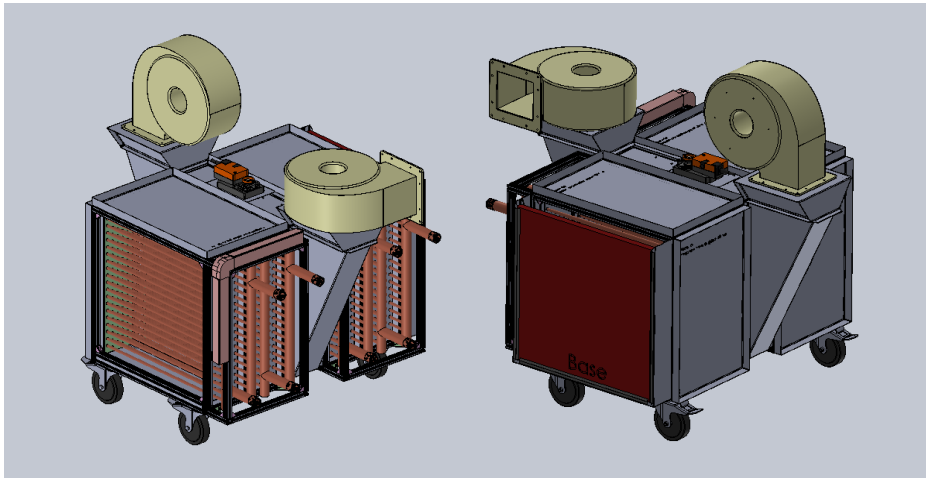


Fig. 3.13 HySun Adsorption Unit. 3D assembly from SolidWorks Software.

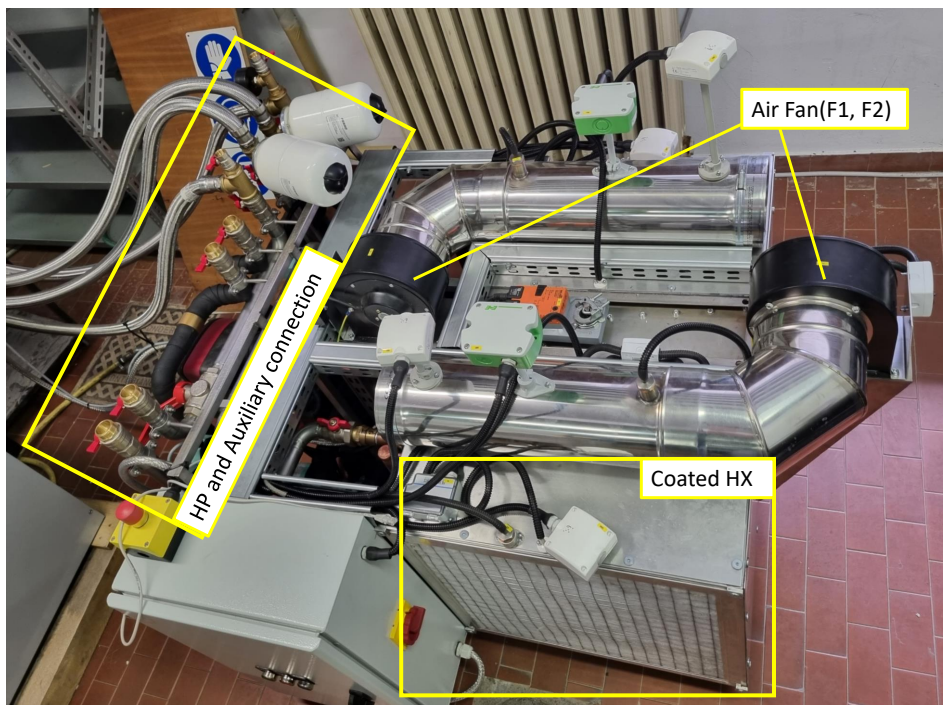


Fig. 3.14 Adsorption Unit. Real Prototype picture

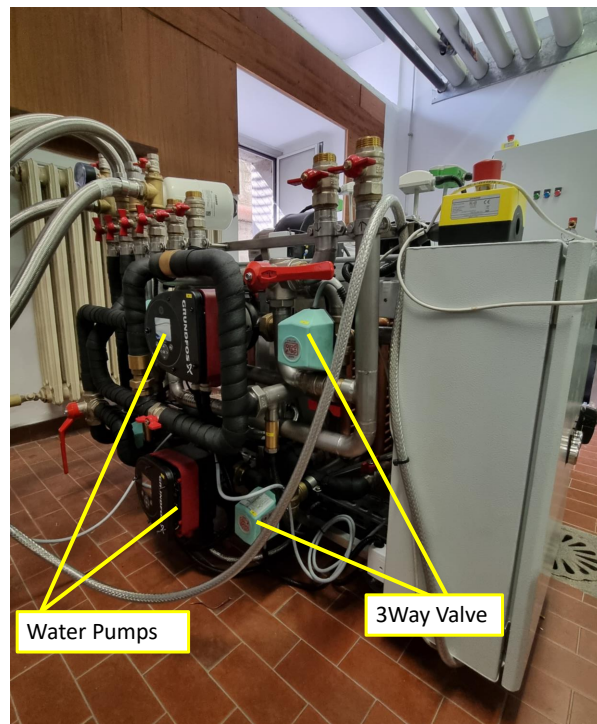


Fig. 3.15 Adsorption Unit. Real Prototype picture

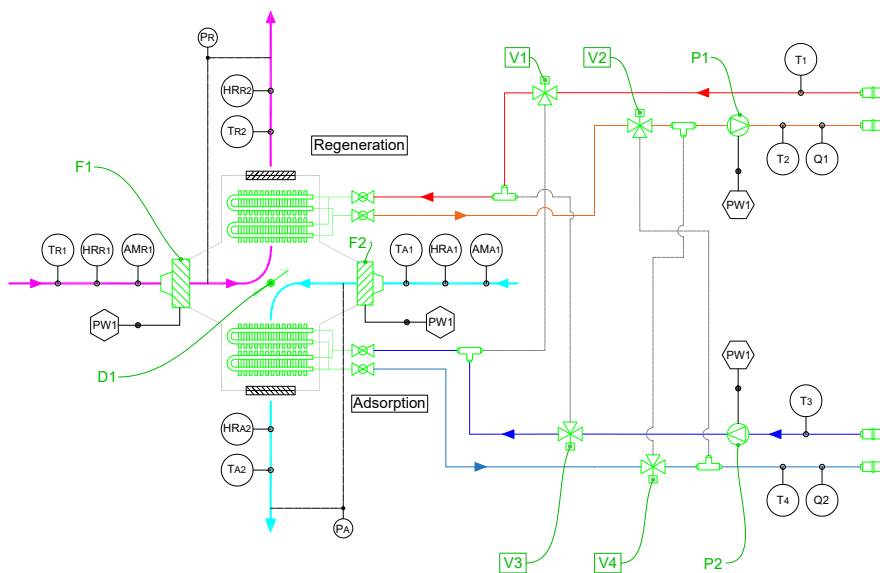


Fig. 3.16 HySun Adsorption Unit, CAD scheme. Extrapolation from the main CAD in figure 3.10

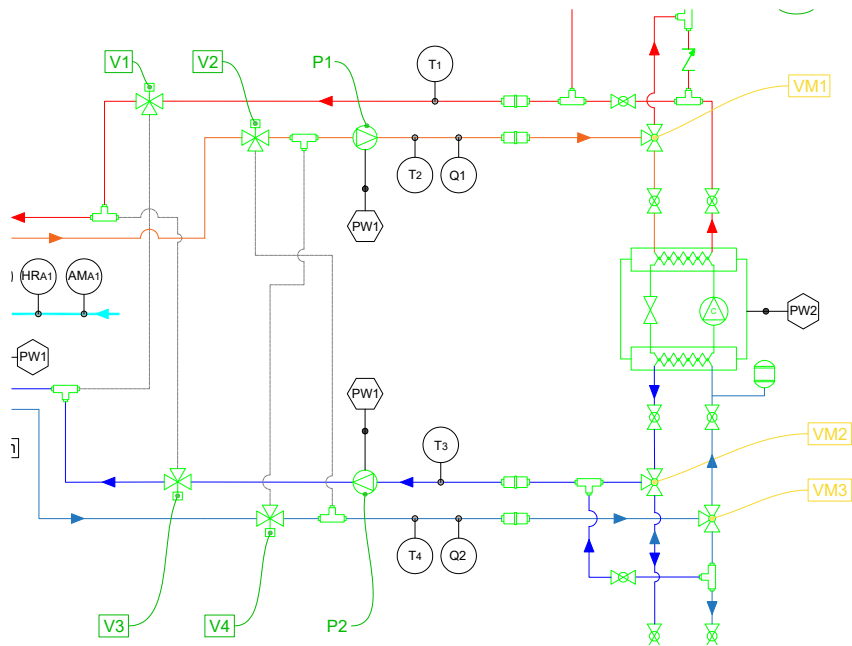


Fig. 3.17 Heat Pump Detail, CAD scheme. Extrapolation from the main CAD in figure 3.10

3.4 Silica Gel Coating

The adsorption batteries are regular fin and coil heat exchangers coated with adsorbent material which allow to trap the water molecules. In this section the coating procedure and the testing are reported together with a brief description of the machine designed to dry the adsorption batteries.

3.4.1 Coating Recipe and Fundamentals

Coating is done on a metal surface and allows the adsorbent material to adhere to the surface. This technique has been used to produce the Silica-gel coating for the adsorption batteries. Safety data sheets of the materials used for the coating can be found at [121] and the reference scientific literature are [122, 123].

The coating is produced as a composite material in which the structural matrix consists of the polymer polydimethylsiloxane (PDMS) and the silica gel is inserted as a second dispersed phase. PDMS has remarkable properties such as good thermal stability, biocompatibility, corrosion resistance, low cost, gas permeability and is chemically inert, easy to handle and manipulate and can develop

microstructures [124, 125]. To obtain the PDMS matrix, two reagents are mixed: trimethylsilyl-terminated polymethylhydrosiloxane (RJ 202) and silanol-terminated polydimethylsiloxane (RJ 107). Once the PDMS matrix is prepared, the silica gel powder is added to the mixture by adding ethanol with which the solution is diluted to facilitate mixing of the components. Once you have obtained a homogeneous mixture, the bis(neodecanoate) tin catalyst, tech-90 is added. The catalyst activates the cross-linking reaction between the two RJs and this process is irreversible. In Table 3.4 it has been reported the theoretical recipe to be followed.

Table 3.4 Theoretical coating recipe

Chemicals	Share [%Mass]	Main Role in the Mixture	Mixing Order
RJ202 (PDMS)	20%	These two chemicals produce the main coating structure and Porosity	1
RJ107 (HMS)	10%		2
Bis(neodecanoate)tin	3%	Is the catalyst which activate the reaction between RJ202 and RJ107	5
Silica Gel Powder	67%	Adsorbent Material	4
Ethanol	(max) Silica% + 14%	It has a fluidising function for the mixture	3

During the mixing process is is important to take some precaution: (i) the component RJ 202 is the most viscous and it is advisable to weigh it first as all the other components are present in a certain % with respect to it. (ii) the catalyst can be dissolved in ethanol before adding it to the compound to facilitate its homogeneous dispersion in the mixture. (iii) ethanol has a liquefying function and slows down the cross-linking reaction, but its use must not be excessive, because in order to perform the percolation on the metal, the viscosity of the solution must be that of 'liquid honey'. (iv) it is advisable to add silica and ethanol gradually in order to precisely control the desired viscosity and, finally, (v) the mixture must always be kept in motion to ensure its homogeneity and, (vi) after adding the catalyst, the coating must be carried out within ten minutes to avoid the solidification of the solution. Before pouring the solution on the metal surface, it is advisable to clean the metal surface thoroughly. The perfect procedure is to use soda, which causes a chemical abrasion on the metal surface, cleans it properly and improves the adhesion of the chemical mixture. Unfortunately, we did not have the facilities to use this procedure safely. Therefore, the metal surface was cleaned with ethanol and physically treated with glass paper to increase the roughness. Once the mixture and the metallic surface are ready, pouring can be performed. Once the metallic surface is fully covered, it must be dried in order to expel the ethanol which, as already pointed out, is just used to reduce the viscosity of the mixture but do not participate on the adsorption process.

The drying stage last 24 to 48 hours using temperature between 60-80 °C in an oven or dedicated drying machine.



Fig. 3.18 (a) Aluminium testing plate with coated surface, (b) mixture in progress

In order to test the coating technique and its performance, the coating has been produced and tested on small aluminium plates (see Fig. 3.18 (a)) and in the following section, a brief recap of the performance tests is reported.

3.4.2 Aluminium plates: adsorption and regeneration tests

The aluminium coated foils has been tested in adsorption and regeneration. Specifically, the samples have been exposed to different relative humidity: 32%, 43%, 70% and 92% and then regenerated at 80°C. So, the dry-mass is evaluated after the regeneration period and it is compared with the wet-mass, after being exposed to the humid environment.

Test Bench

Adsorption was carried out in special boxes reported in the following figure 3.19 in which a solution of water and calcium chloride keeps the environment inside the box in equilibrium at a certain relative humidity condition with a sensibility of $\pm 2\%$. The equilibrium RH condition is a function of the concentration of the salt dissolved in the water and its value was constantly monitored over time. The mass

measurements of the samples were manually performed using the Kern KB 360-3N balance [126] at regular time intervals for 4 hours.



Fig. 3.19 Adsorption Boxes



Fig. 3.20 Kern KB 360-3N

Then, regeneration was performed in the Kern DBS 60-3 thermobalance [127], in which the regeneration temperature can be precisely controlled. In addition, the thermobalance provides the sample mass change every 5 seconds for the 2 hours of desorption.

Adsorption and Regeneration Tests

The selected physical variable to compare the results is the water uptake, here defined in 3 different ways (reported hereafter) where w_{t_1} represent the overall system performance (e.g. the coated hx), w_{t_2} is instead focused on the coating behaviour and, finally, w_{t_3} is focused on the active part of the material, which is the silica gel.

$$wt_1 = \frac{m_{H_2O}}{m_{secca} - m_{aluminio}} \quad (3.4)$$

$$wt_2 = \frac{m_{H_2O}}{m_{secca}} \quad (3.5)$$

$$wt_3 = \frac{m_{H_2O}}{m_{secca} + \%SG} \quad (3.6)$$

where m_{H_2O} is the water mass in the sample, m_{secca} is the sample mass after regeneration, $m_{aluminio}$ is the aluminium foil mass and $\%SG$ is the silica gel percentage in the mixture.

In the following Figure 3.21 are reported the experimental results for the adsorption phase. In particular, the samples have been expose to the relative ambient for 4 hours. Then, a 1 hour regeneration cycle at $80^\circ C$ is performed to have the dry-mass reference. The precise characterization of the used sample is reported in Table 3.6.

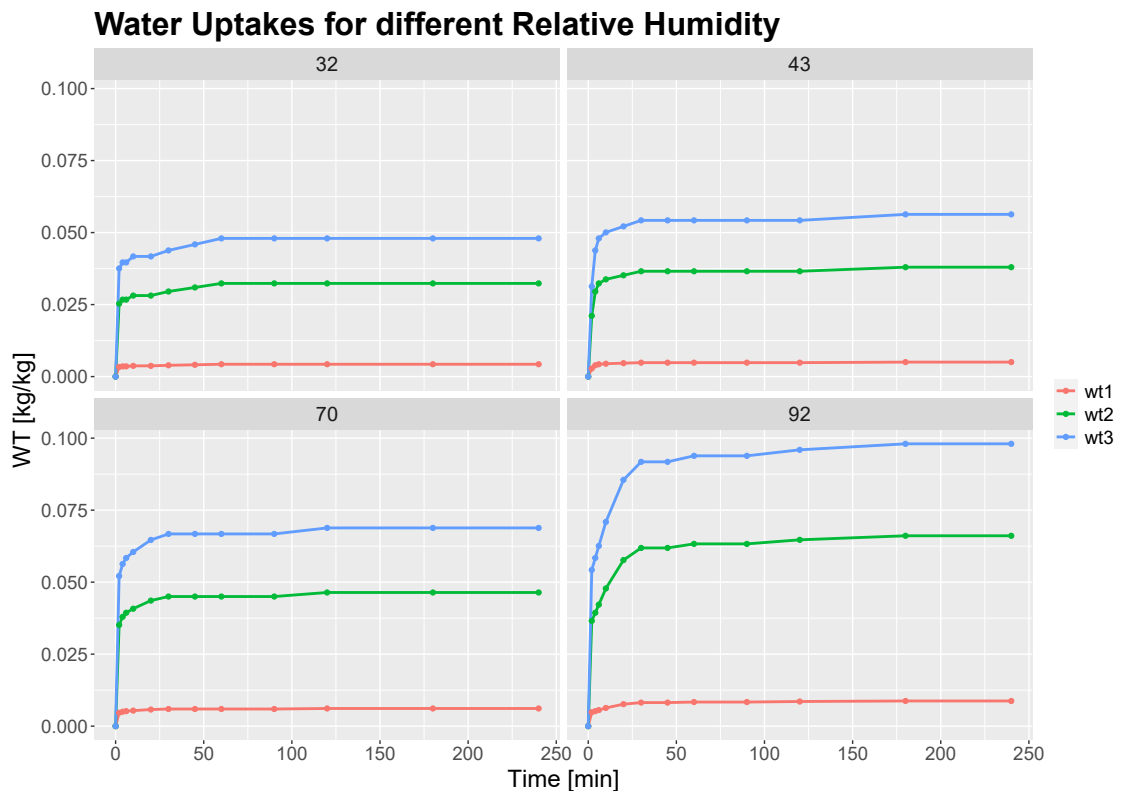


Fig. 3.21 Adsorption tests: experimental results for different tested conditions

Is it possible to notice that the initial transient is generally quite short. In fact, even in the 92% RH case, which is the slowest one, after 30minutes the samples have reached a stable condition. Moreover, it is possible to notice the great difference between w_1 and the other two definition of water uptake due to the denominator of the equation. Nevertheless, it can be seen as an important variable to evaluate the overall performance of the ensemble metallic support + coating. Regarding instead w_3 is the value which can be compared with the pure silica gel powder, in order to have a comparison of the performance between pure material and coating mixture. The comparison is reported in the following table 3.5 and the main outcome is that there the coating presents a performance of 30% with respect to the pure material.

Table 3.5 Water Uptake comparison between pure Silica Powder and Coated Silica

<i>Relative Humidity</i> [%]	<i>WT Pure Silica Powder</i> [kg/kg]	<i>WT₃</i> [kg/kg]
32	0.209	0.050
43	0.261	0.060
70	0.343	0.071
92	0.377	0.098

The reasons for this difference may be various, such as: (i) It is possible that the PDMS matrix holding the silica gel hinders the porosity of the material and disables some of the pores. (ii) A second idea concerns the dispersion of the silica gel. It may not be uniformly dispersed in the mixture during the preparation stage, so that uniform properties are not obtained. (iii) It is still possible that adsorption does not occur throughout the thickness of the coating, but only at the surface layers, limiting the adsorption capacity. If the latter hypothesis were true, the adsorption found in the experimental tests would not take place over the entire average thickness of 350 μm , but only 135 μm (i.e. about 40 %), the water absorption of the active part of this part of the material being equivalent to that of pure silica gel powder.

The very same procedure will be adopted to coat the HySun Heat Exchanger. During the future machine tests, specific attention will be dedicated to adsorption performance and water uptake capabilities in order to verify the results obtained during this first test stage.

Table 3.6 Main sample and coating data

Coating Component	% in Mass	
Silica Gel	67.43 %	
RJ 202	19.70 %	
RJ 107	9.85 %	
Catalyst	3.01 %	
Ethanol	93.4 % of SG	
Aluminium foil	4.664 \pm 0.005	[g]
Aluminium thickness	0.5	[mm]
Coating Surface	2475	[mm ²]
Coating Dry Mass	0.725 \pm 0.010	[g]
Avg. Coating thickness	248	[μ m]
Silica Gel Mass	0.489	[g]

3.4.3 HX Drying Machine

Since the HySun heat exchanger are quite large, it has been decided to design a dryer machine to handle the coating drying phase instead of using a oven. In the following Figure 3.22 is reported the dryer project.

As shown in the illustration, the drying machine has a central main chamber into which the coated HX is placed. A stream of warm air is directed to the heat exchanger to dry it and remove the ethanol from the coating mixture. An air rectifier guarantees a homogeneous and stable air flow over the pipes and fins. A digital scale constantly determines the total weight to monitor the drying process. The process stops if no change in weight is detected for a certain time. The HX water inlet and outlet pipes are accessible to allow warm water to flow through to speed up the drying process. The unit has air ducts for fresh air supply and recirculation controlled by two fans and two manual grilles. The ratio can be selected to (i) control the drying speed and (ii) avoid a high concentration of ethanol in the air flow. In addition, special sensors throughout the machine ensure continuous monitoring of humidity, temperature and ethanol concentration. The ethanol sensors are used for safety, but also to determine, together with the weight, when the drying phase can be stopped. This machine has already been designed and realised. More 3D pictures can be found in appendix B.3, while a picture of the real machine is shown below.



Fig. 3.23 Drying Machine

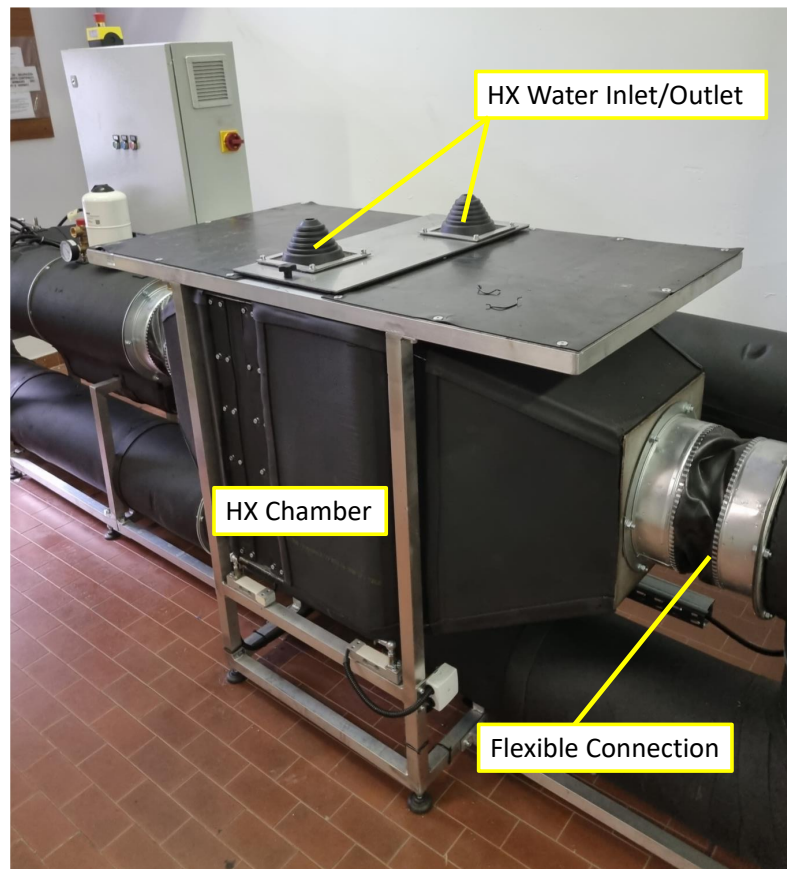


Fig. 3.24 Drying Machine: HX chamber detail

Chapter 4

Dynamic Simulation of the Adsorption Process

The simulation of the adsorption phenomenon and the system as a whole is described in this section. In the first section there is a brief recapitulation of important adsorption models. In section 4.2 the developed model is described with its main equations, which are developed in numerical form in section 4.2.1. For ease of reading, all auxiliary equations used to calculate the properties of air, water and silica (such as specific heat value, density, adsorption equilibrium, etc.) are given in section 4.2.2.

4.1 Main Adsorption Process Models

4.1.1 Langmuir model

One of the models for the description of the adsorption process is the Langmuir model, which assesses the surface coverage in dynamic equilibrium conditions, balancing the relative rates of adsorption and desorption.

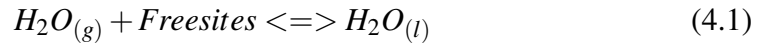
The model assumptions are the following:

- There is only one layer of adsorbate on the surface (monolayer adsorption);
- All the adsorption sites have the same energy;
- The process is reversible (both adsorption and desorption);

- The interactions between sorbate molecules are negligible.

The basic parameter of the Langmuir model is the coverage defined as the ratio between the occupied sites and the total number of sites available on the adsorbent surface.

This approach is a kinetic one, so, the process can be seen as a reversible reaction:



The direct reaction represents the adsorption process (exothermic), while the reverse reaction represents the desorption process (endothermic). Both are associated with a reaction constant, which is useful to evaluate the reaction rate. Thus, an equilibrium constant is defined, which is the ratio between the two individual constants. Furthermore, the equilibrium condition is satisfied if the adsorption rate is equal to the desorption rate. Based on this definition of the equilibrium between the two processes, the following law can be established:

$$\theta(p, T) = \frac{H(T)p}{1 + H(T)p} \quad (4.2)$$

where

$$H(T) = \frac{K_{eq}}{RT} \quad (4.3)$$

which is a constant that for low coverage is precisely the Henry's constant, since the term $H(T)p$ at the denominator of the (2.9) is neglected (pressure tends to zero) and, so, the relation between the coverage and the pressure is linear.

The main drawback of Langmuir model is that it does not well describe the behaviour of silica-gel at equilibrium (except for low coverage) because of its simplifying assumption of a homogeneous monolayer adsorption.

4.1.2 Dubinin-Polanyi model

The main idea behind this theory is that the porous material (adsorbent) is defined as a solid with a certain amount of available empty volume in the pores which can be filled by the adsorbate, considered as a continuous fluid. Consequently, the

fundamental parameter at the core of the model is the specific volume of micropores, expressed as it follows:

$$W_0 = \frac{V}{m_{adsorbent}} \quad (4.4)$$

where V is the volume available for the adsorbate, and $m_{adsorbent}$ is the sorbent mass. The specific volume occupied by the adsorbate, instead, is given by:

$$W_s = \frac{V_{adsorbate}}{m_{adsorbent}} \quad (4.5)$$

Where $V_{adsorbate}$ is the volume occupied by the adsorbate. Under certain pressure and temperature conditions, it is possible to fill only a certain amount of volume. At the saturation pressure, the total volume is occupied so W_s is equal to W_0 . The variation of the free energy between the adsorbate in equilibrium with the adsorbent and the saturated fluid at a fixed temperature is named “adsorption potential” and it is formulated as:

$$A_{DB} = -\Delta g = -RT \ln \frac{p_s(T)}{p} \quad (4.6)$$

where $p_s(T)$ is the saturation pressure of the fluid and p is the equilibrium pressure of the adsorbed phase.

Each adsorbent-adsorbate pair is associated to a characteristic potential curve, since there is only one relation between adsorption potential and the volume of fluid adsorbed at a fixed temperature. Even if all the curves are different, there are analytical formulations for the characteristic curves. One of these is the Dubinin-Astakhov (DA) equation which is the following:

$$W = W_0 \exp \left[- \left(\frac{RT \ln \frac{p_s(T)}{p}}{\gamma E_0} \right)^n \right] \quad (4.7)$$

where E_0 is the characteristic energy which depends only on the adsorbent, is the affinity constant depending on the adsorbate only, n takes count of the heterogeneity of the pores. The interpretation of these fitting parameters is difficult and represent the biggest limitation of the DA equation.

Also the Dubinin-Polanyi model presents disadvantages. The main one is that this

approach does not fit the Henry's Law, according to which, at low coverage, there is a linear relation between the adsorption capacity of the adsorbent and the pressure. Another drawback is that the estimation of the adsorbate molar volume is subject to significant uncertainty. Finally, the temperature-independent characteristic curve is not suitable for many systems [116].

4.2 Developed Adsorption Model

The ADS-HX numerical model has been developed in MATLAB and it is based on a set of balance equations between the hot/cold water, silica gel coating and the humid air stream. The main reference for the mathematical formulation are [128, 116, 129].

The model is based on 6 main hypothesis:

1. Adsorption phenomena involve only the moisture and the silica gel
2. The adsorption heat is generated inside the silica gel coating pores and it is related only with the water uptake
3. Adsorption and release are faster than the other phenomena involved. Due to this hypothesis, the vapor mass transfer between air and silica is a function of the equilibrium condition [130, 116]
4. The model is taking into account just the air flow direction (mono-dimensional)
5. The convective heat transfer is the dominant one. Temperature gradients related to conduction are neglected
6. Thermal losses are minimized due to the use of insulation material

and on 5 main balance equations:

$$\rho_b \frac{dW}{dt} = K_G a_s (x_a - x^*) = \dot{G} \quad \left[\frac{kg}{m^3 s} \right] \quad (4.8)$$

$$\varepsilon_b \rho_a \frac{dx_a}{dt} d_v = -\dot{m}_a \frac{dx_a}{dz} d_z - \dot{G} d_v \quad \left[\frac{kg}{s} \right] \quad (4.9)$$

$$\begin{aligned} \varepsilon_b \rho_a c p_a \frac{dT_a}{dt} d_v = -\dot{m}_a c p_a \frac{dT_a}{dz} d_z + h_a A_f (T_s - T_a) d_v - \\ U_L A_L (T_a - T_{amb}) d_v \quad [W] \end{aligned} \quad (4.10)$$

$$c p_s \rho_s (1 - \varepsilon_b) \frac{dT_s}{dt} d_v = H_{ads} \dot{G} - h_a A_f (T_s - T_a) - U A_f (T_w - T_s) \quad [W] \quad (4.11)$$

$$\rho_w c p_w \frac{dT_w}{dt} d_v = -\dot{m} c p_w \frac{dT}{dz} d_z - U A_f (T_w - T_s) d_v \quad [W] \quad (4.12)$$

which represents (4.8) water mass balance in the silica gel differential volume, (4.9) the air-moisture mass balance, (4.10) the air thermal balance, (4.11) the sorbent thermal balance and (4.12) energy balance in the heat exchanger differential volume.

Silica gel water uptake

The phenomenon is driven by the difference of water vapour concentration between the air stream and the air in the close surroundings of the adsorbent surface (eq. 4.8). As time passes, the adsorption process take places, increasing the amount of adsorbed water while decreasing the moisture content in the air. Indeed, the driving force become increasingly weaker as the concentration difference converge towards zero, which represent the end of the adsorption process. The main equation parameters are: the bulk density of silica gel $\rho_b \left[\frac{kg}{m^3} \right]$, K_G which is the overall mass transfer coefficient, $a_s [m^2/m^3]$ is the specific area of silica gel, $x_a \left[\frac{kg_w}{kg_a} \right]$ is the specific humidity ration of air, x^* is the air humidity ratio in equilibrium with silica gel.

K_G is the overall mass transfer coefficient. The diffusion mechanism is governed by the molecular collision and the Knudsen diffusion which contribute in-series for the diffusion of gas from the bulk to the adsorption site. In parallel with them is acting also the surface diffusion of adsorbate phase over the solid surface. This phenomenon is driven by the gradient of the adsorbate phase along the particle diameters. Using the electrical equivalence [131] (see figure 4.1, 4.2) it is possible to write the global mass transfer coefficient as:

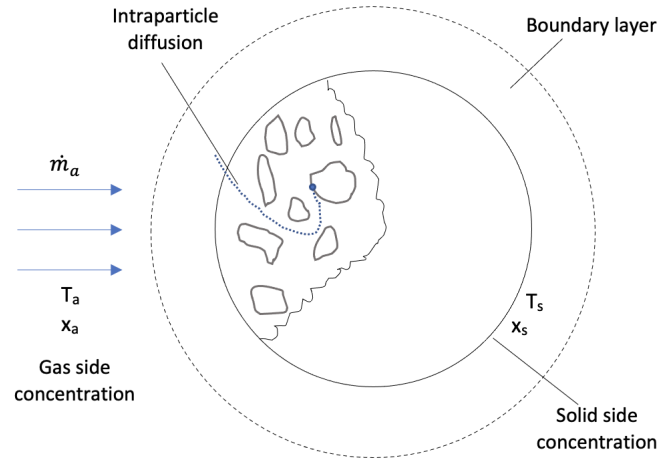


Fig. 4.1 Pictorial representation of the Mass diffusion through pores

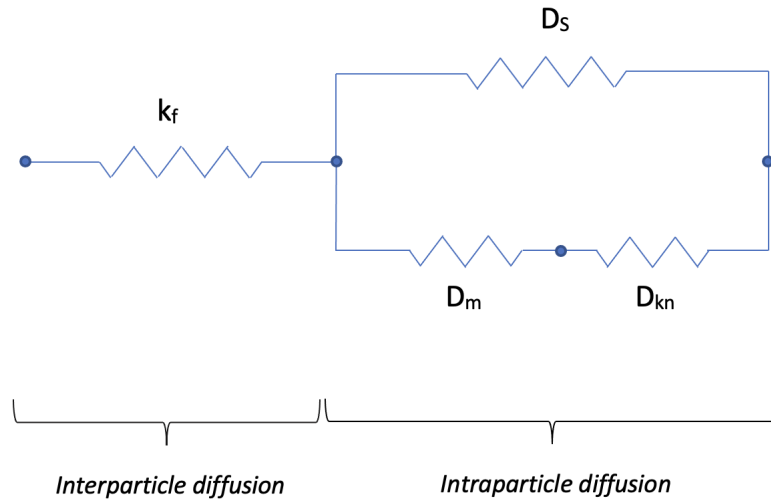


Fig. 4.2 Electrical Equivalent of the mass transfer resistance

$$\frac{1}{K_g} = \frac{1}{h_m} + \frac{t_s}{2D_{eff}\rho_a} \quad (4.13)$$

where, $h_m \left[\frac{kg}{m^2s} \right]$ is the mass transfer coefficient of air, $t_s [m]$ is the thickness of the silica gel coating and $D_{eff} \left[\frac{m^2}{s} \right]$ is the effective diffusion coefficient.

The air mass transfer coefficient h_m can be retrieved through the Sherwood number [131]:

$$Sh_a = \frac{K_f d_h}{D_m} = 0.079 Re_a^{0.71} Sc_a^{0.37} \quad [-] \quad (4.14)$$

$$h_m = K_f \rho_a \quad \left[\frac{kg}{m^2 s} \right] \quad (4.15)$$

where $d_h[m]$ is the hydraulic diameter, $D_m \left[\frac{m^2}{s} \right]$ is the molecular diffusivity in water vapor in air, Re_a is the Reynolds number (eq. 4.17) and Sc_a is the Schmidt number (eq.4.16). In the following lines are reported the main auxiliary equations used to calculate h_m .

$$Sc_a = \frac{\mu_a}{\rho_a D_m} \quad [-] \quad (4.16)$$

$$Re_a = \frac{\rho_a v_a d_h}{\mu_a} \quad [-] \quad (4.17)$$

$$\mu_a = 10^{-7} (2.43T + 157.5) \quad [Pa s] \quad (4.18)$$

$$\rho_a = \frac{P}{RT} = \frac{101325}{287(T + 273.15)} \quad \left[\frac{kg}{m^3} \right] \quad (4.19)$$

$$D_m = 1.73510^{-9} \frac{(T_s + 273.15)^{1.685}}{P} \quad \left[\frac{m^2}{s} \right] \quad (4.20)$$

$$d_h = \frac{4\sigma}{\alpha} \quad [m] \quad (4.21)$$

$$\sigma = \frac{A_0}{A_b} \quad [-] \quad (4.22)$$

$$\alpha = \frac{A_{hx}}{V_b} \quad \left[\frac{1}{m} \right] \quad (4.23)$$

where $T [^{\circ}C]$ is the air temperature and $P [Pa]$ is the ambient pressure, $R \left[\frac{J}{kgK} \right]$ is the gas constant, $T_s [^{\circ}C]$ is the silica gel temperature, $V_b [m^3]$ is the total volume of

the heat exchanger [132]. Then, A_0, A_b and A_{hx} [m^2] are the minimum free flow area, the total frontal area and the total exchange area respectively.

The second term of equation 4.8 is related with the intra-particle diffusion which is governed by three diffusion mechanism [132]:

1. *Surface diffusion*: phenomenon related to the transport of adsorbed phase on the pores drove by the concentration difference of adsorbate. It can be described as:

$$D_s = \frac{D_0}{\tau_s} \exp\left(-0.947 \frac{H_{ads}}{T_s + 273.15}\right) \quad \left[\frac{m^2}{s}\right] \quad (4.24)$$

where D_0 [$\frac{m^2}{s}$] is a constant value equal to 1.610^{-6} , τ_s is the tortuosity factor [131], T_s [$^{\circ}C$] is the silica gel temperature and H_{ads} [$\frac{kJ}{kg}$] is the heat of adsorption calculated as a function of the water uptake [132]:

$$H_{ads} = 3500 - 13400W \quad W \leq 0.05 \quad (4.25)$$

$$H_{ads} = 2950 - 1400W \quad W \leq 0.05 \quad (4.26)$$

2. *Molecular diffusion*: it is related with the gas phase diffusion due to the molecular collision within the pores. It has been presented in equation 4.20.
3. *Knudsen diffusion*: it represent the interaction between the gas molecules and the silica gel surface. It occurs when the pores diameters are comparable with the mean free path:

$$D_{kn} = \bar{r}_p 22.86 (T_s + 273.15)^{0.5} \quad \left[\frac{m^2}{s}\right] \quad (4.27)$$

where \bar{r}_p is the pores average radius.

With all the contribution defined, it is possible to calculate the effective diffusion coefficient (equation 4.28) and so, solve the equation 4.13.

$$D_{eff} = D_s + \frac{\epsilon_p}{\tau_s} \left(\frac{1}{D_m} + \frac{1}{D_{kn}}\right)^{-1} \quad \left[\frac{m^2}{s}\right] \quad (4.28)$$

Air - Moisture mass balance

The air-water mass balance is governed by equation 4.9 which highlight that the the variation of air moisture content over time is related with convection mechanism and the mass transfer rate \dot{G} . The equation is written with respect to the infinitesimal volume of the finned tubes dV and it is related with the void volume fraction eq. 4.29, and the air mass flow rate \dot{m}_a eq. 4.30.

$$\varepsilon_b = \frac{V_{void}}{V_{void} + V_s} \quad [-] \quad (4.29)$$

$$\dot{m}_a = \rho_a A_b v_a \quad \left[\frac{kg}{s} \right] \quad (4.30)$$

Air Thermal Balance

The air temperature variation along the process evolution, is described by equation 4.10. The three right hand side terms of the equation represent the spatial temperature gradient along the flow direction, the convective silica-air heat exchange and the dispersion towards the environment respectively. The convective heat transfer coefficient h_a is calculated through a Nusselt number correlation [133]:

$$Nu_a = \frac{h_a d_h}{k_a} = 0.722 Re^{0.43} Pr^{0.3} \quad (4.31)$$

where $k_a \left[\frac{W}{m^2 K} \right]$ is the air thermal conductivity, (assumed to be constant in the range of interest) and Pr is the Prandtl number. The overall transmittance $U_l \left[\frac{W}{m^2 K} \right]$ through the heat exchange case can be calculated as follow:

$$\frac{1}{U_l} = \frac{1}{h_{amb}} + \frac{t_c}{k_{al}} + \frac{1}{h_a} \quad (4.32)$$

where h_{amb} is the convective heat transfer coefficient between the ambient and the external case surface A_l , t_c is the casing thickness and k_{al} is the aluminium thermal conductivity.

Silica Gel thermal balance

The silica gel thermal balance is described by equation 4.11. The variation of the silica gel temperature over time is dependent on adsorption heat H_{ads} , on the convective heat transfer with the air stream (already seen in the previous sub-section) and with the water flowing in the heat exchanger tubes.

The silica specific heat has been considered dependent on the water content, evaluated as:

$$cp_s = 4178w + 921 \quad \left[\frac{J}{kgK} \right] \quad (4.33)$$

The water - coating interaction is again described through the electrical analogy, considering the overall thermal resistance as a series of thermal resistances (see fig. 4.3).

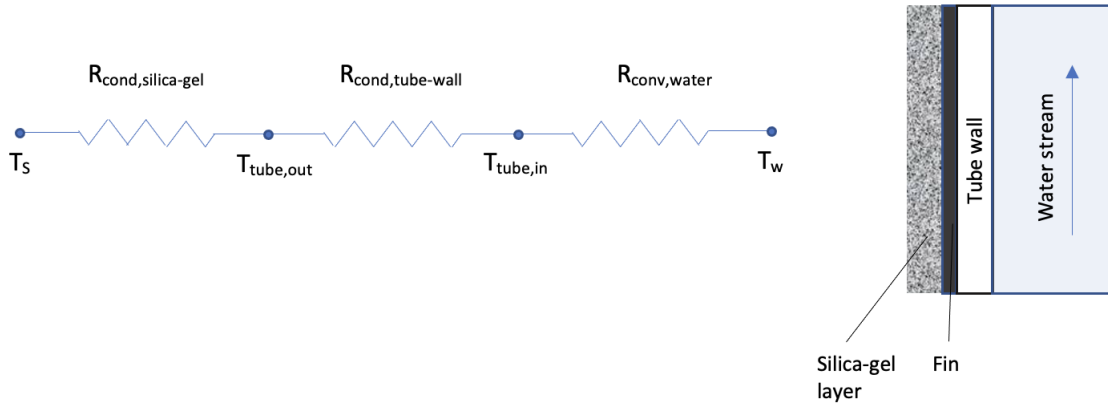


Fig. 4.3 Electric resistance scheme for thermal resistances between silica gel and water

Starting from the heat exchanger surface it is possible to identify the conductive resistance of the silica gel coating layer, the conduction through the tubes surface and, the last one, the convective thermal resistance of the water flowing in the pipes [134].

$$R_{s-to-w} = R_{cond,s} + R_{cond,t} + R_{conv,w} \quad (4.34)$$

$$\frac{1}{UA_{hx}} = \frac{t_s}{\eta_0 k_s A_{hx}} + \frac{\ln \frac{d_o}{d_i}}{2\pi L_p k_{cu}} + \frac{1}{h_w A_w} \quad \left[\frac{K}{W} \right] \quad (4.35)$$

where t_s is the silica gel coating thickness, η_0 is the fin efficiency, k_s is the silica gel conductivity (assumed constant and equal to $0.2 [Wm^{-1}K^{-1}]$), d_o and d_i are the outer and the inner tubes diameters, L_p is the total length of pipes, k_{cu} is the copper thermal conductivity, A_w is the total inner surface of the water pipes and h_w is the thermal convective coefficient of water, retrieved with the Nusselt correlation:

$$Nu_w = \frac{h_w d_i}{k_w} = 0.023 Re_w^{0.8} Pr_w^{0.4} \quad [-] \quad (4.36)$$

$$Re_w = \frac{\rho_w v_w d_i}{\mu_w} \quad [-] \quad (4.37)$$

with k_w equal to $0.6 [Wm^{-1}K^{-1}]$ and the Prantl number of liquid water equal to 6.9.

Finally, the fin efficiency is defined through the following equations:

$$\eta_0 = 1 - \frac{A_{fin}}{A_{hx}} (1 - \eta_f) \quad [-] \quad (4.38)$$

$$\eta_f = \frac{\tanh(mL_f)}{mL_f} \quad [-] \quad (4.39)$$

$$m = \sqrt{\frac{2h_a}{k_{al}\delta_f}} \quad [m] \quad (4.40)$$

with A_f is the finned surface, the characteristic length L_f (selected as half of the distance between two pipes), δ_f is the fin thickness and k_{al} is the aluminium thermal conductivity.

Water loop thermal balance

The water temperature along the pipes is not constant in space and time, as it is affected by the air temperature and the heat released by the adsorption phenomenon.

The main purposes of the water flow is to cool-down/heat-up the air stream and the silica coating. The water temperature evolution is described in equation 4.12, where the variation of water temperature over time depends on the variation along the air stream and the temperature difference with the silica layer (first and second left end side terms).

The water mass flow rate \dot{m}_w is evaluated as

$$\dot{m}_w = \rho_w A_{w,cross} v_w \quad \left[\frac{kg}{s} \right] \quad (4.41)$$

with ρ_w as the water density, $A_{w,cross}$ the pipe cross section and the water stream velocity v_w . The second term is the same used in the previous sub-section, dedicated to the silica gel thermal balance.

4.2.1 Numerical Equations

In order to develop the numerical model, the five main equations have been discretized in both time e space domains. Looking at the time domains it has been chosen a time-step equal to $\Delta t = 1s$ and the Backward Euler (BE) method for the discretization. The BE is an implicit method, unconditionally stable for any time-step (equation 4.42). Concerning the space domain, the finite element size has been chosen equal to $\Delta z = 3mm$ with a Backward finite difference method (equation 4.43). Being n the time-step and i the space element, the time and space derivative are represented as follow:

$$\frac{dT}{dt} = \frac{T_i^{n+1} - T_i^n}{\Delta t} \quad (4.42)$$

$$\frac{dT}{dz} = \frac{T_i - T_{i-1}}{\Delta z} \quad (4.43)$$

The five main equations have been written in numerical form.

Silica gel water uptake (eq. 4.8)

$$\rho_b \frac{W^{n+1} - W^n}{\Delta t} = K_G a_s (x_a - x^*) = \dot{G} \quad (4.44)$$

$$W^{n+1} = W^n + \frac{\Delta t K_G a_s (x_a^n - x^{*n})}{\rho_b} = \dot{G} \quad (4.45)$$

$$W(z, t = 0) = W_0 \quad (4.46)$$

Air - Moisture mass balance (eq. 4.9) with defined initial condition.

$$\varepsilon_b \rho_a \frac{x_{a_i}^{n+1} - x_{a_i}^n}{\Delta t} dv = -\dot{m}_a \frac{x_{a_i}^{n+1} - x_{a_{i-1}}^{n+1}}{\Delta z} dz - K_g a_s (x_{a_i}^{n+1} - \bar{x}_i^n) dv \quad (4.47)$$

defining M_A the bidiagonal sparse matrix of the coefficients and Q_A the matrix of the known terms, the equation (3.30) can be rewritten as:

$$x_a^{n+1} = M_{X_a}^{-1} Q_{X_a} \quad (4.48)$$

where

$$M_{X_a} = \begin{bmatrix} 1 + \Delta t(A_1 + A_2) & \dots & \dots \\ -\Delta t A_1 & 1 + \Delta t(A_1 + A_2) & \dots \\ \dots & -\Delta t A_1 & 1 + \Delta t(A_1 + A_2) \end{bmatrix} \quad (4.49)$$

$$Q_{X_a} = x_a^n + \Delta t A_2 \bar{x}^n \quad (4.50)$$

$$A_1 = \frac{v_a}{\varepsilon_b \Delta z} \quad (4.51)$$

$$A_2 = \frac{K_g a_s}{\varepsilon_b \rho_a} \quad (4.52)$$

In this case, since the spatial derivative appears, it is necessary to define also a boundary condition (for $z=0$), in addition to an initial condition (for $t=0$):

$$x_a(z, t = 0) = x_{a_0} \quad (4.53)$$

$$x_a(z = 0, t) = x_{a_{in}} \quad (4.54)$$

which corresponds to:

$$M_{X_a}(1, 1) = 1 \quad (4.55)$$

$$M_{X_a}(1,2) = 0 \quad (4.56)$$

$$Q_{X_a}(1) = x_{a_{in}} \quad (4.57)$$

In this analysis x_{a0} is set equal to $x_{a_{in}}$.

Air thermal balance (eq. 4.10)

$$\begin{aligned} \varepsilon_b \rho_a c p_a \frac{T_{a_i}^{n+1} - T_{a_i}^n}{\Delta t} dv = & -\dot{m}_a c p_a \frac{T_{a_i}^{n+1} - T_{a_{i-1}}^{n+1}}{\Delta t} dz + h_a a_f (T_{s_i}^n - T_{a_i}^{n+1}) dv \\ & - U_l a_l (T_{a_i}^{n+1} - T_{amb}) dv \end{aligned} \quad (4.58)$$

Defining the matrix of coefficients and known terms, it becomes:

$$T_a^{n+1} = M_{T_a}^{-1} Q_{T_a} \quad (4.59)$$

where the sparse matrix M_{T_a} is equal to:

$$M_{T_a} = \begin{bmatrix} 1 + \Delta t(B_1 + B_2 + B_3) & \dots & \dots \\ -\Delta t B_1 & 1 + \Delta t(B_1 + B_2 + B_3) & \dots \\ \dots & -\Delta t B_1 & 1 + \Delta t(B_1 + B_2 + B_3) \end{bmatrix} \quad (4.60)$$

while, the known term matrix Q_{T_a} is given by:

$$Q_{T_a} = T_a^n + \Delta t B_2 T_s^n + \Delta B_3 T_{amb} \quad (4.61)$$

with

$$B_1 = \frac{v_a}{\varepsilon_b \Delta z} \quad (4.62)$$

$$B_2 = \frac{h_a a_f}{\varepsilon_b \rho_a c p_a} \quad (4.63)$$

$$B_3 = \frac{U_l a_l}{\varepsilon_b \rho_a c p_a} \quad (4.64)$$

The initial condition and the boundary condition are set:

$$T_a(z, t = 0) = T_{a_0} \quad (4.65)$$

$$T_a(z = 0, t) = T_{a_{in}} \quad (4.66)$$

corresponding to:

$$M_{T_a}(1, 1) = 1 \quad (4.67)$$

$$M_{T_a}(1, 2) = 0 \quad (4.68)$$

$$Q_{T_a}(1) = T_{a_{in}} \quad (4.69)$$

Similarly to the air mass balance, the initial value of the air temperature is imposed equal to the air temperature at the entrance of the finned tubes: $T_{a_0} = T_{a_{in}}$.

Silica Gel Thermal Balance (eq. 4.11)

$$(1 - \varepsilon_b) c p_s \rho_s \frac{T_{s_i}^{n+1} - T_{s_i}^n}{\Delta t} = H_{ads} K_g a_s (x_{a_i}^n - \bar{x}_i^n) - h_a a_f (T_{s_i}^{n+1} - T_{a_i}^n) - U a_f (T_{s_i}^{n+1} - T_{w_i}^n) \quad (4.70)$$

from which is possible to obtain and update the silica-gel temperature:

$$T_{s_i}^{n+1} = \frac{T_{s_i}^n + \Delta t C_1 (x_{a_i}^n - \bar{x}_i^n) + \Delta t C_2 T_{a_i}^n + \Delta t C_3 T_{w_i}^n}{1 + \Delta t C_1 + \Delta t C_2 + \Delta t C_3} \quad (4.71)$$

where

$$C_1 = \frac{H_{ads} K_g a_s}{(1 - \varepsilon_b) c p_s \rho_s} \quad (4.72)$$

$$C_2 = \frac{h_a a_f}{(1 - \varepsilon_b) c p_s \rho_s} \quad (4.73)$$

$$C_3 = \frac{U a_f}{(1 - \varepsilon_b) c p_s \rho_s} \quad (4.74)$$

Since there is only a time derivative, in this case, only the initial condition is imposed:

$$T_s(z, t = 0) = T_{s_0} \quad (4.75)$$

the value of T_{s_0} is set to be equal to the inlet air temperature $T_{a_{in}}$.

Water Loop Thermal Balance (eq. 4.12)

$$c\rho_w\rho_w\frac{T_{w_i}^{n+1}-T_{w_i}^n}{\Delta t}dv = -c\rho_w\dot{m}_w\frac{T_{w_i}^{n+1}-T_{w_{i-1}}^{n+1}}{\Delta z}dz - Ua_f(T_{w_i}^{n+1}-T_{a_i}^n)dv \quad (4.76)$$

introducing the matrix of the coefficient and the known term, the equation (4.72) can be rewritten as:

$$T_{w_i}^{n+1} = Q_w M_w^{-1} \quad (4.77)$$

The sparse matrix M_w is given by:

$$M_w = \begin{bmatrix} 1 + \Delta t(C_1 + C_2) & \dots & \dots \\ -\Delta t C_1 & 1 + \Delta t(C_1 + C_2) & \dots \\ \dots & -\Delta t C_1 & 1 + \Delta t(C_1 + C_2) \end{bmatrix} \quad (4.78)$$

The known term matrix Q_w is equal to:

$$Q_w = T_w^n + \Delta t C_2 T_s^n \quad (4.79)$$

with

$$C_1 = \frac{\dot{m}_w}{\rho_w A_b \Delta z} \quad (4.80)$$

$$C_2 = \frac{U a_f}{\rho_w c \rho_w} \quad (4.81)$$

Since both the spacial and the temporal derivatives are present, an initial condition and a boundary condition need to be set:

$$T_w(z = 0, t) = T_{w_{in}} \quad (4.82)$$

$$T_w(x, t = 0) = T_{w0} \quad (4.83)$$

which translates into:

$$M_w(1, 1) = 1 \quad (4.84)$$

$$M_w(1, 2) = 0 \quad (4.85)$$

$$Q_w(1) = T_{w_{in}} \quad (4.86)$$

Again, the value of the temperature at the beginning of the simulation T_{w0} and at inlet temperature $T_{w_{in}}$ are set to be the same.

4.2.2 Auxiliary Equations

Here are reported the auxiliary equations used for calculate the properties of water, air and silica gel. These equations are used in all the 5 main equations.

x_a is the specific humidity ratio of air calculated as a function of the ambient pressure (P_{amb}) in Pa, the saturation pressure of water vapor at a certain temperature (P_{sat}) in Pa and the relative humidity of air (RH_a):

$$x_a = 0.622 \frac{RH_a P_{sat}}{P_{amb} - RH_a P_{sat}} \quad \left[\frac{kg_v}{kg_a} \right] \quad (4.87)$$

The saturation pressure of water vapor P_{sat} is expressed as a function of air temperature:

$$P_{sat} = 0.00046777T^4 + 0.02444T^3 + 1.359T^2 + 45.98T + 604.6 \quad [Pa] \quad (4.88)$$

\bar{x} is the air humidity ratio in equilibrium with silica gel. In order to evaluate it, the equations used above for the air moisture content are also exploited now, having as input the silica gel temperature and its relative humidity. The latter one is calculated using the adsorption isotherm obtained from measurements on how the relative changes at different values of water uptake W and silica gel temperature T_s .

The correlation obtained is the following:

$$RH_s = s_1 \cdot T + s_2 \cdot T^2 + s_3 \cdot W + s_4 \cdot W \cdot T + s_5 \cdot W \cdot T^2 + s_6 \cdot W^2 + s_7 \cdot T \cdot W^2 + s_8 \cdot W^3 + s_9 \cdot T^3 \quad (4.89)$$

where the coefficients are respectively: $s_1=-0.00249434$; $s_2=0.0000529632$; $s_3=5.65527$; $s_4=0.0360887$; $s_5=-0.0000713679$; $s_6=-24.9044$; $s_7=-0.112424$; $s_8=54.8088$; $s_9=-0.000000123558$.

It is possible to notice from Figure 4.4 that the different curves, related to different temperatures, converge into the same point corresponding to a water uptake of $0.3 \text{ kg}_w \text{ kg}_s^{-1}$, meaning that the maximum increment in weight due to water adsorption by dry silica gel is equal to 30 % for the temperatures considered.

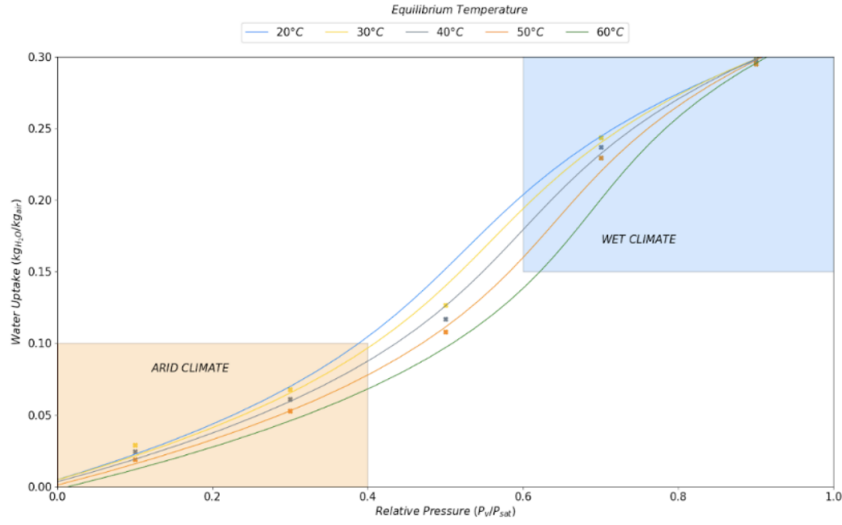


Fig. 4.4 Adsorption Isotherm for silica gel form model

The specific heat for air is calculated as:

$$cp_a = 1884x_a + 1005(1 - x_a) \quad \left[\frac{J}{kg K} \right] \quad (4.90)$$

a_f , which is the specific exchange area between air and silica gel, supposed to be equal to the specific total exchange surface, i.e. the ratio between the total exchange surface (sum of fins and tubes) and the total volume of the finned tubes:

$$a_f = \frac{A_{hx}}{V_b} \quad [m^{-1}] \quad (4.91)$$

a_l is equal to the casing surface divided by the finned tubes volume:

$$a_l = \frac{A_c}{V_b} \quad [m^{-1}] \quad (4.92)$$

4.3 Literature Comparison - A Model Validation

The numerical model described was subjected to preliminary validation comparing output results with experimental results for finned heat exchangers coated with silica gel [135, 136]. Once the experimental setup is ready for operation, validation is car-

ried out on the prototype to fine-tune all the important parameters. The experimental parameters and geometry data are used. However, not all parameters have been clearly specified by the authors of the two references. In case of missing parameters, reasonable hypotheses have been made.

Validation 1 [135]

In [135] the authors propose a novel composite silica gel coated heat exchanger which is experimentally tested and compared with state-of-the-art silica gel coated heat exchanger. The main objective is to enhance cooling and dehumidification performance. The influences of main operation parameters including water temperatures and inlet air conditions on system performance are analysed in terms of average dehumidification capacity and thermal coefficient of performance. The results highlight that the novel composition has better dehumidification performance compared with traditional one. Moreover, pre-cooling has been found as a key variable for improving overall performance.

The main experimental set-up parameters are reported in Table 4.1. The comparison has been done starting from the second adsorption-desorption cycle, since the first cycle is affected by the initial conditions which do not represent properly the system at regime.

Unfortunately, some data are missing, such as the silica-gel layer thickness and porosity, the tubes pitch and outer diameter.

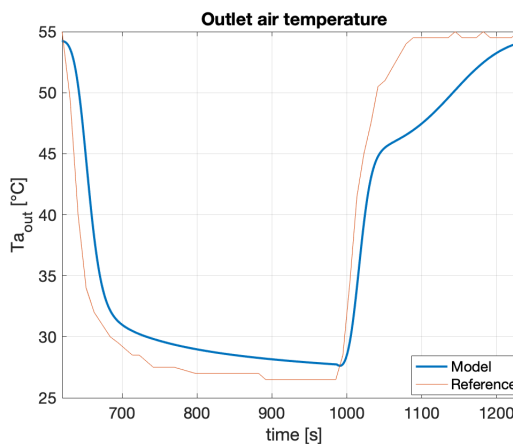


Fig. 4.5 Outlet Air temperature comparison [135]

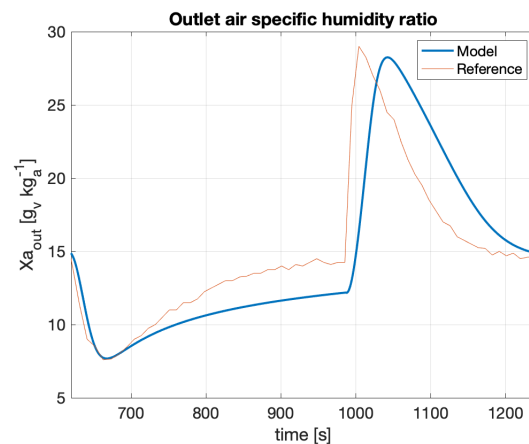


Fig. 4.6 Humidity ratio comparison [135]

Table 4.1 Experimental conditions from [135]

Input data reference [135]	
Silica gel type	Macro pore, ZCX-II
HX length	50 mm
HX height	200 mm
HX width	160 mm
Fin thickness	0.15 mm
Fin pitch	1.5 mm
Tube inner diameter	7 mm
Inlet air temperature	30 °C
Inlet air humidity ratio	14.5 $g_v kg_a^{-1}$
Inlet air velocity	1 $m s^{-1}$
Cooling water temperature	25 °C
Hot water temperature	60 °C
Water flowrate	160 $l h^{-1}$
Adsorption duration	367 s
Regeneration duration	253 s

The obtained results are compared in Figure 4.5-4.6 in terms of outlet air temperature and specific humidity ratio.

Looking at the figures, one can see that the curves are quite coupled in both cases. The biggest differences are in the peak values and the transition period. As for the outlet air temperature, the minimum values of the model and the reference are 27.7°C and 26.5°C, respectively, while the maximum temperatures are 54.2°C and 55°C. The average exhaust air temperature determined with the model during adsorption (31.6°C) is about 7.85% higher than that of the experiment (29.3°C), whereas during regeneration the average exhaust air temperature of the model (46.7°C) is about 6.58% lower than that of the experiment (49.9°C). Looking at the specific humidity ratio of the exhaust air, the minimum value of the model agrees with that of the experiment and is 7.6 $g_v kg_a^{-1}$, while the maximum values are 28.3 $g_v kg_a^{-1}$ for the model and about 29 $g_v kg_a^{-1}$ for the reference. The average value of the difference between the specific humidity ratio of the inlet and outlet air obtained by the model (3.9 $g_v kg_a^{-1}$) is about 25.8% higher than the experiment (3.1 $g_v kg_a^{-1}$) during adsorption. These discrepancies are probably due to the lack of information about the silica gel material, i.e. its density, pore radius, porosity, layer thickness and adsorption isotherm, which are essential for a correct calibration of the model.

Nevertheless, the maximum and minimum values of the model for both the exhaust air temperature and the specific humidity ratio of the exhaust air are quite similar and the relative errors of the average values are generally quite small.

Validation 2 [136]

In [136], the authors propose an experimental test of desiccant-coated heat exchangers. In particular, two materials were tested: Silica gel and polymer. The dynamic performance was recorded and in short, it was found that this desiccant-coated finned heat exchanger overcomes well the side effect of adsorption heat that occurs in the desiccant dehumidification process and achieves good dehumidification performance under the given conditions. The silica gel coated heat exchanger performs better than the polymer heat exchanger. The influences of regeneration temperature, supply air temperature and humidity on system performance in terms of average dehumidification rate and thermal performance coefficient were also analysed. In addition, the ambient air temperature has little effect on the system performance, which can be of utmost importance for a stable performance capacity.

The input data are reported in the following Table 4.2. Again, there are some data missing such as the thickness and the properties of silica-gel used (pore radius, porosity, adsorption isotherm, density), the tubes and fins pitch.

The results are shown in Figure 4.7-4.8 and, as in the previous case, the results are considered from the second cycle onwards.

As far as the outlet air temperature is concerned, the behaviour is quite different. This difference can be explained by the fact that the temperature sensors are not placed exactly at the outlet of the heat exchanger. For this reason, the thermal inertia of the duct, the cladding and the heat exchange between the air and the duct walls cause a discrepancy between the outlet and the read temperature. Nevertheless, the trend is quite similar and the maximum and minimum values are almost identical. The maximum outlet temperature reached by the model simulation and experiment is 41 °C and 40 °C, respectively, while the minimum temperatures during adsorption are 27.6 °C for the model and 26.6 °C for the reference. The average value of the air outlet temperature during adsorption is 29.1 °C for the model and 29.8 °C for the experiment. During regeneration, on the other hand, the air outlet temperature of the model is 39.3 °C, while it is 36.2 °C for the reference.

Table 4.2 Experimental conditions, reference [136]

Input data	
Silica gel type	Mesopore
HX length	45 mm
HX height	280 mm
HX width	200 mm
Fin thickness	0.15 mm
Tube outer diameter	9.52 mm
Tube inner diameter	7.85 mm
Inlet air temperature	30 °C
Inlet air relative humidity	60 %
Inlet air velocity	1.54 m s ⁻¹
Cooling water temperature	25 °C
Hot water temperature	50 °C
Water flowrate	200 l h ⁻¹
Adsorption duration	600 s
Regeneration duration	600 s

As for the specific humidity ratio at the air outlet, there are few deviations here and the trend is maintained. The slight deviations may be due to the fact that the information on the silica gel used is again incomplete. Nevertheless, the minimum and maximum values of the model simulations are 11.8 $g_vkg_a^{-1}$ and 23.4 $g_vkg_a^{-1}$, while the values resulting from the experiment correspond to about 12 $g_vkg_a^{-1}$ and 22.2 $g_vkg_a^{-1}$. The average moisture removal by the model corresponds to 1.51 $g_vkg_a^{-1}$, while the value obtained by the experiment is 0.98 $g_vkg_a^{-1}$.

In summary, the differences between the model and the experiments are probably due to the fact that some data are missing, especially those related to the silica gel used and the silica gel layer thickness. In addition, the curves of the experiments were reproduced based on the graphs presented in the references, so some measurement and transposition errors may occur. Finally, the results of the experiments are affected by uncertainties and external noise, and the sensors measuring the air conditions are in some cases not located immediately behind the outlet section of the heat exchanger. In addition, the model used makes some simplifying assumptions, such

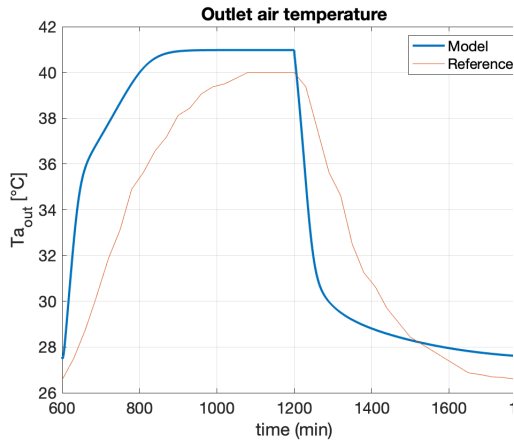


Fig. 4.7 Outlet Air temperature comparison [136]

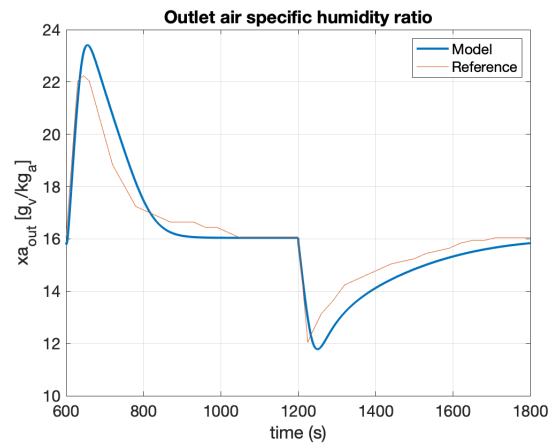


Fig. 4.8 Humidity ratio comparison [136]

as assuming that the problem is one-dimensional, some properties are constant and some contributions to heat transfer are neglected (conduction in the direction of air flow). Considering all these aspects and the fact that the trends and the minimum and maximum values of the parameters considered are quite similar, the model can predict the performance of the HySun finned tubes. The model approximates experimental results in a satisfactory manner, making it suitable for a first performance evaluation of the HySun prototype.

4.4 Parametric Analysis

A parametric analysis is developed to find out what are the best operative conditions and heat exchanger configurations which maximise the system performance. The simulation has been developed with one single adsorption heat exchanger as the main objective of this analysis is to highlight the variation of performance with respect to some geometrical and set-point parameters. The time has been set so that the adsorption and the regeneration have the same period of 1 hour, resulting in an adsorption-regeneration cycle of 2 hours. Moreover, in order to evaluate the full-operation performance, all the calculations have been made starting from the second cycle. In this way, the influence of initial conditions are excluded.

The investigated parameters are the following together with a resuming Tables 4.3-4.4 reporting the main geometrical parameters used for the coated heat exchanger and the air/water stream conditions:

- Heat exchanger length: from 5 cm to 30 cm
- Hot water temperature: from 50 °C to 70 °C
- Cold water temperature: from 15 °C to 25 °C
- Air stream velocity: from 0.2 ms^{-1} to 1.6 ms^{-1}

Table 4.3 Input Parameters for Silica-Gel Layer and Geometrical Shape of the HX

Silica gel properties and conditions	
Density ρ_s	1129 kg/m^3
Porosity ε_s	0.35
Pore radius \bar{r}_p	100 nm
Initial water uptake W_0	0.005 kg_w/kg_s
Geometrical parameters of the heat exchanger	
Longitudinal fin pitch X_l	21.65 mm
Transversal fin pitch X_t	25 mm
heat exchanger length L_z	50-300 mm
heat exchanger width L_x	500 mm
heat exchanger height L_y	500 mm
Outer pipe diameter d_o	9.52 mm
Inner pipe diameter d_i	8.62 mm
Fin pitch p_f	2.5 mm
Silica gel coating thickness t_s	0.55 mm
Fin thickness δ_f	0.1 mm

Table 4.4 Water and Airflow tested condition

Air flow conditions	
Average velocity v_a	0.2-1.6 m/s
Inlet temperature $T_{a_{in}}$	30 °C
Inlet relative humidity $RH_{a_{in}}$	70%
Water flow conditions	
Adsorption mass flowrate $\dot{m}_{w_{ads}}$	0.08 kg/s
Regeneration mass flowrate $\dot{m}_{w_{ads}}$	0.05 kg/s
Cold inlet water temperature T_{w_c}	15-25 °C
Regeneration inlet water temperature T_{w_h}	50-70 °C

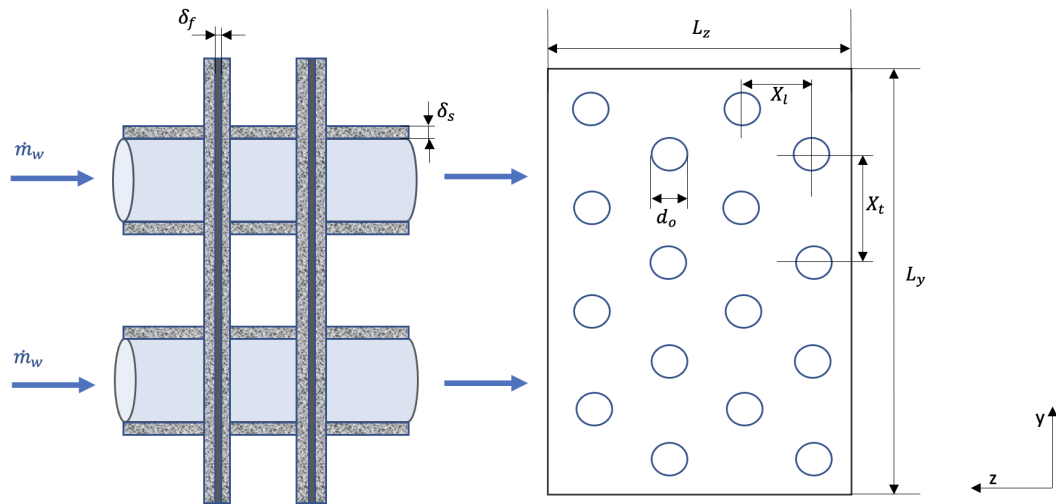


Fig. 4.9 Adsorption heat exchanger geometrical configuration

4.4.1 Performance Coefficients

In order to evaluate the performance of the system under different conditions and configurations, performance coefficients are defined as follow.

COP_{el} - Electric Coefficient of Performance

The COP_{el} is the ratio between the useful effect, the cooling power, and the electric power needed to run the system, which is calculated as the sum of the power required by the fan, the water pump and the heat pump:

$$COP_{el} = \frac{\dot{Q}_{cool}}{\dot{W}_{el_{fan}} + \dot{W}_{el_{pump}} + \dot{W}_{el_{HP}}} \quad [-] \quad (4.93)$$

where the cooling power is calculated as the air mass flow rate multiplied by the difference of the air enthalpy between the inlet and the outlet sections [129]:

$$\dot{Q}_{cool} = \dot{m}_a(e_{a_{in}} - e_{a_{out}}) \quad [W] \quad (4.94)$$

with the air enthalpy obtained as a function of the air temperature and specific humidity:

$$e_a = 10^3(1.006T + x(2501 + 1.86T)) \quad [Jkg^{-1}] \quad (4.95)$$

The $\dot{W}_{el_{fan}}$ is given by:

$$\dot{W}_{el_{fan}} = \frac{\dot{V}_a \Delta P_a}{\eta_{is_{fan}} \eta_{el_{fan}}} \quad [W] \quad (4.96)$$

where \dot{V}_a is the volumetric air flow rate in $m^3 s^{-1}$, $\eta_{is_{fan}}$ and $\eta_{el_{fan}}$ are the isentropic and electric efficiencies (set to be equal to 0.45 and 0.95 respectively), ΔP_a represents the pressure losses along the heat exchanger on air side, evaluated as:

$$\Delta P_a = f_a \rho_a \frac{v_a^2 L}{2 d_h} \quad [Pa] \quad (4.97)$$

with v_a being the air flow velocity in $m s^{-1}$, L the heat exchanger length in m and f_a the friction factor, which, for laminar flows is equal to $\frac{64}{Re_a}$.

Similarly, $\dot{W}_{el_{pump}}$ is calculated as:

$$\dot{W}_{el_{pump}} = \frac{\dot{V}_w \Delta P_w}{\eta_{is_{pump}} \eta_{el_{pump}}} \quad [W] \quad (4.98)$$

where \dot{V}_w is the volumetric water flowrate in $m^3 s^{-1}$, $\eta_{is_{pump}}$ and $\eta_{el_{pump}}$ are set to be equal to 0.65 and 0.95. The pressure loss ΔP_w is the sum of the distributed and concentrated pressure drops:

$$\Delta P_w = f_w \rho_w \frac{v_w^2 L_p}{2 d_i} + N_{pass} \beta \rho_w \frac{v_w^2}{2} \quad [Pa] \quad (4.99)$$

where the friction coefficient f_w , neglecting the pipes roughness, is evaluated as [129]:

$$f_w = \left(-1.8 \log \left(\frac{6.9}{Re_w} \right) \right)^{-2} \quad [-] \quad (4.100)$$

while the friction factor for concentrated losses β is put equal to 2.5 and N_{pass} is the number of tube passes.

The electric power needed by the heat pump, \dot{W}_{elHP} is derived from the definition of COP for the heat pump, that, for example, in the case of adsorption is given by:

$$COP_{HP} = \frac{\dot{Q}_{cond}}{\dot{W}_{elHP}} \quad [-] \quad (4.101)$$

where \dot{Q}_{cond} is the heat power exchanged in the condenser.

The calculation of COP can be simplified by assuming that it corresponds to the efficiency of the inverse Carnot cycle, corrected by a factor of 0.5 to quickly determine a reasonable value [68, 69]. Once the installed HP is calibrated and tested, a custom equation for COP will be developed to perfectly reproduce the behaviour of the prototype HP. Indeed, the results (reported in the following section 4.4.2) are to be intended as guideline for a general machine behaviour and not as a precise point by point operation map.

$$COP_{HP} = 0.5 \frac{T_{cold}}{T_{hot} - T_{cold}} \quad [-] \quad (4.102)$$

where T_{cold} is the temperature of the cold source and T_{hot} , the one of the hot source. Similarly the COP_{HP} for the regeneration case can be calculated.

It can be noticed that the COP_{el} just introduced is defined in terms of power, meaning it is an instant value. In order to evaluate the average electric COP for the entire process, it needs to be integrated over time. This implies that the COP has to be expressed in terms of energy:

$$COP_{el} = \frac{\sum_{i=1}^{n_{ads}} \dot{Q}_{cool} \Delta t}{\sum_{i=1}^{n_{tot}} \dot{W}_{el_{fan}} \Delta t + \sum_{i=1}^{n_{tot}} \dot{W}_{el_{pump}} \Delta t + \sum_{i=1}^{n_{tot}} \dot{W}_{el_{HP}} \Delta t} \quad [-] \quad (4.103)$$

where n_{ads} is the final time-step of the adsorption process, while n_{tot} is the final time-step of the entire process (both adsorption and regeneration). Δt is the duration of each time-step. It should be remembered that only one heat exchanger was simulated for this parametric analysis, so the performance coefficients were developed for this particular case.

COP_{th} - Thermal Coefficient of Performance

The thermal Coefficient of performance COP_{th} differs from the previous COP for the fact that it accounts for thermal power only. It is given by the ratio between the cooling capacity during adsorption and the heat exchange rate of water during regeneration, both integrated over time [136].

It can be deduced that, in this case, it is not possible to evaluate an instant value of the COP_{th} , since the two terms belongs to different periods of time. So, only the average value of COP_{th} can be calculated:

$$COP_{th} = \frac{\sum_{i=1}^{n_{ads}} \dot{Q}_{cool} \Delta t}{\sum_{i=1}^{n_{rig}} \dot{Q}_{heat} \Delta t} \quad [-] \quad (4.104)$$

with n_{rig} corresponding to the final timestep of the regeneration process and \dot{Q}_{heat} to the water thermal power equal to:

$$\dot{Q}_{heat} = \dot{m}_w c p_w (T_{win} - T_{wout}) \quad [W] \quad (4.105)$$

Moisture removal effectiveness

The moisture removal effectiveness is defined as the average moisture removal during adsorption. It is evaluated as (taking into account only the positive values of Δx):

$$\bar{\Delta x} = \frac{\sum_{i=1}^{n_{ads}} (x_{a_{in}} - x_{a_{out}}) \Delta t}{t_{ads}} \quad [g_v k g_a^{-1}] \quad (4.106)$$

4.4.2 Results of the parametric analysis

Heat Exchanger Length

The first analyzed parameter is the HX length with fixed condition: air velocity $v_a = 0.8$ m/s and cold-hot water temperature $T_{w_c} = 20$ °C and $T_{w_h} = 50$ °C respectively.

The main results for (a) air temperature, (b) humidity ratio and (c) silica gel mean water uptake are reported in the following collage (Figure 4.10).

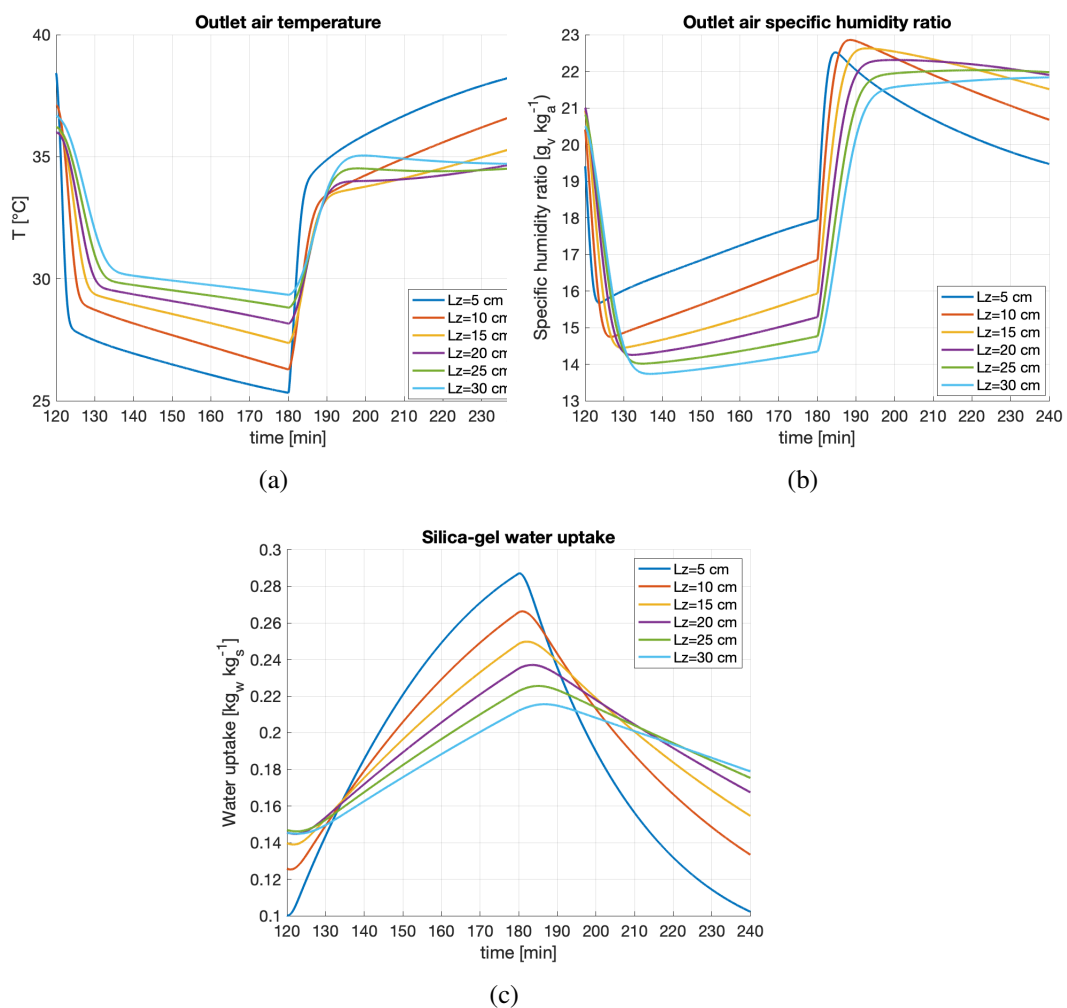


Fig. 4.10 (a) Temperature, (b) specific humidity of outlet air and (c) silica-gel water uptake for different heat exchanger lengths

Based on the air temperature, you can see that the longer the HX is (120 to 180 minutes), the higher the temperature during adsorption. In fact, at the end of the

adsorption phase, the temperature moves from 29.3 °C for $L_z = 30\text{cm}$ to 25.3 °C at $L_z = 5\text{cm}$ (about 12.5% decrease). The longer the HX, the lower the temperature of the outlet air during regeneration. This trend can be explained by the fact that with increasing length the moisture removal effect is higher, but also more adsorption heat is released, so that the water flowing into the pipes can cool the air to a lesser extent. Furthermore, the largest differences in terms of air temperature are between $L_z = 5\text{cm}$ to $L_z = 15\text{cm}$, where the difference is about 5 percentage points.

As for the specific humidity at the outlet (b), we note that the silica gel is closer to saturation at $L_z = 5\text{cm}$. In fact, the humidity at the outlet at the end of the adsorption cycle is almost equal to that at the inlet ($18.0\text{ g}_v\text{kg}_a^{-1}$ for the outlet and $18.8\text{ g}_v\text{kg}_a^{-1}$ for the inlet). As expected, the moisture ratio decreases with increasing HX length as the amount of silica increases. In fact, the specific moisture ratio at the end of the adsorption process for $L_z = 30\text{cm}$ is $14.4\text{ g}_v\text{kg}_a^{-1}$.

Looking at the average water uptake (c), it can be seen that as the length decreases, the average water uptake of the silica gel increases and is about $0.29\text{ kg}_w\text{kg}_s^{-1}$ at the end of the adsorption phase for $L_z = 5\text{cm}$ and $0.10\text{ kg}_w\text{kg}_s^{-1}$ at the end of the regeneration. For longer HX, on the other hand, the water uptake at the end of adsorption is $0.22\text{ kg}_w\text{kg}_s^{-1}$, while at the end of regeneration it drops to $0.18\text{ kg}_w\text{kg}_s^{-1}$. As before, this can be explained by the fact that the amount of silica gel increases as the length of the heat exchanger increases. Furthermore, it can be seen from the figure that the peak values of water absorption are reached during regeneration and not during adsorption, as the saturation of the material is not reached. The hot water flowing through the tubes therefore gradually reaches the regeneration temperature, and in this way the silica gel can still absorb water in the first moments of the regeneration cycle.

Figure 4.11 shows the actual COP_{el} for the adsorption cycle. Please remember that the COP_{el} has been defined for the adsorption phase only, as we are most interested in the cooling effect (see section 4.4.1). The instantaneous COP_{el} starts to be greater than zero after a certain delta time, because the water flowing in the pipes needs some minutes to reach the temperature setpoint at the beginning of the adsorption cycle. In general, it can be seen that as the length of the heat exchanger decreases, the instantaneous COP_{el} increases. The maximum instantaneous COP_{el} for $L_z = 5\text{cm}$ is equal to 8.6, while for $L_z = 30\text{cm}$ it is 6.42. The same behaviour is also seen in the average COP_{el} , which moves from 2.7 for $L_z = 5\text{cm}$ to 2.4 for

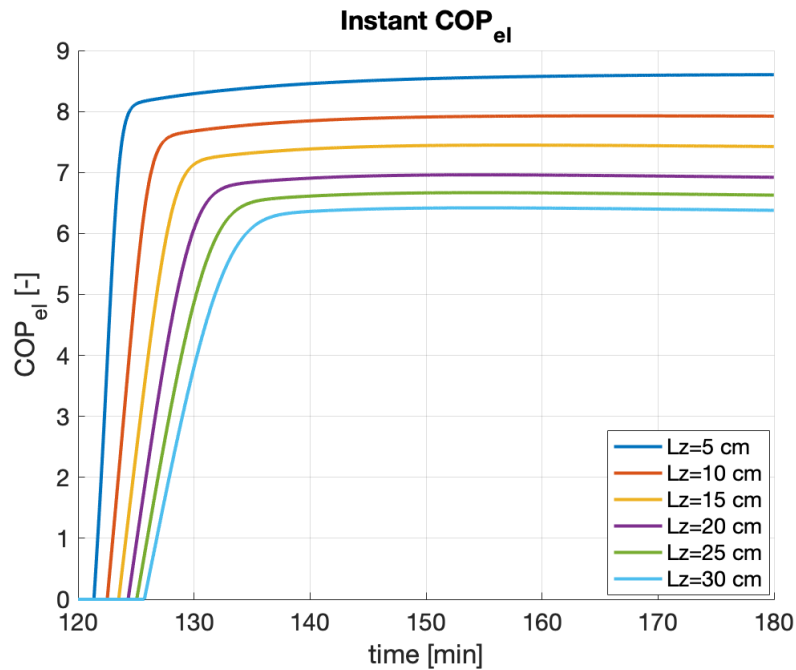


Fig. 4.11 Instant COP_{el} variation during adsorption

$L_z = 30\text{cm}$ (see Figure B.3 in the Appendix B.2 for the corresponding graph). The behaviour of COP can be explained by looking at the trend in cooling power, which is shown in the following figure 4.12:

The sensible cooling power increases as time passes, while the latent cooling power diminishes. This is easily explained by the fact that the latent cooling power is related to the moisture removal which decreases as the silica-gel water uptake raises. At the same time, the sensible cooling power grows, since the cold water has to remove lesser and lesser adsorption heat as time goes on. The global trend of the cooling power follows the one of the latent cooling power since it represents the most significant contribution. The maximum value of cooling power is obtained for $L_z = 30\text{cm}$ with a value of 2.97 kW, while the minimum results from the simulation with $L_z = 5\text{cm}$ with a cooling power equal to 2.35 kW (20.9% lower).

The trend of the heat pump's electricity consumption is shown in Figure 4.13. It consumes more electricity at the beginning of adsorption at $L_z = 5\text{cm}$ because the water temperature (due to the previous regeneration cycle) is higher than the other HX length and it needs to be cooled down. At the beginning of the regeneration, the water in the hoses has a lower temperature than in the longer hoses. Therefore, more energy is needed from the heat pump to bring the water to 50 °C. However, since the

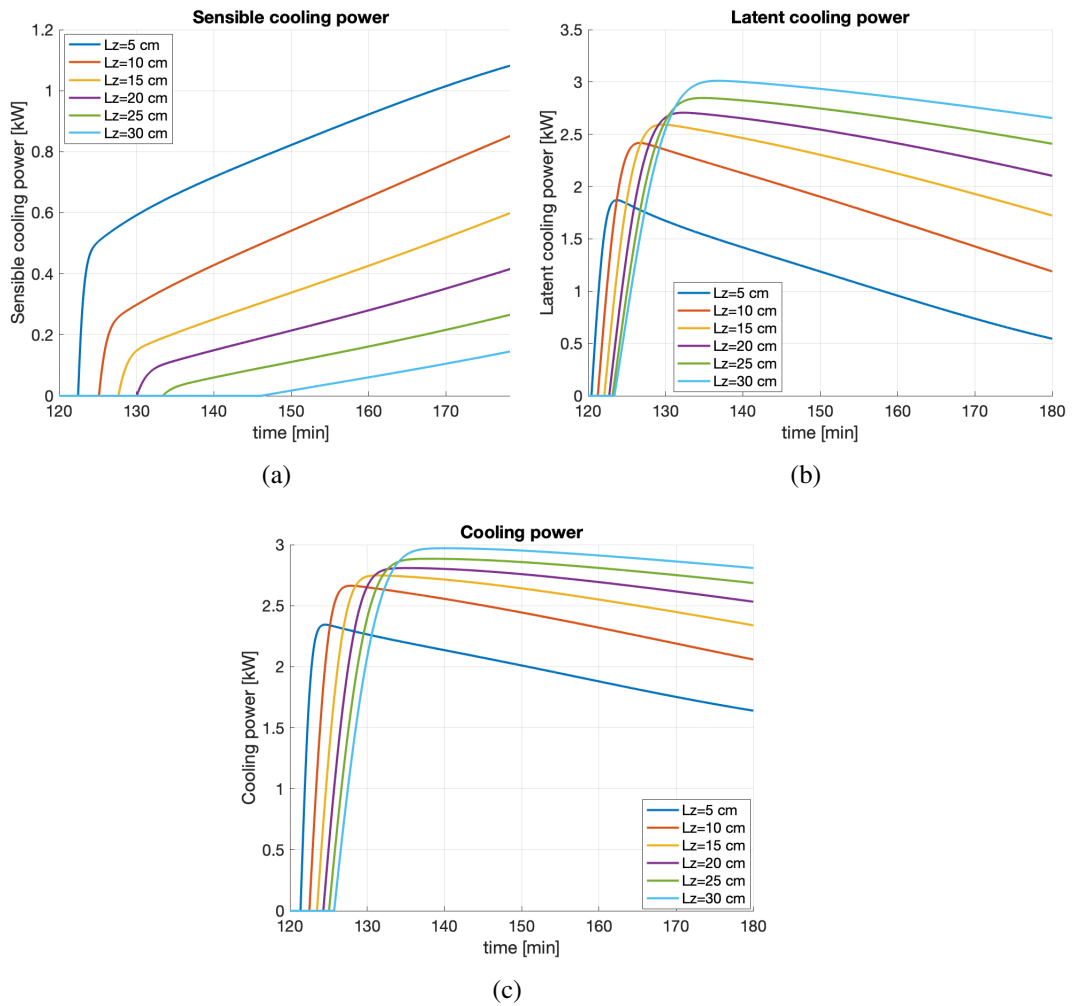


Fig. 4.12 (a) Sensible, (b) latent and (c) global cooling power for different heat exchanger lengths

temperature of the water is closer to the set point at lower values of L_z , the power demand of the heat pump is lower. An interesting result is that the electrical power of the heat pump changes significantly when moving from $L_z = 5$ cm to $L_z = 10$ cm, with the total energy required increasing by 16.9%. After that, it approaches almost the same value. So even though the cooling capacity is lower at $L_z = 5$ cm, at the same time the electrical power required to run the system is much lower. This leads to a higher COP_{el} . As mentioned in the previous section, the fan and the water pumps also contribute to the total power COP. In particular, the power of the fan increases linearly as the length of the heat exchanger increases, ranging from 4.44 W for $L_z = 5$ cm to 26.4 W for $L_z = 30$ cm. The power of the water pump evolves

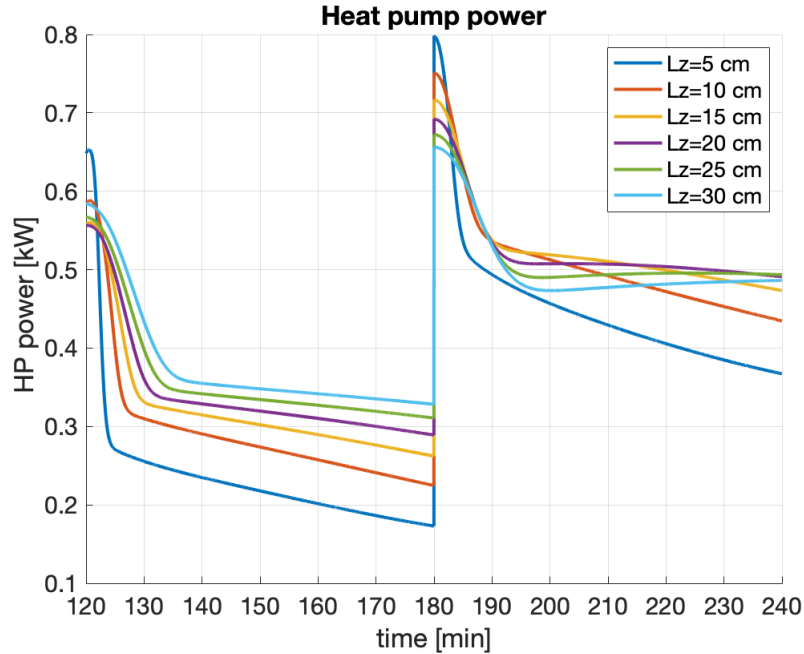


Fig. 4.13 Simulated Heat Pump power load

almost linearly with the increase of the finned tubes length with 13.2 W and 13.2 W during adsorption and 3.31 W during regeneration ($L_z = 5\text{ cm}$), reaching 85.7 W during adsorption and 21.5 W ($L_z = 30\text{ cm}$). For more details, see the appendix B.2 and figure B.4.

Finally, hereafter are reported the COP_{th} and the moisture removal effectiveness. The maximum COP_{th} is obtained with $L_z = 30\text{ cm}$ ($\text{COP}_{th} = 0.75$), then, as the length decreases, it linearly diminishes reaching the value of 0.65 for $L_z = 5\text{ cm}$. Moreover, the heating power reported in figure for $L_z = 5\text{ cm}$ is lower than that of the other lengths. Then, the other values are quite similar, in the range of 3.3-3.45 kWh with a decrement between the values corresponding to $L_z = 30\text{ cm}$ and $L_z = 5\text{ cm}$ of 10.6%. Considering the cooling energy (figure 4.12), instead, it is maximum for $L_z = 30\text{ cm}$ with a value of 2.48 kWh, and it diminishes to 1.92 kWh when $L_z = 5\text{ cm}$. So, since the diminishing of cooling energy is greater than the heating energy supplied by water as the length decreases, the COP_{th} raises with the length.

Regarding the moisture removal, is it possible to notice (figure 4.15) that the average value of moisture removal raises as the length increases. In particular, between $L_z = 5\text{ cm}$ to $L_z = 10\text{ cm}$, the value significantly increases, passing from an average moisture removal of $1.91\text{ g}_v\text{kg}_a^{-1}$ to a value of $2.95\text{ g}_v\text{kg}_a^{-1}$ (54.4% higher)

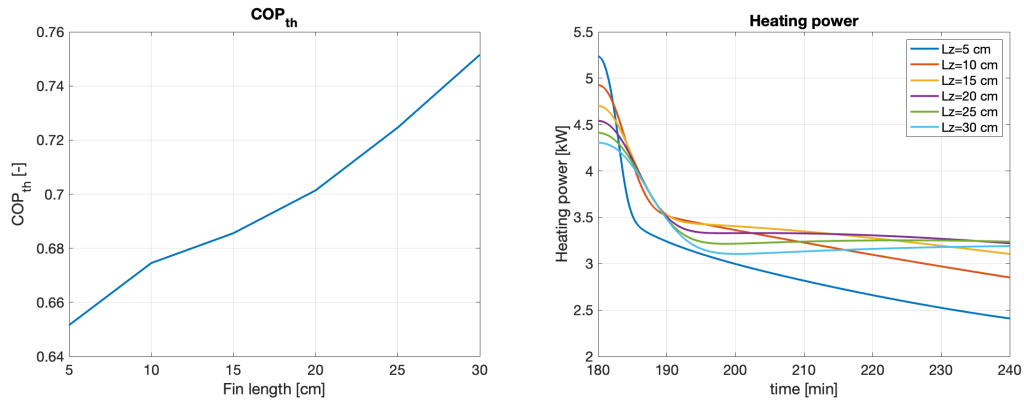


Fig. 4.14 Overall Thermal COP and Water Heating Power during Regeneration

with $L_z = 10\text{cm}$, then, it grows up to the maximum value, equal to $4.27\text{ kg}_v\text{kg}_a^{-1}$, when $L_z = 30\text{cm}$. This trend is, again, easily justified by the fact that as the length increases, the silica-gel quantity raises and so the capacity of the system of removing moisture from air grows.

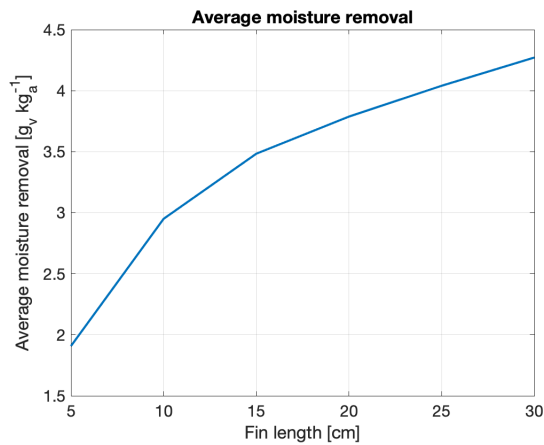


Fig. 4.15 Average moisture removal as a function of heat exchanger length

Influence of Regeneration Water Temperature

The second analyzed parameter is the regeneration water temperature, in the range $50\text{-}70^\circ\text{C}$ with fixed condition: air velocity $v_a = 0.8\text{ m/s}$ and cold water temperature $T_{w_c} = 20^\circ\text{C}$ and the heat exchanger length at 10 cm .

Again, the outlet air temperature, specific humidity and the silica gel average water uptake over time are depicted in the next Figure 4.16.

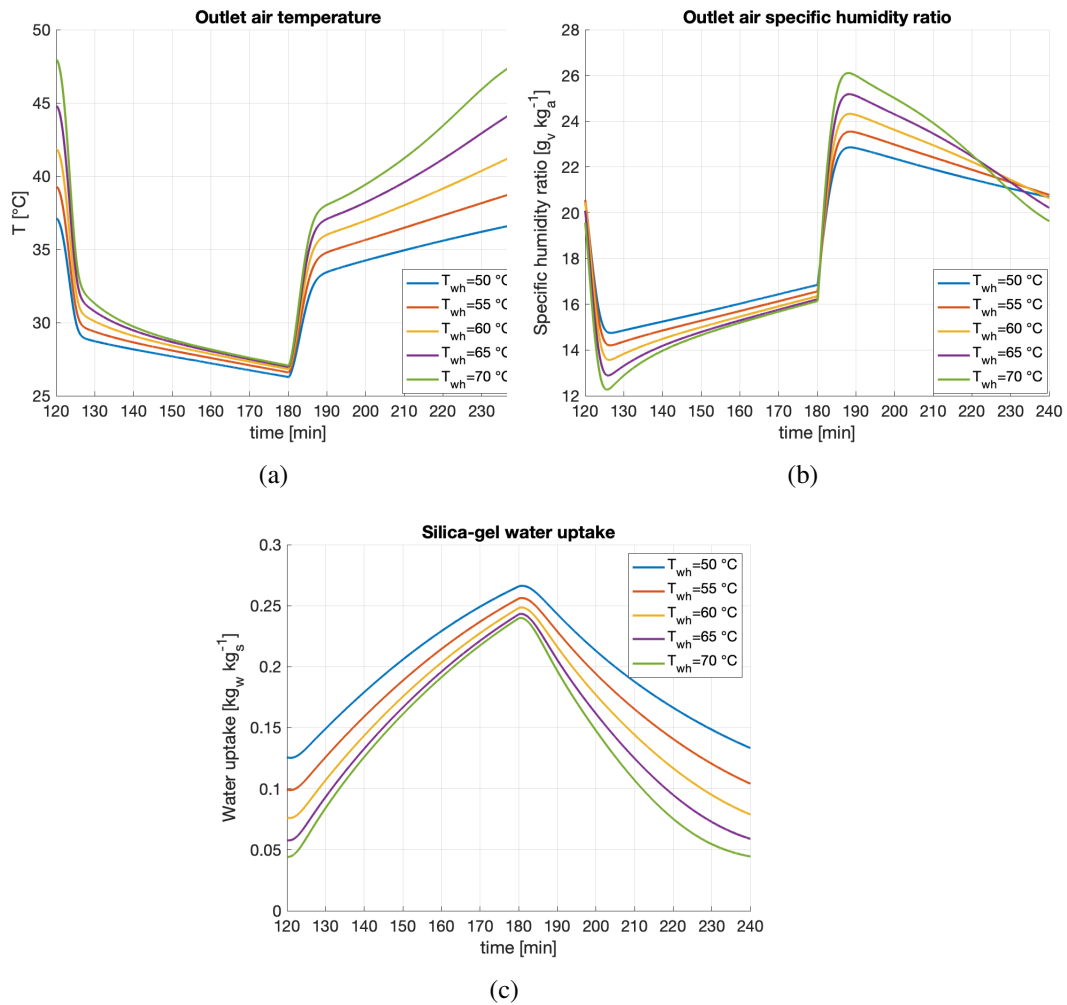


Fig. 4.16 (a) Temperature, (b) specific humidity of outlet air and (c) silica-gel water uptake for different regeneration water temperatures

The temperature of the exhaust air shows quite a large variation during regeneration, ranging from a value of 36.8 °C when T_{wh} is 50 °C to 47.9 °C when T_{wh} is equal to 70 °C, with an increase of 30.2 %. Looking instead at the average temperature, it increases by 19.4% from 34.5 °C and 41.2 °C. It is interesting to see that the average air temperature during adsorption is 29.2 °C for all the hot water temperatures used, which illustrates the small impact on the temperature trend of the adsorption cycle. However, if we look at the specific humidity of the exhaust air, we can see a difference in performance. Namely, as the hot water temperature increases, the

minimum specific humidity value achieved decreases. When T_{wh} is equal to 50°C , the minimum value of specific humidity is $14.8 \text{ g}_v\text{kg}_a^{-1}$, while at $T_{wh} = 70^{\circ}\text{C}$ it is $12.3 \text{ g}_v\text{kg}_a^{-1}$, which corresponds to a decrease of 16.9%. This can be explained by the fact that the amount of desorbed water vapour is higher at a higher regeneration temperature. The average water uptake at the end of regeneration when T_{wh} is set to 50°C is $0.13 \text{ kg}_w\text{kg}_s^{-1}$, while at $T_{wh} = 70^{\circ}\text{C}$ it corresponds to $0.04 \text{ kg}_w\text{kg}_s^{-1}$, which is more than 3 times lower. Moreover, at the end of the regeneration cycle, it can be observed that the specific humidity at the outlet is almost equal to the value at the inlet when the temperature of the hot water increases, which means that the silica gel is almost completely regenerated. A higher regeneration temperature therefore enables better and faster regeneration. However, for a longer regeneration period, lower temperatures are also suitable for almost complete regeneration of the silica gel.

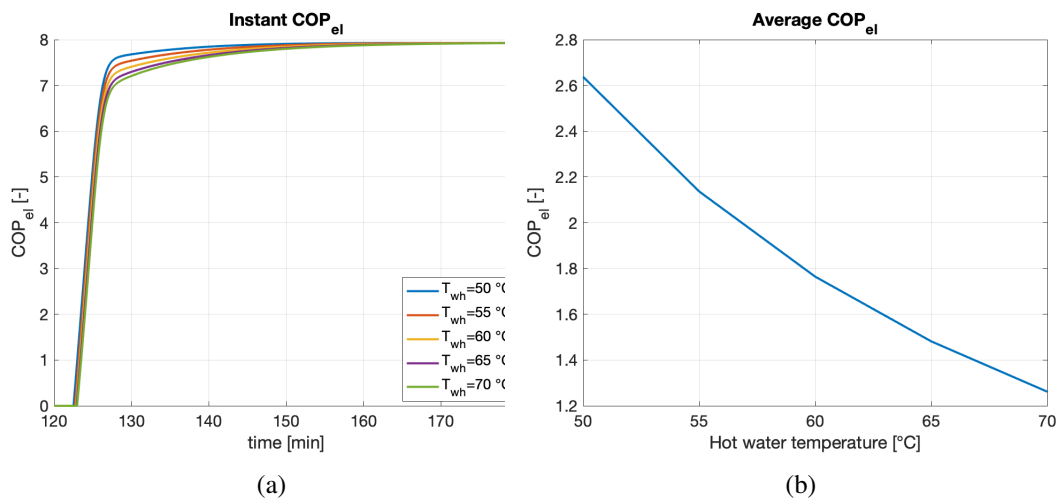


Fig. 4.17 Instant and average COP_{el} as a function of hot water temperature

Interesting to notice that, differently from the previous analysis, the instant COP_{el} is quite the same for all the hot water temperatures (Figure 4.17). This behaviour remarks the strict bound with the adsorption process, highlighting a weak influence of the regeneration temperature on the process (looking at instant values). Instead, the average COP_{el} , considers the entire cycle and it decrease as the hot water temperature grows, moving from 2.64 for $T_{wh} = 50^{\circ}\text{C}$ to 1.26 for $T_{wh} = 70^{\circ}\text{C}$ (-52.3%). This can be addressed analysing the output of all the contributions in terms of requested cooling/heating power, which are reported hereafter in Figure 4.18.

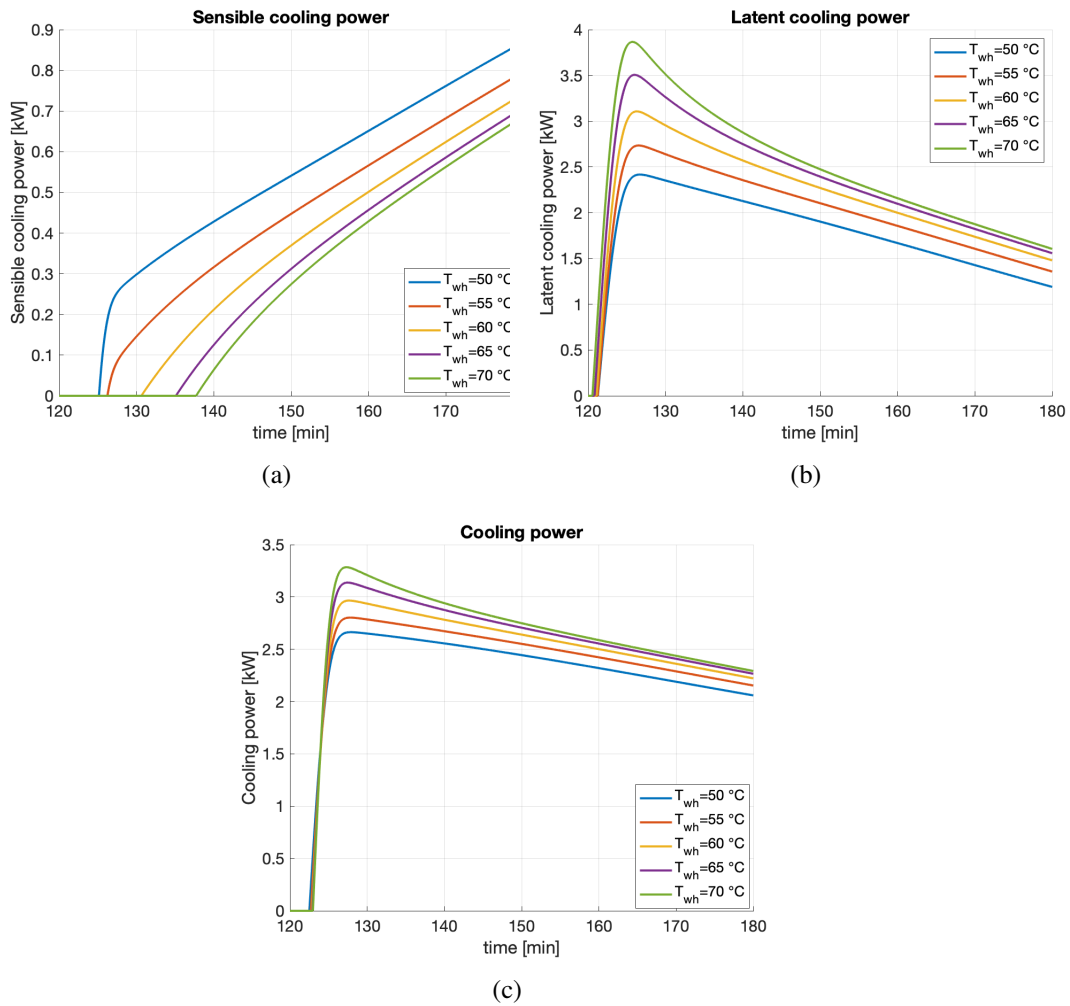


Fig. 4.18 (a) Sensible, (b) latent and (c) total cooling power as a function of the regeneration temperature variation

The total cooling power follows the trend of the latent one, since it is the main contributor. The trend are similar for all the regeneration temperatures analyzed, but with different slope. The maximum sensible cooling power decreases, raising the hot water temperature, from 0.87 kW to 0.69 kW. In particular, the difference between two consecutive hot water temperatures is higher between $T_{wh} = 50\text{ }^{\circ}\text{C}$ and $T_{wh} = 55\text{ }^{\circ}\text{C}$, with a maximum sensible cooling power decreasing by 8.6%. Another interesting point is the huge variation of the maximum latent cooling power which moves between 2.4 and 3.9 kW (+ 60%). The resulting total cooling power is higher as the hot water temperature raises, with a maximum value increasing from 2.66 kW to 3.29 kW between max and min regeneration temperature. In conclusion, a higher

latent cooling power is associated with higher regeneration temperatures, since the capacity of moisture removal increases. In parallel, the sensible cooling power has the opposite trend as the amount of adsorption heat to be removed is higher.

While the electric power required by the fan and the water pump do not change with different regeneration temperature and are equal to $\dot{W}_{el_{fan}}=8.87$ W, $\dot{W}_{el_{pump}}=26.4$ W during adsorption and $\dot{W}_{el_{pump}}=6.62$ W during regeneration the electric power required by the heat pump is reported in Figure 4.19. There is a big difference of heat pump electric power during regeneration as the hot water temperature rises: the maximum value for $T_{wh}=70$ °C is equal to 2.31 kW, while, for $T_{wh}=50$ °C, it correspond to 0.75 kW with a decrement of 67.5%. This is explained by the fact that, when the hot water temperature set point is higher, more heat power has to be supplied to the water in order to bring it and to maintain it at the fixed value. In conclusion, increasing the regeneration temperature means enhancing the cooling effect of the heat exchanger since a better desorption is performed. Nevertheless, this requires more electric power in order to run the heat pump. The contribution of the heat pump is the dominant one, since it significantly varies with hot water temperature, while, the cooling power changes to a lesser extent, so, the average COP_{el} will decrease as the hot water temperature grows.

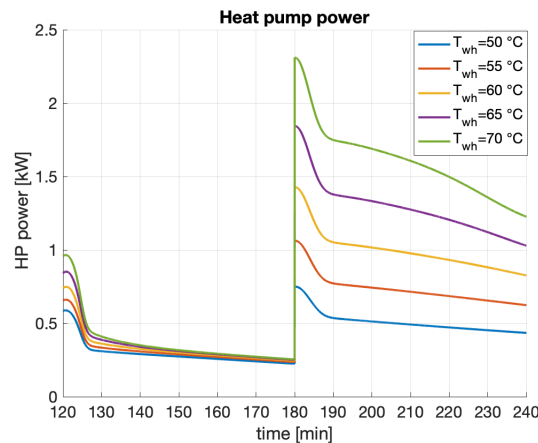


Fig. 4.19 Heat pump electric power load as a function of regeneration temperature

Finally, the resulting COP_{th} decreases as the hot water temperature raises, passing from 0.67 for $T_{wh}=50$ °C to 0.41 for $T_{wh}=70$ °C. The water side thermal power exchanged during regeneration reduces with time, as the regeneration process goes on, and significantly varies with the set point of hot water temperature. In fact, as the temperature level rises, the ΔT between water and air increase, favouring the

heat exchange. The correspondent heat supplied by water goes from 3.33 kWh for $T_{wh}=50\text{ }^{\circ}\text{C}$ to 6.21 kWh with $T_{wh}=70\text{ }^{\circ}\text{C}$ (increment of 86.3%). Since the cooling power does not considerably change with hot water temperature as the heating power does, the heating power has a strong impact on the final COP_{th} shape.

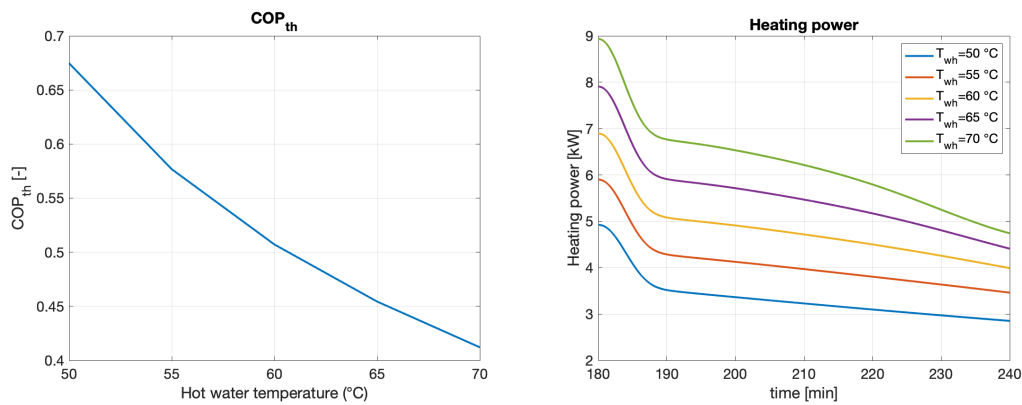


Fig. 4.20 Overall Thermal COP and Water Heating Power during Regeneration with different the regeneration temperature

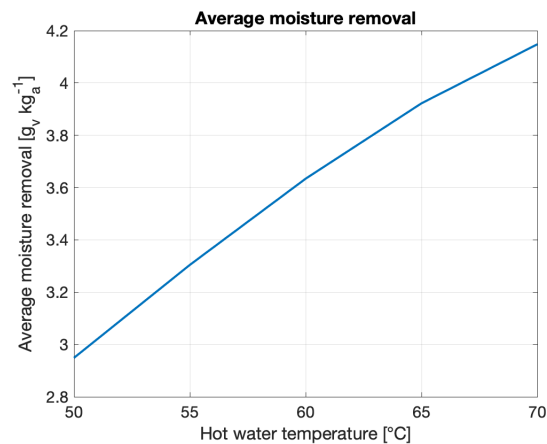


Fig. 4.21 Average moisture removal as a function of regeneration water temperature

Looking at the resulting moisture removal effectiveness (Figure 4.21) it is possible to notice a different behaviour with respect to the other two performance coefficient. In fact, the moisture removal effectiveness increases with higher hot water temperatures because, as already highlighted, the outlet specific humidity presents the minimum value in the case in which the water temperature is equal to $70\text{ }^{\circ}\text{C}$. So, the average moisture removed from air grows in parallel with the hot water

temperature, increasing from $2.95 \text{ g}_v\text{kg}_a^{-1}$ to $4.15 \text{ g}_v\text{kg}_a^{-1}$ between 50°C and 70°C , corresponding to an increment of 40.7%.

Influence of Adsorption Water Temperature

In this section, the performance coefficients are calculated varying the adsorption cold water temperature between 15°C to 25°C (fixing the average v_a at 0.8 m/s , T_{wh} at 50°C and the heat exchanger length at 100 mm .)

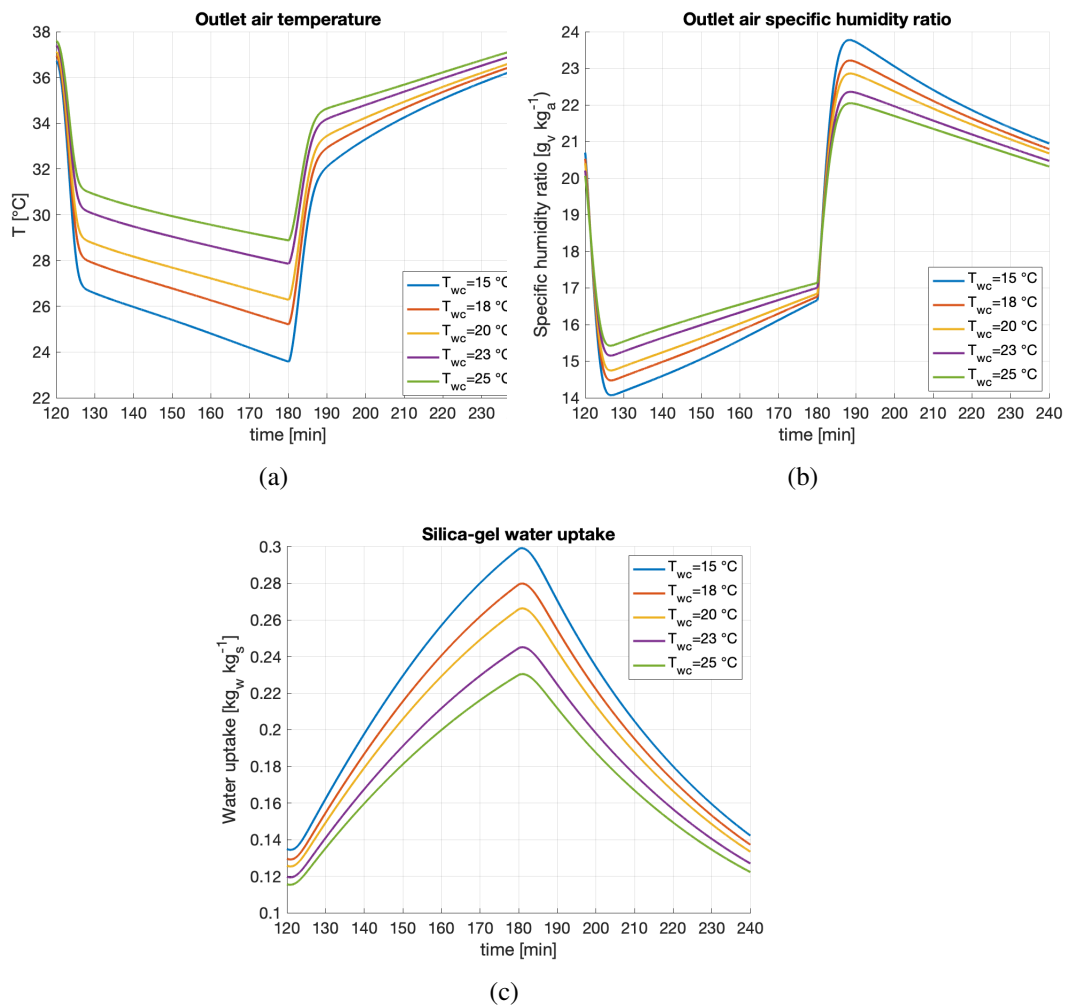


Fig. 4.22 Temperature, specific humidity of outlet air and silica-gel water uptake for different cold water temperatures

In general, the lower is the cold water temperature, the higher are the heat and, consequently, the moisture removed from air. In fact, (see Figure 4.22) the outlet

air temperature at the end of adsorption is equal to 28.9 °C when $T_{w_c}=25$ °C and reduces until 23.6 °C for $T_{w_c}=15$ °C. Afterwards, during regeneration, even if the starting temperatures of air are very different, they converge towards a common value correspondent to around 36.5 °C. Considering the outlet air specific humidity, it diminishes as the temperature lowers, but then converges to the same point ($16.8 \text{ g}_v\text{kg}_a^{-1}$). During regeneration, instead, the maximum value corresponds to the minimum cold water temperature ($23.8 \text{ g}_v\text{kg}_a^{-1}$), while, the lowest outlet air specific humidity peak is obtained with $T_{w_c}=25$ °C ($22.1 \text{ g}_v\text{kg}_a^{-1}$), with a reduction of 11.3%. Finally, the moisture removed from air is higher as the temperature decrease: the silica-gel water uptake almost reaches saturation ($0.30 \text{ kg}_w\text{kg}_s^{-1}$) for the coldest water temperature and decreases down to $0.23 \text{ kg}_w\text{kg}_s^{-1}$ when $T_{w_c}=25$ °C.

The instant COP_{el} significantly changes moving through the analyzed temperatures. Le lower the temperature the lower is the COP_{el} and, specifically, its maximum value for the $T_{w_c}=15$ °C is equal to 6.27, while, for $T_{w_c}=25$ °C reaches 10.2. Looking instead at COP average value of it is possible to notice a stable behaviour till 20°C an then rapidly diminishes as temperature rise.

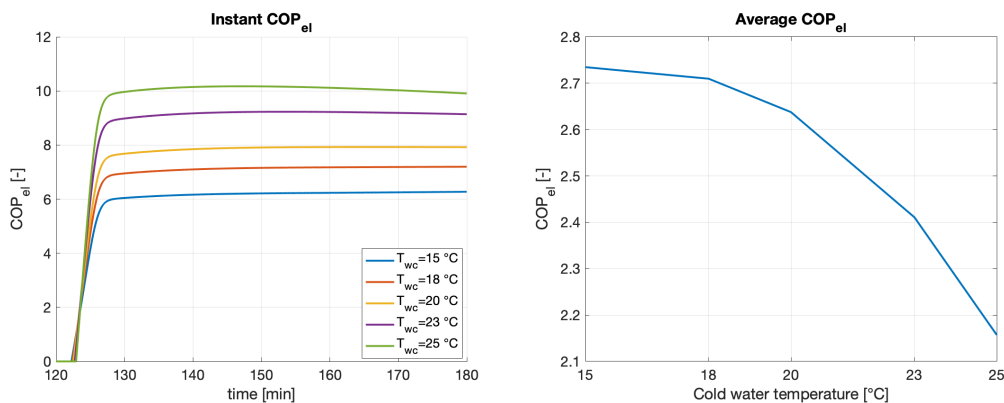


Fig. 4.23 Instant and average COP_{el} for different cold water temperatures

In Figure 4.24, sensible, latent and total cooling power are shown. The cooling power significantly changes as the cold water temperature varies especially for the sensible load (sub-figure (a)). Considering the latent cooling power obtained from each temperature, it almost converges, at the end of adsorption, to a value in the range of 1-1.3 kW. What is changing is the peak value where at $T_{w_c}=15$ °C the maximum latent cooling power is equal to 2.83 kW, while, for $T_{w_c}=25$ °C it corresponds to 2.00 kW (29.3% lower). The resulting total cooling power follows the trend of the latent

cooling power, since it represents the major contribution. In particular, at $T_{wc}=15\text{ }^{\circ}\text{C}$, the peak value reached is equal to 3.58 kW and the cooling energy obtained is equal to 3.07 kWh, while, for $T_{wc}=25\text{ }^{\circ}\text{C}$ they are respectively equal to 1.74 kW and 1.41 kWh.

Considering now the electric power contributions, again the fan and the water pumps represent a marginal values (similar to the previous case) with respect to the HP contribution reported in Figure .

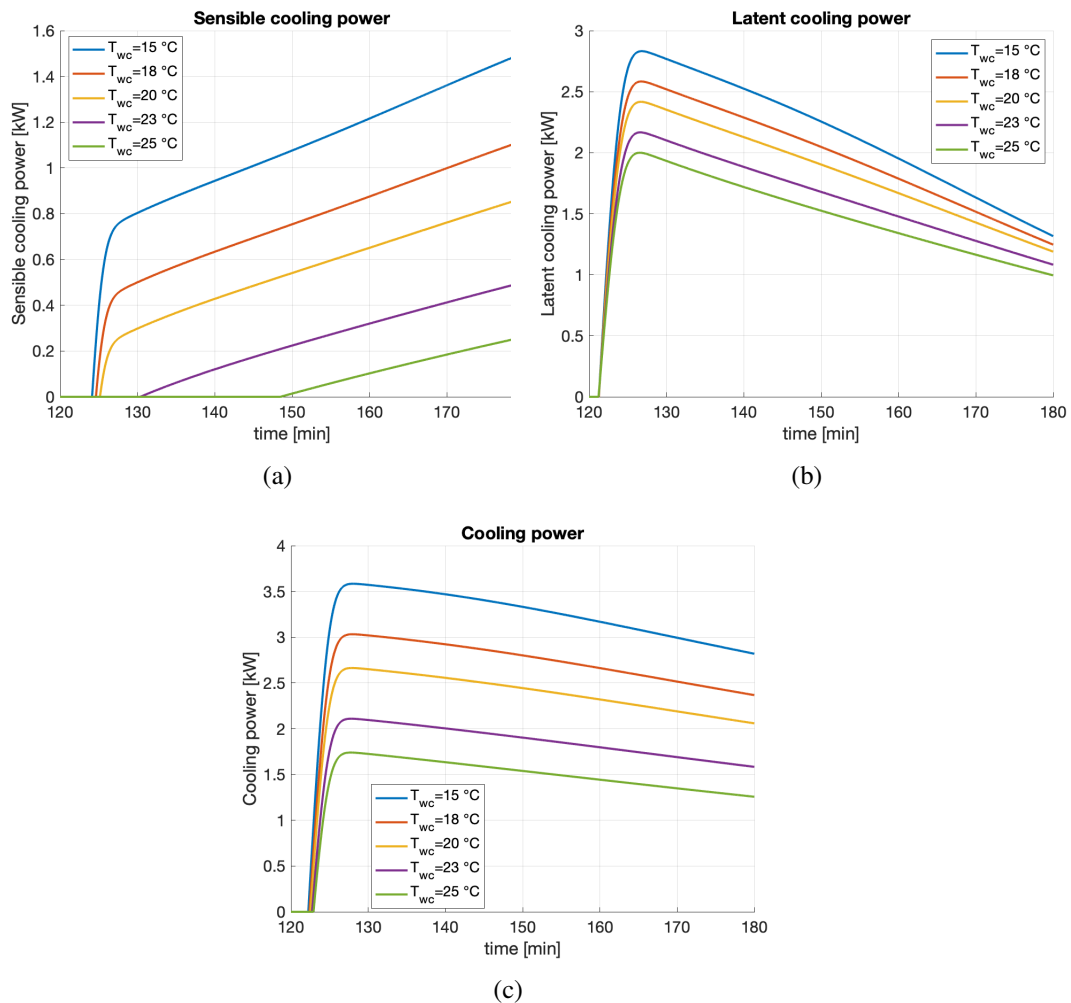


Fig. 4.24 Sensible, latent and total cooling power for different adsorption water temperatures

Again, the higher value of HP adsorption at the beginning of the cycle is due to the temperature transition between regeneration and adsorption. The power required when the cold water temperature is lower, is generally higher and, in fact, it reaches 1.01 kW when $T_{wc}=15\text{ }^{\circ}\text{C}$ and reduces to 0.28 kW for $T_{wc}=25\text{ }^{\circ}\text{C}$, with a decrement

of 72.3%. In energy terms, with a total cycle of 2 h, the electric energy required by the heat pump corresponds to 1.07 kWh in the case $T_{wc}=15\text{ }^{\circ}\text{C}$ and to 604 Wh when $T_{wc}=25\text{ }^{\circ}\text{C}$ marking a strong reduction. During regeneration instead, the values of the electric power are almost coincident.

From these results the instant COP_{el} trend is explained by the fact that, even if the cooling power for lower cold water temperatures rises, also the electric power required by the heat pump is much higher for lower temperatures. The average COP_{el} , instead, considers the entire cycle (adsorption and regeneration), integrating all the power contribution over time, so, the resultant value is higher as the cold water temperature diminishes.

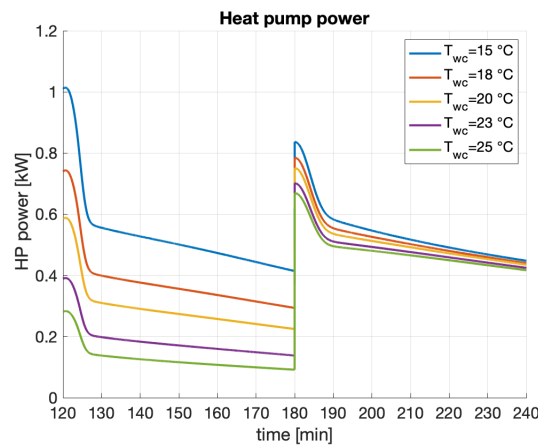


Fig. 4.25 Heat pump electric power consumption for different adsorption water temperatures

Finally, in figure 4.26, are reported the COP_{th} , the water heating power and the moisture removal trend. The thermal COP almost linearly moves as the cold water temperature raises, passing from 0.87 to 0.45, decreasing by 48.3%. Then, it can be observed that the water heating power is higher in the case of the cold water temperature equal to $15\text{ }^{\circ}\text{C}$ with a maximum value correspondent to 5.49 kW. but, generally, the curves for the different temperatures, as time passes tend to converge towards a common value. Therefore, both cooling and heating power are higher for lower cold water temperatures, but, the cooling power contribution is dominant, so, the resulting thermal COP, increases as the cold water temperature diminishes. At last, the average moisture removed from air. It decreases as the cold water temperature increases, ranging between $3.43\text{ g}_v\text{kg}_a^{-1}$ for $T_{wc}=15\text{ }^{\circ}\text{C}$ and $2.42\text{ g}_v\text{kg}_a^{-1}$ for $T_{wc}=25\text{ }^{\circ}\text{C}$ and this can be explained by the fact that with a colder water temperature, both the mass and heat transfer mechanism are enhanced.

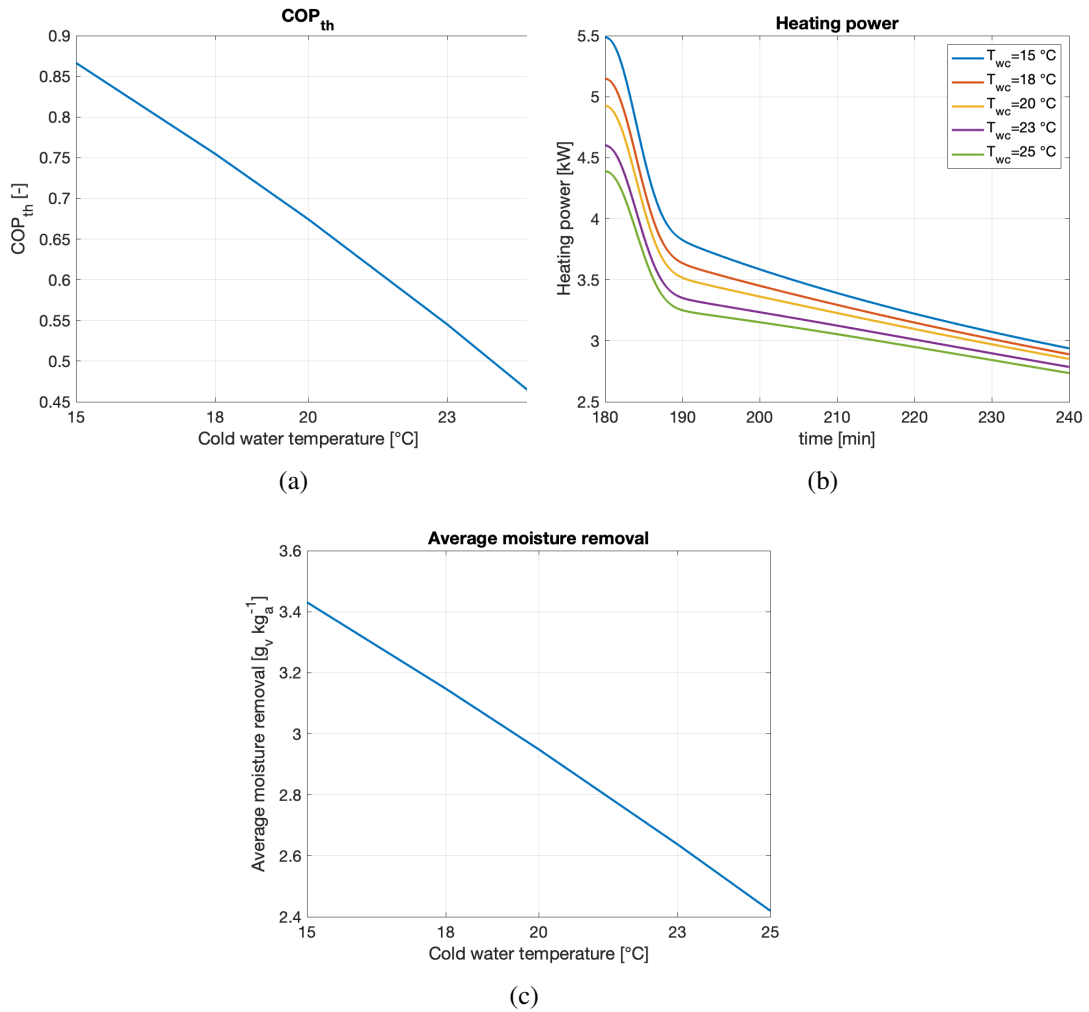


Fig. 4.26 (a) Thermal COP, (b) Water Heating Power and (c) Average moisture removal for different adsorption temperature

Air Stream Velocity

In this last step of the parametric analysis, the simulations are carried out modifying the air stream velocity fixing T_{w_c} at 20 °C, T_{w_h} at 50 °C and a heat exchanger length equal to 100 mm. As usual, in the following figure 4.27, the outlet air temperature, specific humidity and the silica-gel water uptake over time are reported.

First of all, it is noticeable that during adsorption at lower velocity values, the airflow initially has a higher temperature (due to the higher temperatures reached during regeneration), but this then decreases rapidly, with the lowest value corresponding to a velocity of 0.2 m s^{-1} . Moreover, the result at the lowest velocity v_a

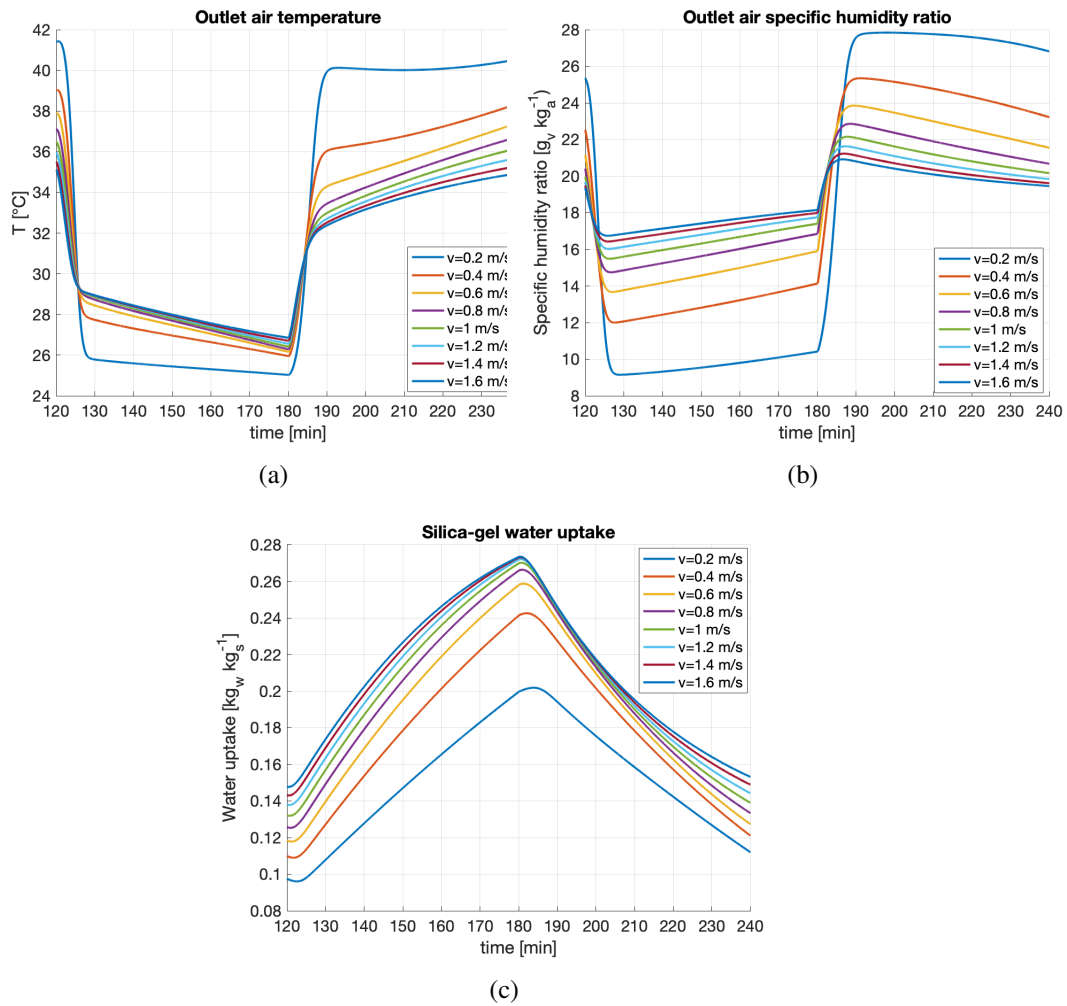


Fig. 4.27 (a) Temperature, (b) specific humidity ratio of outlet air and (c) silica-gel water uptake as a function of air velocity

differs significantly from the other velocities tested. In fact, the average air outlet temperature increases by 4.05% during adsorption when v_a increases from 0.2 ms^{-1} to 0.4 ms^{-1} , while it increases by only 1.15% between $v_a=0.4 \text{ ms}^{-1}$ and $v_a=0.6 \text{ ms}^{-1}$. The same behaviour occurs throughout the regeneration, with the average temperature of the outlet air at $v_a=0.2 \text{ ms}^{-1}$ being much higher than the others (38.8 $^{\circ}\text{C}$ for $v_a=0.2 \text{ ms}^{-1}$ and 33.3 $^{\circ}\text{C}$ for $v_a=1.6 \text{ ms}^{-1}$). The same large jump over 0.2 to 0.4 ms^{-1} is obtained for the specific humidity ratio and water absorption. For the former, the minimum value ($9.16 \text{ g}_v \text{kg}_a^{-1}$) is reached at the lowest air velocity, while for $v_a=1.6 \text{ ms}^{-1}$ it is $16.7 \text{ g}_v \text{kg}_a^{-1}$, an increase of 82.3%. This is because a higher air velocity is associated with a greater air flow rate, i.e. more air enters the

heat exchanger, so a greater amount of water vapour must be removed. This is also confirmed when looking at the results of the water absorption of the silica gel: It is higher when the air velocity increases, because even when the specific humidity at the outlet is higher, the amount of water absorbed is greater than at lower air velocities. The maximum average water absorption for $v_a=0.2 \text{ ms}^{-1}$ is $0.20 \text{ kg}_w\text{kg}_s^{-1}$ and increases to $0.27 \text{ kg}_w\text{kg}_s^{-1}$ at $v_a=1.6 \text{ ms}^{-1}$.

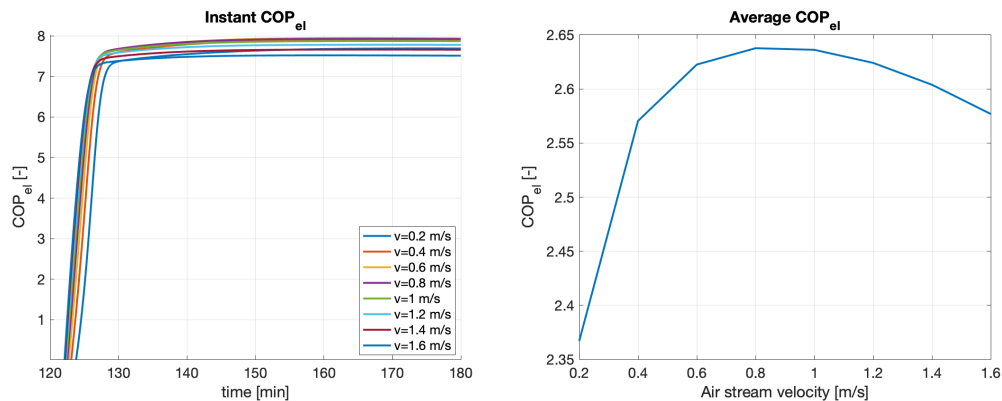


Fig. 4.28 Instant and average COP_{el} as a function of air velocity

While the COP_{el} is similar for all the analyzed velocities, the average COP present an interesting behaviour. It rapidly increases passing from 0.2 ms^{-1} (equal to 2.37) to 0.4 ms^{-1} (correspondent to 2.57). Then, it continues to raise until a maximum value of for $v_a=0.8 \text{ ms}^{-1}$. Afterwards it start to slowly decreases until 2.58 for $v_a=1.6 \text{ ms}^{-1}$. In order to understand these trends, the single cooling load contributions are assessed in figure 4.29 while the electric consumption are reported in figure 4.30.

The sensible cooling power present a divergent behaviour as the air velocity increase. In fact, it reached 0.29 kW for $v_a=0.2 \text{ ms}^{-1}$ and 1.47 kW for $v_a=1.6 \text{ ms}^{-1}$ (about 5 times higher). This huge difference is due to the fact that, even if the difference in temperature (and so the sensible enthalpy) between inlet and outlet air rises as the velocity diminishes, the sensible cooling power is much lower because the air flow rate strongly reduces. Also the latent share considerably varies between $0.2 - 0.6 \text{ ms}^{-1}$, then, it present shorter variation for velocities till the 1.6 ms^{-1} . The maximum values correspondent to $v_a=0.2 \text{ ms}^{-1}$, $v_a=0.4 \text{ ms}^{-1}$ and $v_a=0.6 \text{ ms}^{-1}$ are respectively equal to 1.44 kW, 2.03 kW (50.0% higher) and 2.29 kW (12.8% greater than the value with $v_a=0.4 \text{ ms}^{-1}$). Moreover, it can be observed that the curves

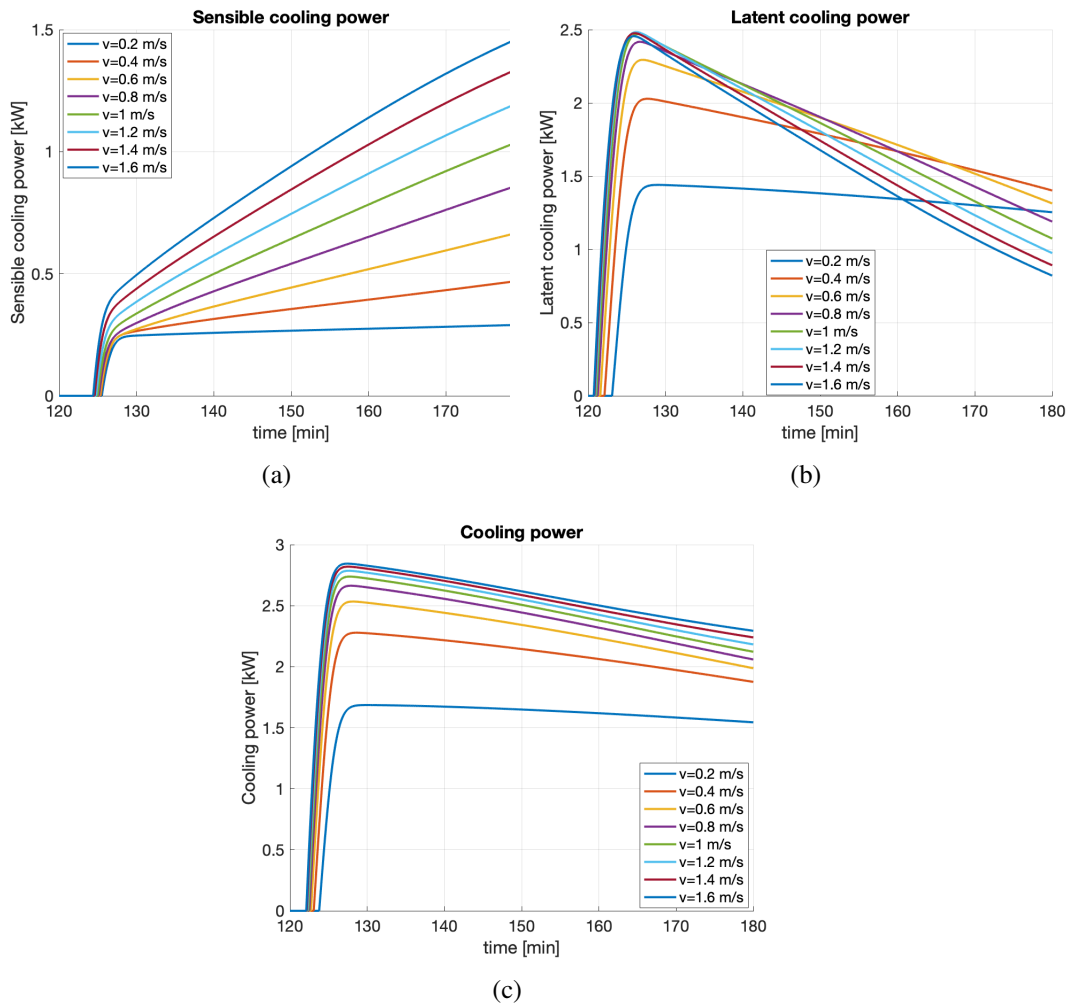


Fig. 4.29 (a) Sensible, (b) latent and (c) total cooling power as a function of air velocity

relative to $v_a=0.2 \text{ ms}^{-1}$ and $v_a=0.4 \text{ ms}^{-1}$, are above the others starting from a certain time and this can be explained by the fact that for low air velocities the outlet air humidity ratio is far from the inlet value, meaning silica-gel is not close to saturation, so, it still has a good capacity in terms of moisture removal. The total cooling power increases as the air velocity grows. For $v_a=0.2 \text{ ms}^{-1}$ the maximum value coincides with 1.69 kW, which is 40.7% lower than that obtained with $v_a=1.6 \text{ ms}^{-1}$.

Considering now the electricity consumption, the water pump electric power is constant and do not provide major variation both during adsorption and regeneration. Instead, the trends of electric power required by the fan and the heat pump present wider differences among the tested velocities.

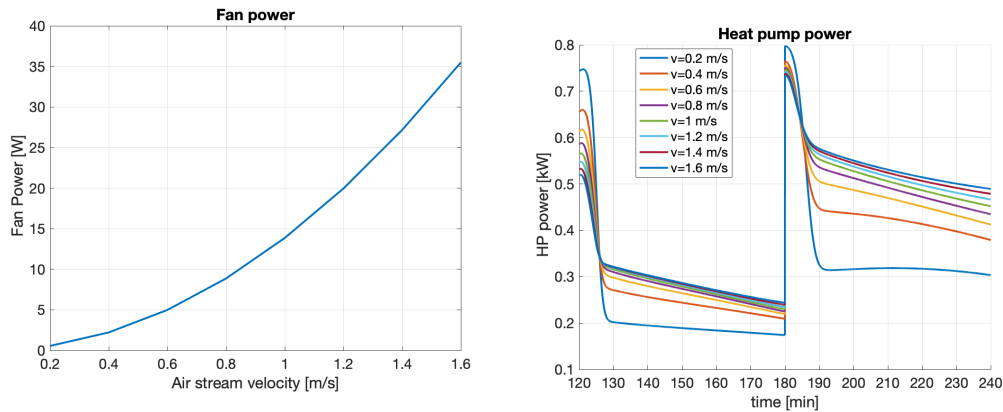


Fig. 4.30 (a) Fan and (b) heat pump electric power for different air stream velocities

The electric power required by the fan plays an important role in this analysis. It increases as the air velocity (and, consequently, the air flow rate) raises, moving from 0.55 W, when $v_a=0.2 \text{ ms}^{-1}$, to 35.5 W with $v_a=1.6 \text{ ms}^{-1}$. The heat pump electric power, instead, is higher at the beginning of both adsorption and regeneration as air velocity lowers, afterwards, it rapidly decreases. The peak values during adsorption are equal to 0.75 kW for $v_a=0.2 \text{ ms}^{-1}$ and to 0.52 kW for $v_a=1.6 \text{ ms}^{-1}$, while, during regeneration, the maximum value is achieved with $v_a=0.2 \text{ ms}^{-1}$ (0.80 kW). It can be noticed that, again, the curve correspondent to $v_a=0.2 \text{ ms}^{-1}$ shows the greatest discrepancy with respect to the others. In fact, the electric heat pump energy required when the minimum velocity is set, for the entire cycle (adsorption and regeneration) is equal to 598 Wh, increasing to 724 Wh for $v_a=0.4 \text{ ms}^{-1}$ and, then, growing until a value of 845 Wh when $v_a=1.6 \text{ ms}^{-1}$. In conclusion, the average COP_{el} increases with air velocity because the cooling power contribution prevails. The flattening of the curve is due to the fact that for air velocity over 0.6 ms^{-1} the trends of all the contributions are quite similar. The fan power is the only term that varies considerably as the air velocity grows (even its absolute value is almost negligible with respect to the other).

At last, Figure 4.31 reports the last performance parameters to be analyzed. At first, the thermal COP: it grows as the air velocity increases, starting from a value of 0.63 for $v_a=0.2 \text{ ms}^{-1}$ and reaching a value of 0.68 when $v_a=1.6 \text{ ms}^{-1}$. Overall, it is not a great modification, but still it represents a +7.9% of increment. In particular, the major value modification is highlighted between 0.2 ms^{-1} and 0.4 ms^{-1} . Then, the thermal power during regeneration (b) is higher for lower air velocities at the

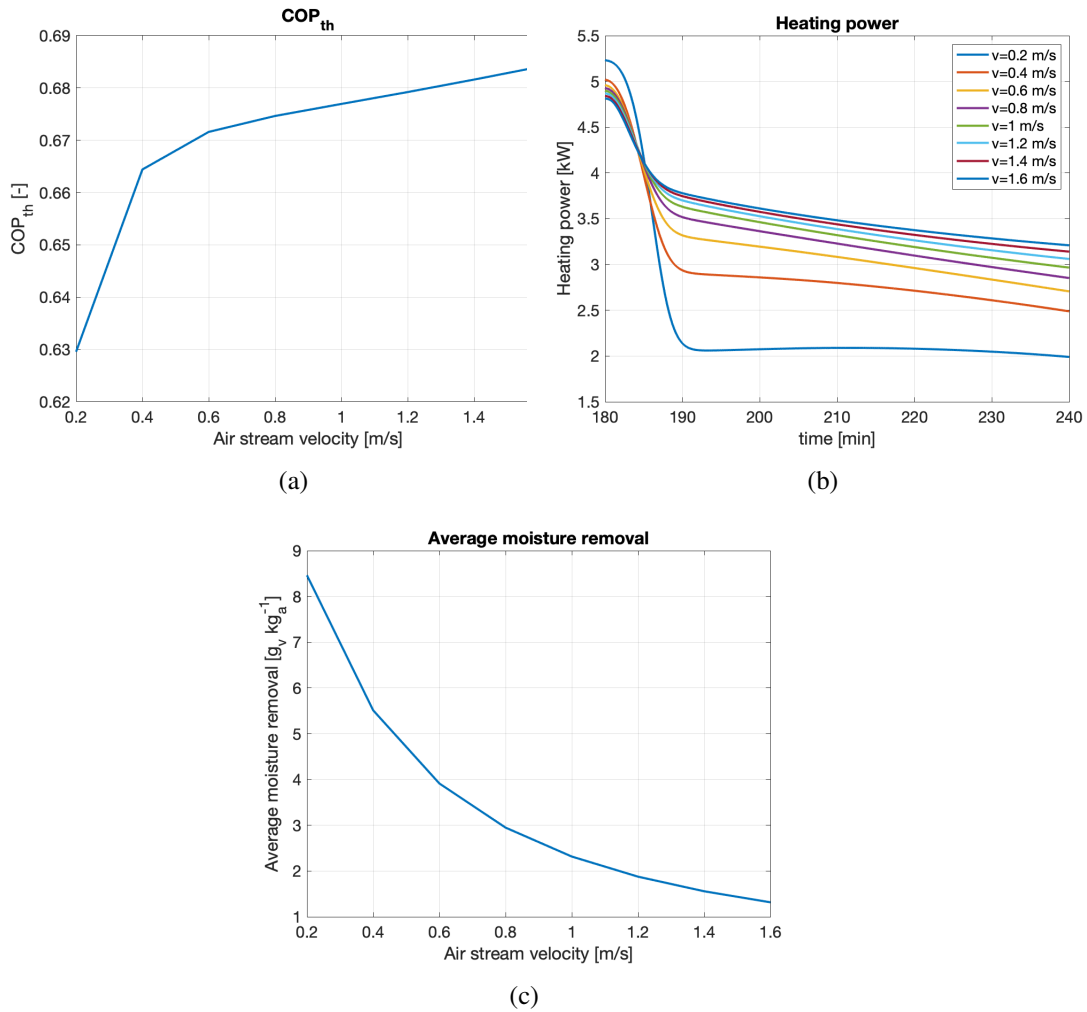


Fig. 4.31 (a) Thermal COP, (b) Water Heating Power and (c) Moisture removal effectiveness for different air stream velocity

beginning of regeneration, but after 5 minutes, this trend is reverted, with lower values correspondent to lower air velocities. Again, the curve obtained from $v_a=0.2 \text{ ms}^{-1}$ presents a significant discrepancy with respect to the others. Therefore, the trend of the thermal COP is explained by the fact that, even if both cooling energy and water heat raise with air velocity, the value of cooling energy grows faster than that of the exchanged water heat.

Finally, (c) the average moisture removal presents a descending trend as the air velocity increases, with a value equal to $8.46 \text{ g}_v \text{ kg}_a^{-1}$ when $v_a=0.2 \text{ ms}^{-1}$, that reduces until $1.32 \text{ g}_v \text{ kg}_a^{-1}$ for $v_a=1.6 \text{ ms}^{-1}$ marking a - 84%. This results can be explained by the fact that the maximum difference between inlet and outlet specific humidity

ratio occurs for the lowest air velocity, because the quantity of air crossing the heat exchanger is smaller, so more moisture can be removed.

COP comparison

Based on these parametric analyses it is possible to depict a rough idea of the overall HySun potential performance with respect to market ready HP technologies. The following histogram in figure 4.32 shows the distribution of nominal COP value for around 1450 HPs of different size (between 2.6kW and 88 kW of Cooling Power) and technology (Air/Water, Water/Water, Brine/Water). The technical data of HP was retrieved from the GitHub repository [137], which takes the data from a number of HP technical data sheets available in [138]. The available data contains various information such as the manufacturer, the HP model, the COP and the respective test conditions. In the table 4.5, for example, you will find a selection of the available data. The complete database can be found at [137].

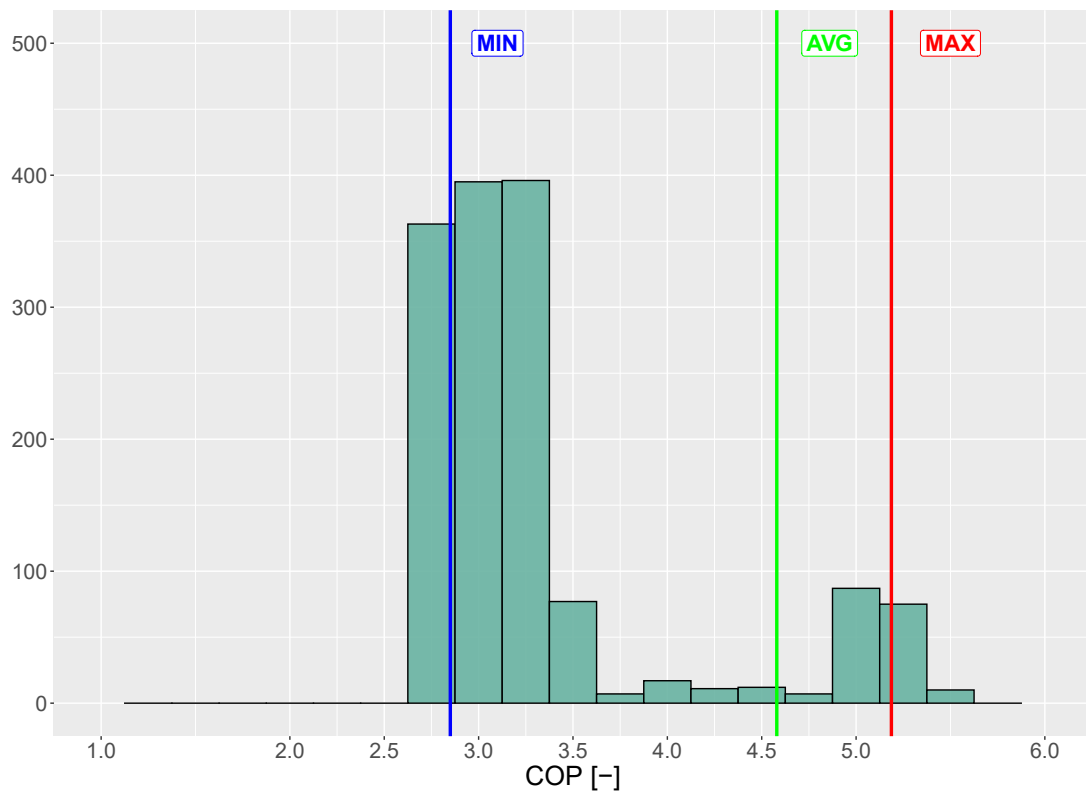


Fig. 4.32 HySun COP comparison with respect to different market ready HP technologies.

Together with the histogram distribution, the maximum (red), minimum (blue) and average (green) of the expected HySun COP have been reported. The calculation of the estimate is based on the equation 4.102, which is referred to the configuration with only one heat exchanger. Therefore, the values calculated with this formula have to be multiplied by a factor to get a value for the machine with two batteries. Theoretically, one expects twice the efficiency with two batteries and thus the COP doubles. Of course, this is a theoretical value, because the increased consumption of fans and water circulation pumps must also be taken into account. From the data of the developed parametric simulations, it was estimated that their share varies between a minimum of 2-3% to a maximum of 23%, with an average value of about 10%. Consequently, the values shown in the graph are the maximum, minimum and average COP, retrieved from the single HX parametric analyses, multiplied by a factor of 1.9 to obtain the expected maximum, minimum and average HySun COP values. It can be seen that the potential COP of the developed prototype is promising. In the worst case scenario (obtained with regeneration temperature set to 65°C), the COP is within the range of most of the heat pumps examined, indicating that, even under unfavourable conditions (high), HySun remains competitive against the market ready machines analysed. On the other hand, the maximum and average COPs are on the right side of the graph, in the high efficiency area, together with a few heat pumps. Furthermore, looking at figure B.5, where the HPs cold power output has been limited to 5 kW, it is possible to see that the two values are in an area where no other machines are present (within the analysed database).

Finally, it is important to remember that the COP values analysed are derived from preliminary simulations and related to the parametric analysis conducted. As soon as the data from the field tests are available, this analysis will be carried out again to compare the quality of the simulations and correct any positive or negative deviations.

4.5 Dynamic Simulation for Turin City

Since the HySun prototype is going to be installed in Turin city and tested there, in this section a dynamic simulations are carried out in order to forecast the system performance in its real operating environment. The simulations have been accomplished for a summer day characterized by high temperatures using typical meteorological

Table 4.5 Heat Pump Technical Data. An Example of available observation from [137].

Manufacturer	Model	Date	Type	Refrigerant	Tot. Refrigerant Mass [kg]	Design Power [kW]	T External [°C]	T out [°C]	COP [-]
Advantix S.p.A.	i-32V506	26/05/2020	Outdoor Air/Water	R32	1.5	5.02	35	7	3.14
Advantix S.p.A.	i-SHWAK V4 06	26/05/2020	Outdoor Air/Water	R410A	2.68	5.07	35	7	2.91
Ariston Thermo Group	ENERGION M PLUS 120T	05/07/2022	Outdoor Air/Water	R32	2.1	9.05	35	7	3.15
August Brötje GmbH	AWHPR 4 MR + BLWSI48MHD	03/12/2021	Outdoor Air/Water	R32	1.2	4.5	35	7	3.6
August Brötje GmbH	AWHPR 4 MR + BLWSI48OHD	03/12/2021	Outdoor Air/Water	R32	1.2	6	35	18	5.35
BAXI Climatización S.L.U	AWHPR 4 MR + iMPI/E 4-8 iR32	03/12/2021	Outdoor Air/Water	R32	1.2	4.5	35	7	3.6
BAXI Climatización S.L.U	AWHPR 6 MR + iMPI/E V200 4-8 R32	12/11/2021	Outdoor Air/Water	R32	1.2	7	35	18	4.88
DAIKIN Europe N.V.	ERGA08EV / ESHB08P50D3	17/08/2018	Outdoor Air/Water	R32	1.5	5.4	35	7	3.14
DAIKIN Europe N.V.	EWSAX06DA9W	14/02/2022	Water/Water	R32	1.7	5.81	35	7	4.21
DAIKIN Europe N.V.	EWSAH06UDA9W	14/02/2022	Water/Water	R32	1.7	5.81	35	7	4.21
DE DIETRICH	AWHPR 6 MR + MIV-S 4-8/EM R32	03/12/2021	Outdoor Air/Water	R32	1.2	6.5	35	7	3.09
Johnson Controls-Hitachi AirConditioning Spain	04. RAS-3WHVRP RWD-3.0NRWE-200S-K	08/08/2019	Outdoor Air/Water	R32	1.3	7	35	18	5
OERTLI	AWHPR 8 MR + MHC/EM 4-8 R32	03/12/2021	Outdoor Air/Water	R32	1.2	7.1	35	18	4.88
Panasonic Marketing Europe GmbH	WH-ADC0309J3E5B / WH-UD09JE5	08/01/2020	Outdoor Air/Water	R32	1.27	7	35	7	2.95
Panasonic Marketing Europe GmbH	WH-ADC0309J3E5C / WH-UD09JE5-1	08/01/2020	Outdoor Air/Water	R32	1.27	7	35	7	2.95
Viessmann	AWO-AC (AF) 101.A16	25/06/2020	Outdoor Air/Water	R32	4	13.8	35	7	3.15
Viessmann	AWO-AC (AF) 101.A14	25/06/2020	Outdoor Air/Water	R32	3.6	11.48	35	7	3.25

data. Afterwards, the influence of different switching times and air flow rates is assessed, with the purpose of understanding which is the best operating point in such external conditions. It has been decided to test this two parameters because they are two of the main controlled variables.

4.5.1 Input Parameters

As already said, the selected location is the city of Turin. In order to run the dynamic simulation, variable meteorological data from [6] are used as input for the simulations. Of course, the data of our interest are the air temperature and the relative humidity. The climate files utilized collect, for each day of the year, average values derived from the years going from 2004 to 2018. To perform the simulation, the worst case scenario has been adopted, in terms of ambient temperature. Moreover, only the central hours of the day are considered (11.00 a.m. to 9.00 p.m), meaning the ones during which the ambient temperature overcomes 28 °C. The correspondent data are reported in the following table. It can be noticed that, during the time period considered of the day chosen, the ambient air which will enter the system, varies from 30 °C to 32 °C, while the relative humidity changes between 0.31 and 0.47.

Since the ones reported are hourly data, it is assumed that, during each hour, the values are constant.

Hour of the day	T_{amb} (°C)	RH (%)
11:00	30	38
12:00	31	36
13:00	30.8	42
14:00	32	31
15:00	32	34
16:00	32	36
17:00	32	36
18:00	31	40
19:00	31.7	47
20:00	30	35

Table 4.6 External Input Conditions

Running the numerical model of the heat exchanger, these values are set, for each time step, as boundary and initial conditions for the inlet air stream. The switching time, between adsorption and regeneration, is set at 30 minutes, meaning a complete cycle lasts 1 hour. This parameter will be then studied more deeply in section 4.5.3. The configuration of the heat exchanger and the silica gel properties and conditions are the ones reported in the previous chapter, in Table 4.3, setting the length of the heat exchanger equal to 200 mm. The air and water flow conditions are, instead, reported hereafter:

Air and water flow conditions	
Average air velocity v_a	0.8 ms^{-1}
Adsorption water mass flow rate $\dot{m}_{w_{ads}}$	0.08 kgs^{-1}
Regeneration water mass flow rate $\dot{m}_{w_{ads}}$	0.05 kgs^{-1}
Cold inlet water temperature T_{w_c}	$15 \text{ }^\circ\text{C}$
Hot inlet water temperature T_{w_h}	$50 \text{ }^\circ\text{C}$

Table 4.7 Air and water flow conditions

4.5.2 Results

As already done for the parametric analysis, the main variables to be observed are the outlet air temperature, specific humidity ratio and silica-gel water uptake (see figure 4.33). It can be noticed how the trend, for all the three parameters, during the first minutes of each adsorption cycle is different: this is the result of the initial conditions setting. Afterwards, the behaviour is always similar for each cycle, with variations of the maximum and minimum values.

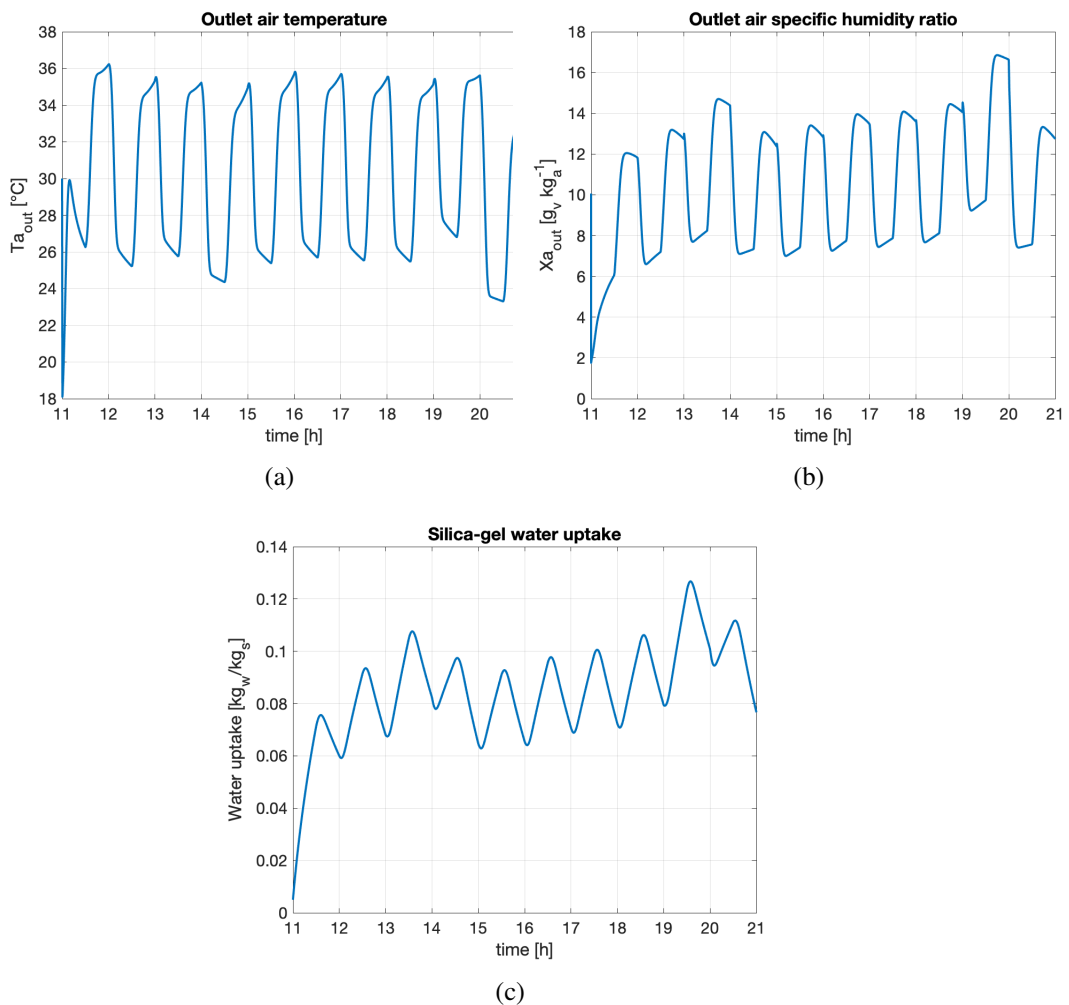


Fig. 4.33 Temperature (a), specific humidity ratio (b) of outlet air and silica-gel water uptake (c)

The outlet air temperature during adsorption it is quickly cooled down from the ending regeneration temperature of the previous cycle to around 25°C. The minimum

outlet temperature is equal to 23.3 °C and it is of course reached during evening (around 8.30 PM). The maximum temperature, instead, is almost the same along the day (around 36 °C) except for the last hour considered, in which the external temperature is at the minimum level and the relative humidity is low. The outlet air specific humidity presents its maximum value ($16.8 \text{ g}_v\text{kg}_a^{-1}$) around 19.43. In fact, the ambient temperature is quite high (31.7 °C) and the relative humidity is at its maximum value in the considered period. The minimum value instead is equal to $6.61 \text{ g}_v\text{kg}_a^{-1}$ achieved around 12.09 during adsorption, with external conditions coinciding with an air temperature of 31 °C and relative humidity equal to 36%. Concerning the water uptake, the highest value, equal to $0.13 \text{ kg}_w\text{kg}_s^{-1}$, is obtained around the end of the adsorption cycle starting at 19.00.

The output of the entire system is now presented, with the intention of understanding, at each time step, the characteristics of the air entering the hypothetical indoor environment. This means the outlet conditions of both the heat exchangers, in adsorption mode, are considered. In fact, as previously explained, the HySun adsorption batteries work simultaneously in opposite modes: when the first heat exchanger is in adsorption mode, the other one is in regeneration mode.

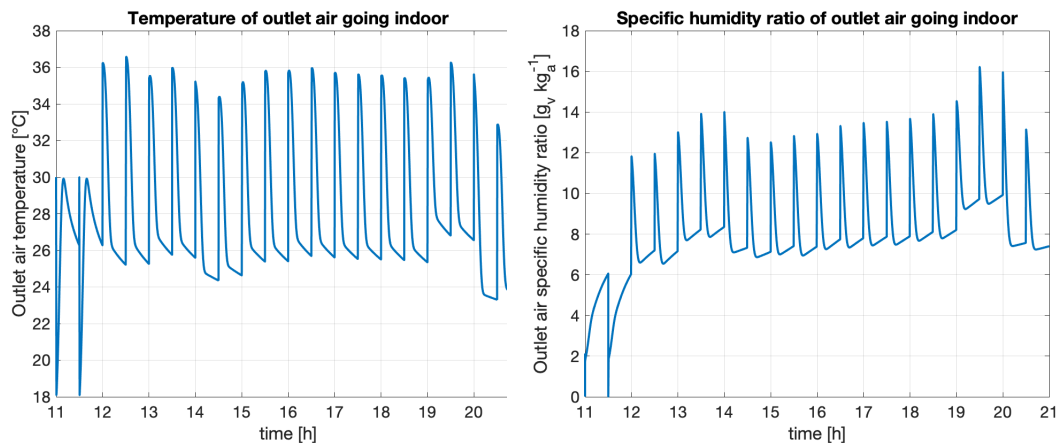


Fig. 4.34 Outlet air temperature and specific humidity ratio for the complete system

It can be noticed that at the beginning of each adsorption cycle, the outlet air temperature and specific humidity are high. This occurs because adsorption is immediately subsequent to regeneration, meaning it takes a while to shift to the new functioning mode. In particular, the water flowing in the tubes of heat exchanger has to change its temperature level from 50 °C to 20 °C. This can be of course a problem

when talking about real implication of this air conditioning machine. Nevertheless, simple solutions could be found as lowering the air flow rate, waiting before inverting the air streams direction or in introducing a pre-cooling cycle before sending the air flow to the conditioned environments.

Another important parameter to be taken into account is of course the cooling power, which is divided in its latent and sensible components in the following figures:

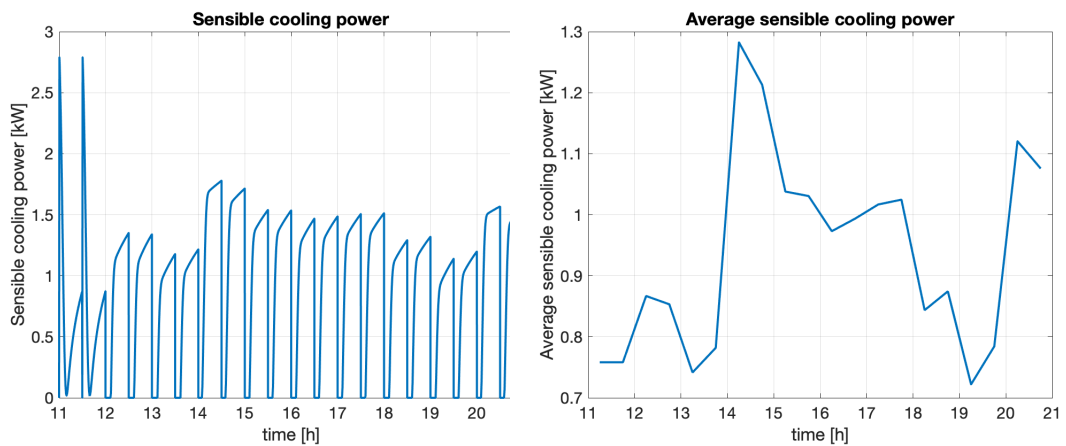


Fig. 4.35 Sensible cooling power

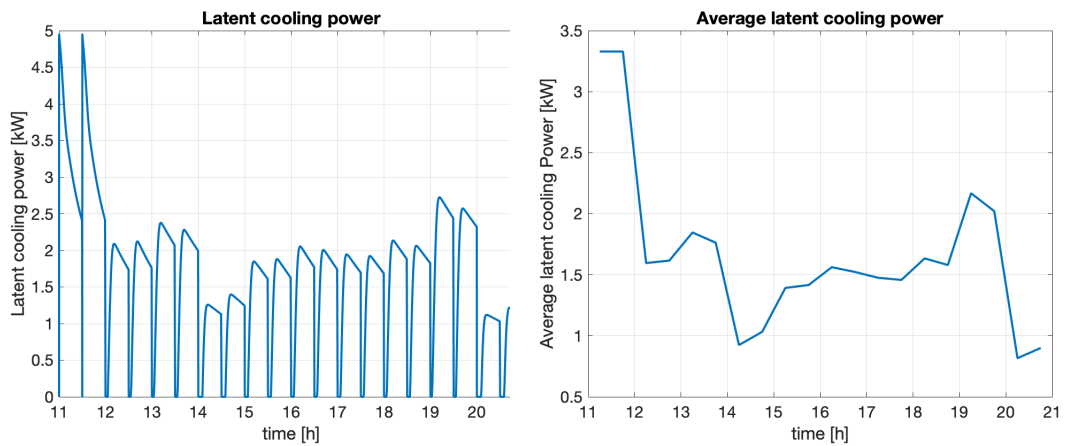


Fig. 4.36 Latent cooling power

The power peaks during the first functioning hour, which are largely out of order, are due to the setting of the initial conditions of the mode. In fact, (i) the water flowing in the tubes is at an uniform temperature equal to the one imposed for the

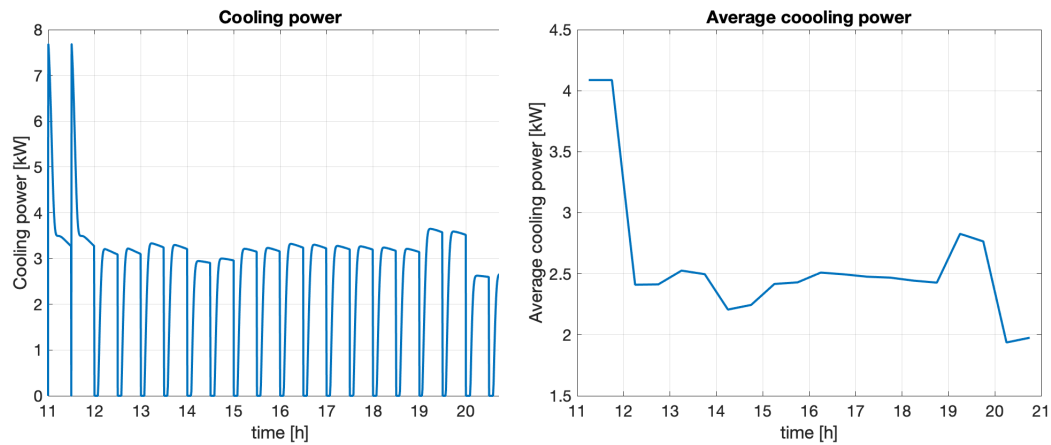


Fig. 4.37 Total cooling power

inlet flow, (ii) the silica-gel is at the temperature of the inlet air stream and (iii) its water uptake is at the set initial value, (iv) the air stream temperature and specific humidity ratio are at the conditions of external environment at each Δz . Looking at the sensible cooling, excluding the first hour affected by the initial condition, its maximum value, equal to 1.78 kW, is reached between 14.00 and 15.00, when the external ambient temperature is the highest and the relative humidity is the lowest. This means that the air stream entering the heat exchanger is characterized by a lower moisture content, in fact the latent cooling power during this hour is reduced, and, so, the system can provide more sensible cooling power. Moreover, the temperature of the air stream is at the highest level, so, a larger temperature difference occurs between air and cold water, allowing a better heat exchange across the fin and tubes. The minimum values of sensible cooling power, instead, are obtained between 13.00 and 14.00 (1.18 kW) and in the hour going from 19.00 to 20.00 (1.14 kW). During these two hours, the ambient air relative humidity is at its maximum values (around 42-47%), meaning the latent cooling power share is higher with respect to the sensible one. The equivalent average sensible power, in these two hours, are equal to 0.74 kW and 0.72 kW, respectively, with a reduction of about 59% with respect to the maximum average value. Concerning the latent cooling power reaches its maximum values in the hours during which the sensible cooling power is minimum, and correspond to 2.38 kW between 13.00 and 14.00 and to 2.72 kW between 19.00 and 20.00, with average values respectively equal to 1.85 kW and 2.17 kW. The lowest values, instead, are obtained between 14.00 and

15.00, with 1.26 kW, (when sensible cooling power is maximum and external air relative humidity is at its minimum) and between 20.00 and 21.00, with 1.12 kW. The minimum average latent cooling power is correspondent to 0.82 kW and it is achieved between 20.00 and 21.00, with a reduction of 69.9% with respect to the maximum average value. The resultant cooling power mainly follows the trend of latent cooling power, since it represents the major contribution.

4.5.3 Influence of switch time

The purpose of this section is to investigate the influence of the switching time on the system performance. The analyzed periods are 15min, 20min and 60min and the reference parameters are average outlet temperature (figure 4.38, moisture removal (figure 4.39) and cooling power (figure 4.40).

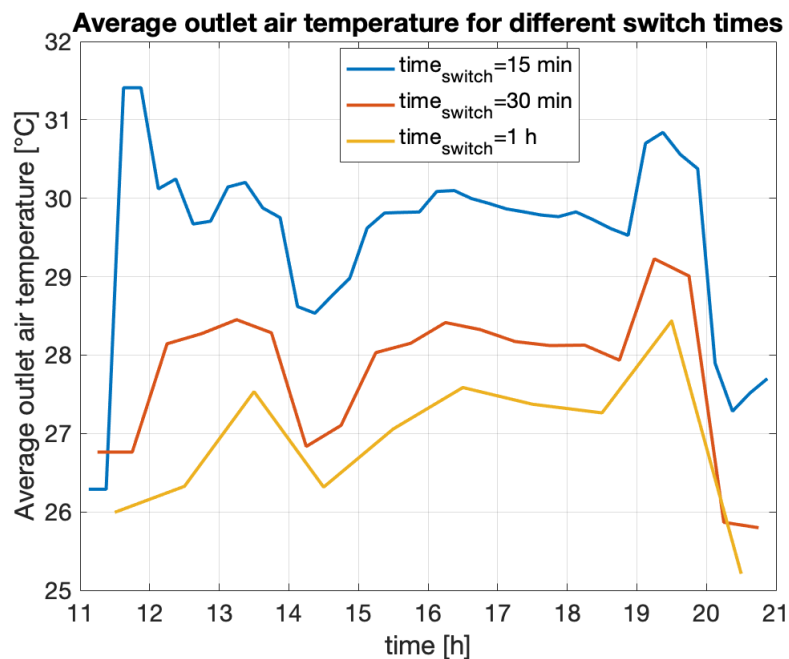


Fig. 4.38 Average outlet air temperature for different switch times

The adsorption outlet air temperature, shows the already seen initial peaks which affects the overall profiles, moving the curves towards up. Nevertheless, major difference between the selected switching time are highlighted. In fact, increasing the switching time produce a decrement of the average temperature curve. This decrease is a consequence of the fact that the outlet air temperature during adsorption,

rapidly reduces and then settles around a certain value. This means that, lengthening the adsorption duration, increases the time in which the outlet air is at a lower temperature. The trend along time is instead similar for all the cases assessed. Few discrepancies are present due to the fact that the average values are calculated for each adsorption cycle, whose duration changes.

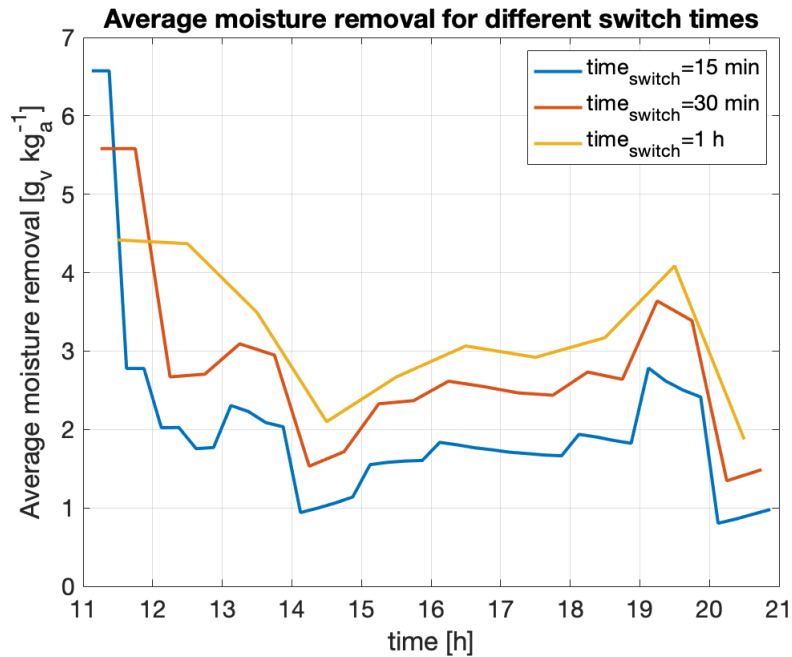


Fig. 4.39 Average air moisture removal

The opposite behaviour is shown in Figure 4.39 for average moisture removal. While the trends over time show similar behaviour, the curve for average moisture removal shows the lower values at shorter switching times. In fact, the average moisture removal increases from 15 minutes to 60 minutes as the peaks in specific exhaust moisture are less numerous due to the alternation with regeneration: In one hour there are four peaks in the case of a switching time of 15 minutes and 2 peaks if the switching time is doubled. This is also reflected in the specific humidity of the exhaust air, which is generally higher at lower switching times, because the silica gel is not completely regenerated, which reduces the useful effect of moisture removal. The maximum average moisture removal at a switching time of 15 minutes is $2.78 g_v kg_a^{-1}$; at 30 minutes it corresponds to $3.64 g_v kg_a^{-1}$ (30.9% higher) and reaches 4.01 at a switching time of 1 hour. Evaluation of the daily average of moisture removal yields $2.0 g_v kg_a^{-1}$, $2.8 g_v kg_a^{-1}$ and $3.2 g_v kg_a^{-1}$, corresponding to 15 minutes,

30 minutes and 60 minutes, respectively. Thus, as the switching time increases, the moisture removal increases, but as the duration of the adsorption cycle increases, the adsorbent approaches saturation. This means that the average moisture removal approaches an asymptotic value as the switching time is further increased.

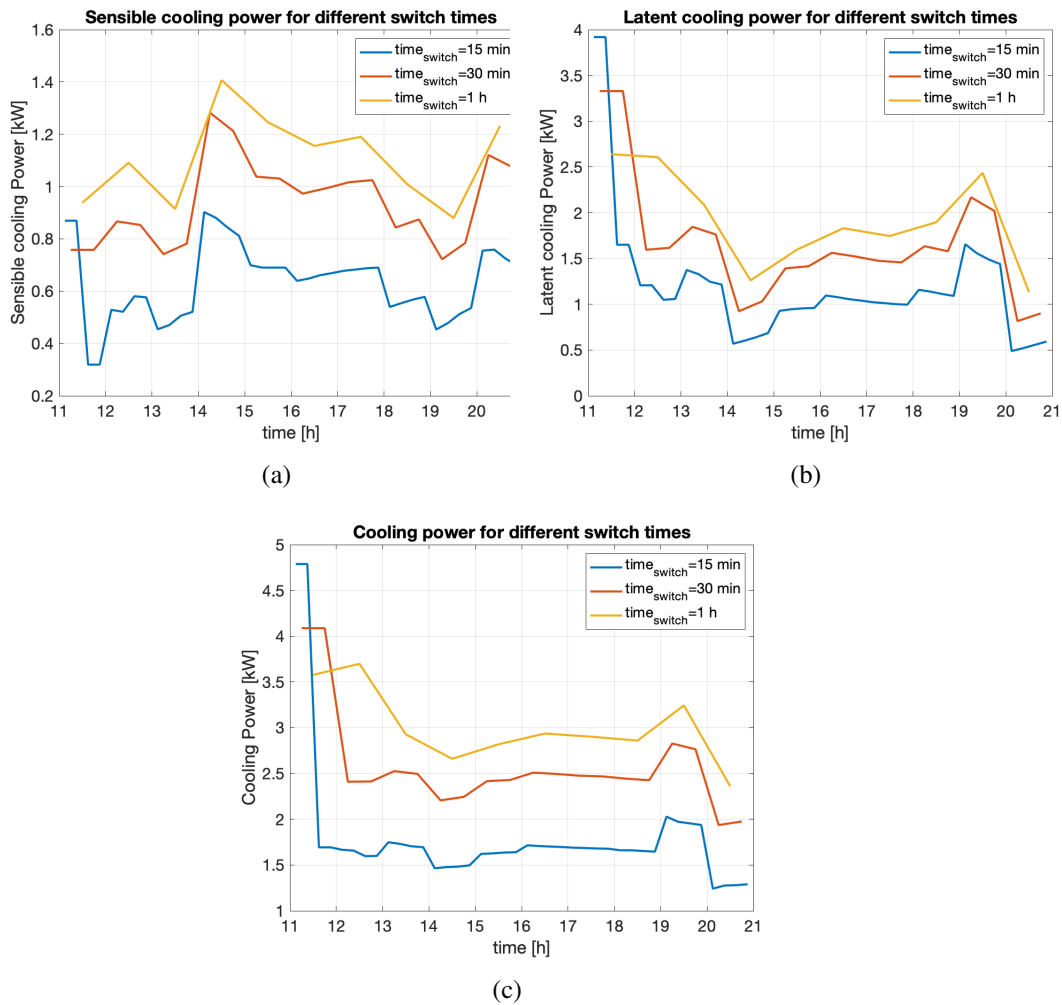


Fig. 4.40 Sensible (a), latent (b) and total (c) cooling power as switch time varies

The results obtained for cooling performance mirror what was said earlier for average exhaust air temperature and moisture removal. Indeed, the sensible cooling capacity, which depends on the temperature difference between inlet and outlet air, is higher for longer switching times, as the outlet temperature decreases with increasing switching time. The latent cooling capacity, on the other hand, follows the trend of the average moisture removal, i.e. it is higher when the switching times are longer. The trend of the total cooling capacity is again more similar to

the latent cooling capacity, as it represents the more significant contribution. The latent cooling capacity shows average values that increase from 1.21 kW to 1.9 kW between 15min and 60min switching time, which is an increase of +58.7%. The sensible cooling capacity shows average values (considering the entire simulation throughout the day) that are 0.63 kW, 0.94 kW and 1.11 kW respectively when the switching time is increased from 15min to 1hour (1.76 times higher than when the switching time is 15min). Furthermore, the maximum average value (excluding the first two cycles) increases from 0.90 kW when the switching time is 15 minutes to 1.28 kW when the switching time is 30 minutes (42.0% higher than the minimum switching time) and then to 1.41 kW when the switching time is set to 1 hour. Finally, the maximum values of the total cooling capacity are 2.02 kW, 2.83 kW and 3.24 kW for a switching time of 15 minutes to 1 hour. The average values, on the other hand, correspond to 1.80 kW, 2.58 kW and 3.00 kW, with an increase of 66.7% between minimum and maximum switching time.

4.5.4 Influence of air flow rate

Similarly to what has been done for the switching time, air flow rate influence is assessed in this section. The air flow rates used are the following: $0.1 \text{ m}^3\text{s}^{-1}$ ($360 \text{ m}^3\text{h}^{-1}$), $0.2 \text{ m}^3\text{s}^{-1}$ ($720 \text{ m}^3\text{h}^{-1}$) and $0.3 \text{ m}^3\text{s}^{-1}$ ($1080 \text{ m}^3\text{h}^{-1}$).

Starting the analysis from the average outlet temperature it can be noticed that the curves are slightly different, in particular, the one referred to an air flow rate of $0.2 \text{ m}^3\text{s}^{-1}$ and $0.3 \text{ m}^3\text{s}^{-1}$ are close to each other.

Only when the air flow rate is reduced to $0.1 \text{ m}^3\text{s}^{-1}$, the average temperature is moderately lower. The average value during the operating period is $26.8 \text{ }^\circ\text{C}$ at an air flow rate of $0.1 \text{ m}^3\text{s}^{-1}$, $27.8 \text{ }^\circ\text{C}$ at an air flow rate of $0.2 \text{ m}^3\text{s}^{-1}$ (3.73% higher than the previous case), and $28.3 \text{ }^\circ\text{C}$ at an air flow rate of $0.3 \text{ m}^3\text{s}^{-1}$ (1.80% higher than the case with an air flow rate of $0.2 \text{ m}^3\text{s}^{-1}$). This behaviour is due to the fact that at lower air flow rates, the amount of air entering the adsorption heat exchanger is smaller and thus a smaller amount of air must be cooled, so heat exchange is more effective. As the air flow rate increases, this effect becomes less significant as the curves tend to converge.

Regarding the moisture removal (Figure 4.42), there is a greater difference between the performance at the lowest and mean airflow rates, while the curves are

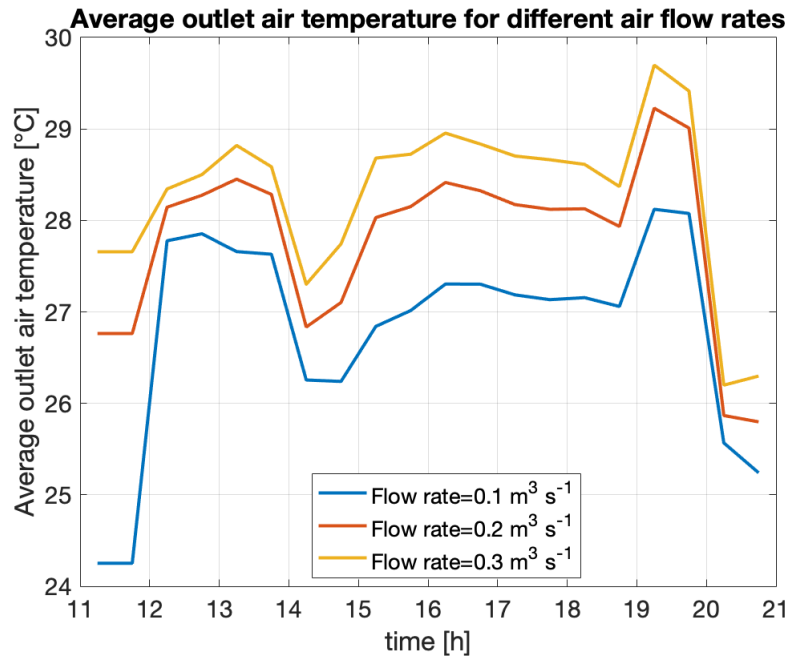


Fig. 4.41 Average outlet air temperature for different air flow rates

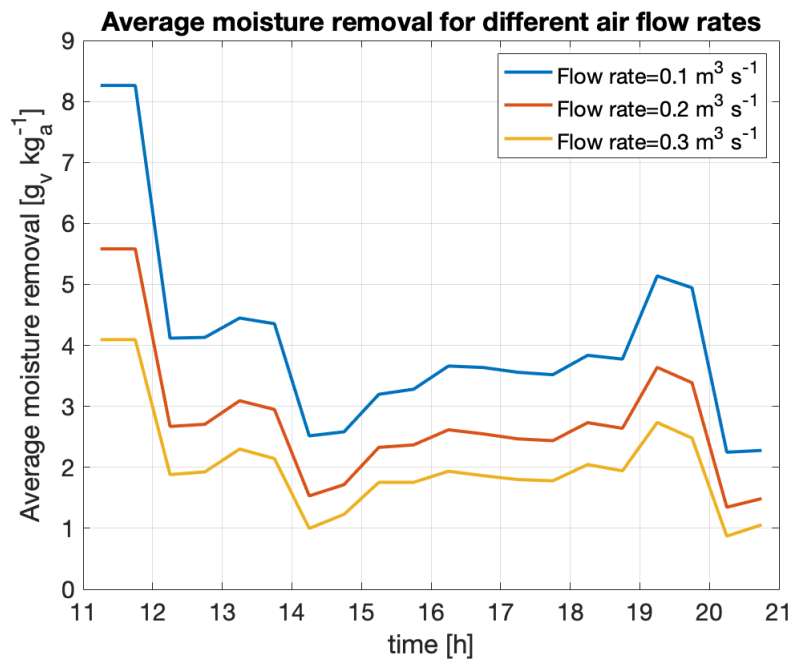


Fig. 4.42 Average air moisture removal for the investigated air flow rates

closer at $0.2 \text{ m}^3 \text{ s}^{-1}$ and $0.3 \text{ m}^3 \text{ s}^{-1}$. The peak value (without considering the first two adsorption cycles) for an air flow rate of $0.1 \text{ m}^3 \text{ s}^{-1}$ is equal to $5.14 \text{ g}_v \text{ kg}_a^{-1}$, it

decreases to $3.64 \text{ g}_v\text{kg}_a^{-1}$ when the air flow rate is $0.2 \text{ m}^3\text{s}^{-1}$ and further decreases to $2.74 \text{ g}_v\text{kg}_a^{-1}$ when the air flow rate is equal to $0.3 \text{ m}^3\text{s}^{-1}$, marking a total reduction of 46.7%. In contrast, the average values for moisture removal during the operating period when the air flow rate is increased from $0.1 \text{ m}^3\text{s}^{-1}$ to $0.3 \text{ m}^3\text{s}^{-1}$ are $4.10 \text{ g}_v\text{kg}_a^{-1}$, $2.80 \text{ g}_v\text{kg}_a^{-1}$ and $2.00 \text{ g}_v\text{kg}_a^{-1}$, respectively. Moreover, if the air flow rate is increased only from $0.1 \text{ m}^3\text{s}^{-1}$ to $0.2 \text{ m}^3\text{s}^{-1}$, the decrease is 31.7%. This behaviour is due to the fact that with an air flow rate of $0.1 \text{ m}^3\text{s}^{-1}$, a smaller amount of air flows through the heat exchanger, so that more moisture can be removed from the incoming air flow.

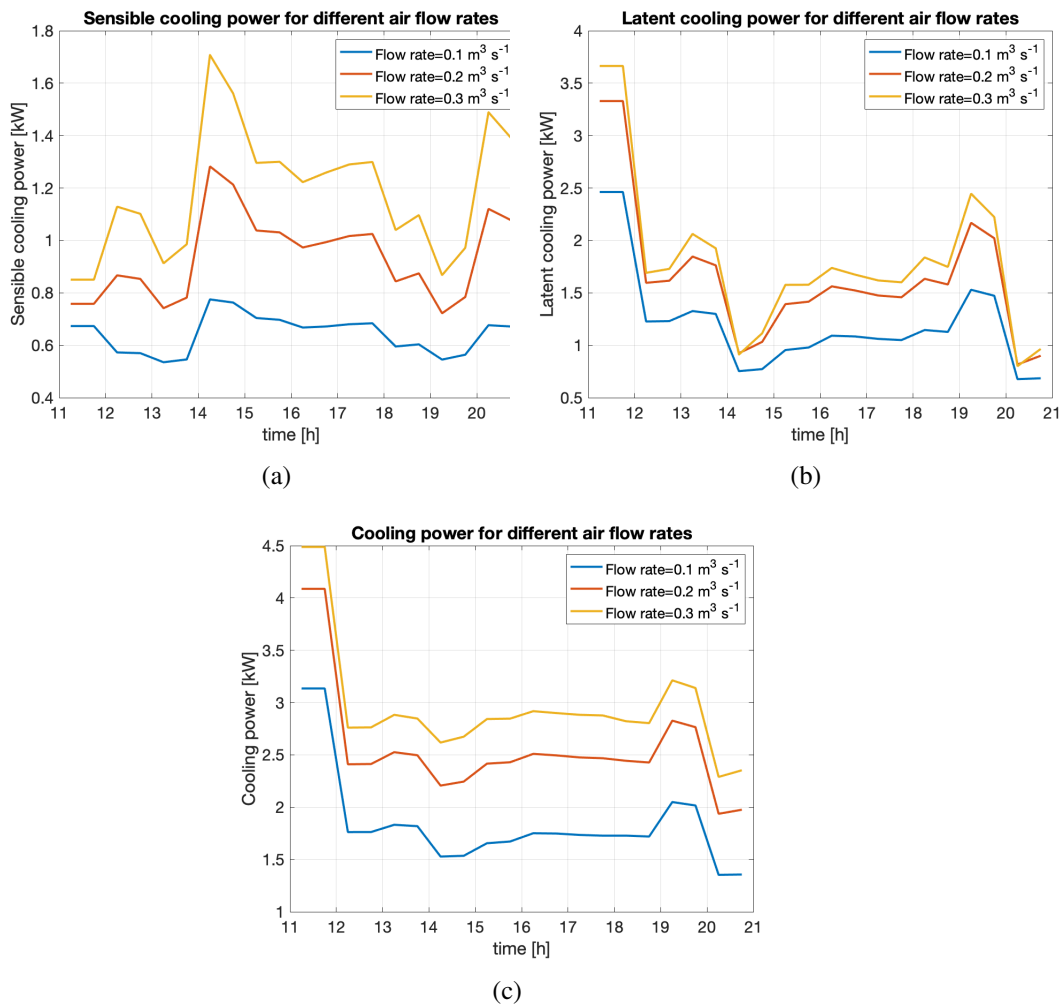


Fig. 4.43 (a) Sensible, (b) latent and (c) total cooling power for the investigated air flow rate

Finally, looking at the sensible cooling capacity, we see that it changes significantly with different air flow rates. Although the average air outlet temperature

curves were close, the sensible cooling capacity is different in the three cases because it is calculated by multiplying the sensible contribution of the enthalpy difference between inlet and outlet air by the air flow rate, which then plays a significant role in the final result.

The maximum average sensible cooling power obtained with the maximum air flow rate ($0.3 \text{ m}^3\text{s}^{-1}$) is 1.71 kW, while when the air flow rate is reduced to $0.2 \text{ m}^3\text{s}^{-1}$ it is 1.28 kW. Finally, with an air flow rate of $0.1 \text{ m}^3\text{s}^{-1}$, the maximum average sensible cooling power is 0.78 kW (54.4 % less than in the case with the maximum air flow rate). The average values during the operating time of the system for air flow rates corresponding to $0.1 \text{ m}^3\text{s}^{-1}$, $0.2 \text{ m}^3\text{s}^{-1}$ and $0.3 \text{ m}^3\text{s}^{-1}$ correspond to 0.64 kW, 0.94 kW and 1.18 kW respectively. As for the latent cooling capacity, although the average moisture removal is highest at the minimum air flow rate, the corresponding latent cooling capacity is lowest, since the air flow rate value is an important contributor to the cooling capacity calculation. When the air flow rate is set to $0.2 \text{ m}^3\text{s}^{-1}$ and to $0.3 \text{ m}^3\text{s}^{-1}$, the power curves are closer because the lower moisture removal at a flow rate of $0.3 \text{ m}^3\text{s}^{-1}$ is compensated by the higher value of the flow rate. The maximum value of latent cooling power achieved with an air flow rate of $0.3 \text{ m}^3\text{s}^{-1}$ corresponds to 2.45 kW; with a flow rate of $0.2 \text{ m}^3\text{s}^{-1}$ it reduced by 11.4%, while at a flow rate of $0.1 \text{ m}^3\text{s}^{-1}$ the maximum average latent cooling power is 1.70 kW. The average values during the system operation time for air flow rates corresponding to $0.1 \text{ m}^3\text{s}^{-1}$, $0.2 \text{ m}^3\text{s}^{-1}$ and $0.3 \text{ m}^3\text{s}^{-1}$ are equal to 1.22 kW, 1.67 kW and 1.83 kW (50.0% higher than that corresponding to the minimum flow rate), respectively. The maximum of the resulting average total cooling power corresponds to the simulation with the maximum flow rate ($0.3 \text{ m}^3\text{s}^{-1}$), while the minimum is achieved by a flow rate of $0.1 \text{ m}^3\text{s}^{-1}$. The maximum values for each flow rate analysed are 2.05 kW (for an air flow rate of $0.1 \text{ m}^3\text{s}^{-1}$), 2.83 kW (for the flow rate corresponding to $0.2 \text{ m}^3\text{s}^{-1}$) and 3.21 kW (for the maximum air flow rate). The average value during the entire operating time of the system is 1.85 kW when the air flow rate is at its lowest, 2.58 kW when the air flow rate corresponds to $0.2 \text{ m}^3\text{s}^{-1}$ (39.5% increase) and 2.97 kW when the air flow rate is $0.3 \text{ m}^3\text{s}^{-1}$ (60.5% more than in the minimum air flow rate case).

In summary, the results show that COP is above average for normal vapour compression devices, indicating a significant increase in efficiency. Furthermore, the simulations confirm that it is possible to obtain conditioned air with tighter temperature levels between the evaporator and condenser. Given the increasing

use of air conditioning and refrigeration equipment, this can make a significant contribution to reducing energy consumption and power peaks, which in conventional systems are often due to the low temperatures (on the evaporator side) required for dehumidification. In addition, a temperature level such as the one used in the above simulation allows the integration of several RES technologies for the adsorption and regeneration phases. However, one of the major drawbacks of this type of system is that, given the non-linear behaviour of the adsorption material, one must envision precise and targeted control to ensure a constant and stable cooled airflow. Furthermore, the properties of the air at the beginning of each adsorption cycle may not match indoor requirements, both in terms of air temperature and specific humidity. This is because in our simulation the regeneration and adsorption in each battery immediately follow each other, so that the temperature transients are not sufficient to reach a stable and appropriate state. This means that pre-cooling of the air is required before it is released into the interior. Furthermore, the fact that the specific humidity is still high at the end of regeneration for the switching times considered means that the silica gel is not fully regenerated. This can be remedied by further extending the switching time or by reducing the length of the heat exchanger, as the ambient conditions in which the system is installed have a low relative humidity.

Chapter 5

Conclusions

This PhD document reports in brief my 3-years journey across the electrification of final energy demand. Starting from the new generation of district heating systems, walking through heat pump systems and electric vehicles and finally analyzing the cooling world. Specifically, the second chapter is dedicated to the electrification of district heating systems and to the effect of detailed analysis on CO_2 emission factor against the annual average values for heat pump systems and electric vehicles. In the third chapter, ReCognition EU project and the HySun prototype are described, with the main objectives and the design parameter for the realized prototype. In the end, the fourth chapter present the simulation code, developed for the adsorption process analysis and performance forecast.

The electrification of end-users is shifting final energy consumption towards electricity-based technologies. In the future, a large proportion of appliances will be powered by electricity, whose generation will play a key role in effectively decarbonising end-users. This push can of course be driven by the increasing installed capacity of renewables and their advances in environmental impact and decentralization model. Nevertheless, the variability of renewables is well known and a major effort needs to be made to harness it. The detailed study of electricity end-use behaviour for heating purpose reported in this thesis is relevant as it highlights critical aspects in the detailed analysis of heat pump electricity consumption. Annual average emissions values have been compared with hourly emissions value for electricity consumed by heat pumps systems. The average difference for the European countries considered remains below 5%, while for certain heat pump users the differences

between the exact calculation and the average calculation can range from a maximum increase of +9.6% (Austria) to a maximum decrease of -3.0% (France). There is a double message in these results. On the one hand, the actual electricity mix of heat pump systems can be reasonably approximated by annual averages, although this result may no longer hold at a very high penetration of variable RES (and thus in future decarbonised energy systems). On the other hand, the use of annual averages may overstate actual emission savings for certain demand profiles. Greater variability was found in the electric vehicle charging study. The results showed greater variability in terms of CO_2 emissions, especially when considering the year of analysis for a given country. The charging profile showed an average variation of 18%, highlighting the significant variability in the electricity mix over the years and emphasising the importance of considering multiple years when estimating emissions associated with e-vehicle use in a given country to account for the potential uncertainty associated with the varying electricity mix over the years. Although the relative difference between generation and consumption in terms of CO_2 emissions is still small in the cases studied, this picture may change radically in the near future. Some limitations of this work lie mainly in the availability and reliability of electricity generation data. The ENTSOE database is an ambitious and important project, but as it is still in its initial phase, it is still subject to errors such as missing data and incorrect grouping of production in relation to the reference technology.

The increasingly stringent policies and the uncertain development of the Russian-Ukrainian war are likely to lead to a faster transition to alternative energy production and the installation of renewable capacities. This means that the low fluctuation highlighted in this work would increase, raising important questions about the effective 'greening' of electrical machinery and equipment. This means that the effective use of increasing installed renewable capacity needs to be considered throughout the life cycle of a project: from planning to implementation. Policy incentives need to be put in place to improve the effective consumption of renewable energy. An example would be a tax rebate scheme based on the effective use of locally generated or grid-sourced renewable energy in a heat pump/electric vehicle/cooling system. In this way, the planner and users are led to choose control strategies that are not only for convenience, but also to use electrical technology at a convenient time for renewable generation. This automatically reduces the surplus of renewable energy and also limits the need for large-scale electricity storage, which still lacks economic competitiveness and reliability in the near future. The biggest challenge for

this incentive system is, of course, the certification of the electricity source. While for locally generated electricity a can ensure a detailed record of effective renewable energy use, it can be much more difficult for grid electricity, as there is no special certificate to ensure the correct source of electricity hour by hour. This presents an interesting and delicate challenge to overcome.

Another important result of this work is the cooperation rather than competition between the world of heat and the world of electricity. Both in the scientific literature and in policy and regulation, there is an unbalanced production of documents towards the electric vector. On the one hand, it is right to push its use for the reasons already mentioned, but on the other hand, it is not possible to eliminate or completely adopt what is done today with conventional technologies. In a long-term transition phase, it is better to take joint measures to exploit the advantages of the power/heat grid and support the respective weak points. As shown in chapter two, district heating systems can have a positive environmental impact as they often provide heat with lower specific emissions than traditional decentralised gas boilers. However, these impacts can vary greatly depending on the allocation method for the CHP system. In fact, the results show a range of variation from +72% to -60% compared to individual gas boilers. Therefore, the choice of an appropriate allocation factor is of utmost importance. An important solution to improve the efficiency of district heating systems and to increase the potential RES integration can already be implemented today in the heating network with the combination of heat pumps and district heating systems. This solution seems to have a remarkable potential as it allows to lower the temperature level in the ring and to avoid unnecessary losses due to the movement of water at high temperature. However, some parameters are crucial for success, including the generation of electricity from renewable sources, which plays a key role. Indeed, booster heat pumps can reduce the energy demand of the district heating network, but at the cost of a non-negligible local electricity consumption.

Finally, the notable importance of cooling for electrification and electricity consumption should be considered. Over the past 20 years, annual demand for air conditioning has grown by an average of about 4 per cent, twice as much as demand for lighting and water heating systems. Moreover, the last two years of the coronavirus pandemic have had a significant impact by further boosting demand for home systems, especially in countries where closures and working from home have been introduced. For this reason, the development of the HySun prototype for ReCognition is in line with the main policies which are posing minimum efficiency

requirements for air conditioning units and systems. The simulations carried out show that HySun can effectively reduce electricity consumption for cooling. Latent heat, which accounts for the largest share of the total load in areas with strong economic and demographic development, is effectively handled by silica gel exchange coils. The coating allowed to lower the temperature levels for chillers, improve the overall efficiency and achieve the same cooling effect. Nevertheless, the poorer performance compared to pure silica gel material was highlighted, which means that the design and implementation in this area must be precise and that further testing and development is needed to find the perfect coating recipe. Finally, the adsorption simulator presents interesting insights into the possible operation of the prototype. The system is able to deliver cooling with a higher temperature level (on the evaporator side of the heat pump) in a stable way than the conventional chiller. However, special attention must be paid to the timing and transitions between the adsorption and regeneration cycles, which can affect the quality of the air delivered to the room. In addition, a suitable control strategy must be developed to effectively control the condition of the process air in terms of temperature and humidity. In fact, adsorption is not a constant phenomena and the dehumidification capabilities are different as the process goes on. The final calibration of the system and the comparison with the real prototype will be the subject of future research in the laboratories of the Polytechnic of Turin. A limitation of the work is obviously that the prototype has not yet been put into operation and its performance has not been tested due to COVID pandemic outbreak, which caused delays in the purchase, assembly and transport of the various components. In addition, the simulator has been partially validated with a literature comparison. Nevertheless, the prototype is ready for use and the research team will soon start test cycles. On top of the technical results achieved, it is important to stress that HySun emphasises the need for targeted investments in this type of technology. The great potential of adsorption systems has never been concretely tapped. A strong impetus should therefore be given by providing funds for research and development of the machines, but above all for their management and control, which is crucial for this type of equipment. Furthermore, cooling device has to be produced and sold with minimum efficiency level especially in the critical areas as Indonesia, China and the other cited countries. National and international economical support needs to be deployed to push population toward more efficient devices.

The PhD research reported here suggests that decisions made about heating, cooling and mobility could have a major impact on the electricity sector. Electrification

of all end users seems to be a challenge, and especially in the transition period, cooperation with traditional heating could deliver stable and profitable results. This means that efforts in the future should be evenly distributed between the electricity and heating sector. A particular focus has to be dedicated to cooling which is expected to be the ruler for electricity consumption in the near future.

References

- [1] United Nations. *World Population Prospects 2019*. Number 141. 2019. URL: <http://www.ncbi.nlm.nih.gov/pubmed/12283219>.
- [2] United Nations. United Nation - SDGs. URL: <https://sdgs.un.org/goals>.
- [3] IRENA, IEA, and REN21. *Renewable Energy Policies in a Time of Transition: Heating and Cooling*. Number November. 2020.
- [4] IEA. *World Energy Outlook 2019*. Technical report, 2019. URL: <https://www.iea.org/reports/world-energy-outlook-2019><https://www.iea.org/reports/world-energy-outlook-2019><https://webstore.iea.org/download/summary/2467?fileName=Japanese-Summary-WEO2019.pdf>.
- [5] IEA. *Power systems in transition*. Technical report, 2020. doi:10.1787/4ad57c0e-en.
- [6] Climate Watch Data. *Historical GHG Emissions*. Technical report, 2016. URL: <https://www.climatewatchdata.org/ghg-emissions?chartType=percentage§ors=614>.
- [7] IEA. *Global EV Outlook 2020*. Technical report, 2020. doi:10.1787/d394399e-en.
- [8] International Energy Agency. *Trends and developments in electric vehicle markets*. URL: <https://www.iea.org/reports/global-ev-outlook-2021/trends-and-developments-in-electric-vehicle-markets>.
- [9] D. Connolly. *Heat Roadmap Europe: Quantitative comparison between the electricity, heating, and cooling sectors for different European countries*. *Energy*, 2017. doi:10.1016/j.energy.2017.07.037.
- [10] European commission. *Heating and Cooling Strategies 2050*. Technical report, European Union, 2016.
- [11] Luis Gomez Echeverri. *Investing for rapid decarbonization in cities*. *Current Opinion in Environmental Sustainability*, 30:42–51, 2 2018. URL: <https://www.sciencedirect.com/science/article/pii/S1877343517301240>, doi:10.1016/J.COSUST.2018.02.010.

- [12] Philip Sterchele, Andreas Palzer, and Hans Martin Henning. Electrify everything?: Exploring the role of the electric sector in a nearly CO₂-neutral national energy system. *IEEE Power and Energy Magazine*, 16(4):24–33, 2018. doi:10.1109/MPE.2018.2824100.
- [13] Philipp Blum, Gisela Campillo, Wolfram Münch, and Thomas Kölbel. CO₂ savings of ground source heat pump systems – A regional analysis. *Renewable Energy*, 35(1):122–127, 1 2010. URL: <https://www.sciencedirect.com/science/article/pii/S0960148109003024>, doi:10.1016/J.RENENE.2009.03.034.
- [14] Sophie Nyborg and Inge Røpke. Heat pumps in Denmark—From ugly duckling to white swan. *Energy Research & Social Science*, 9:166–177, 9 2015. URL: <https://linkinghub.elsevier.com/retrieve/pii/S221462961530044X>, doi:10.1016/j.erss.2015.08.021.
- [15] IEA. Heat Pump Report. Technical report, Paris, 2020. URL: <https://www.iea.org/reports/heat-pumps>.
- [16] EHPA. European Heat Pump Market and Statistics - Report 2020. Technical report, 2020.
- [17] Niall Kerr and Mark Winskel. A Review of Heat Decarbonisation Policies in Europe. *climateXchange*, (February):30, 2021.
- [18] IEA. Cooling Report. Technical report, Paris, 2020. URL: <https://www.iea.org/reports/cooling>.
- [19] OECD/IEA. The Future of Cooling: Opportunities for energy-efficient air conditioning. *The Future of Cooling: Opportunities for energy-efficient air conditioning*, page 92, 2018. URL: <https://webstore.iea.org/the-future-of-cooling>.
- [20] International Energy Agency. *World Energy Outlook*. 2018. URL: <https://www.iea.org/reports/world-energy-outlook-2018/electricity>.
- [21] NASA. NASA prediction of WorldWide Energy Source. URL: <https://power.larc.nasa.gov/>.
- [22] Henrik Lund, Poul Alberg Østergaard, David Connolly, and Brian Vad Mathiesen. Smart energy and smart energy systems. *Energy*, 137:556–565, 10 2017. doi:10.1016/J.ENERGY.2017.05.123.
- [23] Francesco Neirrotti, Michel Noussan, Stefano Rivero, and Giorgio Manganini. Analysis of Different Strategies for Lowering the Operation Temperature in Existing District Heating Networks. URL: www.mdpi.com/journal/energies, doi:10.3390/en12020321.
- [24] D. Connolly. Heat Roadmap Europe: Quantitative comparison between the electricity, heating, and cooling sectors for different European countries. *Energy*, 2017. doi:10.1016/j.energy.2017.07.037.

- [25] Henrik Lund, Sven Werner, Robin Wiltshire, Svend Svendsen, Jan Eric Thorsen, Frede Hvelplund, and Brian Vad Mathiesen. 4th Generation District Heating (4GDH): Integrating smart thermal grids into future sustainable energy systems. *Energy*, 68:1–11, 4 2014. URL: <https://www.sciencedirect.com/science/article/pii/S0360544214002369>, doi:10.1016/J.ENERGY.2014.02.089.
- [26] Francesco Neirotti, Michel Noussan, and Marco Simonetti. Evaluating the Emissions of the Heat Supplied by District Heating Networks through A Life Cycle Perspective. URL: www.mdpi.com/journal/cleantechnol, doi:10.3390/cleantechnol2040024.
- [27] Francesco Neirotti, Michel Noussan, and Marco Simonetti. Towards the electrification of buildings heating - Real heat pumps electricity mixes based on high resolution operational profiles. *Energy*, 195:116974, 3 2020. URL: <https://linkinghub.elsevier.com/retrieve/pii/S0360544220300815>, doi:10.1016/j.energy.2020.116974.
- [28] Michel Noussan and Francesco Neirotti. Cross-country comparison of hourly electricity mixes for EV charging profiles. *Energies*, 13(10):1–14, 2020. doi:10.3390/en13102527.
- [29] Sven Werner. International review of district heating and cooling. *Energy*, 137:617–631, 10 2017. URL: <https://www.sciencedirect.com/science/article/pii/S036054421730614X>, doi:10.1016/J.ENERGY.2017.04.045.
- [30] Behnaz Rezaie and Marc A. Rosen. District heating and cooling: Review of technology and potential enhancements. *Applied Energy*, 93:2–10, 5 2012. URL: <https://www.sciencedirect.com/science/article/pii/S030626191100242X>, doi:10.1016/J.APENERGY.2011.04.020.
- [31] Henrik Lund, Sven Werner, Robin Wiltshire, Svend Svendsen, Jan Eric Thorsen, Frede Hvelplund, and Brian Vad Mathiesen. 4th Generation District Heating (4GDH): Integrating smart thermal grids into future sustainable energy systems. *Energy*, 68:1–11, 4 2014. URL: <https://www.sciencedirect.com/science/article/pii/S0360544214002369>, doi:10.1016/J.ENERGY.2014.02.089.
- [32] Chunhui Liao, Ivar S. Ertesvåg, and Jianing Zhao. Energetic and exergetic efficiencies of coal-fired CHP (combined heat and power) plants used in district heating systems of China. *Energy*, 57:671–681, 8 2013. URL: <https://www.sciencedirect.com/science/article/pii/S0360544213004763>, doi:10.1016/J.ENERGY.2013.05.055.
- [33] Michel Noussan. Allocation factors in Combined Heat and Power systems – Comparison of different methods in real applications. *Energy Conversion and Management*, 173:516–526, 10 2018. URL: <https://www.sciencedirect.com/science/article/pii/S0196890418308446>, doi:10.1016/J.ENCONMAN.2018.07.103.

- [34] Vittorio Verda and Francesco Colella. Primary energy savings through thermal storage in district heating networks. *Energy*, 36(7):4278–4286, 7 2011. URL: <https://www.sciencedirect.com/science/article/pii/S0360544211002647>, doi: 10.1016/J.ENERGY.2011.04.015.
- [35] G.F. Davies, G.G. Maidment, and R.M. Tozer. Using data centres for combined heating and cooling: An investigation for London. *Applied Thermal Engineering*, 94:296–304, 2 2016. URL: <https://www.sciencedirect.com/science/article/pii/S1359431115010388>, doi: 10.1016/J.APPLTHERMALENG.2015.09.111.
- [36] Khosrow Ebrahimi, Gerard F. Jones, and Amy S. Fleischer. A review of data center cooling technology, operating conditions and the corresponding low-grade waste heat recovery opportunities. *Renewable and Sustainable Energy Reviews*, 31:622–638, 3 2014. URL: <https://www.sciencedirect.com/science/article/pii/S1364032113008216>, doi: 10.1016/J.RSER.2013.12.007.
- [37] Abdur Rehman Mazhar, Shuli Liu, and Ashish Shukla. A state of art review on the district heating systems. *Renewable and Sustainable Energy Reviews*, 96:420–439, 11 2018. URL: <https://www.sciencedirect.com/science/article/pii/S1364032118305720>, doi: 10.1016/J.RSER.2018.08.005.
- [38] Hans Christian Gils, Janusz Cofala, Fabian Wagner, and Wolfgang Schöpp. GIS-based assessment of the district heating potential in the USA. *Energy*, 58:318–329, 9 2013. URL: <https://www.sciencedirect.com/science/article/pii/S0360544213005264>, doi: 10.1016/J.ENERGY.2013.06.028.
- [39] Steffen Nielsen and Bernd Möller. GIS based analysis of future district heating potential in Denmark. *Energy*, 57:458–468, 8 2013. URL: <https://www.sciencedirect.com/science/article/pii/S0360544213004581>, doi: 10.1016/J.ENERGY.2013.05.041.
- [40] Erika Zvingilaite and Olexandr Balyk. Heat savings in buildings in a 100% renewable heat and power system in Denmark with different shares of district heating. *Energy and Buildings*, 82:173–186, 10 2014. URL: <https://www.sciencedirect.com/science/article/pii/S0378778814005283?via%3Dihub>, doi: 10.1016/J.ENBUILD.2014.06.046.
- [41] Bernd Möller and Henrik Lund. Conversion of individual natural gas to district heating: Geographical studies of supply costs and consequences for the Danish energy system. *Applied Energy*, 87(6):1846–1857, 6 2010. URL: <https://www.sciencedirect.com/science/article/pii/S0306261909005248>, doi: 10.1016/J.APENERGY.2009.12.001.
- [42] Weiming Xiong, Yu Wang, and Xiliang Zhang. Case study of the constraints and potential contributions regarding wind curtailment in Northeast China. *Energy*, 110:55–64, 9 2016. URL: <https://www.sciencedirect.com/science/article/pii/S0360544216303371>, doi: 10.1016/J.ENERGY.2016.03.093.

- [43] Jin Guo, Ying Huang, and Chu Wei. North–South debate on district heating: Evidence from a household survey. *Energy Policy*, 86:295–302, 11 2015. URL: <https://www.sciencedirect.com/science/article/pii/S0301421515300288>, doi:10.1016/J.ENPOL.2015.07.017.
- [44] Hildigunnur H. Thorsteinsson and Jefferson W. Tester. Barriers and enablers to geothermal district heating system development in the United States. *Energy Policy*, 38(2):803–813, 2 2010. URL: <https://www.sciencedirect.com/science/article/pii/S0301421509007721>, doi:10.1016/J.ENPOL.2009.10.025.
- [45] David Hawkey, Janette Webb, and Mark Winkler. Organisation and governance of urban energy systems: district heating and cooling in the UK. *Journal of Cleaner Production*, 50:22–31, 7 2013. URL: <https://www.sciencedirect.com/science/article/pii/S0959652612006099>, doi:10.1016/J.JCLEPRO.2012.11.018.
- [46] Matteo Jarre, Michel Noussan, and Alberto Poggio. Operational analysis of natural gas combined cycle CHP plants: Energy performance and pollutant emissions. *Applied Thermal Engineering*, 100:304–314, 5 2016. URL: <https://www.sciencedirect.com/science/article/pii/S1359431116301831>, doi:10.1016/J.APPLTHERMALENG.2016.02.040.
- [47] Peifeng Li, Natasa Nord, Ivar Ståle Ertesvåg, Zhihua Ge, Zhiping Yang, and Yongping Yang. Integrated multiscale simulation of combined heat and power based district heating system. *Energy Conversion and Management*, 106:337–354, 12 2015. URL: <https://www.sciencedirect.com/science/article/pii/S0196890415008316?via%3Dihub>, doi:10.1016/J.ENCONMAN.2015.08.077.
- [48] Alessandro Pini Prato, Fabrizio Strobino, Marco Broccardo, and Luigi Parodi Giusino. Integrated management of cogeneration plants and district heating networks. *Applied Energy*, 97:590–600, 9 2012. URL: <https://www.sciencedirect.com/science/article/pii/S0306261912001377?via%3Dihub>, doi:10.1016/J.APENERGY.2012.02.038.
- [49] Wolfgang Rudig. COMBINED HEAT AND POWER technology. 1986.
- [50] Michel Noussan, Matteo Jarre, and Alberto Poggio. Real operation data analysis on district heating load patterns. *Energy*, 129:70–78, 6 2017. URL: <https://www.sciencedirect.com/science/article/pii/S036054421730645X>, doi:10.1016/J.ENERGY.2017.04.079.
- [51] Kristo Helin, Sanna Syri, and Behnam Zakeri. Improving district heat sustainability and competitiveness with heat pumps in the future Nordic energy system. *Energy Procedia*, 149:455–464, 9 2018. URL: <https://www.sciencedirect.com/science/article/pii/S187661021830506X>, doi:10.1016/J.EGYPRO.2018.08.210.

- [52] Elisa Guelpa, Guglielmina Mutani, Valeria Todeschi, and Vittorio Verda. Reduction of CO₂ emissions in urban areas through optimal expansion of existing district heating networks. *Journal of Cleaner Production*, 204:117–129, 12 2018. URL: <https://www.sciencedirect.com/science/article/pii/S0959652618326234>, doi:10.1016/J.JCLEPRO.2018.08.272.
- [53] AIRU. Il Riscaldamento Urbano - Annuario. 2018.
- [54] European Commission. Clean Energy for All Europeans package. URL: https://ec.europa.eu/energy/topics/energy-strategy/clean-energy-all-europeans_en.
- [55] European Commission. Support Activities and Projects about Heating and Cooling Sector. Technical report, European Union, 2016. doi:10.2826/607102.
- [56] Satu Paiho and Francesco Reda. Towards next generation district heating in Finland. *Renewable and Sustainable Energy Reviews*, 65:915–924, 11 2016. URL: <https://www.sciencedirect.com/science/article/pii/S1364032116303768>, doi:10.1016/J.RSER.2016.07.049.
- [57] Elisa Guelpa, Ludovica Marincioni, and Vittorio Verda. Towards 4th generation district heating: Prediction of building thermal load for optimal management. *Energy*, 171:510–522, 3 2019. URL: <https://www.sciencedirect.com/science/article/pii/S0360544219300581>, doi:10.1016/J.ENERGY.2019.01.056.
- [58] Henrik Gadd and Sven Werner. Daily heat load variations in Swedish district heating systems. *Applied Energy*, 106:47–55, 6 2013. URL: <https://www.sciencedirect.com/science/article/pii/S0306261913000391>, doi:10.1016/J.APENERGY.2013.01.030.
- [59] M. Köfinger, D. Basciotti, R.R. Schmidt, E. Meissner, C. Doczekal, and A. Giovannini. Low temperature district heating in Austria: Energetic, ecologic and economic comparison of four case studies. *Energy*, 110:95–104, 9 2016. URL: <https://www.sciencedirect.com/science/article/pii/S036054421501748X>, doi:10.1016/J.ENERGY.2015.12.103.
- [60] D. Bauer, R. Marx, J. Nußbicker-Lux, F. Ochs, W. Heidemann, and H. Müller-Steinhagen. German central solar heating plants with seasonal heat storage. *Solar Energy*, 84(4):612–623, 4 2010. URL: <https://www.sciencedirect.com/science/article/pii/S0038092X09001224?via%3Dihub>, doi:10.1016/J.SOLENER.2009.05.013.
- [61] Bruce Sibbitt, Doug McClenahan, Reda Djebbar, Jeff Thornton, Bill Wong, Jarrett Carriere, and John Kokko. The Performance of a High Solar Fraction Seasonal Storage District Heating System – Five Years of Operation. *Energy Procedia*, 30:856–865, 1 2012. URL: <https://www.sciencedirect.com/science/article/pii/S187661021201613X?via%3Dihub>, doi:10.1016/J.EGYPRO.2012.11.097.

- [62] Patrick Reiter, Hannes Poier, and Christian Holter. BIG Solar Graz: Solar District Heating in Graz – 500,000 m² for 20% Solar Fraction. *Energy Procedia*, 91:578–584, 6 2016. URL: <https://www.sciencedirect.com/science/article/pii/S1876610216303022>, doi:10.1016/J.EGYPRO.2016.06.204.
- [63] Nadège Vetterli, Matthias Sulzer, and Urs-Peter Menti. Energy monitoring of a low temperature heating and cooling district network. *Energy Procedia*, 122:62–67, 9 2017. URL: <https://www.sciencedirect.com/science/article/pii/S1876610217328874>, doi:10.1016/J.EGYPRO.2017.07.289.
- [64] Dymola - Main Webpage. URL: <https://www.3ds.com/products-services/catia/products/dymola/>.
- [65] Building Library for Modelica. URL: <https://simulationresearch.lbl.gov/modelica/>.
- [66] Berkley LAB. Modelica Building Library - Buildings.Fluid.HeatExchangers.Radiators. URL: https://simulationresearch.lbl.gov/modelica/releases/v3.0.0/help/Buildings_Fluid_HeatExchangers_Radiators.html#Buildings.Fluid.HeatExchangers.Radiators.RadiatorEN442_2.
- [67] EnergyPlus Website. URL: <https://energyplus.net/>.
- [68] Romain NOUVEL, Mariela COTRADO SEHGELMEBLE, and Dirk PIETRUSCHKA. European mapping of seasonal performances of air-source and geothermal heat pumps for residential applications. *Proceedings of International Conference CISBAT 2015 Future Buildings and Districts Sustainability from Nano to Urban Scale*, (September):543–548, 2015. URL: <https://infoscience.epfl.ch/record/213404>.
- [69] C Wemhöner and T Afjei. Seasonal performance calculation for residential heat pumps with combined space heating and hot water production (FHBB method). *Swiss Federal Office of Energy, Bern*, (October), 2003.
- [70] ISPRA. *Indicatori di efficienza e decarbonizzazione del sistema energetico nazionale e del settore elettrico*. 2021.
- [71] ISPRA. ISPRA Italia. URL: <https://www.isprambiente.gov.it/en>.
- [72] ISPRA; TERNA. Fattori di emissione per la produzione e il consumo di energia elettrica in Italia (aggiornamento al 2019 e stime preliminari per il 2020). URL: <http://www.sinanet.isprambiente.it/it/sia-ispra/serie-storiche-emissioni/fattori-di-emissione-per-la-produzione-ed-il-consumo-di-energia-elettrica-in-italia/view>.
- [73] IEA. Heating Report. Technical report, 2020. URL: <https://www.iea.org/reports/heating>.

- [74] The european Parliament and the council of the european union. DIRECTIVE 2009/28/EC. 2009. URL: <https://eur-lex.europa.eu/legal-content/EN/TXT/PDF/?uri=CELEX:32009L0028&from=IT>.
- [75] IEA. WORLD ENERGY BALANCES 2020 EDITION. Technical report, 2020. URL: https://iea.blob.core.windows.net/assets/4f314df4-8c60-4e48-9f36-bfea3d2b7fd5/WorldBAL_2020_Documentation.pdf.
- [76] IEA International Energy Agency. Net Zero by 2050. A Roadmap for the Global Energy Sector. Technical report, 2021.
- [77] Didier Vuarnoz and Thomas Jusselme. Temporal variations in the primary energy use and greenhouse gas emissions of electricity provided by the Swiss grid. *Energy*, 161:573–582, 10 2018. doi:10.1016/J.ENERGY.2018.07.087.
- [78] Michel Noussan, Roberta Roberto, and Benedetto Nastasi. Performance Indicators of Electricity Generation at Country Level—The Case of Italy. *Energies*, 11(3), 2018. URL: <https://www.mdpi.com/1996-1073/11/3/650>, doi:10.3390/en11030650.
- [79] Imran Khan, Michael W. Jack, and Janet Stephenson. Analysis of greenhouse gas emissions in electricity systems using time-varying carbon intensity. *Journal of Cleaner Production*, 184:1091–1101, 5 2018. doi:10.1016/J.JCLEPRO.2018.02.309.
- [80] Iea International Energy Agency. Austria Energy Data. Technical report. URL: <https://www.iea.org/countries/austria>.
- [81] Energy Information Administration. EIA - Hourly Electricity Data. URL: <https://www.eia.gov/electricity/>.
- [82] ENTSOE Transparency Platform. Actual Generation per Production Type. URL: <https://transparency.entsoe.eu/generation/r2/actualGenerationPerProductionType/show>.
- [83] GSI. GSI s.r.l. URL: <https://www.gsicontrol.it/>.
- [84] Greater London Authority. London Datastore website. URL: <https://data.london.gov.uk/>.
- [85] Intergovernmental Panel on Climate Change. IPCC website. URL: <https://www.ipcc.ch/>.
- [86] Intergovernmental Panel on Climate Change. IPCC emissivity factors - Dataset. URL: https://github.com/tmrowco/electricitymap-contrib/blob/master/config/co2eq_parameters.json.
- [87] Intergovernmental Panel on Climate Change. 5th Assessment Report - Synthesis. URL: <https://www.ipcc.ch/report/ar5/syr/>.

- [88] Intergovernmental Panel on Climate Change. 5th Assessment Report - Metrics and Methodology. URL: https://www.ipcc.ch/site/assets/uploads/2018/02/ipcc_wg3_ar5_annex-ii.pdf.
- [89] Intergovernmental Panel on Climate Change. 5th Assessment Report - Technology-specific Cost and Performance Parameters. URL: https://www.ipcc.ch/site/assets/uploads/2018/02/ipcc_wg3_ar5_annex-iii.pdf.
- [90] Jianfeng Guo, Xuemei Zhang, Fu Gu, Hanqi Zhang, and Ying Fan. Does air pollution stimulate electric vehicle sales? Empirical evidence from twenty major cities in China. *Journal of Cleaner Production*, 249:119372, 3 2020. doi:10.1016/J.JCLEPRO.2019.119372.
- [91] Daniel Heinz. Erstellung und Auswertung repräsentativer Mobilitäts- und Ladeprofile für Elektrofahrzeuge in Deutschland. Technical report, Karlsruher Institut für Technologie (KIT), 2018. doi:10.5445/IR/1000086372.
- [92] ReCognition official Website. URL: <https://re-cognition-project.eu/>.
- [93] European Commission. Energy Efficient Buildings webPage. URL: https://ec.europa.eu/energy/topics/energy-efficiency/energy-efficient-buildings_en.
- [94] European Union. European Green Transition - Fit for 55. URL: <https://www.consilium.europa.eu/en/policies/green-deal/fit-for-55-the-eu-plan-for-a-green-transition/>.
- [95] H2020 WebSite. URL: <https://ec.europa.eu/programmes/horizon2020/en/home>.
- [96] European Commission. COM(2020) 662 final. A Renovation Wave for Europe. 53(9):1689–1699, 2020.
- [97] POLITECNICO DI TORINO. URL: www.polito.it.
- [98] ETHNIKO KENTRO EREVNAS KAI TECHNOLOGIKIS ANAPTYXIS. URL: WWW.CERTH.GR.
- [99] ENERGY@WORK SOCIETA' COOPERATIVA A R.L. URL: WWW.ENERGYATWORK.IT.
- [100] INTRACOM SA DEFENSE ELECTRONIC SYSTEMS. URL: www.intracomdefense.com.
- [101] ZH SRL. URL: www.zh-spinoff.it.
- [102] ECOLE POLYTECHNIQUE FEDERALE DE LAUSANNE. URL: www.epfl.ch.
- [103] CSEM CENTRE SUISSE D'ELECTRONIQUE ET DE MICROTECHNIQUE SA - RECHERCHE ET DEV. URL: www.csem.ch.

- [104] WINDCITY SRL. URL: www.windcity.it.
- [105] MICRO TURBINE TECHNOLOGY BV. URL: www.mtt-eu.com.
- [106] ELLINIKΑ PETRELAIA AE. URL: www.helpe.gr.
- [107] UNIVERSITY OF BRISTOL. URL: www.bristol.ac.uk.
- [108] ELECTRIC CORBY COMMUNITY INTEREST COMPANY. URL: www.electriccorby.co.uk.
- [109] ETREL SVETOVANJE IN DRUGE STORITVE DOO. URL: www.etrel.com.
- [110] UNIVERSITATEA TEHNICA CLUJ-NAPOCA. URL: <http://www.utcluj.ro>.
- [111] T S Ge, Y J Dai, R Z Wang, and Y Li. Feasible study of a self-cooled solid desiccant cooling system based on desiccant coated heat exchanger. *Applied Thermal Engineering*, 58(1-2):281–290, 2013. doi:10.1016/j.applthermaleng.2013.04.059.
- [112] Y. D. Tu, R. Z. Wang, and T. S. Ge. New concept of desiccant-enhanced heat pump. *Energy Conversion and Management*, 156:568–574, 1 2018. doi:10.1016/J.ENCONMAN.2017.11.068.
- [113] L. J. Hua, T. S. Ge, and R. Z. Wang. Extremely high efficient heat pump with desiccant coated evaporator and condenser. *Energy*, 170:569–579, 3 2019. doi:10.1016/J.ENERGY.2018.12.169.
- [114] Y D Tu, R Z Wang, T S Ge, and X Zheng. Comfortable, high-efficiency heat pump with desiccant-coated, water-sorbing heat exchangers. *Scientific Reports*, 7(1):40437, 2017. doi:10.1038/srep40437.
- [115] G. Angrisani, C. Roselli, M. Sasso, and F. Tariello. Dynamic performance assessment of a solar-assisted desiccant-based air handling unit in two Italian cities. *Energy Conversion and Management*, 113:331–345, 4 2016. doi:10.1016/J.ENCONMAN.2016.01.052.
- [116] Douglas M. Ruthven. Principles of Adsorption and Adsorption Processes, 1984.
- [117] Elyse Canosa, Sara Norrehed, Anders Karlsson, Andreas Fischer, and Charlotta Rigbrandt. Adsorbents for Pollution Reduction in Cultural Heritage Collections. *Researchgate Review*, (November), 2019.
- [118] Hao Wu, Fabrice Salles, and Jerzy Zajac. A Critical Review of Solid Materials for Low-Temperature Thermochemical Storage of Solar Energy Based on Solid-Vapour Adsorption in View of Space Heating Uses. *Molecules*, 24(5), 2019. URL: <https://www.mdpi.com/1420-3049/24/5/945>, doi:10.3390/molecules24050945.
- [119] ENEREN. ENEREN webpage. URL: <https://eneren.it/>.

- [120] ENEREN. ENEREN HP. URL: https://drive.google.com/file/d/1tIHbu_d4oG6-uMnqMzsryGcT9kpQnDDO/view?usp=sharing.
- [121] Gelest. Gelest Website. URL: <https://www.gelest.com/>.
- [122] Angelo Freni, Andrea Frazzica, Belal Dawoud, Stefanie Chmielewski, Luigi Calabrese, and Lucio Bonaccorsi. Adsorbent coatings for heat pumping applications: Verification of hydrothermal and mechanical stabilities. *Applied Thermal Engineering*, 50(2):1658–1663, 2013. doi:10.1016/j.applthermaleng.2011.07.010.
- [123] Angelo Freni, Lucio Bonaccorsi, Luigi Calabrese, Angela Caprì, Andrea Frazzica, and Alessio Sapienza. SAPO-34 coated adsorbent heat exchanger for adsorption chillers. *Applied Thermal Engineering*, 82:1–7, 2015. URL: <https://www.sciencedirect.com/science/article/pii/S135943111500160X>, doi: <https://doi.org/10.1016/j.applthermaleng.2015.02.052>.
- [124] Alvaro Mata, Aaron J Fleischman, and Shuvo Roy. Characterization of Polydimethylsiloxane (PDMS) Properties for Biomedical Micro/Nanosystems. *Biomedical Microdevices*, 7(4):281–293, 2005. doi:10.1007/s10544-005-6070-2.
- [125] Ronaldo Ariati, Flaminio Sales, Andrews Souza, Rui A Lima, and João Ribeiro. Polydimethylsiloxane Composites Characterization and Its Applications: A Review. *Polymers*, 13(23), 2021. URL: <https://www.mdpi.com/2073-4360/13/23/4258>, doi:10.3390/polym13234258.
- [126] KERN. KERN KB360-3N.
- [127] KERN. Moisture analyser KERN DBS, 2021.
- [128] T. S. Ge, Y. J. Dai, and R. Z. Wang. Performance study of silica gel coated fin-tube heat exchanger cooling system based on a developed mathematical model. *Energy Conversion and Management*, 52(6):2329–2338, 6 2011. doi:10.1016/J.ENCONMAN.2010.12.047.
- [129] Mrinal Jagirdar and Poh Seng Lee. Mathematical modeling and performance evaluation of a desiccant coated fin-tube heat exchanger. *Applied Energy*, 212:401–415, 2 2018. doi:10.1016/J.APENERGY.2017.12.038.
- [130] Amir Sharafian, Khorshid Fayazmanesh, Claire McCague, and Majid Bahrami. Thermal conductivity and contact resistance of mesoporous silica gel adsorbents bound with polyvinylpyrrolidone in contact with a metallic substrate for adsorption cooling system applications. *International Journal of Heat and Mass Transfer*, 79:64–71, 12 2014. doi:10.1016/J.IJHEATMASSTRANSFER.2014.07.086.
- [131] Y. Zhao, Y. J. Dai, T. S. Ge, X. Y. Sun, and R. Z. Wang. On heat and moisture transfer characteristics of a desiccant dehumidification unit using fin tube heat exchanger with silica gel coating. *Applied Thermal Engineering*, 91:308–317, 12 2015. doi:10.1016/J.APPLTHERMALENG.2015.07.075.

- [132] Ahmad A. Pesaran and Anthony F. Mills. Moisture transport in silica gel packed beds—I.Theoretical study. *International Journal of Heat and Mass Transfer*, 30(6):1037–1049, 6 1987. doi:10.1016/0017-9310(87)90034-2.
- [133] X. Y. Sun, Y. J. Dai, T. S. Ge, Y. Zhao, and R. Z. Wang. Experimental and comparison study on heat and moisture transfer characteristics of desiccant coated heat exchanger with variable structure sizes. *Applied Thermal Engineering*, 137:32–46, 6 2018. doi:10.1016/J.APPLTHERMALENG.2018.03.071.
- [134] A. Li, K. Thu, A.B. Ismail, and K.C. Ng. A heat transfer correlation for transient vapor uptake of powdered adsorbent embedded onto the fins of heat exchangers. *Applied Thermal Engineering*, 93:668–677, 2016. doi:10.1016/j.applthermaleng.2015.09.057.
- [135] T. S. Ge, Y. J. Dai, R. Z. Wang, and Z. Z. Peng. Experimental comparison and analysis on silica gel and polymer coated fin-tube heat exchangers. *Energy*, 35(7):2893–2900, 7 2010. doi:10.1016/J.ENERGY.2010.03.020.
- [136] Y. Jiang, T. S. Ge, R. Z. Wang, and L. M. Hu. Experimental investigation and analysis of composite silica-gel coated fin-tube heat exchangers. *International Journal of Refrigeration*, 51:169–179, 3 2015. doi:10.1016/J.IJREFRIG.2014.11.012.
- [137] RE-Lab-Projects / hplib. URL: <https://github.com/RE-Lab-Projects/hplib>.
- [138] CEN KEYMARK. URL: <https://keymark.eu/en/products/heatpumps/certified-products>.

Appendix A

Heat Pump Profiles and Electricity Energy Mix

Hereafter are reported the different HP profiles, compared with the different EU countries generation mix.

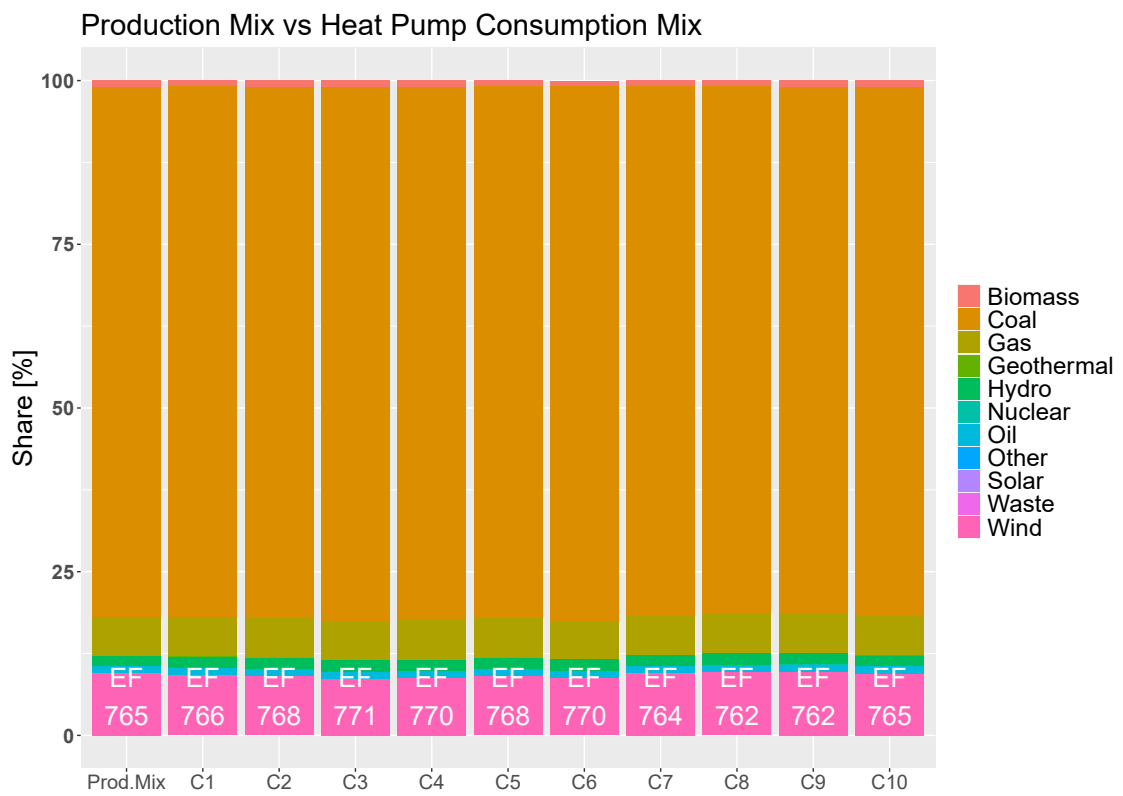


Fig. A.1 POLAND - electricity production mix compared with the electricity consumption mix of the different HP systems

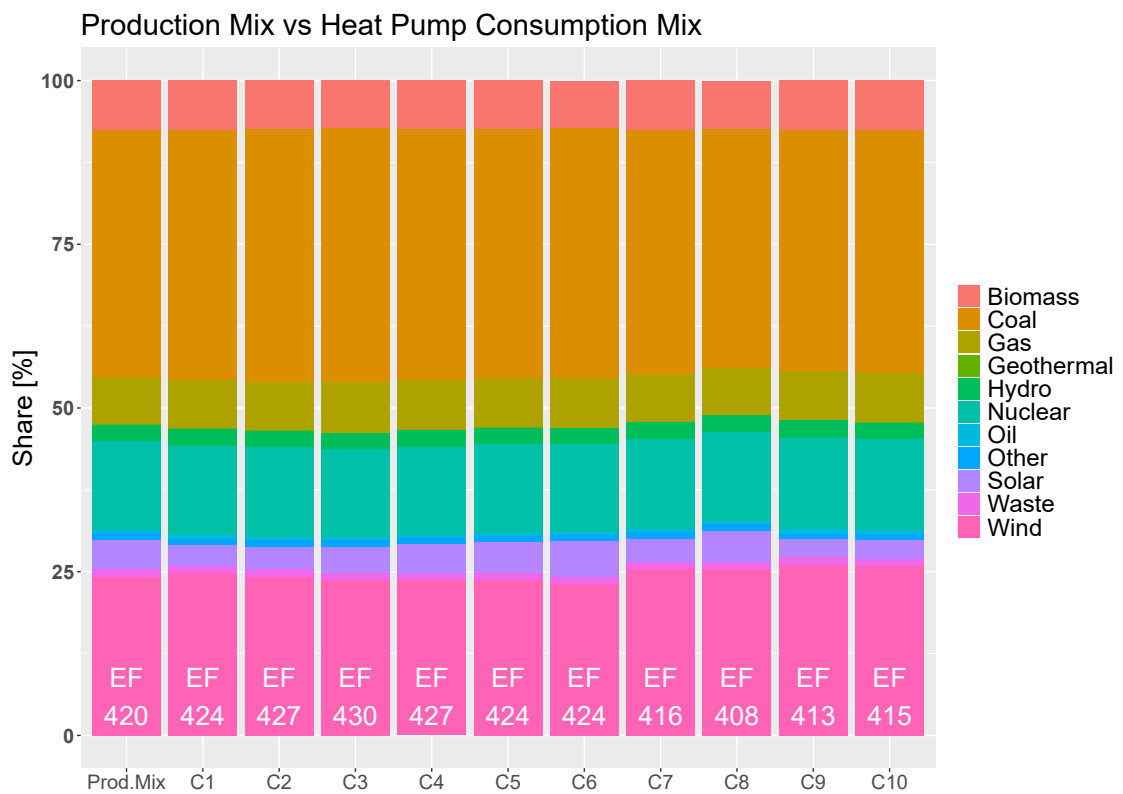


Fig. A.2 GERMANY - electricity production mix compared with the electricity consumption mix of the different HP systems

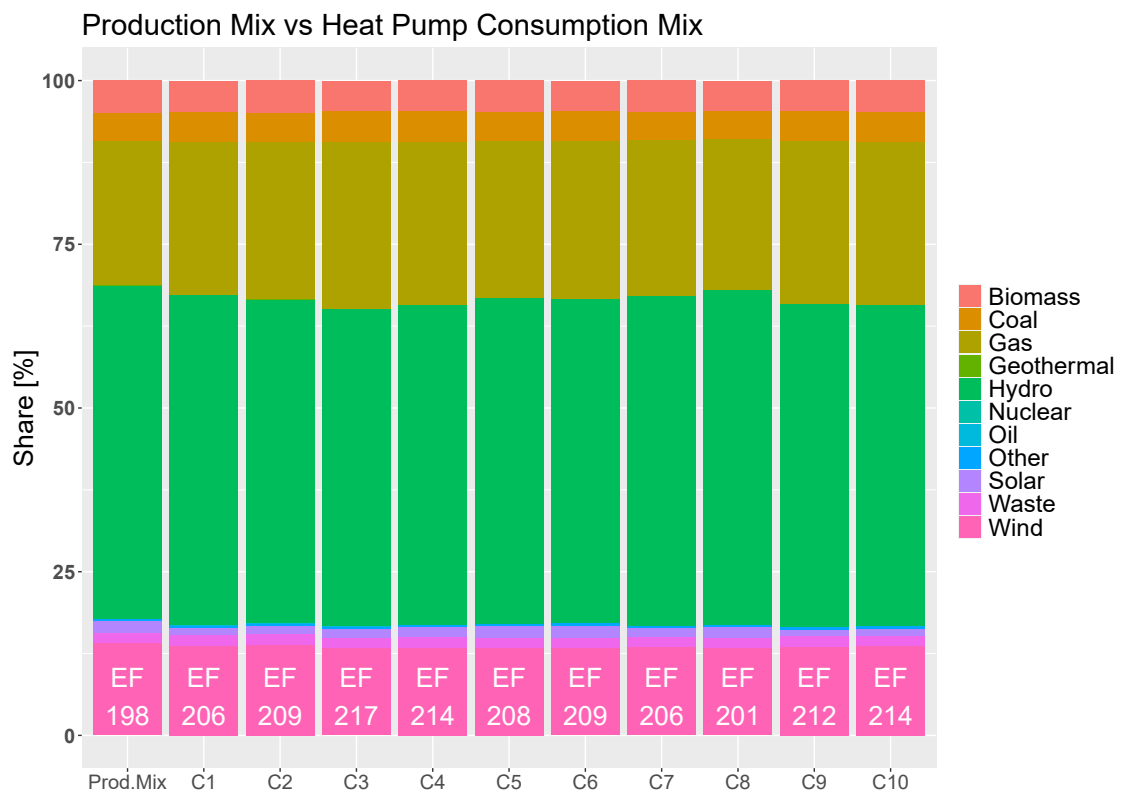


Fig. A.3 AUSTRIA - electricity production mix compared with the electricity consumption mix of the different HP systems

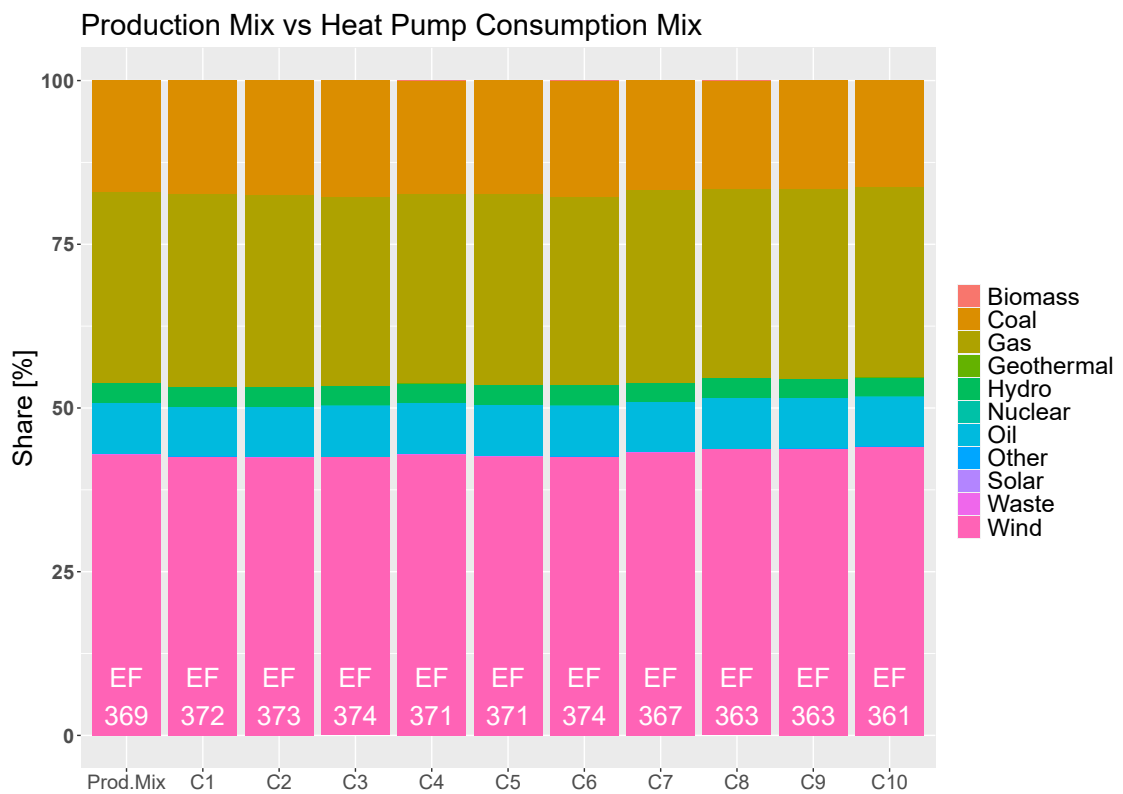


Fig. A.4 IRELAND - electricity production mix compared with the electricity consumption mix of the different HP systems

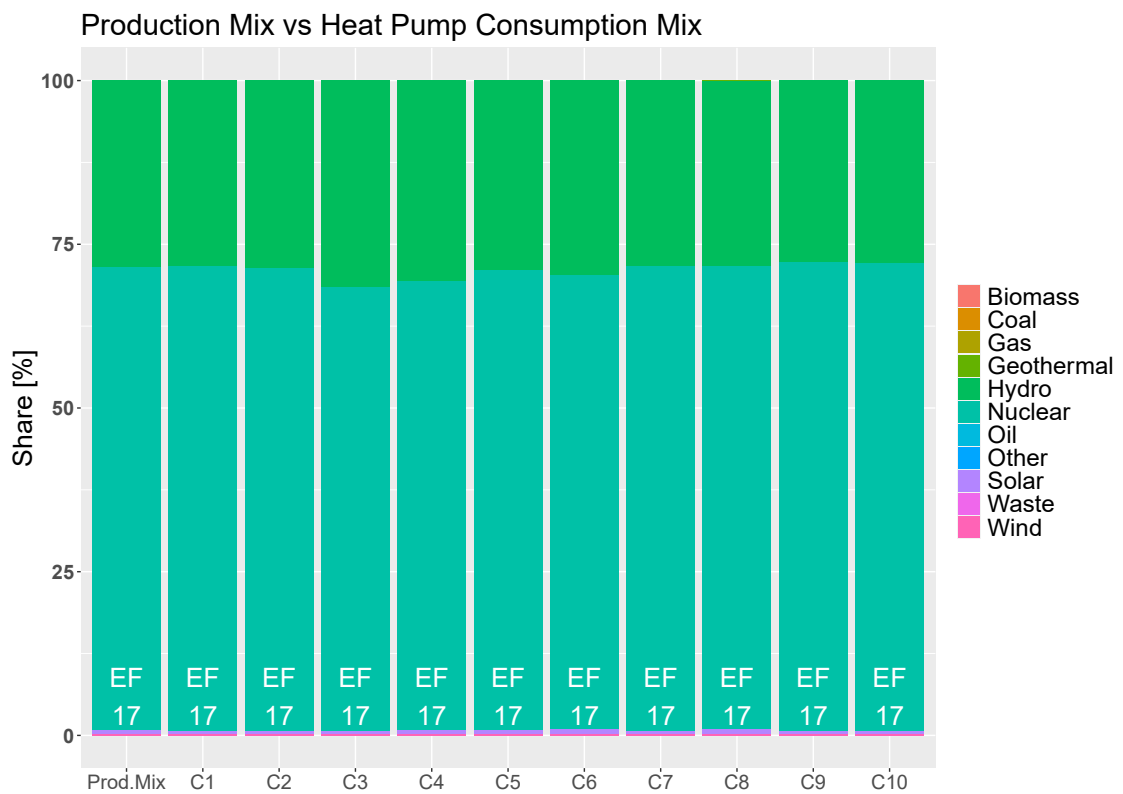


Fig. A.5 SWITZERLAND - electricity production mix compared with the electricity consumption mix of the different HP systems

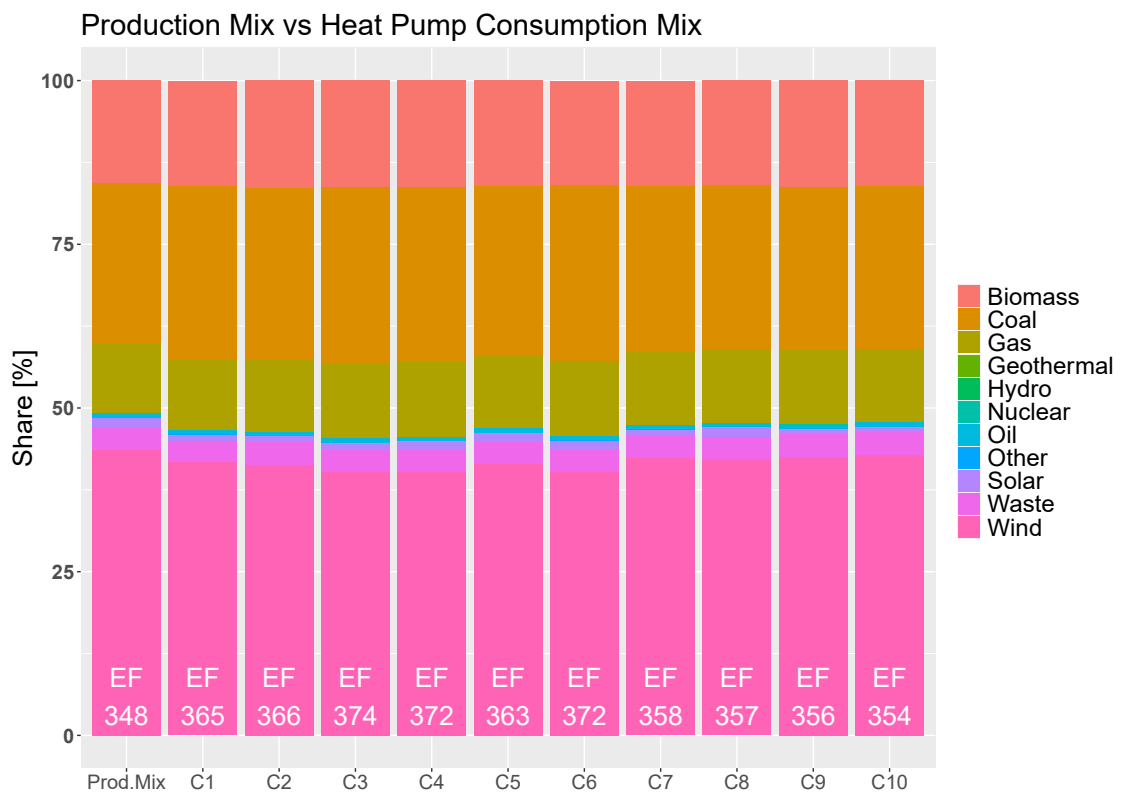


Fig. A.6 DENMARK - electricity production mix compared with the electricity consumption mix of the different HP systems

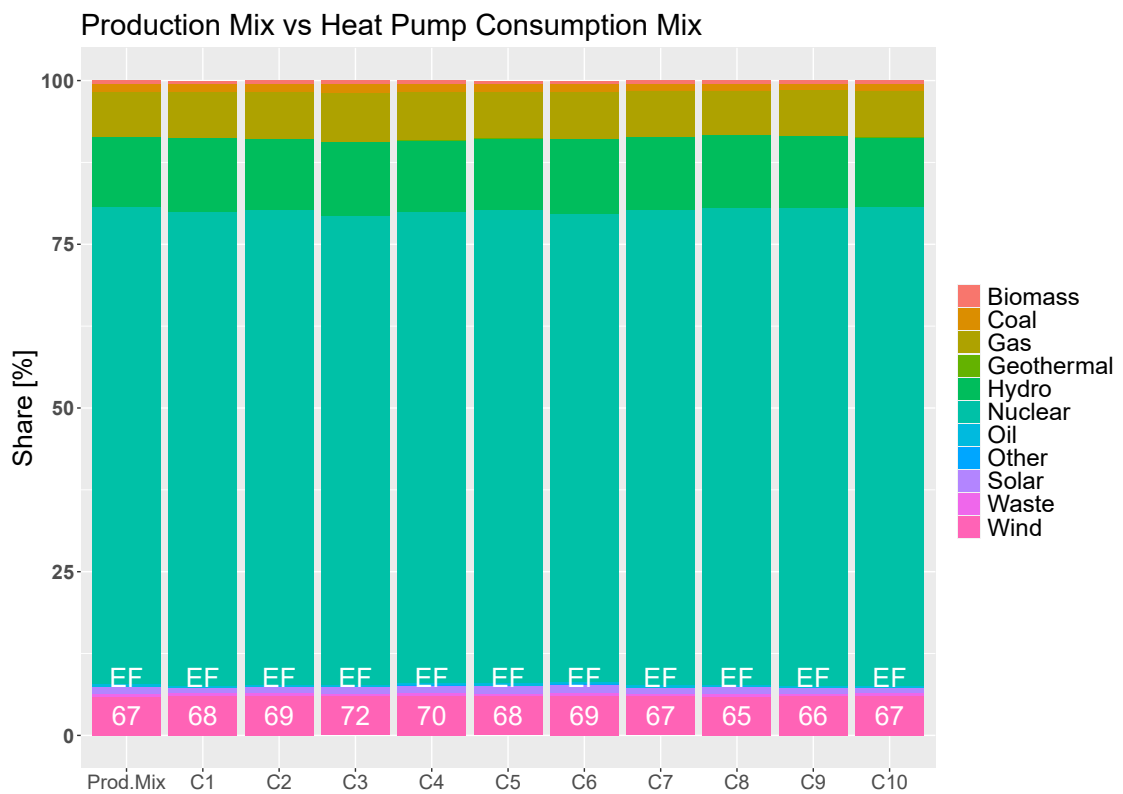


Fig. A.7 FRANCE - electricity production mix compared with the electricity consumption mix of the different HP systems

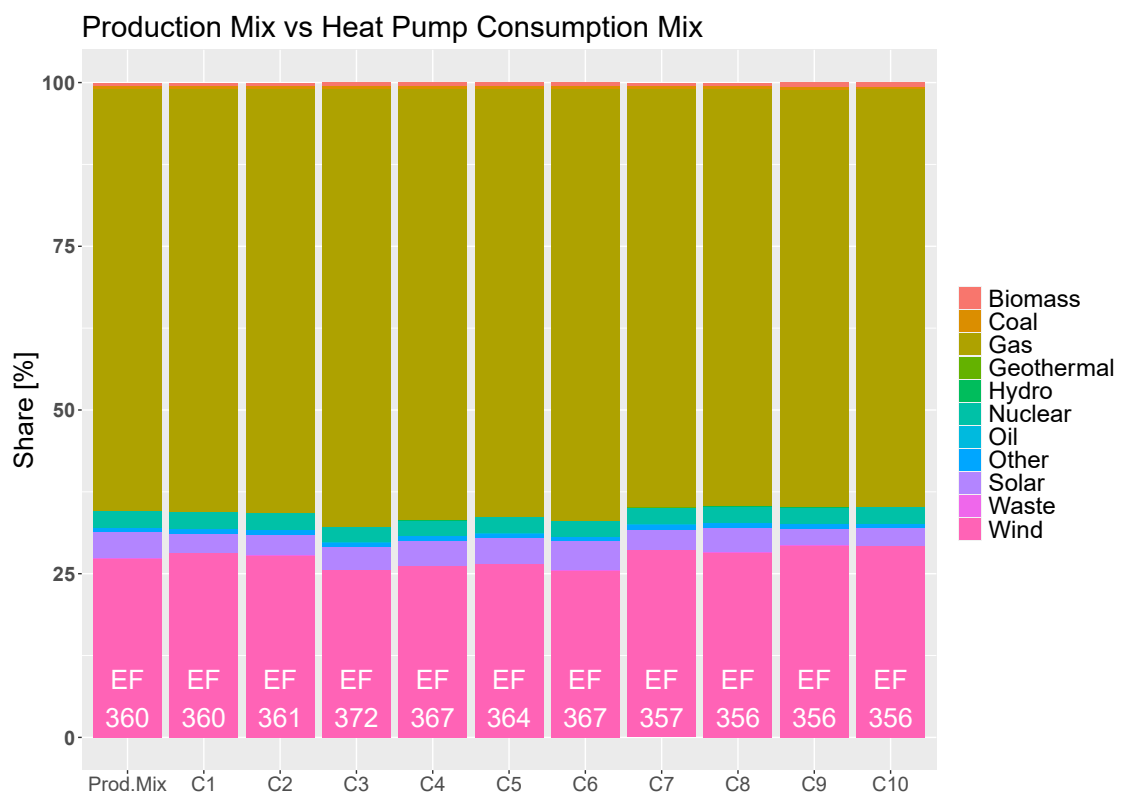


Fig. A.8 NETHERLANDS - electricity production mix compared with the electricity consumption mix of the different HP systems

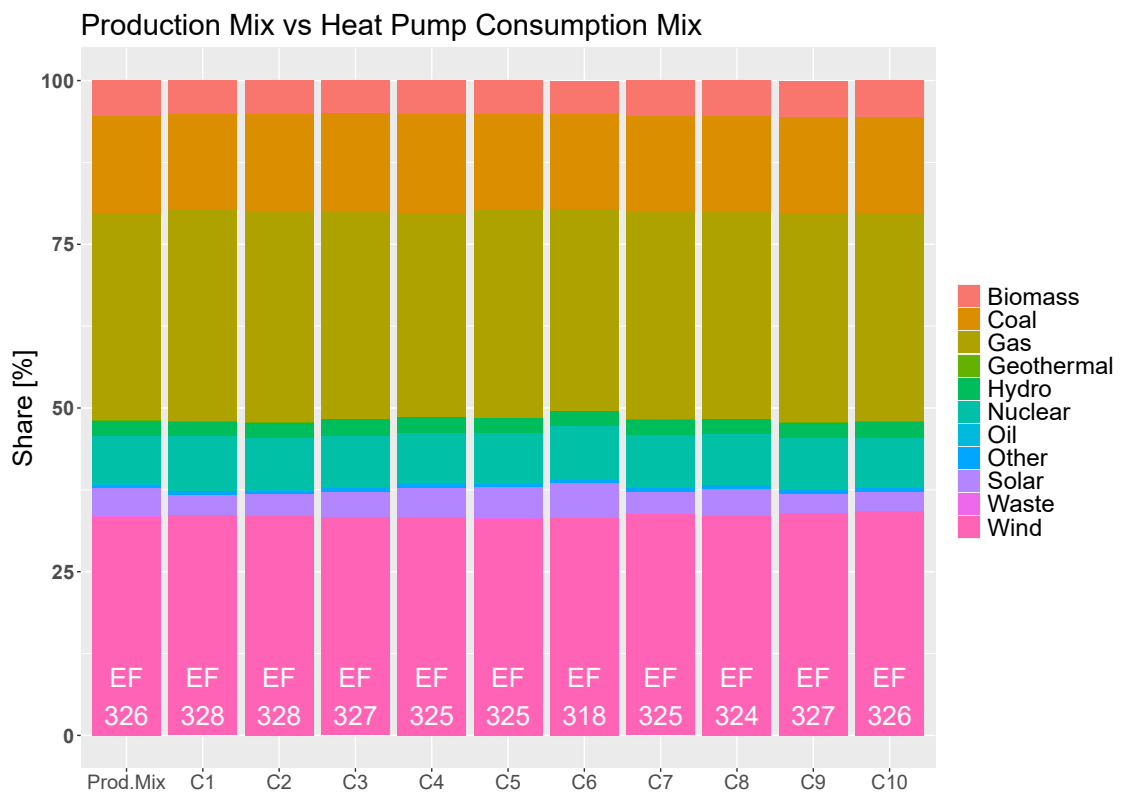


Fig. A.9 UNITED KINGDOM - electricity production mix compared with the electricity consumption mix of the different HP systems

Appendix B

Adsorption model

B.1 Convergence analysis

This section is dedicated to the convergence study of the model in terms of space and time. A numerical model is convergent if the model reaches a fixed value as space and time domains are refined. Consequently, at the same time, it is possible to find out if the time step and the size of the finite space elements utilized allow to obtain an accurate solution. Moreover, a comparison among the computational times for the various domain definitions is executed with the purpose of understanding if there are significant differences.

Space convergence

The space convergence has been based on a range of different Δz to discretize the space domain: $\Delta z = 0.5mm$, $\Delta z = 1mm$, $\Delta z = 3mm$, $\Delta z = 5mm$, $\Delta z = 10mm$, $\Delta z = 30mm$ and $\Delta z = 50mm$.

Then, a chosen output is selected and calculated using the different Δz . In this case the maximum outlet air temperature in adsorption mode, during the first cycle, is used for the study. The results obtained are presented in the following figures.

As the Δz decreases, the trend of the temperature becomes flat, converging to a specific value, that is equal to about $38.6\text{ }^{\circ}\text{C}$. The chosen Δz gives a value approximately equal to $38.3\text{ }^{\circ}\text{C}$ with a relative error with respect of the most refined solution of 0.73% .

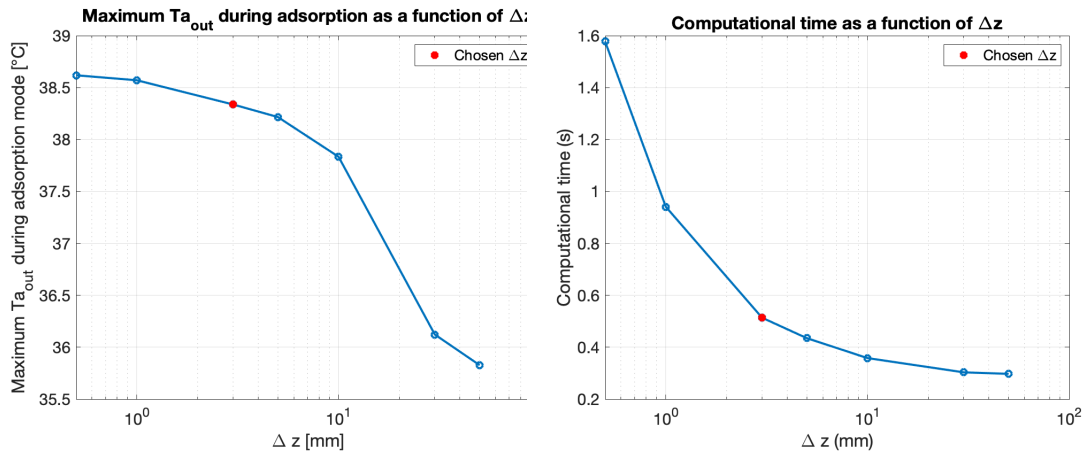


Fig. B.1 Maximum air outlet temperature during adsorption and computational time as a function of Δz

Concerning the computational time, which is calculated over the first adsorption phase, it significantly decreases shifting from $\Delta z = 0.5\text{mm}$ to $\Delta z = 3\text{mm}$ and, then, it settles, reaching a duration around 0.3 s. Therefore, the solution given by the chosen Δz is a good compromise between an accurate solution and a limited computational time (equal to 0.54 s).

Time convergence

In order to execute the time convergence study, a range of time step is set: $\Delta t = 0.1\text{s}$, $\Delta t = 0.5\text{s}$, $\Delta t = 1\text{s}$, $\Delta t = 5\text{s}$, $\Delta t = 10\text{s}$, $\Delta t = 15\text{s}$, $\Delta t = 20\text{s}$.

Again, the maximum outlet air temperature during the first adsorption cycle is considered with the purpose of comparing the solutions obtained through the definition of different time domains.

As the time step reduces, the temperature converges to a fixed value (about 38.5 °C). The chosen Δt gives the same solution as before, since, in both cases, the Δz is equal to 3mm and the Δt is equal to 1s. The relative error relating to the most refined solution is equal to 0.47%.

The computational time has a trend which flattens as the Δt increases (reaching almost 0.03 s when $\Delta t = 20\text{s}$), with a substantial reduction passing from $\Delta t = 0.1\text{s}$ to $\Delta t = 0.5\text{s}$.

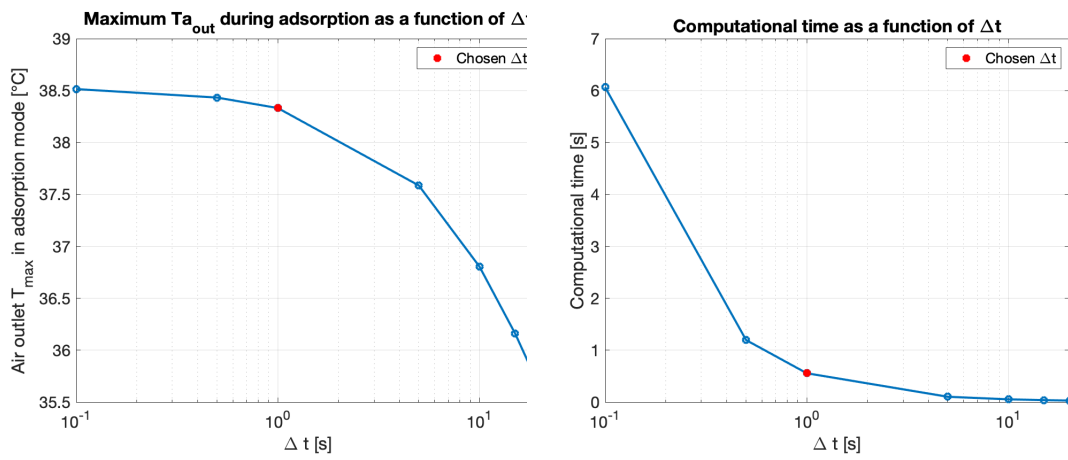


Fig. B.2 Maximum air outlet temperature during adsorption and computational time as a function of Δt

B.2 Parametric Analysis

B.2.1 Heat Exchanger Length

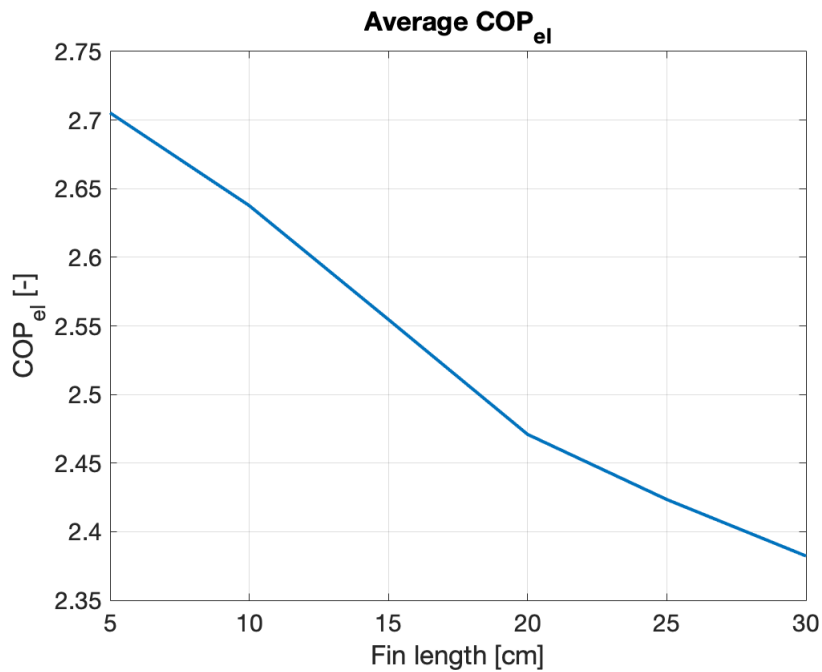


Fig. B.3 Average COP_{el} variation

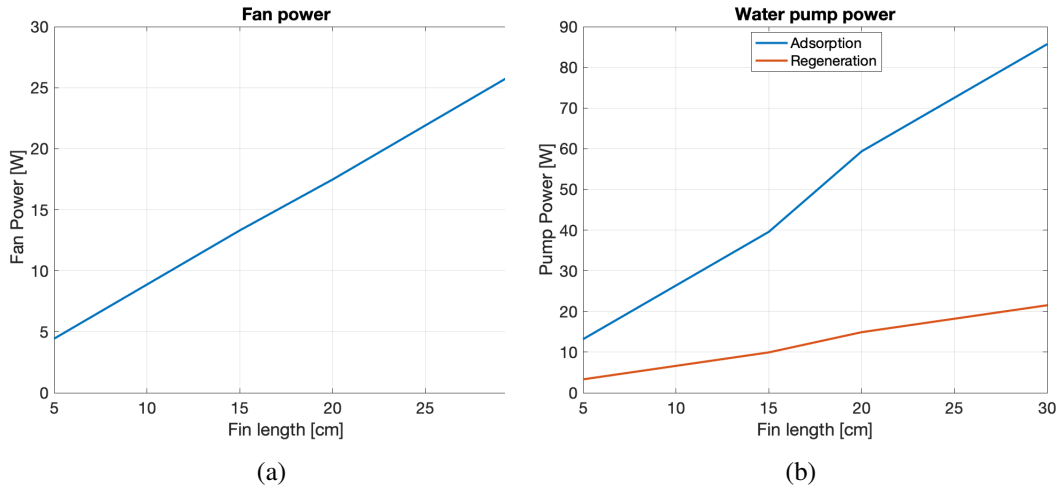


Fig. B.4 (a) Fan and (b) water pump electric power request for different heat exchanger lengths

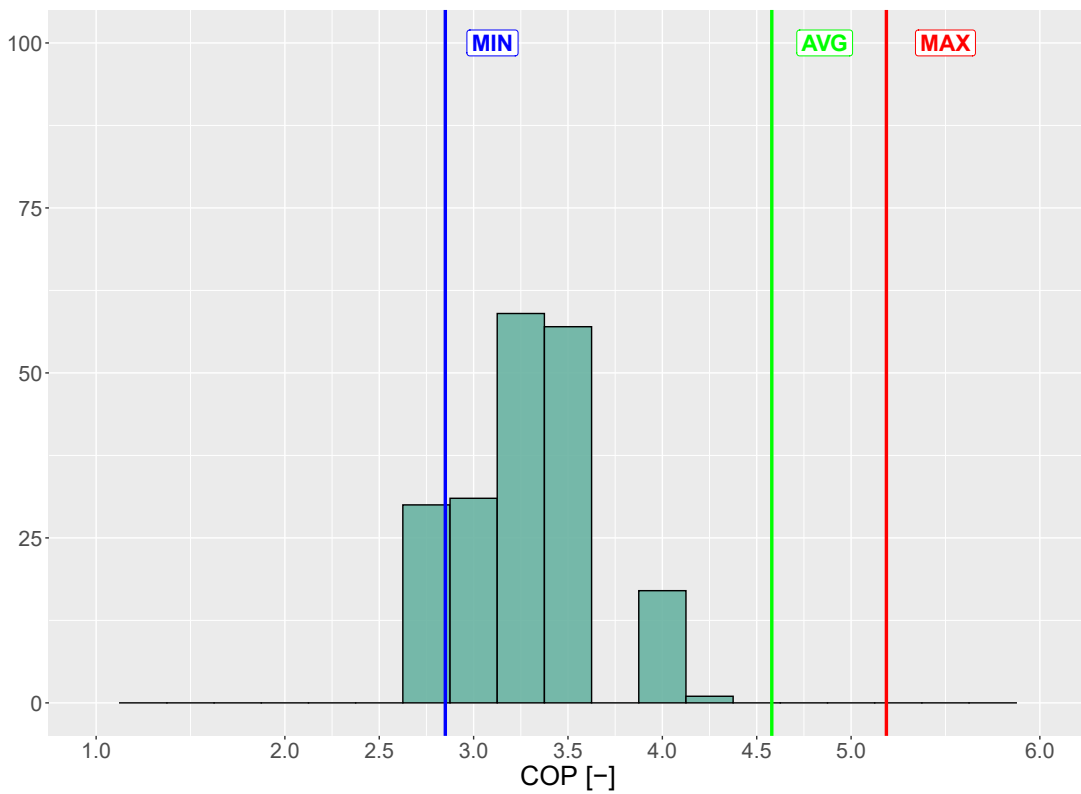


Fig. B.5 HySun COP comparison with respect to different market ready HP technologies. Cooling Output Power Limited to 5kW

B.3 HySun and Dryer: Scheme and Drawings



Fig. B.6 Adsorption Unit. Real Prototype



Fig. B.7 Adsorption Unit. Real Prototype

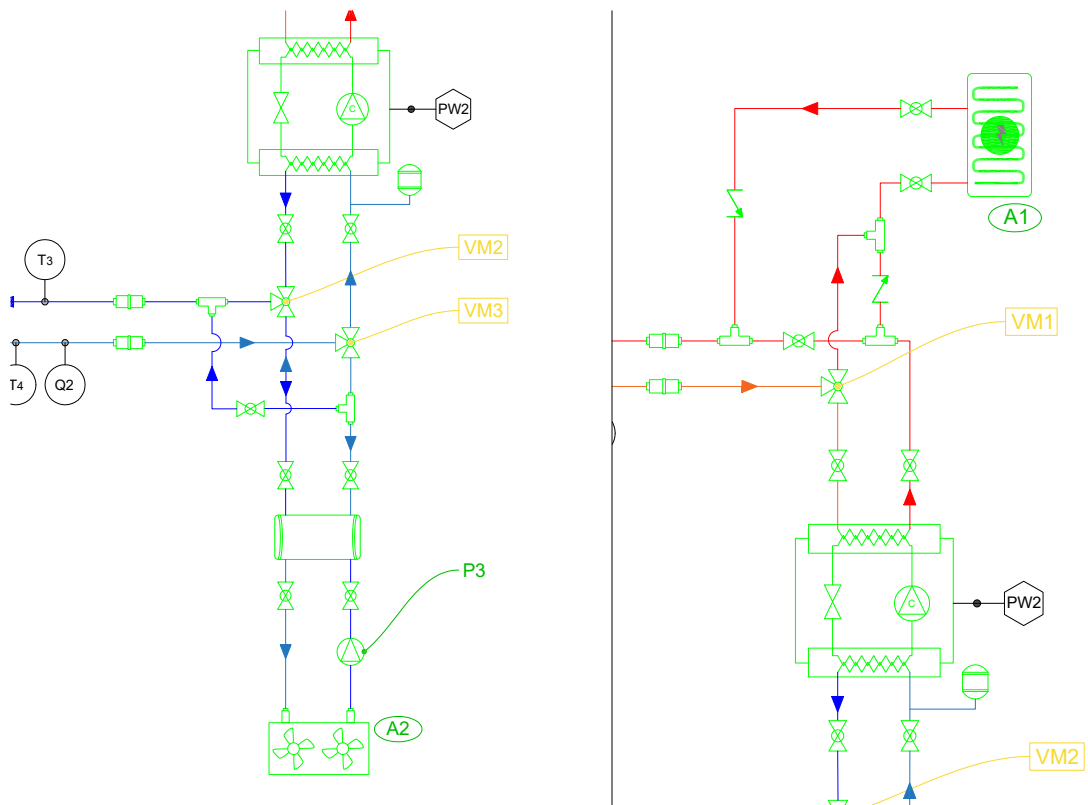


Fig. B.8 CAD scheme: Auxiliary Cooler connection(left) and Heater (right)



Fig. B.10 Dryer Machine



Fig. B.11 Dryer Machine